University of Alberta

Evaluation of a Hollow Cathode Atomic Emission Source Designed for Continuous Sample Introduction and Time Resolved Investigations of Laser Ablated Plumes by ICP-AES.

by

Stuart G. Schroeder 

A thesis submitted to the Faculty of Graduate Studies and Research in partial fulfillment of the requirements for the degree of Doctor of Philosophy.

Department of Chemistry

Edmonton, Alberta

Fall, 1996

ISBN 0-612-18104-9

Canada

University of Alberta

Library Release Form

Name of Author:	Stuart G. Schroeder
Title of Thesis:	Evaluation of a Hollow Cathode Atomic Emission Source Designed for Continuous Sample Introduction and Time Resolved Investigations of Laser Ablated Plumes by ICP-AES.
Degree:	Doctor of Philosophy
Year this Degree Granted:	1996

300 Regency Dr.
Sherwood Park, Alberta
T8A 5P4

Date: Sept 30, 1996

University of Alberta

Faculty of Graduate Studies and Research

The undersigned certify that they have read, and recommend to the Faculty of Graduate Studies and Research for acceptance, a thesis entitled EVALUATION OF A HOLLOW CATHODE ATOMIC EMISSION SOURCE DESIGNED FOR CONTINUOUS SAMPLE INTRODUCTION AND TIME RESOLVED INVESTIGATIONS OF LASER ABLATED PLUMES BY ICP-AES submitted by Stuart G. Schroeder in partial fulfillment of the requirements for the degree of Doctor of Philosophy.

Dr. G. Horlick

Dr. F. F. Cantwell

Dr. L. Li

Dr. J. Bertie

Dr. R. Fedosejevs

Dr. R. E. Russo

Date: Sept. 19, 1996

To Betsy, Garth, Bradley, and Wesley...

...keep on shining

Abstract

Two plasma emission techniques have been studied. The description of a high power hollow cathode discharge (HCD) with a unique sample introduction interface is presented. Time resolved measurements showing detection of individual particles with inductively coupled plasma-atomic emission spectrometry (ICP-AES) is also presented.

A HCD capable of continuous operation with solid, solution, and gaseous sample introduction is described. Emphasis is placed on the solution sample interface with a high power HCD. Discharge current densities up to 0.64 A/cm^2 are maintained in a helium plasma. Analyte emission intensities are optimized in terms of anode placement in relation to the hollow cathode, carrier gas flow rate, discharge current, and sample solution flow rate. Detection limits for selected elements are reported and range from 0.03 ng/ml for Li to 200 ng/ml for Zn. Temporal stability of the discharge is examined and a calibration curve for Li is presented. Solid samples are introduced into the HCD and preliminary results are presented. Observation of Cl ionic emission is observed for gaseous analysis.

Entire emission profiles of a single laser ablation event are presented in a time resolved manner by ICP-AES. Emission profiles from the vapor plumes of individual particles are observed. Detection limits in the fg range illustrate the high sensitivity of this technique. Particle size distributions are constructed from the emission profiles originating from one laser ablation event and reflect the transport efficiency of particles with different compositions. Simultaneous multi-element analysis of individual particles shows that the elemental concentrations on a particle to particle basis do not represent the concentrations found in the bulk sample. A comparison between lateral and axial viewing of the ICP is made for the observation of individual particles. For axial viewing,

the emission profiles originating from single particles reveal spatial emission characteristics. Emission due to ion-electron recombination is observed for selected atomic emission lines.

Acknowledgments

I would like to thank Professor Gary Horlick for his patience, encouragement, and ability to transfer his vision of atomic spectroscopy to his students.....for always looking for the better way. Thanks also goes to the members of the research group.

Most of all, I would like to thank my wife Betsy for standing by me, believing in me, and allowing me to pursue my dreams. I would also like to thank my sons Garth, Bradley, and Wesley for their smiling faces and many hugs.

Lastly, I would like to acknowledge family and friends for their continued support.

TABLE OF CONTENTS

CHAPTER		PAGE
1.	Introduction	1
	1.1 Introduction	1
	1.2 Characteristics of a Glow Discharge Device used for atomic spectroscopy	2
	1.2.1 Electrical breakdown of gases and operation regimes	2
	1.2.2 Fundamental collision processes in glow discharge devices	9
	1.2.3 Analytical methods used with GDDs	14
	1.3 The hollow cathode discharge	18
	1.3.1 Historical development of the HCD	18
	1.3.2 Characteristics of the HCD	20
	1.4 Sample introduction into an operating GDD	21
	1.4.1 Introduction	22
	1.4.2 Literature review of sample introduction into an operating GDD	23
	References	32
2.	Evaluation of a HCD designed for continuous sample introduction	36
	2.1 Introduction	36
	2.2 Description of the hollow cathode source	37
	2.3 Sample introduction	39
	2.4 Instrumentation	41
	2.5 Reagents	43
	2.6 Results and discussion	43
	2.6.1 Voltage-current characteristics of the HCD	43
	2.6.2 Emission spectra from Ca and Mg	45
	2.6.3 Optimization of instrumental conditions	48
	2.6.3.1 Effect of anode position relative to hollow cathode	49

CHAPTER PAGE

2.6.3.2 Effect of carrier gas flow rate..... 49
2.6.3.3 Effect of discharge current..... 51
2.6.3.4 Effect of sample solution flow rate..... 51
2.6.4 Emission spectra from selected elements..... 55
2.6.5 Memory effect, signal stability and linear dynamic range for Li detection..... 60
2.7 Attempted solution sample introduction by electrospray nebulization..... 63
2.8 Solid sample introduction by laser ablation..... 63
2.9 Halogen emission..... 69
2.10 Conclusions and future prospects..... 69
References..... 72
3. Introduction to time resolved particle analysis of laser ablated plumes by ICP-AES..... 74
3.1 The importance of particle analysis..... 74
3.2 Single particle analysis by ICP-AES..... 75
3.3 Laser ablation as a method of sample introduction..... 85
3.4 Introduction to time resolved measurements..... 94
References..... 101
4. Time resolved particle analysis by LA-ICP-AES: lateral viewing..... 103
4.1 Purpose of this study..... 103
4.2 Instrumentation..... 104
4.3 Samples..... 107
4.4 Calibration..... 107
4.4.1 Calibration procedure..... 112
4.5 Time resolved analysis by LA-ICP-AES: fundamental properties..... 114
4.5.1 Particle emission observed from one laser pulse..... 115

CHAPTER PAGE

4.5.2 Comparison to a conventional laser ablation acquisition..... 124
4.5.3 Comparison of frequency spectra: time resolved versus conventional analysis..... 128
4.6 Detection limit calculations..... 133
4.7 Cu emission from a steel sample..... 139
4.8 Correlation of particle emission and baseline noise..... 141
4.9 Baseline shifts as a result of undetected particle emission..... 145
4.10 Particle size distributions..... 147
4.11 Simultaneous multi-element determinations..... 150
4.11.1 Instrumentation..... 150
4.11.2 Simultaneous multi-element emission profiles..... 152
4.12 Summary and future direction..... 160
References..... 161
5. Preliminary investigation of axially viewed emission profiles from individual particles..... 162
5.1 Introduction..... 162
5.2 Axial viewing of ICP emission..... 163
5.3 Time resolved emission from individual particles in an axially viewed helium microwave induced plasma..... 166
5.4 Instrumentation..... 167
5.5 Axially viewed emission profiles from individual particles..... 170
5.5.1 Preliminary optimization..... 170
5.5.2 Entire emission profiles from one laser ablation pulse..... 174
5.5.3 Examples of emission profiles from vapor plumes of individual particles..... 177
5.5.4 Emission peak widths from individual particles..... 186

CHAPTER **PAGE**

5.5.5 Detection limits for Ca emission..... 194

5.6 Conclusion..... 196

References..... 197

6. Summary and future directions..... 198

6.1 Continuous sample introduction to a HCD..... 198

6.2 Time resolved detection of individual particles by ICP-AES..... 199

References..... 202

Appendix..... 203

LIST OF TABLES

TABLE	PAGE
1.1 Excitation and ionization processes in the glow discharge	11
2.1 Operating conditions for the HCD and sample introduction	42
2.2 Effect of Ca ion and atom, and ion to atom line intensity ratios on anode position relative to hollow cathode	50
2.3 Hollow cathode detection limits for nebulized solution samples	59
3.1 Calculation of mass and detection limits from micrometer sized particles, assuming a particle density of 8 g/cm^3 and an absolute detection limit of 0.17 pg	79
4.1 Hardware specifications and operating parameters for LA-ICP-AES: lateral viewing	108
4.2 Samples used for LA-ICP-AES	109
4.3 Emission characteristics of 10 of the most intense peaks of Fig. 4.3a	121
4.4 Emission characteristics of 10 low intensity peaks of Fig. 4.3a	121
4.5 Summary of detection limits obtained by different methods	138
5.1 Hardware specifications and operating parameters for axially viewed emission profiles from individual particles	168
5.2 Samples used for axially viewed ICP-AES investigation	169
5.3 Baseline peak widths of atomic emission profiles	188
5.4 Baseline peak widths of ionic emission profiles	188

LIST OF FIGURES

FIGURE		PAGE
1.1	Schematic representation of a simple glow discharge device.....	3
1.2	Operating regimes of various gas discharges. Vb, breakdown voltage and Vn, normal cathode fall voltage.....	4
1.3	Paschen curve for a hollow cathode discharge and a glow discharge in helium. The anode-to-cathode distance is d=1 cm.....	7
1.4	Fundamental collision processes in glow discharge devices.....	10
1.5	Collisional cross-section $\sigma(v)$ as a function of v, together with the Maxwell velocity distribution function f(v).....	13
1.6	Analytical methods which utilize the glow discharge.....	15
1.7	Schematic representation of a hollow cathode discharge.....	19
1.8	Exterior (a) and cutaway (b) views of the gas-sampling glow discharge.....	25
1.9	Cross-section view of glow discharge device.....	27
1.10	Detailed cross-section view of sample delivery port.....	27
1.11	Nebulizer and particle beam interface coupled to the heated hollow cathode atomic emission source.....	29
2.1	Cross-sectional scale drawing of HCD source.....	38
2.2	Experimental setup for solution sample introduction into the HCD source.....	40
2.3	Voltage-current relationship.....	44
2.4	PDA spectra of (a) background and 10 µg/ml Ca, 5.3 s integration and (b) background subtracted 1 µg/ml Ca, 5 scans averaged, 21.2 s integration per scan, low pass digitally filtered.....	46
2.5	PDA spectra of (a) background and 10 µg/ml Mg, 5.3 s integration and (b) background subtracted 10 µg/ml Mg, 10 scans averaged 10.6 s integration per scan, low pass digitally filtered.....	47

FIGURE **PAGE**

2.6 Effect of carrier gas flow rate on Ca and Mg, ion and atom line intensities and ion to atom line intensity ratios..... 52

2.7 Effect of discharge current on Ca ion and atom line intensities..... 53

2.8 Effect of sample solution flow rate on Ca ion and atom line intensities for a 10 µg/ml Ca solution..... 54

2.9 Background subtracted PDA spectra of (a) 0.1 µg/ml Li, 10.6 s integration, (b) 1 µg/ml Na, 5.3 s integration per scan, 5 scans averaged, (c) 1 µg/ml Cs, 42.5 s integration per scan, 5 scans averaged, and (d) 10 µg/ml K and Rb, 21.2 s integration per scan, 5 scans averaged..... 56

2.10 Background subtracted PDA spectra of (a) µg/ml Mn, Cd, and Zn, 21.2 s integration per scan, 5 scans averaged, low pass digitally filtered and (b) 10 µg/ml Al, 21.2 s integration per scan, 5 scans averaged, low pass digitally filtered... 58

2.11 Short term stability of the HCD during 1 µg/ml Li aspiration..... 61

2.12 Calibration curve for Li 670.8 nm, slope = 0.90. Emission intensities are the average of 600 digitized values collected at 100 ms/point..... 62

2.13 ES-MS interface and voltage biasing arrangement..... 64

2.14 Experimental setup for laser ablation with hollow cathode discharge excitation..... 65

2.15 Temporal emission profile of Cu. Sample was SRM 1265a, 0.0058% Cu in steel..... 67

2.16 Background subtracted PDA spectrum showing atomic Cu emission. Sample was SRM 1265a, 0.0058% Cu in steel..... 68

2.17 Ionic Cl emission observed in a HCD..... 70

3.1 Simulated low level signal of ICP-AES with conventional nebulization..... 77

3.2 Simulated signal from the same mass of analyte as in Fig. 3.6, but introduced as a single particle..... 77

FIGURE **PAGE**

3.3 Processes of laser ablation..... 87

3.4 Particle size distribution from the ablation of Mo metal. Ablated material was transported to the particle counter under the same conditions as transportation to the ICP torch..... 92

3.5 Calculated transport efficiency for Mo particles for various flow rates, tube i.d.'s, and lengths (a, 1.5 l/min, 4.5 mm, 80 cm; b, 1.5 l/min, 4.5 mm, 40 cm; c, 1.5 l/min, 2.25 mm, 80 cm)..... 93

3.6 Schematic representation of signal acquisition and digitization using a PMT as the detector..... 95

3.7 Amplifier frequency response at various rise times (a, 10 ms; b, 1.0 ms; c, 0.1 ms; d, 0.01 ms)..... 97

3.8 Photoelectric current pulses observed from a PMT..... 99

4.1 Schematic representation of experimental setup..... 105

4.2 Laser ablation chamber showing the directional flow of Ar..... 106

4.3 The entire (a) and scale expanded (b) emission profiles of Fe from a steel sample, SRM 1261a..... 117

4.4 Further scale expansion of the Fe emission profile found in Fig. 4.3..... 118

4.5 Emission profiles of large particles found from Fig. 4.3a..... 119

4.6 Emission profiles of small particles from Fig. 4.3a..... 120

4.7 Emission profiles of Cu in Brass, SRM C1106, (a) and Al in an Aluminum sample, Alcoa SS-380-6, (b)..... 123

4.8 Emission profile from Zn in steel, SRM 1261a, 0.0001%, (a) and Cu in steel, SRM 1261a, 0.042%, (b)..... 125

4.9 Emission profile of Fe, SRM 1261a, from a conventional laser ablation acquisition (a) and from a time resolved acquisition (b)..... 127

FIGURE **PAGE**

4.10 Frequency spectra of the emission profile shown in Fig. 4.3a (a) and from a laser blank (b)..... 130

4.11 Frequency spectra of the emission profile shown in Fig. 4.9a (a) and laser blank (b)..... 131

4.12 Frequency spectra of emission from 5 µg/ml Fe solution (a) and solution blank (b)..... 132

4.13 Expanded portion of frequency spectrum shown in Fig. 4.12a..... 134

4.14 Emission profiles of Fe in steel, SRM 1261a, single particle profile (a), average of 10 profiles (b), and digitally filtered average profile (c)..... 135

4.15 Emission profiles of Cu in steel, SRM 1261a, single particle profile (a), average of 5 profiles (b), and digitally filtered average profile (c)..... 136

4.16 Emission profiles of Zn in steel, SRM 1261a, single particle profile (a), average of 6 profiles (b), and digitally filtered average profile (c)..... 137

4.17 Sum of 649 individual emission profiles of Cu in steel, SRM 1261a..... 140

4.18 Correlation of baseline noise with emission profile of Fe in steel, SRM 1261a..... 142

4.19 Correlation of baseline noise with emission profile of Cu in steel, SRM 1261a..... 143

4.20 Correlation of baseline noise with emission profile of Zn in steel, SRM 1261a..... 144

4.21 Observation of baseline shifts due to an abundance of unresolved particles. Emission profile of Cu in brass, SRM C1106, (a) and Cu in aluminum, Alcoa SS-380-6, (b)..... 146

4.22 Particle size distributions for Fe in steel, SRM 1261a, (a) and Al in aluminum, Alcoa SS-380-6 (b)..... 148

FIGURE **PAGE**

4.23 Emission profile of a single Fe particle showing poor response of digital oscilloscope..... 151

4.24 Simultaneous multi-element emission profiles of Cu (a), Cr (b), and Fe (c) from stainless steel, SRM 1171..... 153

4.25 Cross correlation functions from emission profiles of Fe, Cu, and Cr..... 155

4.26 Expanded view of the cross correlation functions shown in Fig. 4.25..... 156

4.27 Simultaneous multi-element emission profiles of Fe, Cu, and Zn from steel, SRM 1261a..... 158

4.28 Simultaneous multi-element emission profiles of Fe, Cu, and Zn from steel, SRM 1261a..... 159

5.1 Schematic of axially oriented ICP..... 164

5.2 Solution nebulization of 5 µg/ml Cu. Emission intensity as a function of plasma length (a) and signal-to-background noise as a function of plasma length (b) at various aperture diameters. Cu I 324.754 nm..... 171

5.3 Baseline peak width as a function of aperture diameter at various plasma lengths. Particle emission monitored from Cu I 324.754 nm..... 173

5.4 Emission profiles of Fe in steel, SRM 1261A, Fe I 373.487 nm (a) and Mg in steel, SRM 1261a, Mg II 279.553 nm (b)..... 175

5.5 Emission profile of Co, Co powder Fisher Scientific Co., Co I 345.351 nm... 176

5.6 Individual particle emission profiles of Cu in steel, SRM 1261a, Cu I 324.754 nm (a) and Cu II 224.700 nm (b)..... 178

5.7 Individual particle emission profiles of Cu in Aluminum, SS-380-6, Cu I 324.754 nm (a) and Cu II 224.700 nm (b)..... 179

5.8 Individual particle emission profiles of Mg in steel, SRM 1261a, Mg I 285.213 nm (a) and Mg II 279.553 nm (b)..... 180

FIGURE **PAGE**

5.9 Individual particle emission profiles of Cd, Mossy Cadmium Matheson Coleman and Bell, Cd I 228.802 nm (a) and Cd II 226.502 nm (b)..... 181

5.10 Individual emission profiles of Fe in steel, SRM 1261a, Fe I 373.487 nm (a) and Co, Co powder Fisher Scientific Co., Co I 345.351 nm (b)..... 182

5.11 Emission profiles of Co., Co powder Fisher Scientific Co., Co I 345.351 nm. Profiles (a) and (b) both show secondary emission effect..... 183

5.12 Individual particle emission profile of Ca in steel, SRM 1261a, Ca II 393.367 nm..... 184

5.13 Emission profiles of Cu in brass, SRM C1106, for various plasma lengths. Atom profiles Cu I 324.754 nm (a) and ion profiles Cu II 224.700 nm (b)..... 189

5.14 Baseline peak widths of particle emission profiles as a function of plasma length. Ion lines..... 191

5.15 Baseline peak widths of particle emission profiles as a function of plasma length. Atom lines..... 192

5.16 Emission profiles of Ca in steel, SRM 1261a (0.000028%), single particle profile (a), average of 10 profiles (b), digitally filtered average profile (c)..... 195

A.1 Experimental attempts at ES nebulization into a GDD with a pin-cathode (a) and a hollow cathode (b)..... 205

Chapter 1

Introduction

1.1 Introduction

Spectrochemical sources used for multi-element determinations are continually being developed and improved because of the growing demands placed on environmental, industrial, and clinical laboratories. In the mid 1960's, inductively coupled plasma atomic emission spectroscopy (ICP-AES) was introduced as a technique for the elemental analyis of solution samples [1-2]. ICP-AES has become a dominant instrumental method because of its low detection limits (0.1-10 ng/mL), linear dynamic range of six orders of magnitude, and relative freedom from matrix effects. Inductively coupled plasma mass spectroscopy (ICP-MS) was first reported in 1980 [3] and has become a very successful technique for trace metal analysis. Detection limits for ICP-MS are roughly 100-1000 times lower than ICP-AES. To complement the capabilities of ICP-AES and ICP-MS, the glow discharge device (GDD) has been pursued as a technique to directly determine elemental concentrations in solid materials. The simplicity, low cost of operation, and ability to directly analyze solid samples has created a lot of interest in these devices, as illustrated by two issues of the journal *Spectrochimica Acta* devoted to GDDs [4]. The GDD acts as a source of atomization, excitation, and ionization in techniques such as atomic absorption, emission, fluorescence, and mass spectroscopy. Different types of GDDs exist and are designed for specific applications. The Grimm GDD [5] is used extensively for the analysis of solid samples by AES and is commercially available. Another type of GDD is the hollow cathode discharge (HCD) which is used as the primary radiation source in atomic absorption spectroscopy (AAS). Continued interest in GD

spectroscopy is directed at designing the GDD to be suitable for the analysis of all sample forms and types.

1.2 Characteristics of a Glow Discharge Device used for atomic spectroscopy

A GDD is usually made from a low pressure plasma, with gas pressures typically ranging from 0.1 to 10 Torr. A simple schematic representation of a GDD is shown in Fig. 1.1. It is composed of two electrodes, a vacuum vessel, and a high voltage power supply. For dc operation, the power supply is run in either a constant current or constant voltage mode with currents ranging from several mA to several A and voltages ranging from a few hundred volts to a few kilovolts. There are three distinct regions in the device which are common to all GDDs. These regions are the cathode dark space, the negative glow, and the Faraday dark space. The origins of these regions will be discussed later in section 1.2.2. The negative glow is the region of analytical interest since this is where excitation and ionization processes are most favorable. In its standard mode of operation, the sample to be analyzed is either made into the cathode or placed onto the cathode. The most important feature of the GDD as an analytical tool is its ability to directly sample and determine elemental concentrations of materials in the solid state.

1.2.1 Electrical breakdown of gases and operation regimes

As can be seen in Fig. 1.2, gas discharges can be classified into three operating regimes according to the current which they carry. These are:

(i) The Townsend discharge, which carries currents up to 10^{-6} A.
(ii) The glow discharge, which carries currents from approximately 10^{-6} to 10^{-1} A. The glow discharge regime can be further subdivided into the sub-normal, normal, and abnormal regimes.
(iii) The arc discharge, which carries currents in excess of 10^{-1} A.

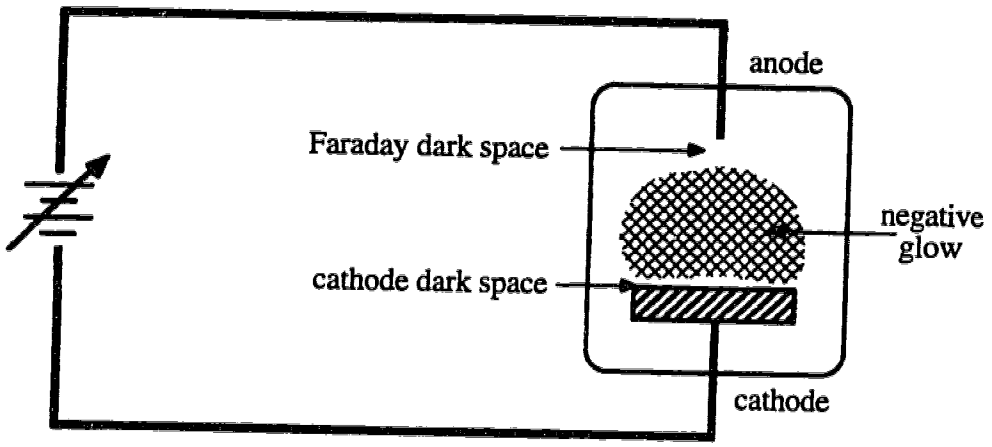

Fig. 1.1 Schematic representation of a simple glow discharge device [6].

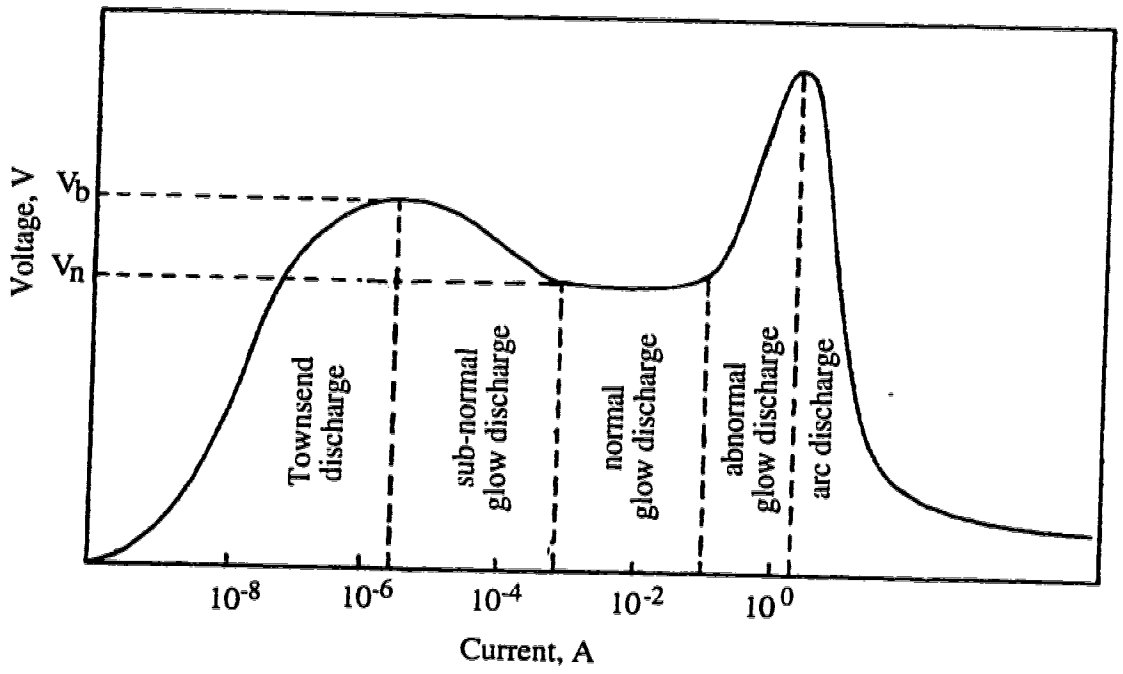

Fig. 1.2 Operating regimes of various gas discharges. Vb, breakdown voltage and Vn, normal cathode fall voltage [7].

The values of current assigned to each regime are not always strictly followed and are only included here as an approximate guideline. For the Townsend discharge and for some types of glow discharges, it may be more appropriate to reverse the axis of Fig. 1.2 since it is voltage which is controlled and determines the operating current.

The Townsend discharge is characterized by its very small currents and can be observed by applying a potential between two electrodes in gas at a pressure of a few Torr. As soon as a voltage is applied between two electrodes, a current will flow since any gas sample will contain naturally occurring ions and electrons. For example, due to cosmic radiation, at ground level the atmosphere contains approximately 1000 positive and negative ions per cm^3. Eventually, as current and voltage increase in the Townsend discharge, the current will begin to increase rapidly due to multiplication processes (see Fig. 1.2). Electrons will be accelerated until their energy, upon collision with neutral atoms, is above the ionization value of the atom. In this way electrons will ionize atoms, producing positive ions and additional electrons. The additional electrons will also be involved in ionizing collisions and the current will increase rapidly with voltage, up to the point of electrical breakdown of the gas. Other sources of electrons in the Townsend discharge can originate from thermionic emission, photoelectric emission, and secondary emission from the anode as a result of electron bombardment. The Townsend discharge is not self-sustaining, which means that it depends on external radiation to maintain it.

The breakdown voltage (V_b) is defined as the electrode voltage which is necessary to produce a self-sustained discharge. When one electron is produced by ionizing collisions for every electron emitted from the cathode, a self-sustained discharge is achieved i.e., the cosmic radiation responsible for the initial ionization of the gas could be eliminated and the discharge would still be maintained. According to Paschen's law, V_b depends on the gas pressure (p) and the electrode separation (d). The (pd) product

determines the breakdown characteristics for a given filler gas and electrode separation according to Equation 1.1, which is commonly referred to as Paschen's law.

$$V_b = \frac{Bpd}{\ln\left(\frac{Apd}{\ln(1+1/\gamma)}\right)} \qquad 1.1$$

A and B are constants determined by the gas composition and γ is Townsend's second ionization coefficient which depends on both the gas and the electrode material. A plot of V_b versus (pd) is known as a Paschen curve and is shown in Fig 1.3. The general shape of the curve can be explained as follows: for a fixed electrode separation, the collision frequency of electrons with gas atoms is low at low pressures. Therefore, the only way the breakdown condition can be satisfied is by increasing the probability of ionization and this is achieved by increasing the applied voltage. Therefore, when the gas pressure is reduced below the minimum V_b, V_b increases. At high pressures the collision frequency is high so electrons do not acquire much kinetic energy during the mean free path of the electron. Consequently the probability of ionization is low and the applied voltage must be increased as pressure increases. The Paschen curve helps explain the operation of the Grimm glow discharge lamp. In the Grimm design, portions of the anode and cathode are within a few hundred μm of each other. No discharge develops between the parts of the anode and cathode which immediately face each other because the applied voltage is below that required by the pd product.

Paschen curves and breakdown characteristics for HCDs have been described [8-9] and show that HCDs have lower breakdown voltages compared to conventional glow discharges of similar dimensions and gas parameters. This is due to the hollow cathode effect and will be discussed in further detail in section 1.3.2.

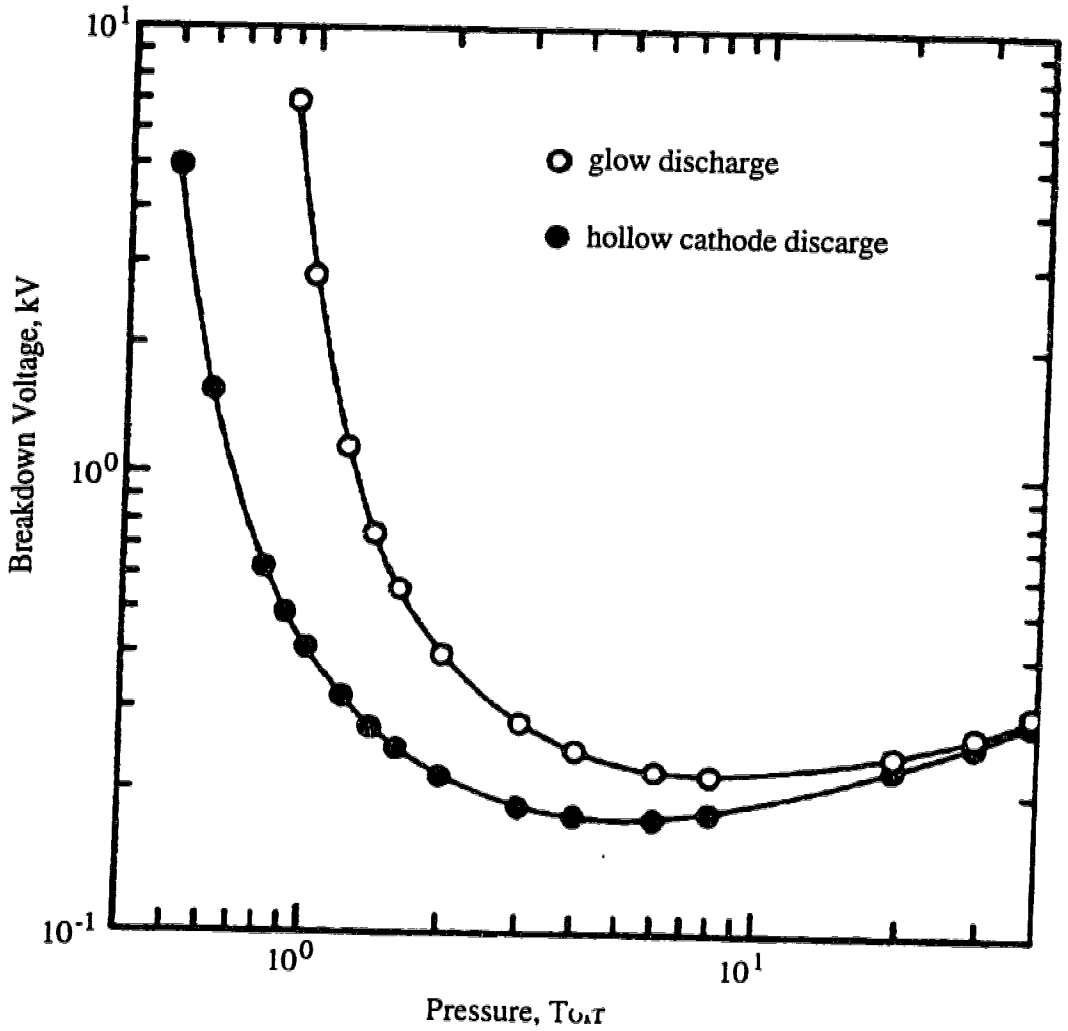

Fig. 1.3 Paschen curve for a hollow cathode discharge and a glow discharge in helium. The anode-to-cathode distance is d=1 cm [8].

Referring back to Fig. 1.2, a glow discharge is obtained between the regimes of the Townsend discharge and the arc discharge. For the subnormal glow discharge, a faint glow appears in the device and the voltage between the electrodes gradually falls as the current is increased. The voltage falls because additional processes of electron emission become important. Positive ions bombard the cathode which will dislodge electrons from the cathode. Heat produced from the bombardment of the cathode will increase the cathode temperature and can result in thermionic emission. Also, electron emission from the photoelectric effect can become important. For the normal glow discharge regime, the current density at the cathode remains constant while the area of the cathode covered by the glow expands proportionally with the current. The normal operating regime likely gets it's name from the vacuum tube industry since a GDD can be used as a voltage regulator in the normal regime. When the whole cathode surface is covered by the glow, an increase in current will result in an increase in current density. More electrons are required to be emitted from the cathode and this is only accomplished by an increase in the operating voltage. Most GDDs used for spectrochemical analysis operate in the abnormal glow discharge regime.

As the current density increases, the temperature of the cathode can reach a value where thermionic emission contributes significantly to the current and increases the current density still further. A transition to an arc discharge will follow which is characterized by very high currents and low operation voltages. The arc voltage is often less than 50 V which is an order of magnitude lower than that of the glow discharge. The arc discharge is maintained by high current density which sustains the necessary cathode temperature for thermionic emission. Although arcs are widely used in industrial applications for welding torches, there usefulness as an analytical source is limited.

1.2.2 Fundamental collision processes in glow discharge devices

Fig. 1.4 and Table 1.1 highlight the fundamental collisional processes in the GDD which are responsible for sputtering, atomization, ionization, and excitation. These processes will be described in this section along with the characteristics of the cathode dark space, negative glow, and Faraday dark space.

The cathode fall or cathode dark space, which is the region right next to the cathode in a self-sustained glow discharge, is depicted in Fig. 1.4. Almost the entire applied voltage is dropped over the cathode fall region as a result of the differential mobility of electrons and positive ions. In the steady state, slow moving positive ions must reach the cathode in the same numbers as electrons reach the anode. To reconcile these facts there must be an accumulation of space charge in different regions. Near the cathode, the slow moving positive ions accumulate until their concentration is much greater than that of the electrons. This space charge distorts the originally uniform electric field. Since most of the applied voltage is dropped across the cathode fall distance, an effective anode is placed at the cathode fall distance. This distance corresponds with the pd product of the Paschen minimum. In this way, the discharge assumes an optimum configuration whereby the necessary ionization to maintain the current is produced in the most economical manner. It is clear to see why the cathode fall distance varies inversely with pressure since the pd product is maintained at the optimum value.

As their names imply, the cathode dark space and Faraday dark space are regions of very low light emission and the negative glow is a region of high light emission. This can be explained by considering the collisional excitation cross-section for the atomic species. Assume for a moment that all electronic excitation is a result of electron impact according to Equation 1.2.

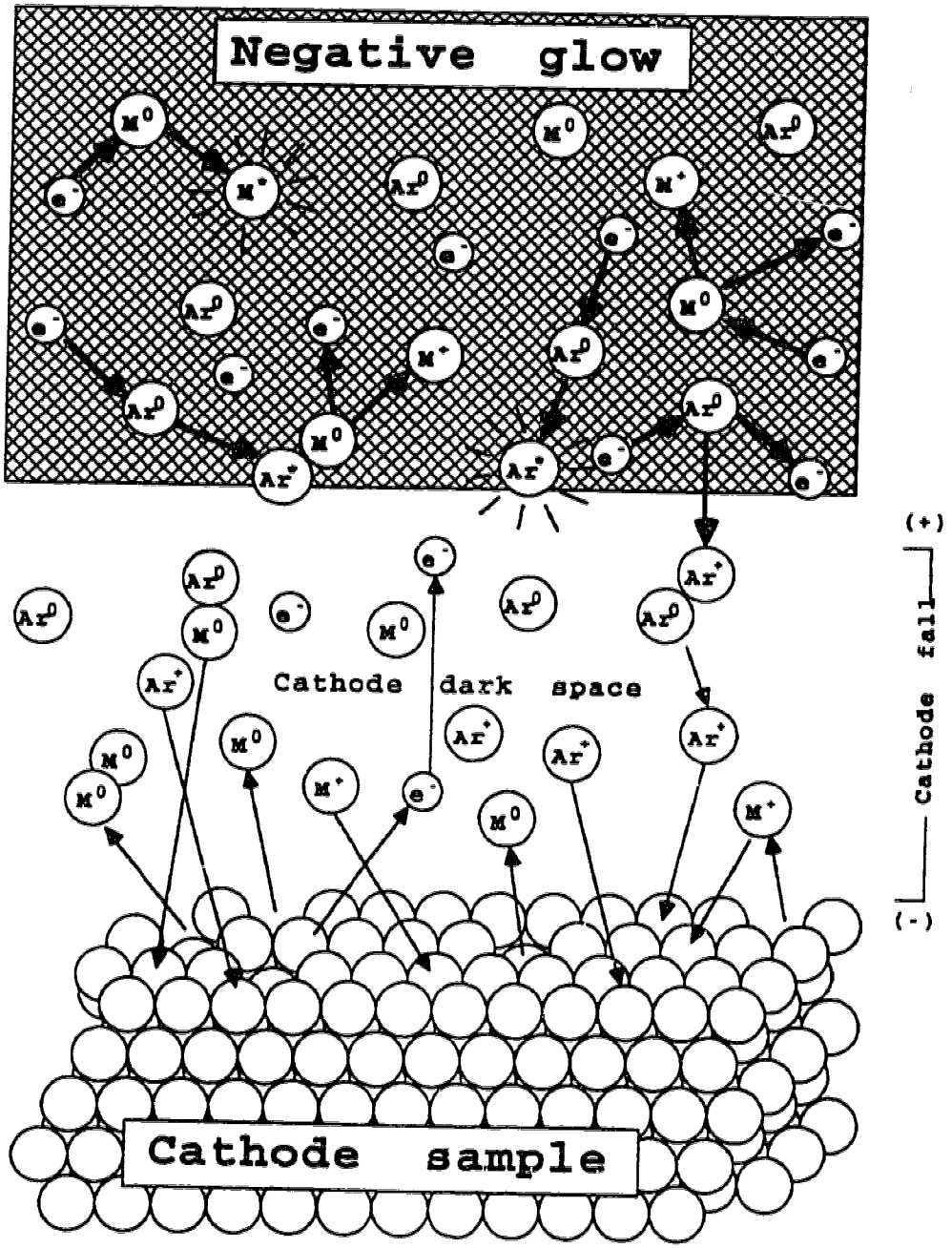

Fig. 1.4 Fundamental collision processes in glow discharge devices [6].

Table 1.1 Excitation and ionization processes in the glow discharge [6].

I. Primary excitation/ionization processes

A. Electron impact

$$M^o + e^-(\text{fast}) \rightarrow M^* + e^-(\text{slow}) / M^+ + 2e^-$$

B. Penning collisions

$$M^o + Ar_m^* \rightarrow M^* + Ar^o / M^+ + Ar^o + e^-$$

II. Secondary processes

A. Charge transfer

1. Nonsymmetric

$$Ar^+ + M^o \rightarrow M^+(M^{+*}) + Ar^o$$

2. Symmetric

$$X^+(\text{fast}) + X^o(\text{slow}) \rightarrow X^o(\text{fast}) + X^+(\text{slow})$$

3. Dissociative

$$Ar^+ + MX \rightarrow M^+ + X + Ar^o$$

B. Associative ionization

$$Ar_m^* + M^o \rightarrow ArM^+ + e^-$$

C. Photon-induced excitation/ionization

$$M^o + h\nu \rightarrow M^* / M^+ + e^-$$

D. Cummulative ionization

$$M^o + e^- \rightarrow M^* + e^- \rightarrow M^+ + 2e^-$$

$$M^0 + e^- (fast) \rightarrow M^* + e^- (slow) \qquad 1.2$$

The cross-section for electron impact excitation depends both on the transition moment of the atom for the pair of states involved and on the velocity (v) of the electron. If all of the electron kinetic energy is converted to excitation energy, there will be a threshold velocity (v_t) below which no excitation will occur.

$$\frac{1}{2}mv_t^2 = E_2 - E_1 \qquad 1.3$$

According to classical arguments, for $v >> v_t$ the cross section should decrease as $1/v^2$[10]. However, Fig. 1.5 illustrates that it is only the electrons in the high energy tail of the Maxwell distribution that are effective in collisional excitation. The Faraday dark space is dark since all the electrons in this region have a velocity below v_t. The negative glow is luminous since the electrons in this region have a high probability of colliding with atoms and causing electronic transitions in the optical range. Finally, the cathode dark space is dark because the electrons in this region are too fast to have a high probability of causing excitation. Electrons are rapidly accelerated away from the cathode and some of them reach the end of the cathode dark space with energies equivalent to the cathode fall potential.

The removal of cathode material in the solid state and into the gaseous state of the low pressure discharge is referred to as sputtering. Sputtering occurs due to the bombardment of the cathode surface with inert gas ions, typically Ar or He, and ions of the cathode material itself. Fast atoms may also strike the cathode surface and produce sputtering to a lesser extent. Positive ions which enter the cathode dark space will be accelerated towards the cathode and strike the cathode with a range of kinetic energies. If the energy of the ions are greater than approximately 30 eV, there is a good chance that an

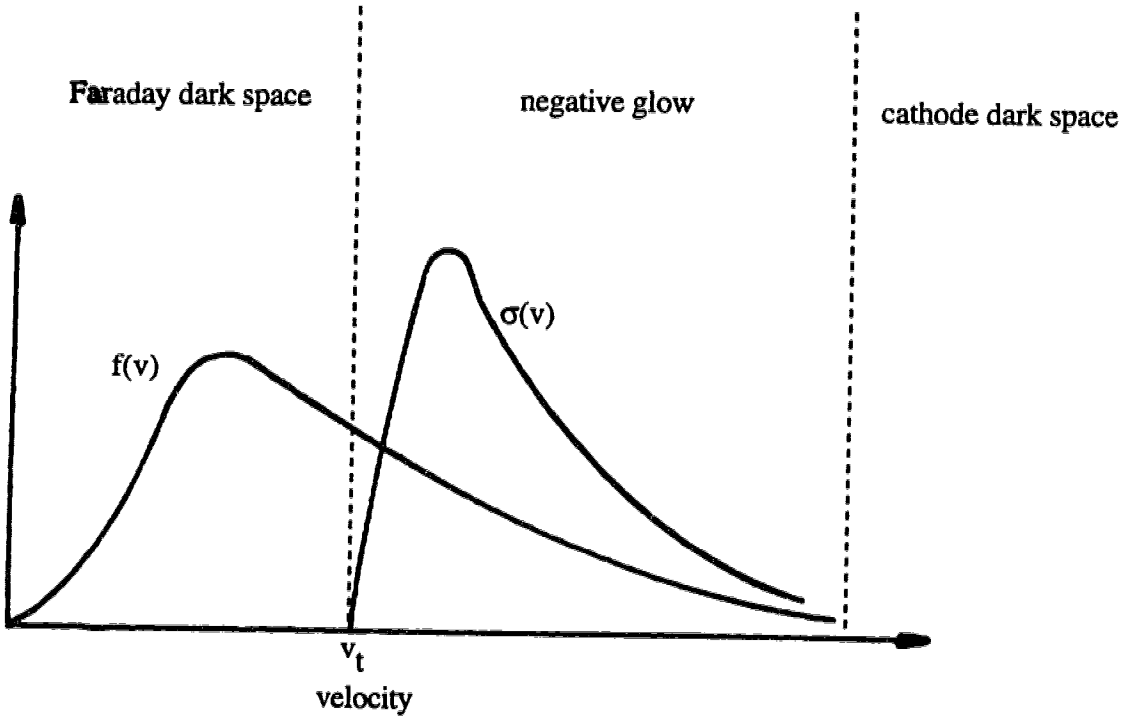

Fig. 1.5 Collisional cross-section σ(v) as a function of v, together with the Maxwell velocity distribution function f(v) [10].

atom will be removed from the cathode surface. The process of sputtering also emits ions, electrons, photons, and atom clusters from the cathode surface.

Excitation and ionization processes occurring in the negative glow of the glow discharge are listed in Table 1.1. Collisions of the first kind describe inelastic collisions with plasma electrons and collisions of the second kind describe collisions with massive particles. The relative role of these processes will be determined by the discharge conditions and source geometry. While GDDs are relatively easy to construct and operate, their spectrochemical behavior is the result of a very complex set of collisional processes. Of the collisional processes listed in Table 1.1, the most prominent are electron impact, Penning, and charge transfer reactions. Electron impact is perhaps the most dominant excitation mechanism. However, for the Grimm and hollow cathode sources which operate at large current densities, asymmetric charge exchange from discharge gas ions can become dominant for the production of excited state ions [11].

1.2.3 Analytical methods used with GDDs

Many elemental techniques utilize the GDD as the sampling and excitation/ionization source, as shown in Fig. 1.6. The most commonly used method is atomic emission spectroscopy. Other optical techniques include atomic absorption and fluorescence spectroscopies. The GDD is used as an ion source in mass spectroscopy for more sensitive measurements and optogalvanic effect spectroscopy (OGE) has been used, but to a lesser extent. The following section briefly outlines the major areas of usage of the GDD.

In 1968 the Grimm-type glow discharge was developed [5] and it is still this design which dominates the practical usage of GDDs for emission spectroscopy. The Grimm design is popular since the requirements for the cathode dimensions are simply that the

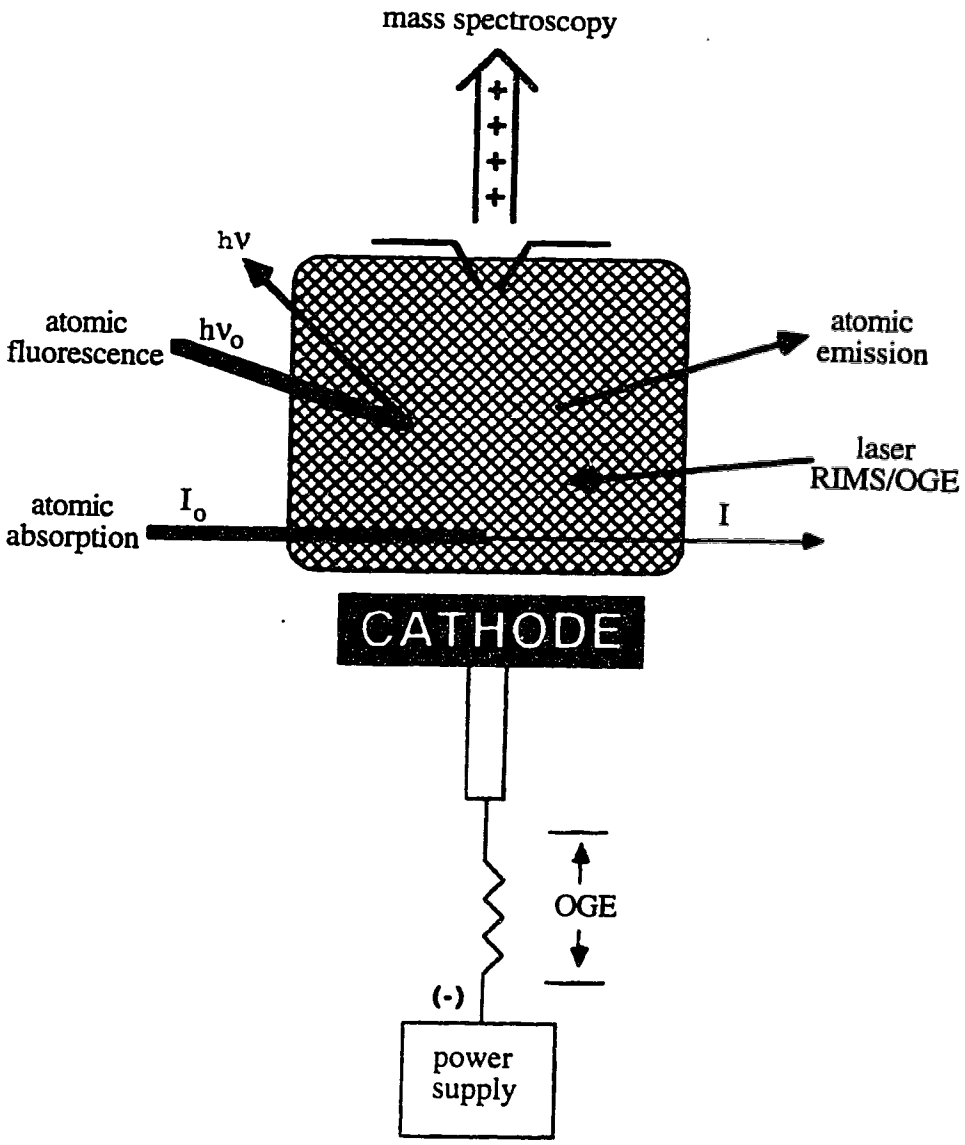

Fig. 1.6 Analytical methods which utilize the glow discharge [6].

cathode, which is the sample, has a flat planar surface. The discharge is confined to the sample by keeping the distance of the anode and the cathode housing below the mean free path of the electrons, which is on the order of 0.1 mm. In other words, the discharge is operated on the left hand side of the Paschen curve as shown in Fig. 1.3. Cathodic sputtering samples the electrically conductive cathode and emission in the negative glow of the discharge allows for simultaneous multielement determinations. A surface diameter of 8-10 mm is sampled by sputtering and the discharge current and voltage can range up to 200 mA and 2 kV respectively. Leco (R) has introduced a commercially available GDD based on the Grimm design with detection limits in the μg/g range.

For AA and fluorescence measurements, the GDD is used to generate sample atoms in the gaseous state [12]. A commercial product called the Atomsource (Analyte Corporation) is available as an add-on component to modern AA instrumentation. It takes the place of the burner head and is used to generate ground state atoms in the gaseous state from solid samples. Data are collected in a typical fashion, as in any other AA technique, and detection limits from solid samples have been reported to range from 0.04-0.0003% [13]. As an example, this technique has been used to determine platinum and rhodium concentrations in automotive catalyst materials [14] and has been shown to be accurate to within 2-3%. Internal standardization is necessary to compensate for differences in sputtering efficiency from sample to sample. Typical operating conditions for this device are a discharge pressure of 10 Torr argon and a dc current ranging up to 300 mA. Atomic fluorescence inside a HCD has been described by Winefordner el. al. [15] as applied to the analysis of dried solution residues. The aqueous sample was placed inside the demountable graphite cathode and heated to dryness. Discharge conditions of 2-14 Torr argon and a discharge current ranging from 28-207 mA were used. A copper vapor laser pumped dye laser was used as an excitation source and gave detection limits of 15 fg and 2 pg for lead and iridium respectively.

The ionization mechanisms outlined in Table 1.1 allow the glow discharge to be used as an ion source for glow discharge mass spectrometry (GD-MS) [16-17]. Compared with optical techniques, MS offers spectral simplicity since there are only a few different isotopes for any given element. There are numerous advantages of using GD-MS compared with ICP-MS. Solvent based species prevalent in ICP-MS, which add spectral complexity to the background, are absent in GD-MS. This results in a simpler spectral character with fewer isobaric overlaps. Since solid samples are directly analyzed, contamination from acids used for sample dissolution is not a factor. Detection limits are in the 10-100 ng/g range which makes GD-MS a very sensitive technique for the direct analysis of solid samples.

Detection of small changes in the electrical properties of a gaseous sample in the presence of resonant radiation is the basis of impedance spectroscopy. When the sample is contained in a dc discharge, changes in the current can be directly measured and the term 'optogalvanic' is used to describe the measurement. Optogalvanic effect spectroscopy is most often used for fundamental studies of the glow discharge, however, applications of OGE as an analytical technique are possible [18-19]. Laser excitation is used to alter the ionization rate of the discharge which in turn alters the electrical resistance of the discharge circuit. By tuning the laser to the transition of interest and monitoring the voltage/current characteristics of the discharge, useful analytical information can be obtained regarding plasma species. Although this technique has not been widely adopted, it offers the advantage of being highly selective since the laser radiation is monochromatic and accurately tuned to the desired wavelength.

1.3 The hollow cathode discharge

The hollow cathode discharge has been studied extensively as an emission source for atomic spectroscopy and has been the subject of several reviews [7, 20-23] which detail the fundamental properties and emission characteristics of the discharge. The HCD is a specialized type of GDD where the cathode takes the form of a cup, cylinder, or closely spaced parallel plates and the negative glow is entirely confined within the electrode cavity (see Fig. 1.7).

1.3.1 Historical development of the HCD

The first reported operation of a HCD was in 1916 by Paschen [24]. Paschen described a low pressure dc discharge where the cathode was formed by bending Al foil in the shape of a hollow cavity. At a helium pressure lower than 1 Torr, a glow formed that was entirely contained within the cathode cavity. Paschen was able to study the structure of the helium spectrum with this simple device. Later, Schuler was one of the first researchers to utilize the HCD as an emission source for studying small quantities of materials placed inside the hollow cavity [25-27]. The development of AA as an analytical technique in 1955 significantly affected the direction of HCD research, since a HCD is used as the primary radiation source in modern AA instrumentation. Due to the widespread popularity of AAS, studies of the HCD have been primarily directed towards improving it as a line source for AAS rather than developing it as a source of atoms and ions. However, there has always been interest from the academic community for the development of the HCD as an emission source. Recent developments by Winefordner [28], Caroli [29], Falk [30], and Williams [31-33] have illustrated both the fundamental characteristics of the HCD as well as its utility for sensitive measurements by AES.

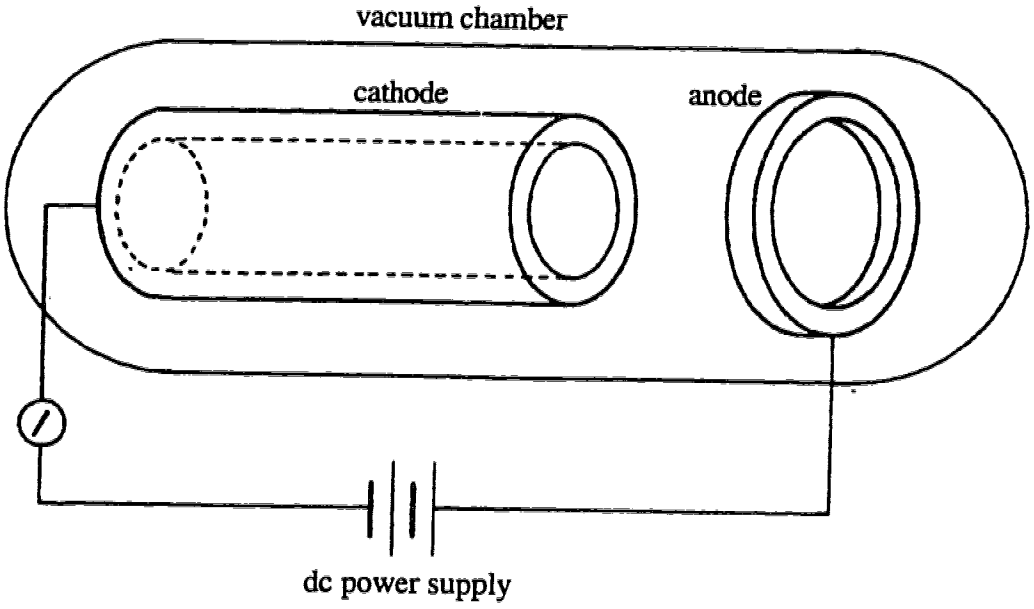

Fig. 1.7 Schematic representation of a hollow cathode discharge [6].

1.3.2 Characteristics of the HCD

The unique spectral and discharge properties of the HCD can be attributed to what is commonly referred to as the hollow cathode effect. The hollow cathode effect can be understood by considering two planar parallel cathodes which have a common anode. When the cathodes are separated by a large distance, they behave independently from each other and the two negative glows are separate. As the intercathode distance is reduced, the two negative glows begin to merge and coalesce. When this occurs, the discharge current rises sharply and reaches values 100-1000 times larger than in a normal glow discharge operated at the same potential. At the same time, the light emitted from the negative glow increases dramatically. The discharge consists of a dark space close to the walls of the cathode and the negative glow which fills the remaining space between the cathodes. The energetic species in the discharge have a low probability of escaping the cavity and this greatly increases the ionization and excitation efficiency. At pressures typically used, the mean free path of the electrons is of the same order as the magnitude of the cathode diameter, in reference to cylindrical cathodes. Therefore, a significant portion of the electrons will acquire sufficient acceleration across the dark space to reach the opposite wall of the cathode. When this happens, the electron will be repelled backwards and reiteration of this process results in higher densities of ions and photons than obtained with a planar GDD operated at equivalent gas pressure and electric power. It is the enhanced production of ions and photons which make the HCD a popular emission source in atomic spectroscopy.

Langmuir probe measurements [34] have identified three different groups of electrons in the HCD. They identified one group of electrons with very high energies of >100 eV. These electrons are the result of the strong acceleration in the cathode fall region and can approach the potential of the cathode fall. Another group of electrons derive their

energy via inelastic ionization collisions and possess energy levels of approximately 3 eV. The last group of electrons is a group of slow or thermalized electrons with an energy of <0.5 eV. Electron densities vary with discharge parameters but typically are between 10^{11} and 10^{13} cm^{-3}. The temperature of the gas atoms can have values up to 1200 K [35] which is much lower than the electron temperature (1 eV ≈ 10,000 K), indicating an absence of local thermodynamic equilibrium (LTE).

The non-thermal nature of excitation in the HCD have made it a popular plasma source for metal ion lasers. Laser transitions from Zn, Cd, Se, I, Cu, Ag, Au, Al, Sr, and Hg have been observed and a review of this topic [36] shows that upper laser levels are selectively populated via charge transfer collisions. A wide variety of designs, based on the HCD, have been implemented which range from small discharge tubes carrying a few hundred mA [37], to long discharge tubes nearly a metre long and operating at 5 A [38].

1.4 Sample introduction into an operating GDD

In the past few decades, numerous systems for continuous sample introduction into a GDD have been devised. This contrasts the standard method of GDD analysis where a sample (i.e. a conducting solid) is the cathode or is manually placed onto the cathode. Researchers have developed a variety of sample introduction interfaces which all have the same goal: to deliver a controllable amount of analyte at atmospheric pressure into the reduced pressure environment of the GDD. This is not a trivial feat to accomplish, especially for liquid samples, since the majority of the solvent should be selectively removed prior to analyte introduction.

1.4.1 Introduction

The elemental analysis of liquid samples is dominated by ICP-AES and ICP-MS, however, attempts have been made to take advantage of the energetic plasma of the HCD for the analysis of solutions in the form of dried solution residues. Traditionally, the analysis of liquids by the HCD involves numerous steps. First the sample is placed inside the cathode bore which is then heated to dry the sample. The device is then sealed, evacuated, and filled ($\approx$ 1 Torr) with an inert discharge gas (i.e. He, Ne, or Ar). Power is applied to the electrodes and a discharge is maintained between the anode and cathode. Sputtering of the thin salt layer, left by the liquid sample, transports the sample to the negative glow of the discharge where energetic species excite and ionize the analyte. Much of the recent work in this area has been done by Williams and co-workers [31-33] who have developed a HCD to quantify Ca, K, Li, and Na with sub pg detection limits. Although this method seems able to compete with electrothermal AAS in terms of detection limits, there are fundamental problems with this technique and its characteristics fall short of those of an ideal emission source. The emission event is transient in nature and there is complex temporal emission behavior for both background and analyte species. Signal processing for transient signals requires the use of high gain photomultiplier tubes coupled with fast readout electronics to capture the analytical signal. This means that only a few analytical wavelengths can be monitored simultaneously. However, a state-of-the-art detector used with multi-element atomic emission sources has been developed and is based on solid-state charge-coupled-device (CCD) technology [39]. This detector is designed to measure the three to four primary analytical lines of 72 elements and covers over 5000 emission lines in total. The main advantage of the CCD detector, relative to photomultiplier tubes, is the large increase in spectral coverage which can be used for simultaneously detecting many emission lines together with spectral background. The CCD requires long integration times ($\approx$ 40 s) to achieve maximum sensitivities and therefore is not ideally

suited to measure transient signals which last only fractions of a second. Research is necessary to provide a means of continuous solution sample introduction into a HCD so that a steady state emission signal is realized. This would complement the recent advances in solid state optical detection.

There are numerous techniques used for elemental analysis which produce transient signals. These techniques include electrothermal AAS, furnace atomization plasma excitation spectrometry (FAPES), furnace atomization nonthermal excitation spectrometry (FANES), and the HCD method described above. The most striking characteristic of all these techniques is their high sensitivity as sub pg detection limits are obtained for many elements. However, all these techniques suffer from the same limitations. Placement of the sample is tedious and time consuming and the transient signal which is generated is not ideally compatible with recent advancements in solid state detection. Clearly there is a need for a sample introduction interface which allows for continuous discharge operation and solution sample introduction. The first part of this thesis will focus on a continuous solution sample introduction interface into a continuously operating HCD.

1.4.2 Literature review of sample introduction into an operating GDD

In 1967, Zanzucchi [40] was the first person to attempt direct solution introduction into a GDD. Elemental emission from Na, Cu, Ca, Li, K, Mg, and B were observed by injecting 1-3 µl of sample into the negative glow of a hollow cathode discharge with a syringe. A rubber septum, similar in design to an injection port in gas chromatography, was used as the vacuum seal between the atmosphere and the reduced pressure discharge. It is interesting to note that Zanzucchi did not observe analyte emission with an argon plasma; instead, he used an oxygen discharge in combination with a graphite cathode. It was postulated, although unverified, that the mechanism of analyte excitation was a result

of charge transfer collisions between CO. The CO was formed by a reaction between the oxygen plasma and the graphite cathode. This method of analyte introduction into the HCD proved to be reproducible, sensitive to ng quantities of analyte, and quantitative. Two years later, Buger and Fink [41] also attempted to directly introduce solution samples into a HCD. They found that strong interferences from band spectra limited the usefulness of the technique.

Unique excitation sources based on GDDs have been designed for gas sampling. Hieftje *et al.* have built a gas sampling glow discharge which has been coupled with a continuous-flow hydride generator and is also capable of exciting emission from non-metals [42-44] (see Fig. 1.8). Sample gases enter the discharge through a capillary in the centre of the cathode and the rate of sample delivery is determined by the inner diameter of the capillary. Gas flow rates up to 234 mL/min have been sustained with a discharge pressure between 3-9 Torr. A maximum discharge power of 112.5 W was achieved at discharge potential of 900 V and a current of 125 mA. The sample passes directly through the cathode fall and negative glow regions of the glow discharge where energetic electrons and ions atomize and excite the sample. This device has also been used as an ion source for mass spectrometry. When coupled with a hydride generator for sample introduction, a detection limit of 20 ng/mL in an argon discharge was obtained for As. When gas samples were introduced via an exponential dilution flask into a helium discharge, detection limits for C, S, F, and Cl were 0.4, 1, 82, and 5 ng respectively. A gas sampling hollow cathode GDD has been developed by Grove and Loseke to monitor the major gaseous constituents in space cabin atmospheres [45]. Atmospheric gases were bled into a helium discharge maintained at 1- 6 Torr. Elemental emission of H, O, N, and C was observed from the HCD operating at 400 V and 25 mA.

a) Outside View

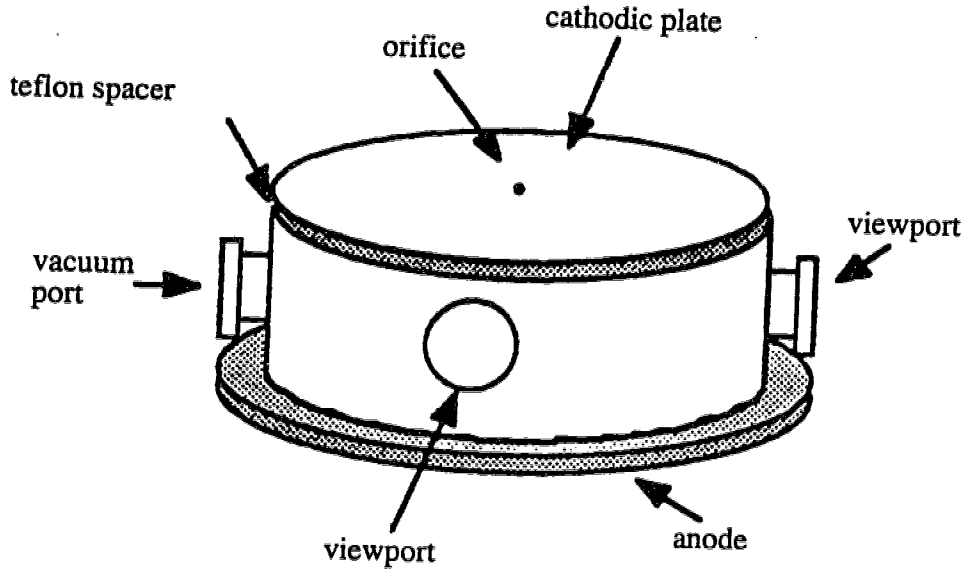

b) Inside View

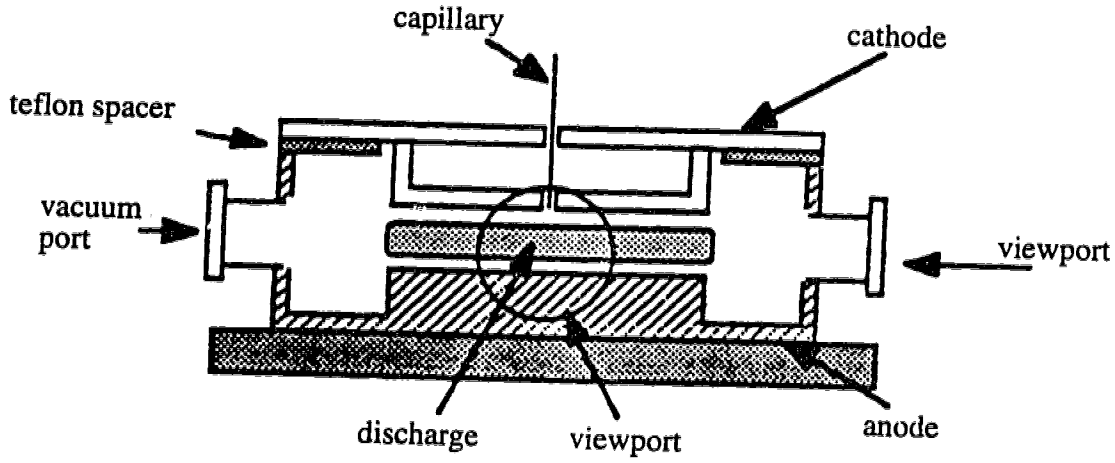

Fig. 1.8 Exterior (a) and cutaway (b) views of the gas-sampling glow discharge [43].

Several researchers have constructed HCDs with the specific goal of using them as detectors for gas chromatographic effluents. Non-metal detection was achieved by Winefordner *et al.* in a helium discharge with detection limits in the ng range [46]. The discharge was maintained at 30-40 Torr, a helium flow rate of 600 mL/min, a current of 180 mA and a voltage of 650 V. This system showed poorer detection limits than the helium microwave induced plasma when used as a detector for gas chromatography. Sacks *et al.* [47-48] have also developed the HCD as a detector for gas chromatography which has detection limits for non-metals in the ng range. This discharge was maintained at helium pressures ranging from 10-100 Torr, a helium flow rate of 10 mL/min, and discharge currents from 15-150 mA. The passage of the solvent peak through the detector altered the detector response for as long as a minute. This was due to the formation of a poorly conducting polymer coating in the cathode cavity. This problem was avoided by switching the discharge off just prior to the entry of the solvent peak into the cathode.

Brackett and Vickers [49-50] were the first researchers to develop a GDD in which liquid samples were continuously delivered to the discharge. Their sample introduction interface is shown in Figs. 1.9 and 1.10 and is similar to liquid sample introduction developed for liquid chromatography/mass spectrometry. A sample delivery port deposits the solution sample onto the sample conveyor chain which then passes through a reduced pressure oven to provide solvent evaporation. The directional flow of argon is such that the water vapor is swept away from the discharge region. The dried solution residue is transported to the discharge by the conveyor chain. The chain becomes part of the cathode and in this way the analyte residue is removed by sputtering and the sample is atomized and excited by plasma processes. Detection limits for Pb, Cd, B, and Cu are 0.8, 1.2, 1.0, and 3.2 μg/mL respectively when the discharge current is maintained between 52 and 90 mA. This device demonstrated that solution samples could be delivered to a GDD in a controllable and continuous manner and pointed the way for future development.

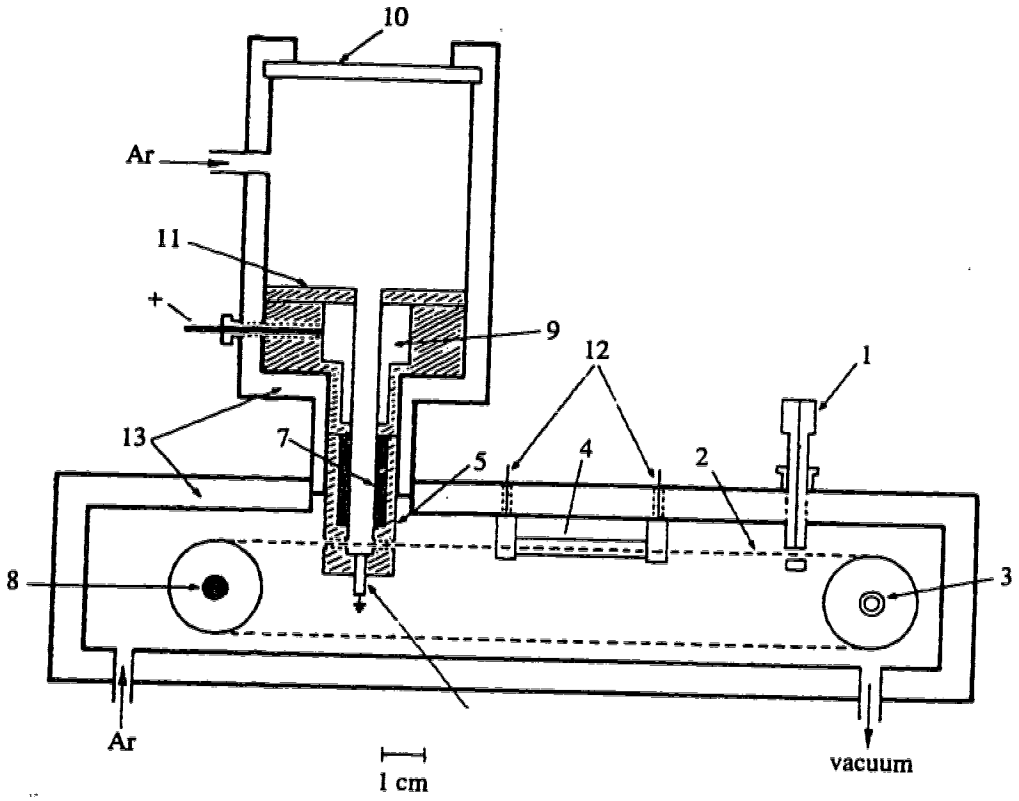

Fig. 1.9 Cross-section view of glow discharge device. 1, sample delivery port; 2, sample conveyor chain; 3, chain drive sprocket; 4, desolvation furnace; 5, machineable glass electrode support; 6, cathode rod; 7, graphite cylinder; 8, idler sprocket; 9, copper anode; 10, quartz window; 11, machineable glass shield; 12, electrical feed-throughs for furnace; 13, brass body [49].

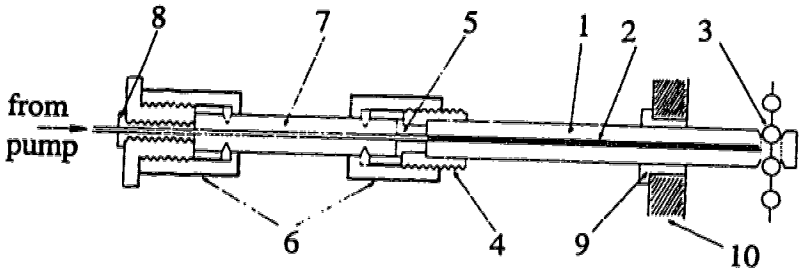

Fig. 1.10 Detailed cross-section view of sample delivery port. 1, thick wall, glass capillary tube; 2, tungsten wire; 3, bead chain conveyor; 4, bolt epoxied to capillary tube; 5, frit; 6, Cheminert glass-to-teflon unions; 7, glass capillary tube; 8, Cheminert teflon tube fitting; 9, Swagelok fitting; 10, wall of sample chamber [49].

Marcus *et al.* have developed a pin-type GDD [51] which provides aqueous sample introduction via a particle beam interface. In a later paper [52], Marcus used the same interface to introduce aqueous samples into a HCD. This system is shown in Fig. 1.11. The particle beam interface employs a heated concentric nebulizer which generates a finely dispersed aerosol, a heated spray chamber which desolvates the analyte, and a momentum separator which injects dry particles into the HCD. Water vapor is separated from the dried salt particles in the two stage momentum separator. The light weight water molecules are removed to the vacuum pumps while the analyte or particle beam enters the discharge. The HCD could be maintained in either argon or helium from 0.2-4.0 Torr and at a discharge current up to 100 mA. The advantage of this aqueous sample introduction interface is that it introduces dried particles continuously into an operating discharge with minimal observation of molecular band emission. In other words, the particle beam interface is efficient at selectively removing the solvent from the analyte. Also, the carrier gas flow rates through the discharge are low which results in long residence times for the analyte. One disadvantage of this particular design is that it relies on electrothermal heating of the cathode for vaporization of the analyte. This introduces vaporization interferences for different species since sample vaporization is no longer due to cathodic sputtering. A detection limit of 8 ng/mL was reported for Cs.

The most direct way of analyzing solution samples by glow discharge spectroscopy is by having the solution sample be the cathode. This has been done by either cryogenically cooling the aqueous sample and freezing it into the shape of the hollow cathode or by using water as the cathode in an atmospheric pressure glow discharge. Conzemius *et al.* [53] used a cryogenic hollow cathode ion source for mass spectrometric determinations of trace elements in solution. This unique ion source was operated at 1 Torr with water vapor from the sample as the plasma gas. The discharge current was limited to 3-5 mA to prevent the water vapor pressure from becoming too large. There was no

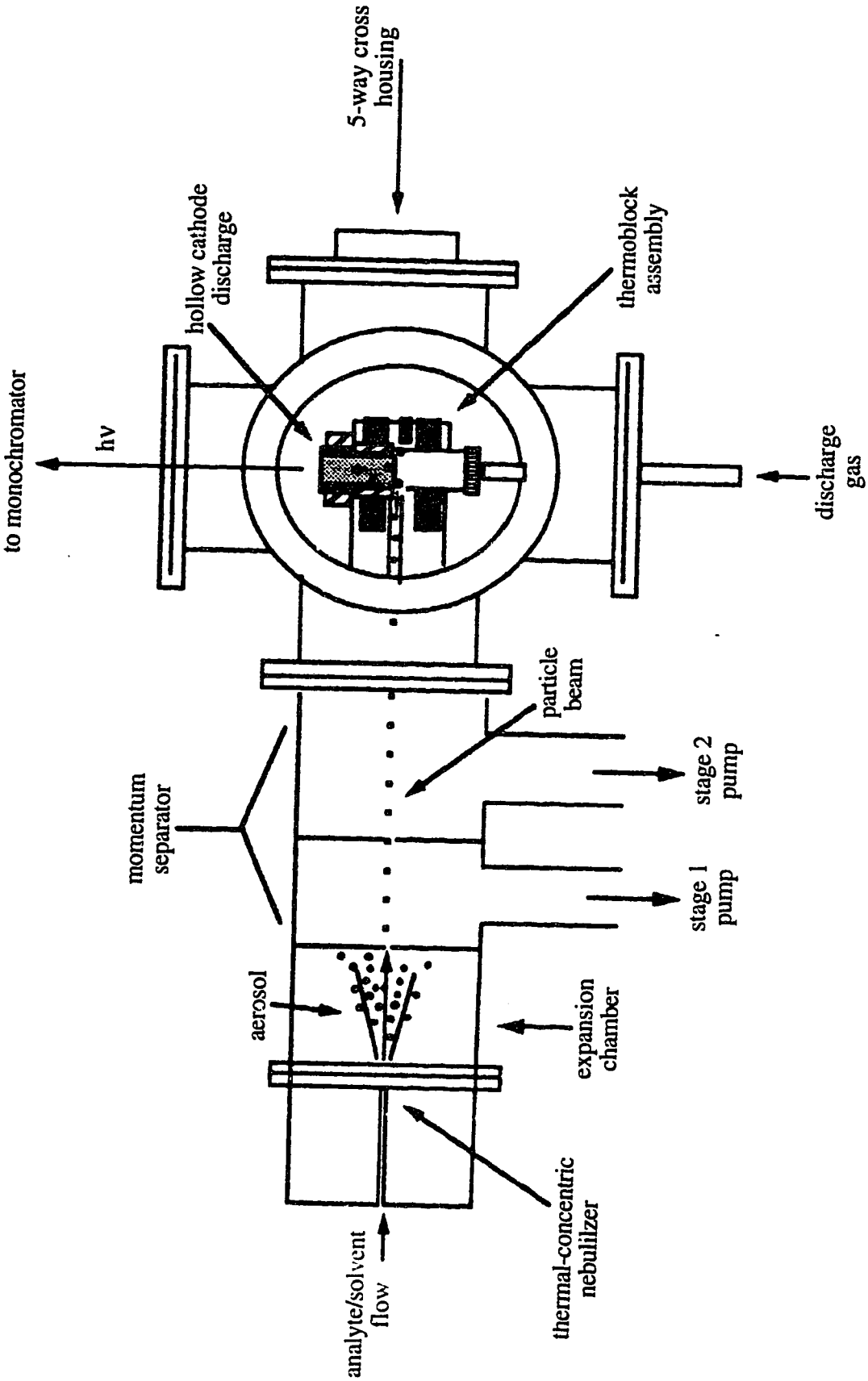

Fig. 1.11 Nebulizer and particle beam interface coupled to the heated hollow cathode atomic emission source [52].

observed advantage to using argon as the discharge gas. Detection limits were as low as 1 ppba for Br, Rb, I, and Cs and as high as 100 ppma for Mg, Si, and Ca. Detection limits in ppma refer to the number of atoms of trace elements per million atoms of oxygen as molecules of water. By far, the most simple and direct way of analyzing solution samples by glow discharge spectroscopy has been accomplished by Mezei *et al.* [54-55]. They reported on a device which used air as the discharge gas, operated at atmospheric pressure, and used a flowing water stream as the cathode. This technique grew out of glow discharge electrolysis which has been used in the past for investigating the influence of the glow discharge plasma on the oxidation processes taking place in the solution phase [56-57]. Mezei and co-workers have extended the use of glow discharge electrolysis and have found that the emission spectra were representative of the metal ions in solution. Detection limits ranged from 0.06 μg/mL for Na and Cu to 0.8 μg/ml for Mg, Pb, and Mn and were found to be dependent on the pH of the solution. Atomic emission lines from dissolved metals were more intense at low pH and emission intensities were optimized between the pH values of 1 and 2. The discharge was maintained at a voltage of 600-1200 V and a current of 50-150 mA. This device showed the possibility of on-line and continuous analysis of water in the range of 1-50 μg/ml for alkaline and heavy metals.

Laser ablation of solid samples with subsequent atomization and excitation in a HCD has been performed by Iida [58]. Although solid samples can be analyzed directly with a GDD, the use of laser ablation as a sampling step allows the analysis of non-conducting samples in a simple dc discharge. Iida reported detection limits for various elements in the range of 3 μg/g for Mg and up to 16 μg/g for Ni and stated that the main restriction to achieving lower detection limits came from background emission in the form of molecular bands. The external laser ablation chamber was connected to the HCD by rubber tubing and the laser ablated aerosol was swept to the discharge by a flow of argon. Poor design of the HCD limited the discharge current to 160 mA and analyte emission

intensity increased with discharge current up to this value. A discharge pressure of 6 Torr argon was shown to be an optimal value for many elements.

References

1. S. Greenfield, I. L. Jones and C. T. Berry, *Analyst* **89**, 713 (1964).
2. R. H. Wendt and V. A. Fassel, *Anal. Chem.* **37**, 920 (1965).
3. R. S. Houk, V. A. Fassel, G. D. Flesch, H. J. Svec, A. L Gray, and C. E. Taylor, *Anal. Chem.* **52**, 2283 (1980).
4. *Spectrochim. Acta* **46B**, No. 2, 111-314 and No. 4, 457-546 (1991).
5. W. Grimm, *Spectrochim. Acta* **23B**, 899 (1968).
6. *Glow Discharge Spectroscopies* (R. K. Marcus, ed.), Plenum Press, New York, 1993.
7. S. Caroli, *J. Anal. At. Spectrom.* **2**, 661 (1987).
8. H. Eichhorn, K. H. Schoenbach and T. Tessnow, *Appl. Phys. Lett.* **63**, 2481 (1993).
9. P. D. Mixon, S. T. Griffin and J. C. Williams, *Appl. Spectrosc.* **47**, 1567 (1993).
10. *Spectrophysics* 2nd edition (A.P. Thorne), Chapman and Hall, London, 1988.
11. Y. Shao, A spectral study of excitation processes in a glow discharge. Thesis, University of Alberta (1995).
12. P. Hannaford and A. Walsh, *Spectrochim. Acta* **43B**, 1053 (1988).
13. D. S. Gough, *Anal. Chem.* **48**, 1926 (1976).
14. M. R. Winchester, S. M. Hayes and R. K. Marcus, *Spectrochim. Acta* **46B**, 615 (1991).
15. J. B. Womack, E. M. Gessler and J. D. Winefordner, *Spectrochim. Acta* **46B**, 301 (1991).
16. N. Jakubowski, D. Stuewer and W. Vieth, *Fresenius Z. Anal. Chem.* **331**, 145 (1988).
17. G. Horlick, *Spectroscopy* **7**, 22 (1992).

18. R. B. Green, R. A. Keller, G. G. Luther, P. K. Schenck and J. C. Travis, *Appl. Phys. Lett.* **29**, 727 (1976).

19. M. Francesconi, L. Gianfrani, M. Inguscio, P. Minutolo, A. Sasso and G. M. Tino, *Appl. Phys. B* **51**, 87 (1990).

20. J. V. Sullivan, *Prog. analyt. atom Spectrosc.* **4**, 311 (1981).

21. S. Caroli, *Prog. analyt. atom Spectrosc.* **6**, 253 (1983).

22. M. E. Pillow, *Spectrochim. Acta* **36B**, 821 (1981).

23. P. J. Slevin and W. W. Harrison, *Appl. Spectrosc. Rev.* **10**(2), 201 (1975).

24. F. Paschen, Ann. Phys., **50**, 901 (1916).

25. H. Schuler, *A. Phys.*, **35**, 323 (1926); Chem. Abstr., **20**, 2121 (1926).

26. H. Schuler, *A. Phys.*, **59**, 149 (1929); Chem. Abstr., **24**, 1287 (1930).

27. H. Schuler and H. Gollnow, *Z. Phys.*, **93**, 611 (1935), Chem. Abstr., **29**, 3233 (1935).

28. C. A. Morgan, C. L. Davis, B. W. Smith and J. D. Winefordner, *Appl. Spectrosc.* **48**, 261 (1994).

29. S. Caroli, O. Senofonte, N. Violante and L.D. Simone, *Appl. Spectrosc.* **41**, 579 (1987).

30. D. Littlejohn, J. Carroll, A. M. Quinn, J. M. Ottaway and H. Falk, *Fresenius Z. Anal. Chem.* **323**, 762 (1986).

31. F. Chen and J. C. Williams, *Anal. Chem.* **62**, 489 (1990).

32. J. Y. Ryu, R. L. Davis, J. C. Williams and J. C. Williams Jr., *Appl. Spectrosc.* **42**, 1379 (1988).

33. J. Tseng, J. C. Williams, R. B. Bartlow, S. T. Griffin and J. C. Williams Jr., *Anal. Chem.* **62**, 1933 (1991).

34. F. Howorka and M. Pahl, *Z. Naturforsch.*, **27A**, 1425 (1972).

35. H. Falk, *Progr. Anal. At. Spectrosc.*, **5**, 205 (1982).

36. D. C. Gerstenberger, R. Solanki and G. J. Collins, *IEEE J. Quantum Electron.* **16**, 820 (1980).

37. H. Tsuda and J. A. Piper, *J. Phys. E: Sci. Instrum.* **22**, 462 (1989).

38. J. A. Piper and C. E. Webb, *J. Phys. D: Appl. Phys.* **6**, 400 (1973).

39. J. M. Mermet, paper no. 164, presented at the 45th Pittsburgh Conference (Chicago, IL, February 1994).

40. P. Zanzucchi, A study of direct solution analysis with a new hollow cathode discharge system. Thesis, University Microfilms, Ann Arbor, MI, U.S.A., 68-8278 (1967).

41. P. A. Buger and W. Fink, *Fresenius Z. Anal. Chem.* **244**, 314 (1969).

42. J. A. C. Broekaert, R. Pereiro, T. K. Starn and G. M. Hieftje, *Spectrochim. Acta* **48B**, 1207 (1993).

43. T. K. Starn, R. Pereiro and G. M. Hieftje, *Appl. Spectrosc.* **47**, 1555 (1993).

44. R. Pereiro, T. K. Starn and G. M. Hieftje, *Appl. Spectrosc.* **49**, 616 (1995).

45. E. L. Grove and W. A. Loseke, *Can. J. Spectrosc.* **18**, 83 (1973).

46. K. C. Ng, A. H. Ali and J. D. Winefordner, *Spectrochim. Acta* **46B**, 309 (1991).

47. L. Puig and R. Sacks, *Appl. Spectrosc.* **43**, 801 (1989).

48. M. Klemp, L. Puig, K. Trivedi and R. Sacks, *J. Chromatogr. Sci.* **30**, 136 (1992).

49. J. M. Brackett and T. J. Vickers, *Spectrochim. Acta* **38B**, 979 (1983).

50. J. M. Brackett and T. J. Vickers, *Spectrochim. Acta* **39B**, 837 (1984).

51. C. M. Strange and R. K. Marcus, *Spectrochim. Acta* **46B**, 517 (1991).

52. J. You, J. C. Fanning and R. K. Marcus, *Anal. Chem.* **66**, 3916 (1994).

53. G. O. Foss, H. J. Svec and R. J. Conzemius, *Anal. Chim. Acta* **147**, 151 (1983).

54. T. Cserfalvi, P. Mezei and P Apai, *J. Phys. D: Appl. Phys.* **26**, 2184 (1993).

55. T. Cserfalvi and P Mezei, *J. Anal. At. Spectrom.* **9**, 345 (1994).

56. Y. Kanzaki, N. Nishimura and O. Matsumoto, *J. Electroanal. Chem.***167**, 297 (1984).

57. A. Hickling in: *Modern Aspects of Electrochemistry*, no. 6 (J. O'M. Bockris and B. E. Conway, eds.), Plenum Press, New York, 1971.

58. Y. Iida, *Spectrochim. Acta* **45B**, 427 (1990).

Chapter 2

Evaluation of a HCD designed for continuous sample introduction

2.1 Introduction

A sample introduction interface was designed which allowed for continuous discharge operation and solution sample introduction. The primary focus of this project was to extend the use and acceptance of the hollow cathode source to include the analysis of nebulized solution samples with a continuously operating helium discharge. The effect of carrier gas flow rate, discharge current, and sample solution flow rate on the emission intensity will be presented along with preliminary analytical results and construction details of the HCD. An attempt at solution sample introduction by electrospray nebulization was also made.

It was also anticipated that the sample introduction interface could be used to introduce both solid and gaseous sample types. Preliminary attempts at solid sample introduction by laser ablation will be presented. Introduction of halogen vapors was attempted to show that the sample introduction interface and helium HCD could also be used for gaseous analysis. The goal of this project was to develop a HCD which would be able to analyze all sample forms and types. If successful, this emission source would prove to be an attractive alternative to ICP-AES since it would function at low power levels and be economical to operate.

2.2 Description of the hollow cathode source

A cross-sectional scale drawing of the HCD source (Fig. 2.1) shows the hollow cathode disc (i), anodes (g) placed on both sides of the hollow cathode tube, and the path taken by the sample as it enters and exits the discharge. For clarity, the 2 mm o. d. glass tube and tube holder (a, b) are shown removed from the hollow cathode. This design makes extensive use of Cajon ultra-torr fittings with Viton O-rings to make vacuum seals between glass and metal.

The hollow cathode disc is demountable, machined from type 304 stainless steel, and has an inner diameter of 1.5 mm and a length of 10 mm. Stainless steel was chosen as the cathode material because of its mechanical toughness and resistance to sputtering. Insulators made of Macor (h) covered the exposed ends of the cathode disc to restrict the discharge to the inner surface of the hollow cathode tube. A maximum current density of 0.64 A/cm^2 was achieved, limited only by the power supply.

Multiple anode configurations have been used in hollow cathode lasers to provide a uniform and stable discharge [1]. With this in mind, anodes were placed on both sides of the hollow cathode tube. To achieve stable discharge operation, the relative placement of the anodes with respect to the cathode was critical. The optimum distance between the cathode and anodes was determined empirically to be approximately 4 mm. Distances in excess of 4 mm led to erratic discharge behavior.

The helium plasma gas and sample aerosol directly entered the discharge through a glass tube (inner diameter of 1 mm and an outer diameter of 2 mm) which was inserted into the hollow cathode via a hole drilled through the wall of the cathode. Flame

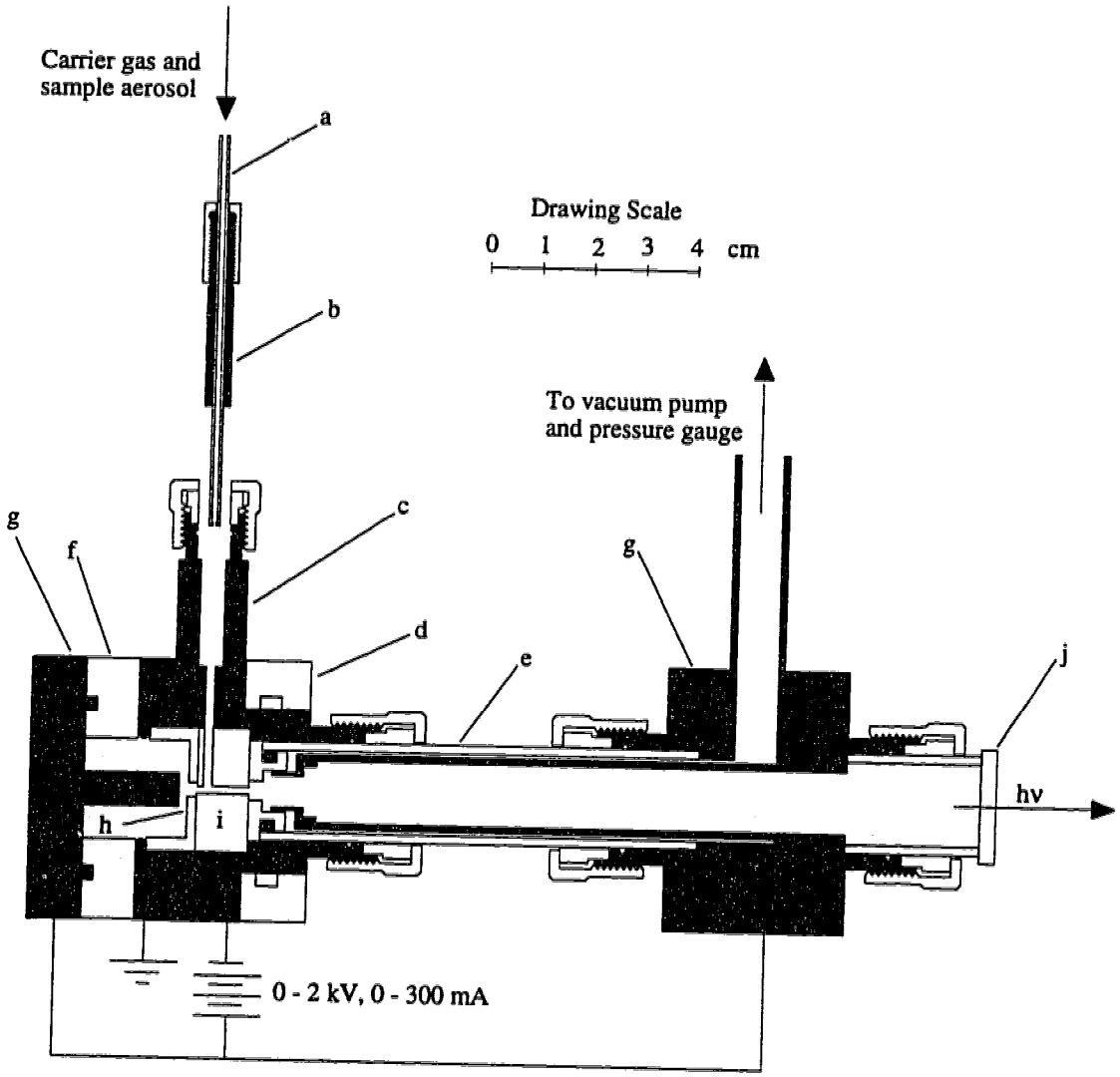

Fig. 2.1 Cross-sectional scale drawing of HCD source: (a) 2 mm o.d. glass tube, (b) tube holder (brass), (c) cathode housing (stainless steel), (d) water cooling jacket, (e) 3/4" o.d. glass tube, (f) Teflon insulator, (g) anode (brass), (h) Macor insulators on both sides of hollow cathode, (i) hollow cathode, (j) quartz window.

polishing the end of the tube which was in contact with the plasma reduced the inner diameter of the tube. Note that this is the tube that provides the interface from atmospheric pressure to the low pressure in the HCD. By varying the inner diameter of the end of the tube, plasma gas flow rates were optimized. An O-ring seal between the glass tube and the tube holder made for fast tube replacement when a different plasma gas flow rate was desired. The tubular configuration of the anode caused the plasma gases to be removed from the line of sight of the detector as soon as the gases passed through the hollow cathode, thereby minimizing the effects of self absorption. Carrier gas flow rate and discharge gas pressure were controlled by the restricted inner diameter of the 2 mm o. d. glass tube and a gate valve located between the discharge chamber and the vacuum pump. Since carrier gas flow rate and discharge gas pressure could not be controlled independently from each other, the discharge pressure was maintained at 20 Torr throughout this study.

The design of the HCD source allowed discharge operation for weeks at a time before internal cleaning of the source was required. Deposition of sputtered material was directed away from the quartz window by the tubular anode design. Also, since the anode approached the cathode through a 8.4 cm long 3/4" o. d. glass tube, electrical shorting between the cathode and anode as a result of deposition of sputtered material was not a problem. Water cooling along with the rugged design of the HCD source allowed for continuous discharge operation at the high current densities which were used in this study.

2.3 Sample introduction

The experimental setup for solution sample introduction into the HCD source is shown in Fig. 2.2. A peristaltic pump (Rainin, Rabbit Model) drives the sample to a

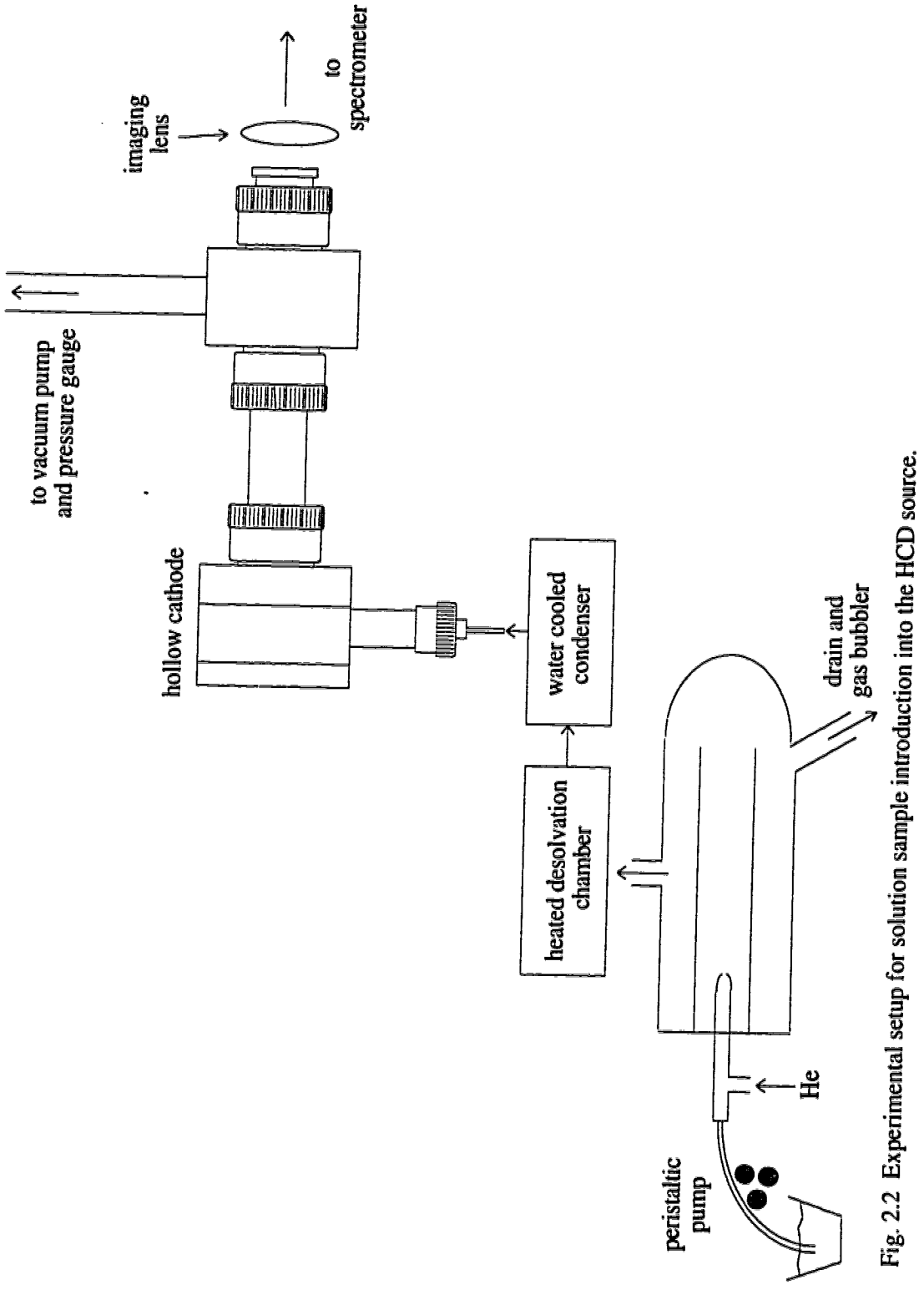

Fig. 2.2 Experimental setup for solution sample introduction into the HCD source.

Meinhard nebulizer and Scott type spray chamber. The carrier gas flow rate was matched to the uptake rate of the vacuum pump by observing bubbles exiting the drain tube. Helium was used as the nebulizing gas. The glass desolvation chamber was heated with a Variac power supply and an electrically conductive braided wire to a temperature of 270° C. The heated chamber was 17 cm long and had an inner diameter of 5 cm. Next, the sample aerosol was transported to a glass water cooled condenser maintained at approximately 17° C. The condenser was 24 cm long and had an internal diameter of 3.5 cm. The purpose of the desolvation chamber and condenser was to remove as much water from the sample aerosol as possible before introducing the aerosol into the HCD.

It is important to note that the transition from atmospheric pressure to discharge pressure occurred directly at the hollow cathode discharge (*i. e.*, parts (a) and (b) of Fig. 2.1 are inserted into (c) so that the tip of the glass tube (a) is right inside the hollow cathode (i)). Previous studies showed that when this transition occurred upstream of the discharge, the sample would not reach the plasma but would form deposits immediately after the transition to low pressure. Operating conditions for the HCD and sample introduction are summarized in Table 2.1.

2.4 Instrumentation

The HCD was powered by a Glassman high voltage dc power supply (Model PS/EW02R300-115) which can deliver a maximum of 300 mA and 2kV. The power supply was operated in the constant current mode, which means that when the current is selected, the discharge conditions determine the operating voltage. No ballast resistors between the power supply and the anode were required to maintain a stable discharge. Vacuum was provided by an Edwards (Model E2M18, 25.0 m^3/h) rotary vacuum pump and was monitored by a mechanical pressure gauge (Wallace and Tiernan Model FA

Table 2.1 Operating conditions for the HCD and sample introduction.

Discharge Current	295 mA
Pressure	20 Torr He
He flow rate	1.0 - 3.7 l/min
Solution flow rate	0.3 - 1.2 ml/min
Blank solution	2% HNO_3

160). The cathode was imaged 1:1 with a quartz lens onto the entrance slit (100 μm) of a modified Heath 0.35-meter Model EU-700 spectrometer [2]. This spectrometer could be used in its normal configuration with a PMT detector, or a folding mirror could be swung in front of the normal exit folding mirror bringing the exit focal plane to a 1024-element photodiode array (Reticon Model 1024S, RC1024S evaluation circuit). Signals from the PMT (RCA Model P28A biased at -700 V) were amplified using a Keithley 427 current amplifier. With photodiode array (PDA) detection, a wavelength coverage of about 50 nm was possible. Data acquisition was performed using a Macintosh IIsi computer with a National Instruments Lab-NB board and SpectoPlot [3] as the data acquisition and processing software.

2.5 Reagents

All solutions samples were prepared from Leco (ICP grade) standards. Samples were diluted with distilled and deionized water and stored in 2% HNO_3.

2.6 Results and discussion

2.6.1 Voltage-current characteristics of the HCD

Due to the "hollow cathode effect", HCDs operate at lower voltages and are able to sustain much higher currents when compared to glow discharges with planar cathodes. Voltage-current curves from 20 - 295 mA, with and without blank solution aspiration, are shown in Fig. 2.3. As current is increased, moderate voltage increases are observed which is indicative of an abnormal glow discharge before transition to an arc [4-5]. Stable discharge operation was achieved with and without blank aspiration.

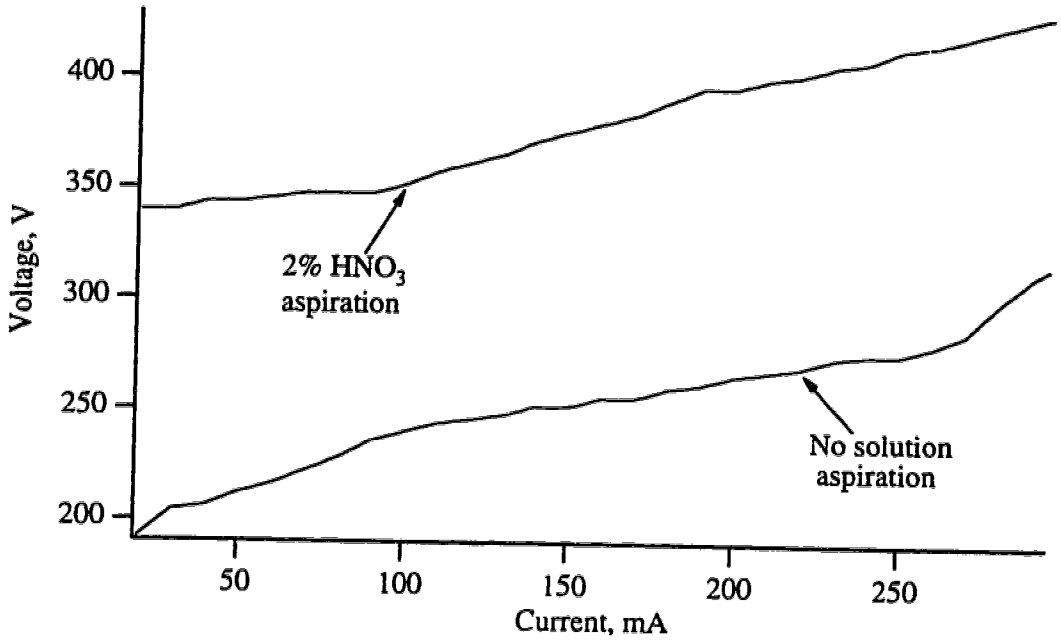

Fig. 2.3 Voltage-current relationship.

The effect of water vapor on the voltage characteristics of the discharge are illustrated in Fig. 2.3. Water vapor exists in the discharge since the condenser is unable to completely remove all traces of water. For the lower curve (no solution aspiration), helium was introduced directly from the high pressure tank in order to ensure that water vapor was completely absent from the discharge. At all currents investigated, the presence of water vapor increased the discharge voltage by approximately 120 V. This effect has been observed for a glow discharge with a planar cathode [6] and is a result of H^+ ion formation. Hydrogen ion impact with the cathode has a lower secondary electron yield than helium. Therefore, since the HCD power supply was operated in the current controlled mode, a higher discharge voltage is required. The presence of water in the discharge is not desirable because water is known to seriously degrade the analytical performance of glow discharges [7]. However, with high discharge currents and carrier gas flow rates, HCDs can be used for analytical purposes while water is present in the discharge.

2.6.2 Emission spectra from Ca and Mg

The spectra presented in Figs. 2.4 and 2.5 show the atom and ion line emission from Ca and Mg and indicate the types of background spectral features common to this discharge. Integration times and solution concentrations were chosen to provide a convenient comparison between the emission intensity of Ca and Mg to the background emission. The spectra shown in Figs. 2.4b and 2.5b were obtained under optimized experimental conditions for analyte emission and clearly show the ability of background subtraction using the PDA spectrometer to isolate analyte emission from a crowded spectral background.

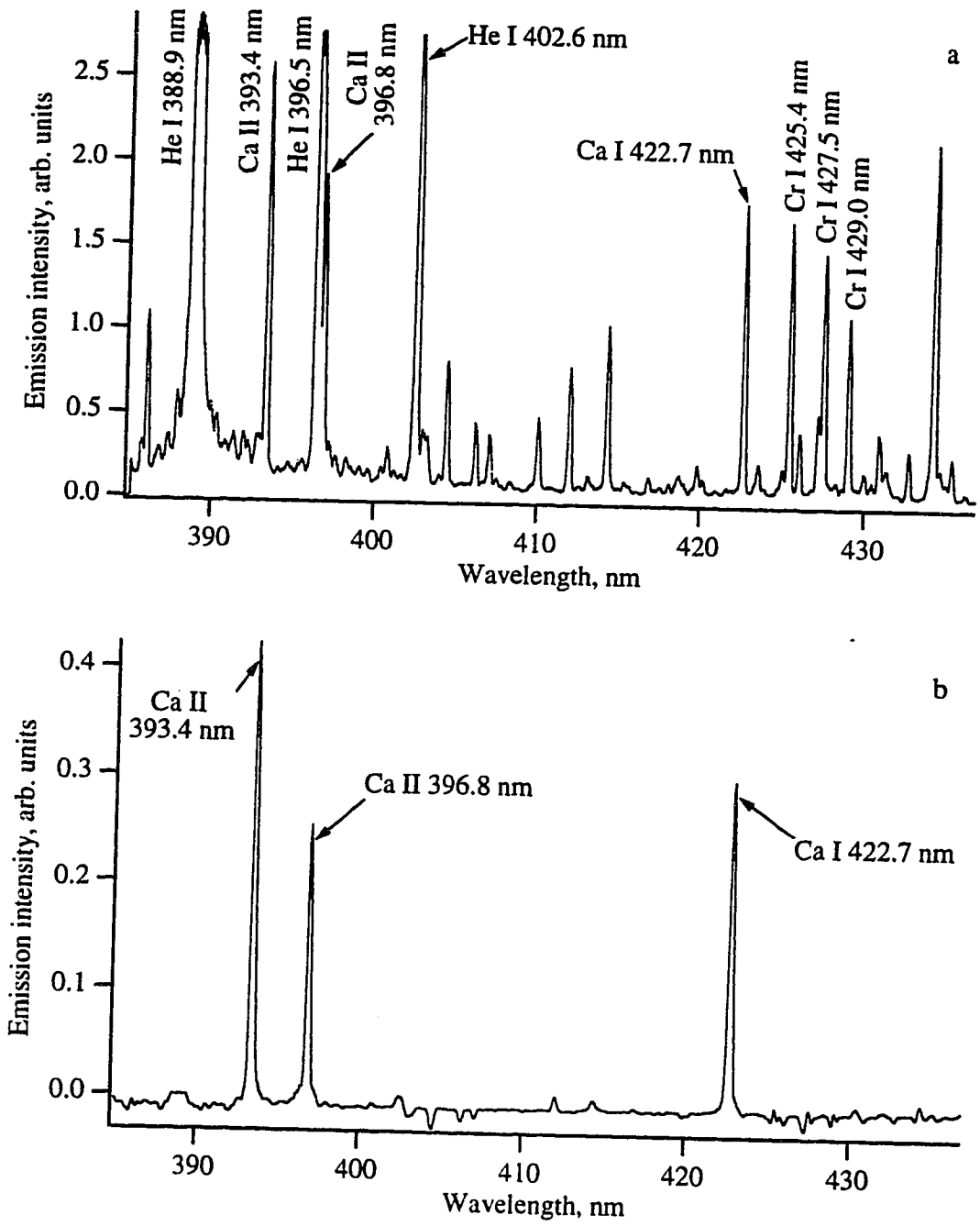

Fig. 2.4 PDA spectra of (a) background and 10 μg/ml Ca, 5.3 s integration and (b) background subtracted 1 μg/ml Ca, 5 scans averaged, 21.2 s integration per scan, low pass digitally filtered.

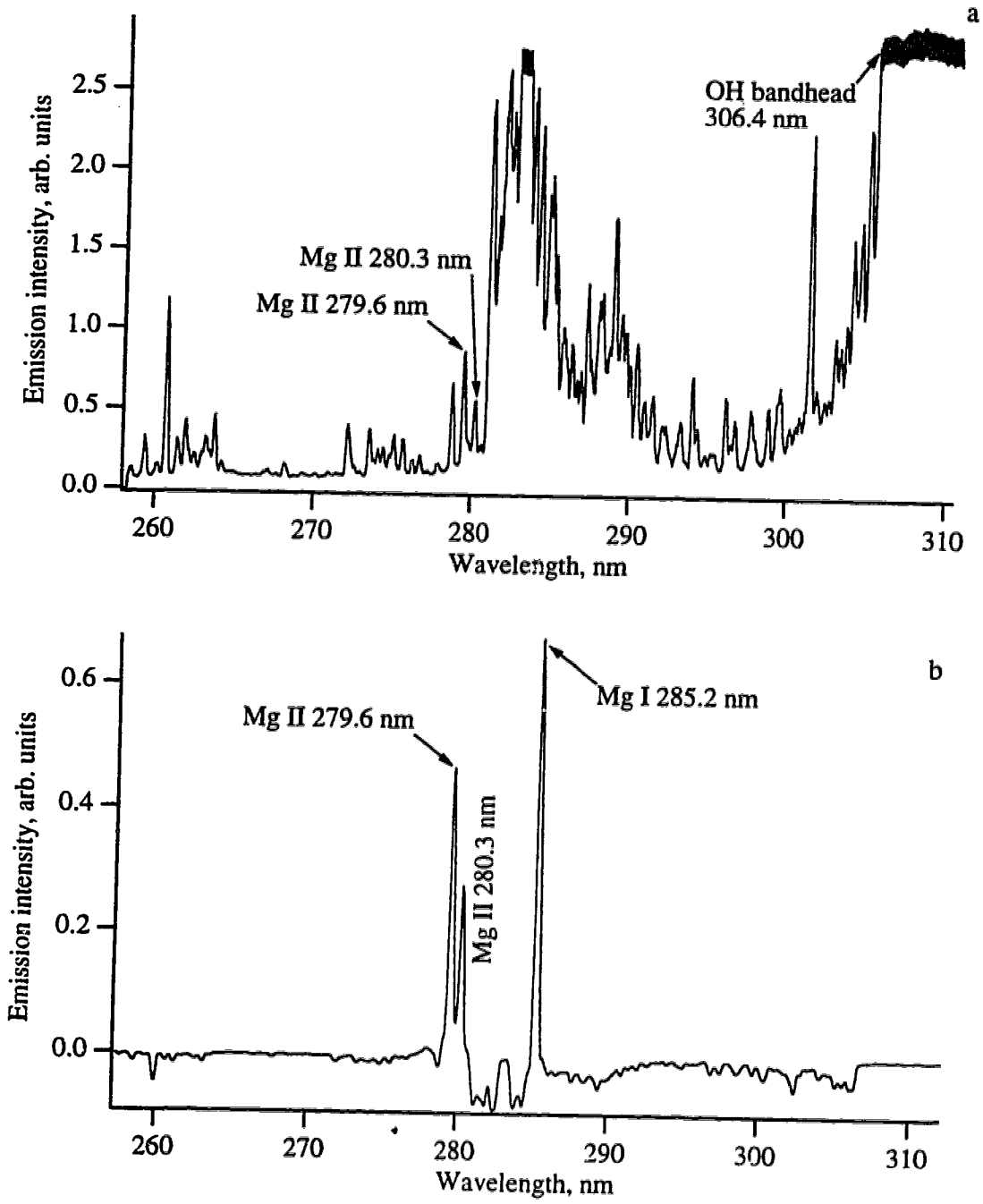

Fig. 2.5 PDA spectra of (a) background and 10 µg/ml Mg, 5.3 s integration and (b) background subtracted 10 µg/ml Mg, 10 scans averaged 10.6 s integration per scan, low pass digitally filtered.

Emission bands originating from OH were observed at 281.1 and 306.4 nm during solution aspiration (Fig. 2.5a), and emission from NH (not shown here) was also detected at 336.0 nm. The origin of these molecular species is a combination of residual water vapor not removed by the condenser, HNO_3 from the solution blank, and air entrainment. Intense background emission is undesirable for any emission source; and in this case, detection of the Cu I resonance lines at 324.7 and 327.4 nm would be difficult and detection of Al at 309.3 nm would be nearly impossible. Due to the OH bandhead at 281.1 nm, identification of Mg at 285.2 nm is only possible after background subtraction (see Fig. 2.5).

The spectral region from 300 to 340 nm was basically the only region from 200 to 800 nm where any molecular emission was observed with this source. In contrast, intense background emission from CO^+, N_2, and N_2^+ is problematic for furnace atomization plasma excitation spectrometry (FAPES) [8] over a much broader spectral region. Molecular background emission is also troublesome for furnace atomic nonthermal excitation spectrometry (FANES) [9-10] since it degrades detection limits due to background fluctuations. Other than molecular emission from NH and OH, background spectral features are exclusively due to atomic transitions of the helium plasma gas and elements such as Fe, Ni, and Cr from the stainless steel cathode.

2.6.3 Optimization of instrumental conditions

For the initial characterization of the HCD the instrumental parameters that were varied included the relative anode position with respect to the hollow cathode, the carrier gas flow rate, the discharge current, and the sample solution flow rate to the pneumatic nebulizer. The spectral lines used to monitor the effect of these parameters were the Mg 279.553 nm ion line and 285.213 nm atom line and the Ca 393.367 nm ion line and

422.673 nm atom line. Emission line intensities were background subtracted and recorded using the PDA spectrometer. Optimum parameter settings, in general, were considered to be those that maximized net line intensities. In addition, ion/atom emission intensity ratios were also evaluated for Ca and Mg. This ratio has been used [11] to monitor the performance of ICP-AES. For an ICP, a high ion/atom emission intensity ratio was sought as it was indicative of optimum excitation conditions. In our case this ratio was calculated to monitor excitation conditions, but it was felt that maximization of net line intensities was the best criterion to optimize overall analytical performance.

2.6.3.1 Effect of anode position relative to hollow cathode.

Excitation conditions are not uniform across the length of the 1 cm long hollow cathode tube, but are enhanced at positions which are nearest to the anode. Multiple anode configurations are possible with this HCD design. The anode can be located to the left, right, or both left and right sides of the hollow cathode (see Fig. 2.1). Ion and atom line intensities and ion to atom line intensity ratios for Ca are summarized in Table 2.2 as positive potential is supplied to the left, right, and both left and right anodes. Emission intensities and the ion/atom intensity ratio were maximized when anodic potential was supplied to only the left anode. Unfortunately, this configuration led to unstable discharge conditions as arcing occurred every 5 to 10 sec. Further work was carried out with anodic potential supplied to only the right anode.

2.6.3.2 Effect of carrier gas flow rate.

Helium is used as the carrier gas and its flow rate is determined by the restricted inner diameter of the 2 mm o. d. glass tube (Fig. 2.1) and by a gate valve located between the discharge chamber and vacuum pump. The effect of carrier gas flow rate on

Table 2.2 Effect of Ca ion and atom, and ion to atom line intensity ratios on anode position relative to hollow cathode*.

Anode position relative to cathode (see Fig. 2.1)	Ca II 422.7 nm	Ca I 393.4 nm	Ca II / Ca I
Left	0.422	0.244	1.73
Right	0.280	0.283	0.99
Left and Right	0.160	0.173	0.92

*Experimental conditions were as follows:

Concentration of aspirated Ca solution was 1.0 μg/ml.

Sample aspirated at 0.6 ml/min.

Emission intensities were background subtracted with a PDA integration time of 10.6 sec.

Carrier gas flow rate was 3.7 l/min.

Ca and Mg, ion and atom line emission intensities and ion to atom line intensity ratios is shown in Fig. 2.6. Similar effects were observed for both Ca and Mg. As flow rate increases, the emission intensities of ion and atom lines increase. But, the ion to atom line intensity ratio seemed to be maximized at a low flow rate. This suggests that there are conflicting processes involved in the transportation and excitation of the sample. Transport efficiencies to the HCD are optimized at high flow rates, while excitation conditions in the HCD, as indicated by a high ion/atom emission intensity ratio, are optimized at low flow rates. A flow rate of approximately 3.5 l/min, which maximized ion and atom line intensities, was selected for all subsequent analysis.

2.6.3.3 Effect of discharge current.

The effect of discharge current on analyte emission is easy to determine and was investigated up to the maximum current available on the high voltage power supply. The effect of discharge current from 145 to 295 mA on Ca ion and atom line intensities is shown in Fig. 2.7. As discharge current is increased, Ca ion emission increases in intensity at a faster rate than Ca atom emission, but both ion and atom line intensities appear to reach a plateau at high currents. This suggests that, under the present experimental conditions, the current limit of the high voltage power supply is near the optimum current for analyte emission. For all elements investigated in this report, atomic emission intensity always increased with increasing current. A discharge current of 295 mA was used for all further work.

2.6.3.4. Effect of sample solution flow rate.

The effect of sample solution flow rate on Ca ion and atom line intensities for a 10 μg/ml solution is shown in Fig. 2.8. An increase in flow rate produces moderate

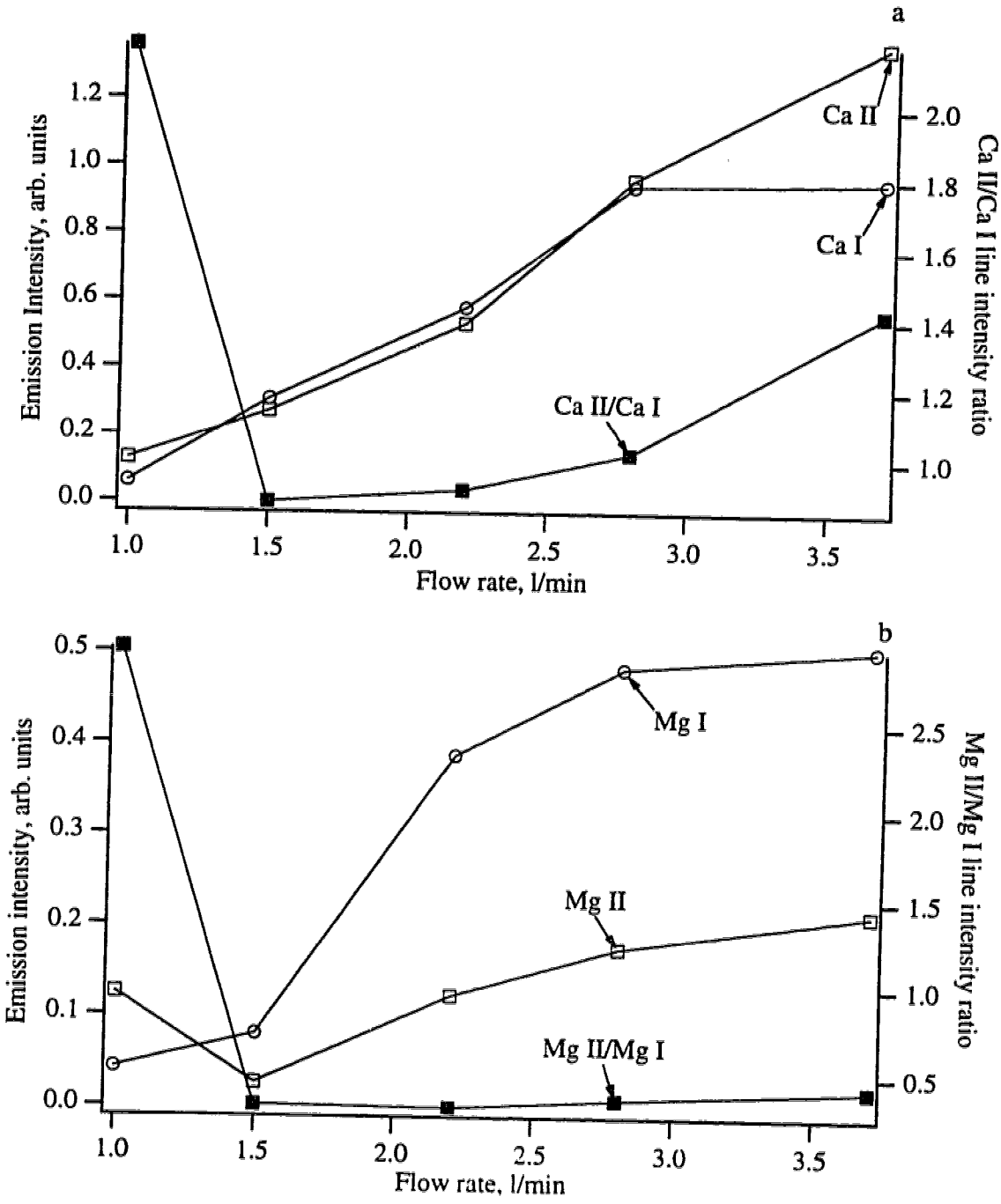

Fig. 2.6 Effect of carrier gas flow rate on Ca and Mg, ion and atom line intensities and ion to atom line intensity ratios. Concentration of Ca and Mg was 10 µg/ml and the sample solution was aspirated at 0.3 ml/min. PDA integration time was 10.6 s per scan with 10 scans averaged for both the blank and sample. All emission intensities were background subtracted.

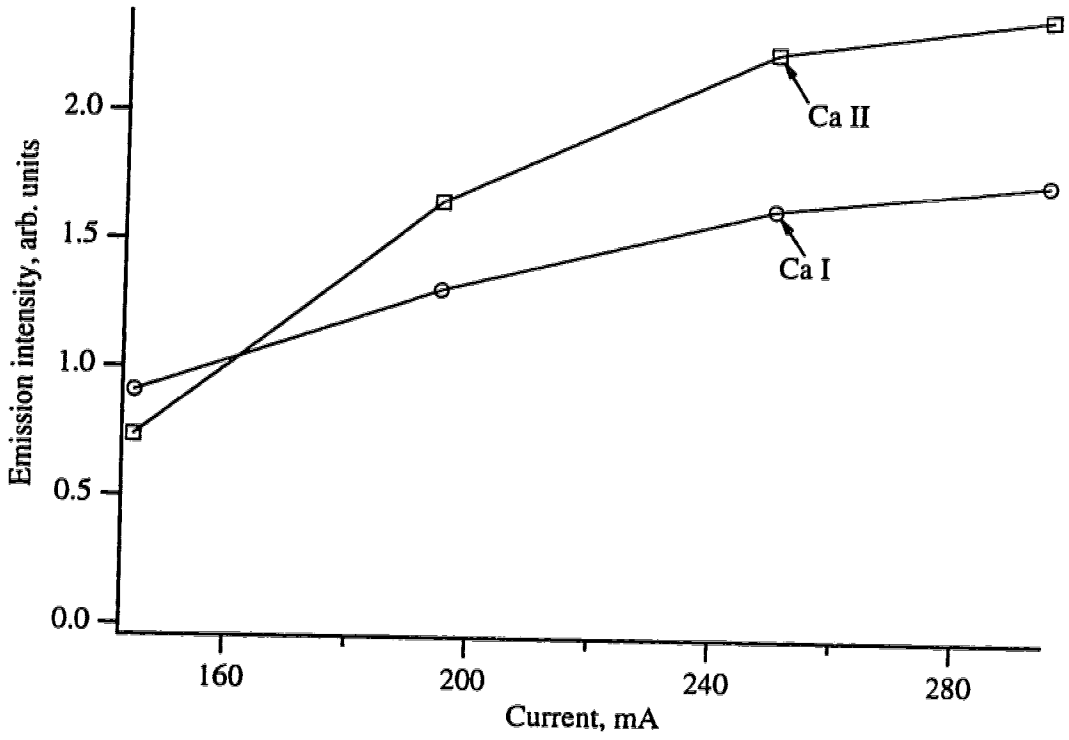

Fig. 2.7 Effect of discharge current on Ca ion and atom line intensities. Concentration of Ca was 10 μg/ml and the sample solution was aspirated at 0.3 ml/min. PDA integration time was 10.6 s per scan with 10 scans averaged for both blank and sample. All emission intensities were background subtracted.

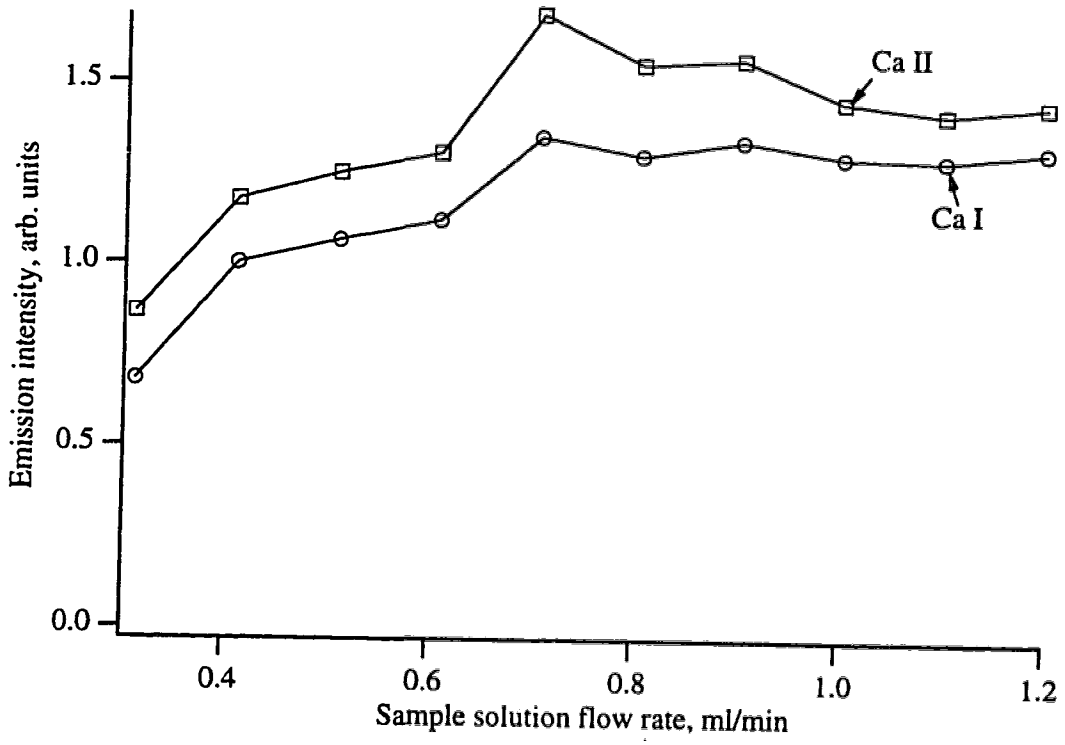

Fig. 2.8 Effect of sample solution flow rate on Ca ion and atom line intensities for a 10 µg/ml Ca solution. PDA integration time was 10.6 s per scan with 5 scans averaged for both blank and sample. All emission intensities were background subtracted.

increases in both ion and atom emission and a flow rate of 1.0 ml/min was used for further studies.

Conventional wisdom states that water vapor must always be rigorously excluded from glow discharge devices [7] because traces of water vapor are known to inhibit excitation conditions. If we assume that more water vapor reaches the plasma as solution flow rate increases, the negative effect that water vapor should have is not observed. The high discharge currents and carrier gas flow rates used in this study are likely responsible for limiting the negative effects of water vapor in the discharge.

2.6.4 Emission spectra from selected elements.

A variety of elements with lines of different excitation potentials were aspirated into the discharge to gain an overview of the analytical capabilities of the HCD design. Relative anode position with respect to the cathode, carrier gas flow rate, discharge current, and solution flow rate were set to the values determined in the last section. All spectra were recorded with the PDA detector and are background subtracted.

The alkali and alkaline earth metals have lines with low excitation potentials and are relatively easy to excite. Typical spectra are shown in Figs. 2.4, 2.5, and 2.9. The two best emission spectra in terms of strong signal intensity and low background fluctuations were seen from Li (0.1 μg/ml) and Na (1 μg/ml) (Figs. 2.9a and 2.9b). Cs emission (1 μg/ml) was somewhat less intense (Fig. 2.9c) and a concentration of 10 μg/ml was required for K and Rb (Fig. 2.9d) in order to obtain strong emission with low background fluctuations. The ion and atom emission lines used for instrumental optimization were clearly seen in the Mg and Ca spectra (Figs. 2.4 and 2.5) as noted earlier.

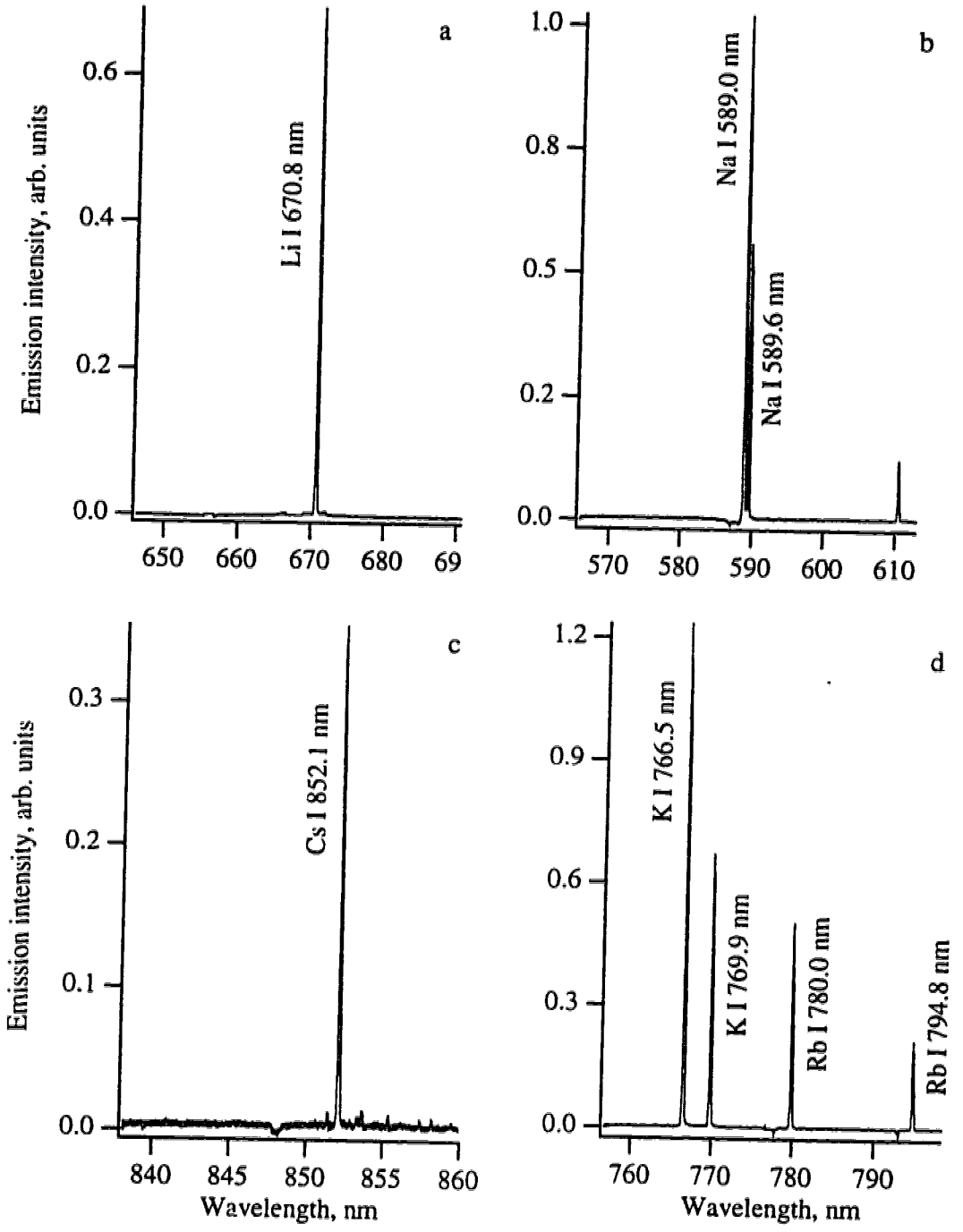

Fig. 2.9 Background subtracted PDA spectra of (a) 0.1 μg/ml Li, 10.6 s integration, (b) 1 μg/ml Na, 5.3 s integration per scan, 5 scans averaged, (c) 1 μg/ml Cs, 42.5 s integration per scan, 5 scans averaged, and (d) 10 μg/ml K and Rb, 21.2 s integration per scan, 5 scans averaged.

The transition metals Mn, Cd, and Zn have higher energy electronic transitions and are more difficult to excite. As shown by the spectrum presented in Fig. 2.10a ion lines of Mn, ion and atom lines of Cd, and an atom line of Zn are easily detectable using a 10 μg/ml solution of these metals. The noisy baseline is due to changes in the spectral features of the background emission. The spectrum from a 10 μg/ml Al solution is shown in Fig. 2.10b. Aluminum is considered a refractory element since it has the tendency to form strong metal oxide bonds, making it difficult to vaporize in some emission sources. Also, when Al is used as the cathode in glow discharge spectrometry, a long warm up period can be required to remove the surface oxide layer before a stable discharge can be maintained. In this HCD design, stability problems were not a factor when Al was aspirated and atomic emission was easily measured.

To assess the detection capability of the HCD, detection limits were calculated (Table 2.3) from the spectra presented in Figs. 2.4b, 2.5b, 2.9, and 2.10. Detection limits were calculated by dividing 3 times the standard deviation of the baseline noise by the analyte sensitivity. The standard deviation of the noise was taken to be the standard deviation of 32 neighboring pixels, located near the analyte peak, from the background subtracted and low pass digitally filtered spectra. Low pass digital filtering can be used to smooth a spectrum and remove unwanted spatial frequencies, thereby improving the signal-to-noise ratio [12]. The lowest detection limit was obtained for Li and the rest of the alkali and alkaline earth metals have much lower detection limits than the transition metals. The detection limit of Zn (200 ng/ml) appears high when compared to plasma sources like the ICP [13]. However, relatively high ICP detection limits for Zn of 50 [14] and 30 [2] ng/ml have been determined with the same PDA spectrometer used in this study. Detection limits calculated with PDAs are generally poorer than the best published ICP detection limits with PMT detectors.

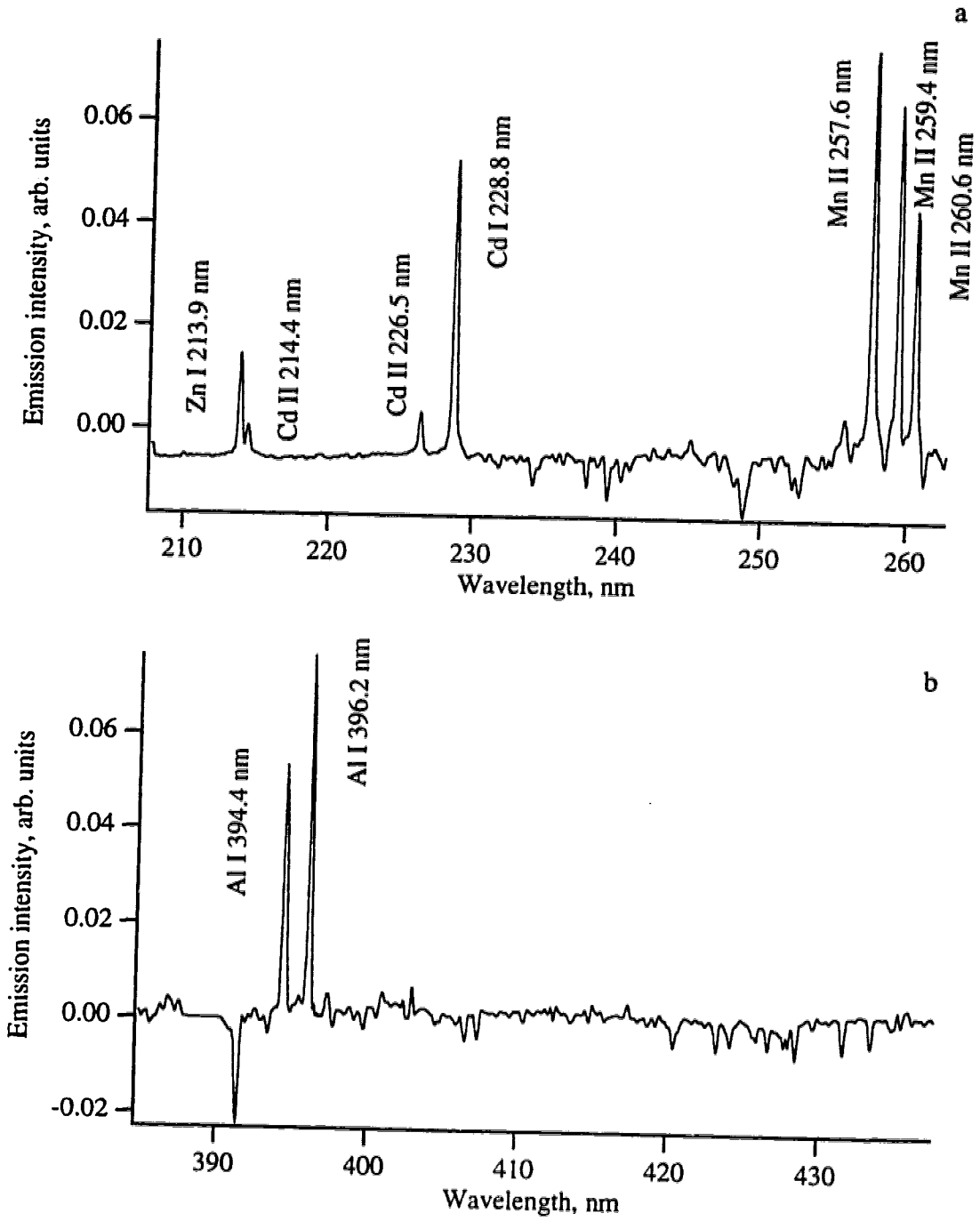

Fig. 2.10 Background subtractd PDA spectra of (a) 10 µg/ml Mn, Cd, and Zn, 21.2 s integration per scan, 5 scans averaged, low pass digitally filtered and (b) 10 µg/ml Al, 21.2 s integration per scan, 5 scans averaged, low pass digitally filtered.

Table 2.3 Hollow cathode detection limits for nebulized solution samples.

Element	Emission Line, nm	Detection Limit, ng/ml
Li	670.8	0.03
Na	589.0	0.2
Cs	852.1	0.6
Ca	393.4	3
K	766.5	4
Rb	780.0	10
Mg	285.2	20
Mn	257.6	40
Cd	226.5	50
Al	305.7	100
Zn	213.9	200

2.6.5 Memory effect, signal stability and linear dynamic range for Li detection

A closer look at the analytical performance of the HCD was undertaken in terms of memory effect, signal stability, and linear dynamic range. Lithium was chosen as the test element since it showed the lowest detection limit of all elements determined. For the following study, PMT detection of emission intensity was used.

Short term temporal stability of the HCD with 1 μg/ml Li introduction is shown in Fig. 2.11. Analyte transportation from the spray chamber to the plasma is very rapid as seen by the sharp increase in signal intensity. The signal reaches a plateau level and the stability of the discharge is indicated by stable signal levels during blank and analyte aspiration. The analyte is quickly removed from the sample introduction glassware and hollow cathode tube when the blank solution is aspirated into the spray chamber. When the blank enters the spray chamber, only 23 sec are required to reduce the signal to within 10% of what it was before the analyte entered the discharge. Memory effects are minimal and can be attributed to the high carrier gas flow rate which quickly transports the analyte to the discharge. Also, the high current densities sustained in the discharge are responsible for keeping the surface of the cathode clean and free from residual analyte deposits.

To determine the ability of the HCD to respond quantitatively to changes in analyte concentrations, a calibration curve was constructed. A calibration curve for Li from 0.01 to 10 μg/ml is shown in Fig. 2.12. Signal intensities are the average of 600 digitized points collected over a one minute period. A slope of 0.90 indicates a nearly linear relationship between Li concentration and emission intensity over 3 orders of magnitude.

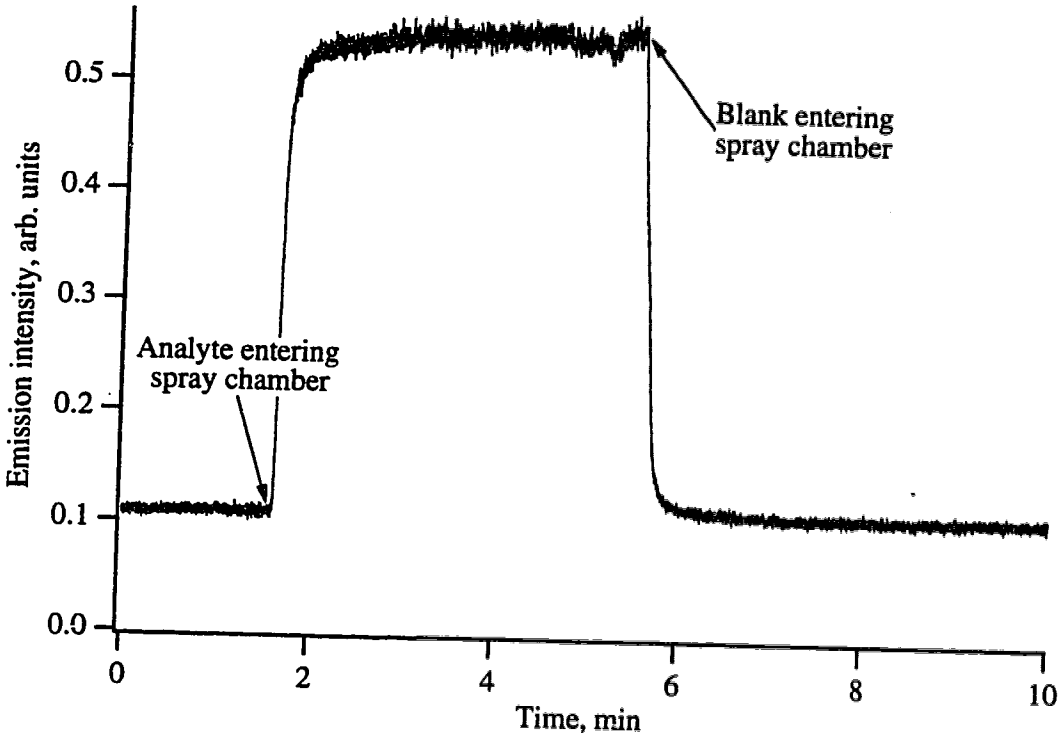

Fig. 2.11 Short term stability of the HCD during 1 μg/ml Li aspiration.

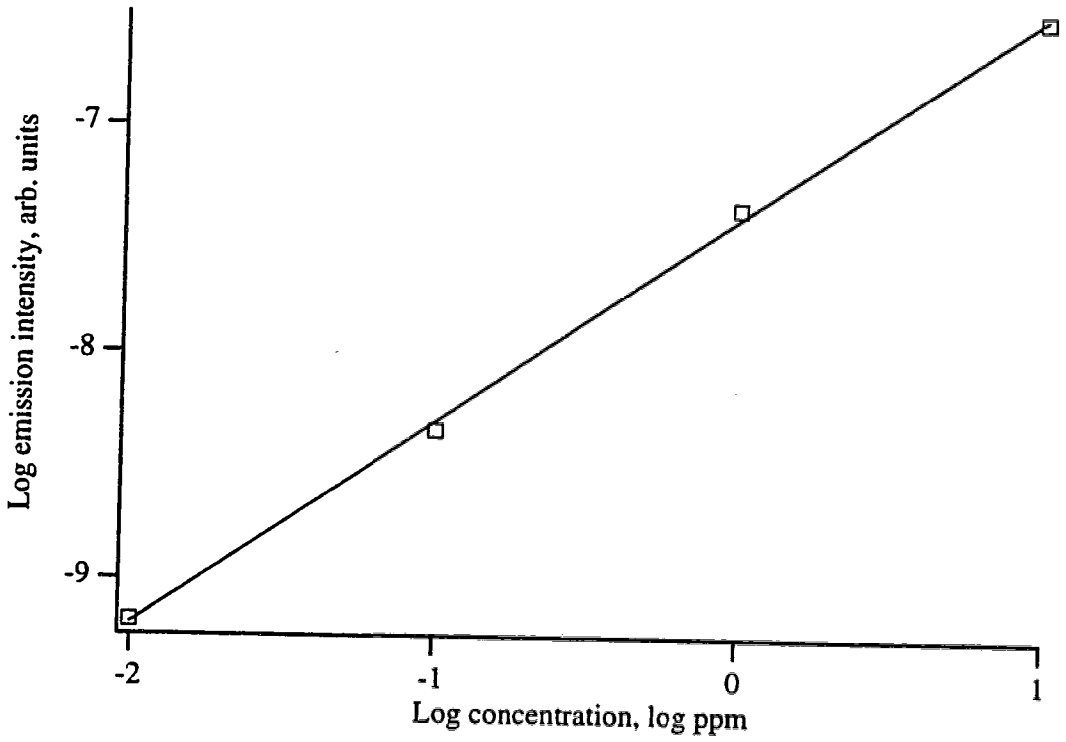

Fig. 2.12 Calibration curve for Li 670.8 nm, slope = 0.90. Emission intensities are the average of 600 digitized values collected at 100 ms/point.

2.7 Attempted solution sample introduction by electrospray nebulization

The phenomena of electrospray (ES) has been used as an atmospheric-pressure ionization source for mass spectrometry (MS) [15-18]. Recent work has shown that ES-MS can be used to observe bare metal ions directly from solution samples [19]. It was thought that the phenomena of ES could be used to introduce analyte ions into an operating HCD. A schematic diagram showing how ES is interfaced to introduce ions into a mass spectrometer is shown in Fig. 2.13. The sample solution was pumped through a charged capillary and emerged from the ES tip. Gas-phase ionic species were generated which represented the components in the sample solution. A counter-current flow of Ar was used as a curtain gas to exclude uncharged solvent droplets from entering the interface. For ES sample introduction into a HCD, the skimmer was replaced by a HCD open at both ends. Many different combinations of acceleration potentials, gas flow rates, and solution flow rates were attempted. However, detection of atomic or ionic emission from analyte species was never observed. Further work is required to optimize solution sample introduction by ES nebulization.

2.8 Solid sample introduction by laser ablation

Laser ablation has been used as a method of introducing solid samples into secondary emission sources such as the ICP [20-21]. There has also been one report of the successful combination of laser ablation and the HCD [22]. The same interface and HCD described for solution sample introduction in section 2.2 was used to introduce the ablated plumes from solid samples. The experimental setup for laser ablation coupled with a HCD is shown in Fig. 2.14. The ablated plumes from solid samples were swept into the HCD by a He carrier gas stream. The ablation chamber was positioned near the

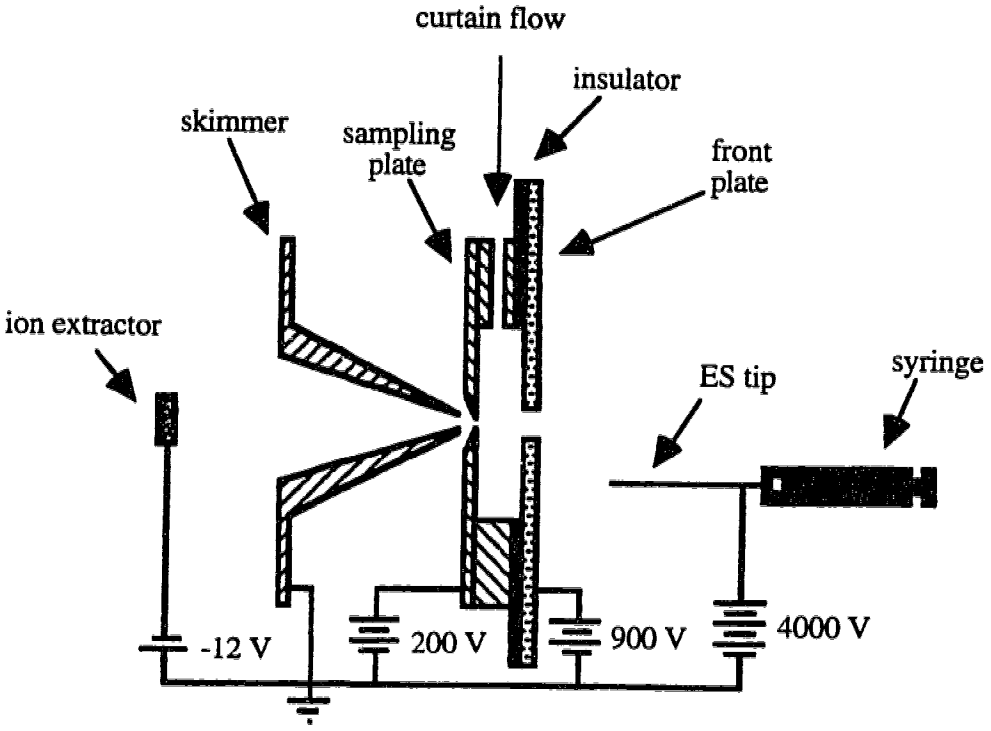

Fig. 2.13 ES-MS interface and voltage biasing arrangement [19].

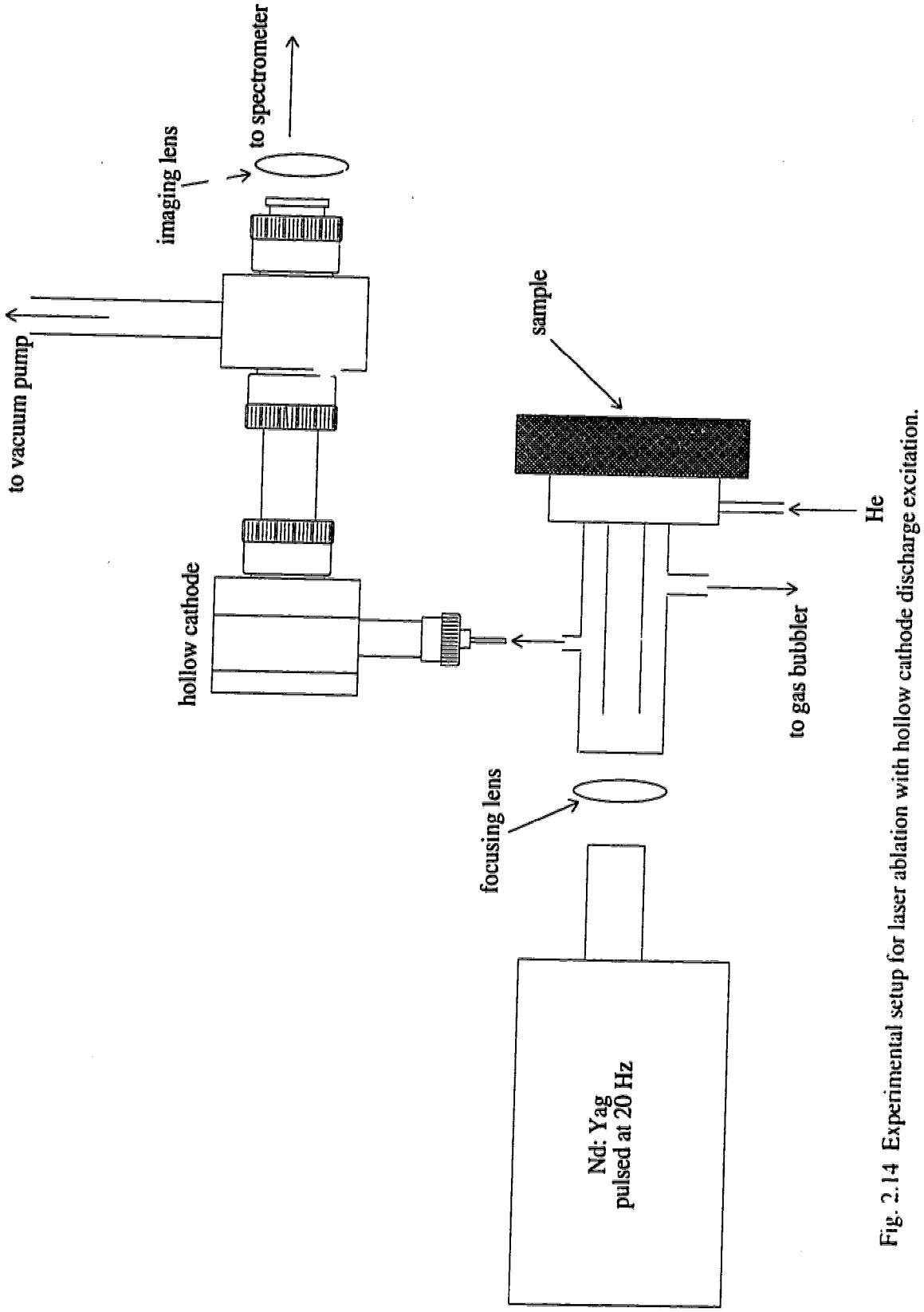

Fig. 2.14 Experimental setup for laser ablation with hollow cathode discharge excitation.

HCD to maximize the transport efficiency of ablated material to the HCD. The laser and ablation chamber are described in more detail in section 4.2.

A temporal emission profile of Cu with PMT detection is shown in Fig. 2.15. For this acquisition, the laser was fired at 20 Hz for 3 s and the signal was digitized at 50 ms/pt with an amplifier rise time of 300 ms. The sample was the National Bureau of Standards, Standard Reference Material (SRM) 1265a and contained 0.0058% Cu. To ensure that the observed emission was from Cu and not from a shift in the baseline level, a background subtracted PDA spectrum is presented in Fig. 2.16. This spectrum was collected under similar conditions as the temporal profile shown in Fig. 2.15 and clearly indicates the Cu resonance emission lines. Although this technique appears to be sensitive towards analyte detection, the emission response was not quantitative. The emission intensity observed for Cu from various samples was not correlated with the Cu concentrations found in the samples. Ion and atom emission lines were monitored from other elements with similar results.

A lack of quantitative response could be due to several factors but is likely due to the low plasma power of the HCD. To explore this further, a high bandwidth signal acquisition was collected for the temporal emission profile. High bandwidth acquisitions are explained in Chapter 3 and examples of high bandwidth acquisitions for laser ablation ICP-AES are presented in Chapters 4 and 5. Chapters 4 and 5 show emission from vapor plumes originating from individual particles produced from laser ablation. However, individual particle detection was not possible with the HCD and seems reasonable when the operating power of the HCD is compared to the power of the ICP. The HCD operated at approximately 125 W, while the ICP operated at 1250 W. The insufficient power of the HCD prevented individual particles from being detected. This contributed to the poor quantitative response for laser ablation coupled with the HCD.

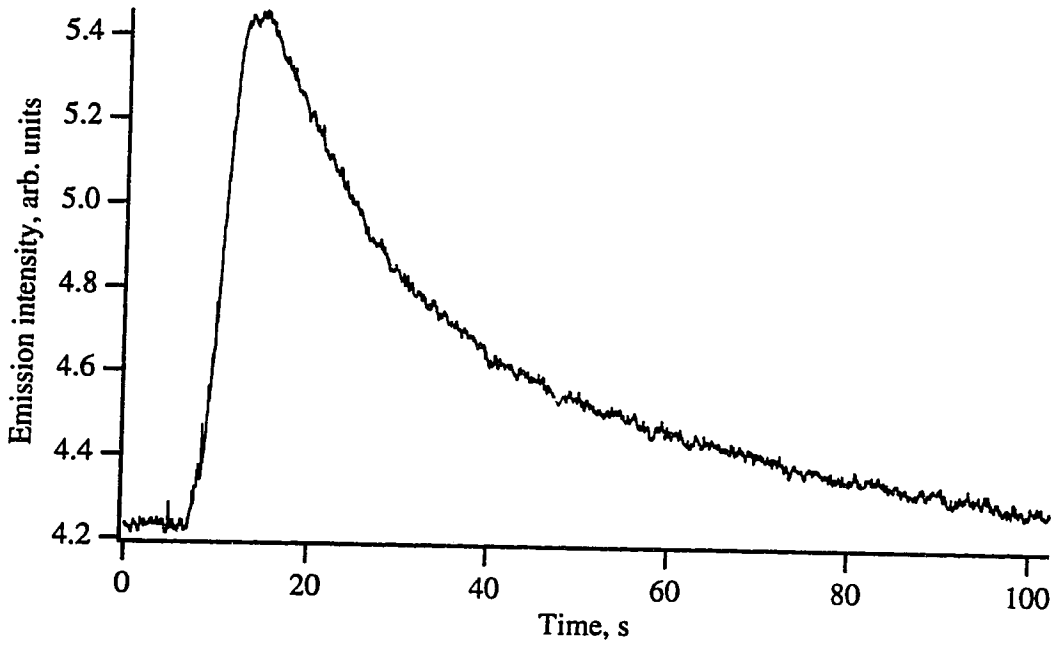

Fig. 2.15 Temporal emission profile of Cu. Sample was SRM 1265a, 0.0058% Cu in steel.

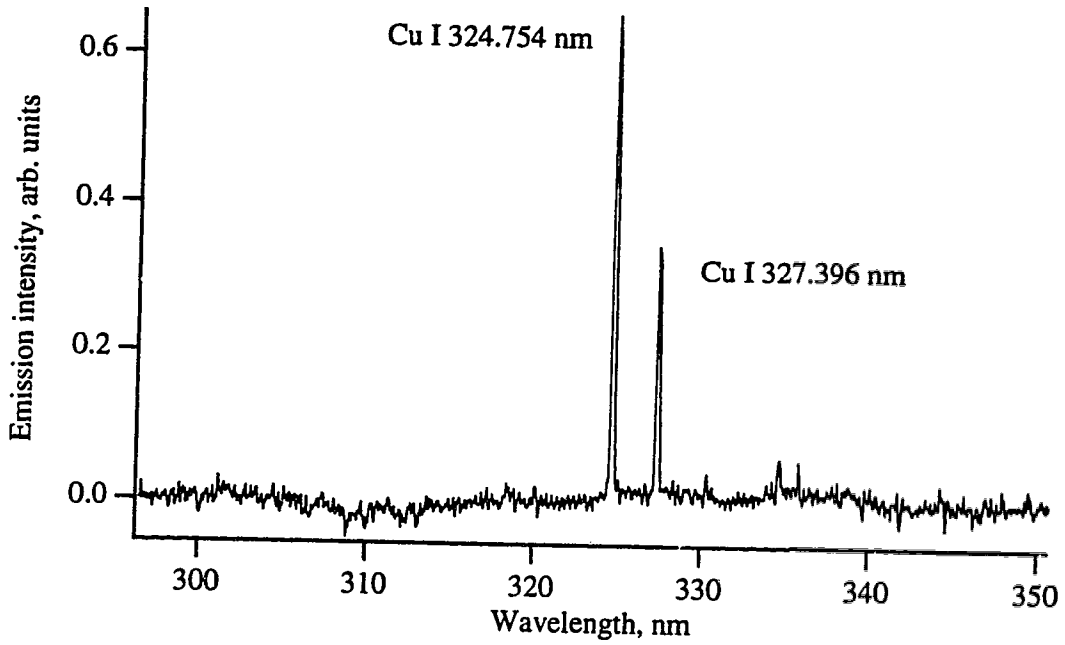

Fig. 2.16 Background subtracted PDA spectrum showing atomic Cu emission. Sample was SRM 1265a, 0.0058% Cu in steel.

2.9 Halogen emission

HCDs have been used for the detection of the halogens when the discharge is used as a detector for gas chromatographic effluents [23-25]. Fundamental properties of nonmetal determinations have been reviewed [26] and ionic emission from Cl is shown in Fig. 2.17. Vapor from a flask containing CCl_4 was drawn into the HCD along with the He plasma gas. The strong ionic emission from Cl illustrates the high excitation energies associated with the He HCD. Emission from O, S, and N was also observed. Gas analysis with the HCD was not explored in detail.

2.10 Conclusions and future prospects

This chapter described how a HCD could be used for the analysis of solution samples and examples of solid and gas sample analysis were also presented. The HCD was optimized for stable discharge operation at very high current densities. The energetic gas discharge was capable of atomizing and exciting a wide variety of nebulized solution samples in a simple and economic system. In spite of the presence of water vapor in the discharge for solution analysis, quantitative analytical results were obtained. It has been shown that any analyte can easily be introduced into the HCD by means of solution nebulization. In certain ways this system has analytical capability not unlike classic flame emission spectrometry with N_2O-C_2H_2 flames but in an all electronic package.

To improve the atomization and excitation conditions in the HCD for solution sample analysis, more efficient water vapor removal from the sample aerosol needs to be incorporated into the experimental design. New discharge designs must also include means of independently controlling carrier gas flow rates and discharge gas pressures. Analyte emission intensities have been optimized at high carrier gas flow rates. But, high

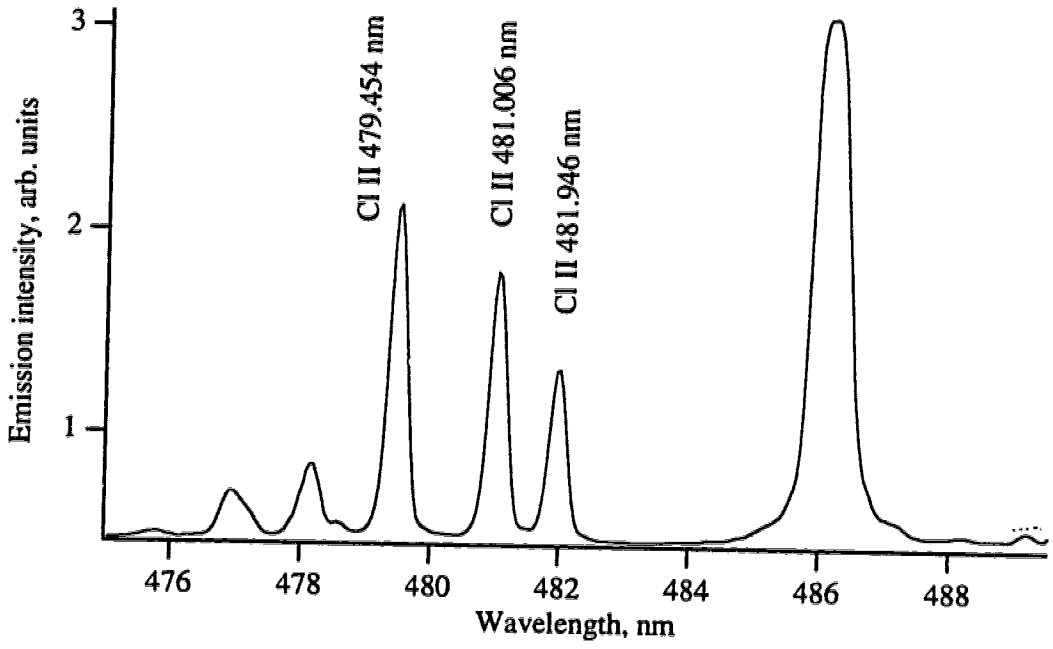

Fig. 2.17 Ionic Cl emission observed in a [illegible]

flow rates require relatively high pressures. Since emission intensities are likely optimized at lower pressures than used in this study, independent control of pressure is required. New experimental setups and HCD designs need to be considered in order to extend the use and acceptance of the HCD as an emission source.

A hollow cathode laser was designed to oscillate on Zn II 491.2/492.4 nm and Zn II 758.8 nm lines. This laser was strongly influenced by past designs of hollow cathode lasers systems [27-28]. This laser was designed so that sample could be introduced in a continuous manner into the optical cavity of the laser. In this way, the sample itself would form the gain medium of the laser and would offer unique and exciting possibilities for analytical analysis. Although stable plasma operation was achieved, stimulated laser emission was not observed. Further work was required to optimize all system variables.

References

1. J. A. Piper and C. E. Webb, *J. Phys. D: Appl. Phys.* **6**, 400 (1973).
2. K. C. Lepla and G. Horlick, *Appl. Spectrosc.* **43**, 1187 (1989).
3. G. B. King and G. Horlick, *Spectrochim. Acta* **47B**, E353 (1992).
4. M. E. Pillow, *Spectrochim. Acta* **36B**, 821 (1981).
5. P. J. Slevin and W. W. Harrison, *Appl. Spectrosc. Rev.* **10**(2), 201 (1975).
6. C. M. Strange and R. K. Marcus, *Spectrochim. Acta* **46B**, 517 (1991).
7. W. W. Harrison, *J. Anal. At. Spectrom.* **7**, 75 (1992).
8. T. D. Hettipathirana and M. W. Blades, *Spectrochim. Acta* **47B**, 493 (1992).
9. H. Falk, E. Hoffmann, Ch. Ludke, J. M. Ottaway and S. K. Giri, *Analyst* **108**, 1459 (1983).
10. H. Falk and Ch. Ludke, *Spectrochim. Acta* **39B**, 283 (1984).
11. E. Poussel, J. M. Mermet, and O Samuel, *Spectrochim. Acta* **48B**, 743 (1993).
12. G. Horlick, *Anal. Chem.* **44**, 943 (1972).
13. V. A. Fassel and R. N. Kniseley, *Anal. Chem.* **46**, 1110A (1974).
14. E. D. Salin and G. Horlick, *Anal. Chem.* **52** , 1578 (1980).
15. J. B. Fenn, M. Mann, C. K. Meng, S. F. Wong and C. M. Whitehouse, *Mass Spectrum. Rev.* **9**, 37 (1990).
16. R. D. Smith, J. A. Loo, C. G. Edmonds, C. J. Barinaga and H. R. Udseth, *Anal. Chem.* **62**, 882 (1990).
17. E. C. Huang, T. Wachs, J. J. Conboy and J. D. Henion, *Anal. Chem.* **62**, 713A (1990).
18. M. Hamdan and O. Curcuruto, *Int. J. Mass Spectrom. Ion Processes* **108**, 93 (1991).
19. G. R. Agnes and G. Horlick, *Appl. Spectrorsc.* **46**, 401 (1992).
20. L. Moenke-Blankenburg, *Spectrochim. Acta Rev.* **15**, 1 (1993).
21. R. E. Russo, *Appl. Spectrosc.* **49**, 14A (1995).

22. Y. Iida, *Spectrochim. Acta* **45B**, 427 (1990).

23. K. C. Ng, A. H. Ali and J. D. Winefordner, *Spectrochim. Acta* **46B**, 309 (1991).

24. L. Puig and R. Sacks, *Appl. Spectrosc.* **43**, 801 (1989).

25. M. Klemp, L. Puig, K. Trivedi and R. Sacks, *J. Chromatogr. Sci* **30**, 136 (1992).

26. D. A. McGregor, K. B. Cull, J. M. Gehlhausen, A. S. Viscomi, M. Wu, L. Zhang and J. W. Carnahan, *Anal. Chem.* **60**, 1089A (1988).

27. J. A. Piper and C. E. Webb, *J. Phys. D: Appl. Phys.* **6**, 400 (1973).

28. H. Tsuda and J. A. Piper, *J. Phys. E: Sci. Instrum.* **22**, 462 (1989).

Chapter 3

Introduction to time resolved particle analysis of laser ablated plumes by ICP-AES

3.1 The importance of particle analysis

Beyond the study of laser ablation (LA), particle characterization is important in its own right since particles impact environmental and commercial concerns. Particles play an important role in a variety of chemical and physical processes which include air pollution, acid deposition, combustion, materials synthesis and processing, and clean-room technology. Particles facilitate the transport of material in water and in air and influence the global climate. They are found in the air, oceans, lakes, drinking water, soil, ocean bottoms, and even in the outer most reaches of our galaxy. Particles originate from either natural or man-made (anthropogenic) sources. Natural sources of particles include volcanoes, forest fires, the weathering of rocks, and the salt spray from oceans. For example, a significant portion of wind-blown dust comes from the steppes of China and sub-Saharan Africa. Anthropogenic sources of particles include biomass burning, power plant emissions, industrial processes, and transportation systems. Individual particle analysis impacts environmental science since it provides detailed information concerning the particles' origin, formation, transport, and reactivity. Traditional methods of particle analysis include X-ray fluorescence and particle induced X-ray emission spectrometry, among others [1-3]. These methods are time consuming since the analysis of a large number of particles is required for statistical relevance. It is interesting to note that in a recent review of the analysis of individual particles [1], ICP-AES and ICP-MS

were not even mentioned as applicable techniques. The high throughput and sensitivity of particle characterization by ICP-AES and ICP-MS needs to be addressed.

3.2 Single particle analysis by ICP-AES

The capability of analyzing individual particles by ICP-AES offers considerable practical advantages compared with traditional analysis by this method. This section will show how the detection limits of ICP-AES with particle introduction methods, such as laser ablation and slurry nebulization, can be greatly improved by appropriate signal acquisition. Single particle analysis provides information on the chemical composition and mass of individual particles in a mixture. This can give a rapid and detailed characterization in the analysis of paints, oils, powders, dusts, metallurgical materials, and environmental samples. Also, an inventory of particle types and masses can be acquired from a mixture of particles.

Single particle detection by ICP-AES contrasts solution sample introduction and detection. The follow sequence of events occurs when a solution sample is nebulized into an ICP. The pneumatic nebulizer produces a polydisperse aerosol and more than 10^8 droplets/s enter the plasma. The droplets are desolvated as they enter the ICP, leaving dried salt particles of the analyte. Considering a 50 ppm Sr solution, a droplet of 65 pl will yield a particle which contains 3 pg of Sr when completely desolvated [4]. The desolvated particle will then be vaporized and atomized/ionized, followed by electronic excitation in the high energy plasma. The size of the largest droplets that can be completely vaporized in the plasma is not accurately known, but is estimated to be between 10-20 μm. A nearly steady-state signal is produced since the injected droplets are so small and numerous. The signal is similar to that produced by introduction of analyte in the gas phase. For this type of analysis, amplifiers act as low-pass filters and

integration of the signal over 1-10 s is appropriate. As discussed in section 3.4, a high bandwidth acquisition is required to capture the transient emission signal from an individual particle. Figs. 3.1 and 3.2 are shown to emphasize the difference between analyte introduction by solution nebulization compared to analyte introduction as discrete particles.

The signal from the nebulization of a solution sample over a 10 s period is illustrated schematically in Fig 3.1. In this case, the analyte level is only a few times greater than the detection limit and the signal is seen to be barely observable above the background noise. Thompson *et al.* [5] have estimated an absolute (mass) detection limit of 17 pg, from the signal trace shown in Fig. 3.1, by assuming typical ICP-AES conditions i.e., solution flow rate = 1 ml/min, nebulization transport efficiency = 1%, integration time = 10 s, and a concentration detection limit of 10 ng/ml. To contrast to solution nebulization, a particle containing the same mass of analyte as shown in Fig. 3.1 would give rise to a signal as shown in Fig. 3.2. This assumes that the plasma is viewed side-on and the particle passes through the spectroscopic viewing window in about 1 ms. For the signal in Fig. 3.2, integration over a 10 s period as used for the solution nebulized sample would be inappropriate, since the signal duration is only 1 ms. Correct treatment of the data in Fig. 3.2 would lower the detection limit by a factor of 100, bringing the absolute detection limit to 0.17 pg for this hypothetical case. These calculations assume that the plasma conditions remain the same when comparing solution nebulization versus single particle introduction.

For a multi-element particle which is completely vaporized in the plasma, the mass detection limit for any given element is independent of the particle's mass. However, as the mass of the particle increases, the concentration detection limit will decrease if the emission signal is acquired as shown in Fig. 3.2. Concentration

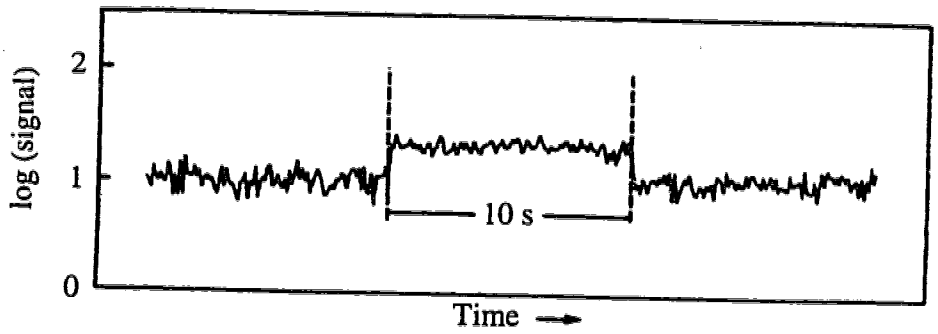

Fig. 3.1 Simulated low level signal of ICP-AES with conventional nebulization [5].

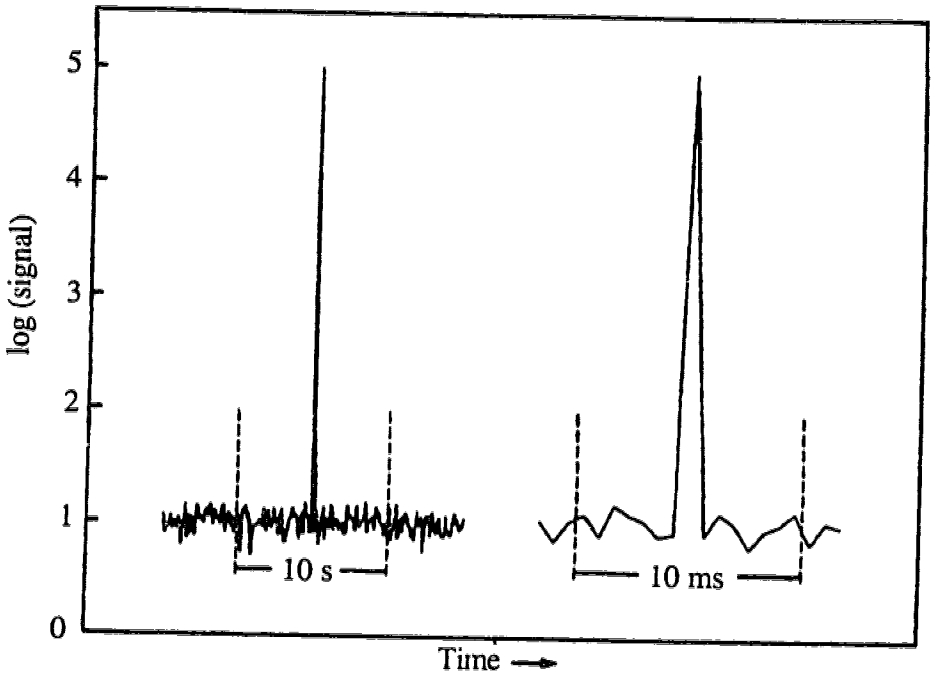

Fig. 3.2 Simulated signal from the same mass of analyte as in Fig. 3.6, but introduced as a single particle [5].

detection limits for μm sized particles are shown in Table 3.1. These values assume a particle density of 8 g/cm^3 and a mass detection limit of 0.17 pg. For a relatively large particle of 5.0 μm, a detection limit of 0.03% w/w is obtained and shows that even minor constituents of single particles can be determined. Multi-element analysis of individual particles is possible by ICP-AES and will be discussed in section 4.11. For LA-ICP-AES, it is necessary to ensure that the elemental concentrations found in individual particles represent the concentrations found in the original solid sample.

Observation of individual particle emission from LA plumes has been made by Chan and Russo [6]. A KrF eximer laser was used with a pulse width of 20 ns FWHM and a pulse energy ranging from 200 to 550 mJ. A PMT based monochromator was used to observe the temporal behavior of the emission signal and an ADC, with a 80 ns sample and hold time, was used to digitize the analog signal. With the laser firing at 1 Hz at a Cu sample, an emission profile was generated at the same frequency. Random spikes in the signal were also observed in addition to the 1 Hz emission profile. When the laser frequency was increased to 5 Hz, a steady state signal was observed which also contained randomly spaced spikes. These spikes were the result of the size distribution of particles entrained and transported to the ICP. Most of the large particles larger than about 2 μm were not transported to the ICP because of low transport efficiency. However, a small percentage of large particles found their way to the ICP and it is these relatively large particles which gave rise to the random spikes in the emission profile. Data acquisition rates were severely limited in this study and ranged between 5 and 500 Hz. With the laser firing at 10 Hz, many more spikes were observed in the emission profile as the data acquisition rate increased from 20-500 Hz. This resulted from severe under-sampling of the emission profile. Since the occurrence of large particles entering the plasma was random, as the acquisition rate increased, more spikes were observed. Although the ADC had an acquisition rate of up to 27 kHz, rates much lower than this were used to limit the

Table 3.1 Calculation of mass and detection limits from micrometer sized particles, assuming a particle density of 8 g/cm^3 and an absolute detection limit of 0.17 pg [5].

Diameter, μm	Mass, pg	Detection limit, % w/w
0.5	0.52	33
1.0	4.2	4
2.0	34	0.5
5.0	520	0.03
10.0	4200	0.004

size of the data files. Increased memory or storage size on the computer would have allowed for faster ADC rates and it was speculated that, at high enough ADC rates, it might be possible to correlate emission intensity of the spikes to the particle diameters.

Olesik and Hobbs [4] used a monodisperse dried microparticulate injector (MDMI) to study spatially and temporally resolved emission intensities for Sr atoms and ions. The MDMI produced monodispersed droplets from a 50 μg/ml solution of Sr. The droplets were injected into a flowing stream of Ar where they were desolvated to the desired extent in a furnace. At the exit of the furnace, the droplets or desolvated particles were carried to the centre of a conventional ICP torch. Unlike a conventional pneumatic nebulizer, an MDMI introduces sample into the ICP with 100% efficiency since there is no drain or waste i.e., all of the analyte exiting the MDMI enters the plasma. Vertical emission profiles were acquired sequentially by vertical translation of the ICP torch box and aligning the entrance slit to the monochromator horizontally with respect to the plasma. Emission from pg quantities of analyte originally contained in a 60 μm droplet were easily detectable although a detection limit was not calculated. This study focused on plasma fundamentals, such as the relationship between vertical emission profiles and particle vaporization for both Sr atom and ion emission signals. It is expected that the MDMI will be used extensively to generate reproducible particle sizes for fundamental studies of the ICP.

A series of papers by Kawaguchi *et al.* have illustrated some practical analyses of individual particles [7-9]. An investigation of airborne particles by ICP-AES was performed by using monodisperse aerosols for calibration and PMT detection [7]. The study of airborne particles is important in the area of environmental sciences and in the development of air pollution control technologies. The emission signal from solid particles was observed as single pulses when the particle concentration was sufficiently

low i.e., when pulses from successive particles did not overlap, and the emission pulses were sufficiently intense to be observed above the shot noise. Solid particles were introduced by the use of a monodisperse droplet generator for Ca and by a small arc at the switch of a lamp socket for the analysis of Cu. The smallest particles that could be measured were 0.1 μm and 0.3 μm for calcium oxide and Cu respectively. This research showed the potential of using ICP-AES for real time monitoring of various air control systems.

Another paper by Kawaguchi *et al.* [8] showed how the Ca content of individual biological cells could be determined. The determination of trace elements in cells is important for an understanding of processes including metabolism, cell growth, gene expression, and cancer growth. A cell suspension was sprayed by a pneumatic nebulizer and the droplets were made to contain, at most, a single cell. The cells were desolvated in a drying chamber before being introduced into the ICP. Emission pulses from elements contained in individual cells were generated in the plasma and detected with a PMT. The distribution of Ca content in individual cells for several mammalian cell samples was determined. For example, the mean Ca content in cultured mouse fibroblast cells was determined to be 0.057 pg. Since the size of the cells ranged from 10-15 μm, the Ca concentration of the cells was calculated to be in the range of 0.82-2.8 mM. The detection limit for Ca contained in cells was calculated to be 0.01 pg. This paper showed that it is possible to measure the distribution of the Ca content in a large number of cells as well as show distributions of different groups of cells in a cell mixture. The extensive application of ICP-AES determination of trace elements in cells may be limited by insufficient sensitivity. The application of ICP-MS may overcome the sensitivity problem due to the very low detection limits achieved with this technique.

To address the sensitivity problems, Kawaguchi *et al.* [9] showed how ICP-MS could be used for the analysis of individual airborne particles. A monodisperse aerosol generator was used to introduce particles containing 6.4-130 fg of Zn into the plasma. A linear calibration curve was established and a detection limit of 3 fg of Zn was determined. Signal intensities and fluctuations were affected by the carrier gas flow rate, applied rf power, and sampling depth.

Thompson *et al.* have also published a series of papers dealing with single particle analysis by ICP-AES with PMT detection [5, 10-11]. The analysis of laser ablated plumes, on a particle-to-particle basis, was demonstrated for particles in the mass range of 10-100 pg [10]. Data were collected on a two channel digital storage oscilloscope which had a fast enough acquisition rate to show individual emission pulses originating from particles in the laser ablated plume. For a single laser shot on a stainless steel sample, a considerable degree of overlapping of emission pulses was observed in the more densely crowded regions of the temporal profile. Simultaneous emission from Fe and Ni was observed from a single particle by using both channels on the oscilloscope. This illustrated the capability of ICP-AES for multi-element analysis within individual particles. The peak-height ratios of Ni/Fe were constant over a large number of peaks, implying that the composition of particles produced by laser ablation represented the bulk composition of the sample for these two elements. It was suggested that recording the area of a large number of emission pulses and rejecting all the background signal between the pulses would result in a superior measurement technique for LA-ICP-AES. This strategy would provide the highest signal to background ratios since the measurement would be made only during an emission event. It was also suggested that the spatially and temporally resolved emission output from single particles could provide insightful data regarding plasma mechanisms, such as atomization, ionization, and excitation

The advantages of time resolved analysis were highlighted in another paper by Thompson *et al.* [5] and these inherent advantages are documented at the beginning of section 3.2. The capabilities of multi-element characterization of individual particles were explored by collecting data on a four channel oscilloscope. For the laser ablation of a stainless steel sample, simultaneous acquisition was collected for Fe, Cr, Mn, and Ni on a direct-reading spectrometer. For a single particle containing Cr, which was less abundant than the other metals, the emission signal consisted of a burst of discrete spikes. The authors claimed that these spikes were the result of single photon emission and suggested using photon counting as a technique to provide the lowest detection limits for single particle characterization. The four channel acquisition showed particles of different chemical composition i.e., one particle contained all four elements while another particle contained only Fe and Mn. Proper signal calibration was not achieved but it was anticipated that the nebulization of fully characterized particles as slurries would solve this problem. Slurry nebulization was attempted for particles of olivine [$(Mg, Fe)_2SiO_4$] and a multi-element temporal profile was presented for Fe, Si, and Mg. This illustrated the potential for particle characterization from suspended particles in solution.

A more detailed study of time resolved particle analysis by the nebulization of dilute suspensions was also performed by Thompson *et al.* [11]. In this study, Si, Al, Fe, Zr, and Ca were detected from particles of refractory oxides and silicates. Recognition of a particular type of particle from a complex mixture of particles was demonstrated. A mixture of three minerals, zircon ($ZrSiO_4$), olivine [$(Mg, Fe)_2SiO_4$], and albite ($NaAlSi_3O_8$) was prepared by grinding the minerals to a fine powder and preparing a suspension of 0.3 g/l. These minerals each contained an element which was absent from the other two and, therefore, it was shown how these particles could be differentiated from each other by observing their emission profiles. Similarly, two pyroxenes, orthopyroxene (Mg, Fe)$2Si_2O_8$ and clinopyroxene [$(Ca, Mg, Fe)_2Si_2O_8$], were also

differentiated based on their element characteristic emission profiles. Evidence was presented which suggested that larger particles (~7 μm) of olivine were not completely atomized.

An early attempt at on-line inorganic aerosol analysis by ICP-AES [12] showed that individual particles of manganese carbonate could be temporally resolved. Even though the emission pulses were undersampled at a rate of 1 kHz and the bandwidth of the amplifier was inadequate, a detection limit of 0.11 pg of Mn was obtained.

In the past, signal acquisition parameters and sample pre-treatment steps have overlooked and destroyed the information content found in individual particles. For example, acid digestion of atmospheric particles followed by conventional solution nebulization was performed by Broekaert *et al.* [13]. The particles were collected with a cascade impactor for 12 h before a sufficient mass (0.1-1 mg) of analyte was deposited. Acid digestion of the collected material homogenized the sample and removed all information contained in individual particles. In a study by Guevremont *et al.* [14], a commercially available powder sample delivery system was used to deliver powdered geological materials to an ICP. However, instead of PMT detection, a photodiode array spectrometer was used to capture the emission signal. Since photodiode arrays are not capable of sensitive time resolved measurements, all signal information contained in individual particles was lost. Individual particle analysis by ICP-AES has not become a routine technique since it requires high speed electronics to capture the transient emission events. Commercially available ICP spectrometers are designed for acquiring data from solution nebulized samples and, therefore, are not optimized for the detection of transient signals.

The significance of environmental particles has recently been emphasized by an International Union of Pure and Applied Chemistry (IUPAC) Series [15] dedicated to this topic. Also, a recent atomic spectrometry update for environmental analysis showed a significant number of papers dealing with particle analysis. However, few of these papers have analyzed environmentally significant particles on an individual particle basis. Significant advances in environmental chemistry will be achieved when more researchers perform multi-element characterization on single particles.

3.3 Laser ablation as a method of sample introduction

The ablation of a solid surface by a laser pulse produces a combination of atoms, ions, and particles which range in size from a few nm to several μm in diameter. When this laser ablated sample plume is swept into an emission source, such as the ICP, the temporal emission profile consists of discrete emission events produced from the individual particles. Observation of these emission pulses in a time resolved manner requires a detection scheme which is optimized to capture the temporal emission events.

Laser ablation of solid materials, while using an ICP as a secondary excitation source, offers the advantage of avoiding the time consuming sample digestion and preparation procedures often associated with sample introduction techniques. Direct solid sampling of any material without sample preparation is possible and results in unique characteristics for LA-ICP-AES. Elimination of sample preparation is important for the analysis of refractory carbides and oxides which are difficult to digest. Also, hazardous materials can be analyzed in a simplified manner. Another unique feature of laser ablation is spatial analysis since the sampling area is very small. Compared to solution nebulization, laser ablation results in much more efficient use of the sample

since a high percentage of the ablated material reaches the excitation source. These advantages have resulted in the commercial availability of LA-ICP-AES.

The ability of lasers to sample solid materials is a result of the very high radiation densities attained when a lens is used to focus pulsed laser radiation. Radiation incident upon a surface is often denoted as irradiance (I) and is defined as the power flux across the surface.

$$I = \frac{P_{peak}}{\pi r^2} \qquad 3.1$$

$$P_{peak} = \frac{E}{t} \qquad 3.2$$

Where r = radius of focal spot; P_{peak} = power of laser pulse, (W); E = energy of laser pulse, (J); and t = laser pulse duration, (s) [16]. Sample evaporation is a key parameter necessary for laser ablation and a minimum absorbed irradiance (I_{min}) necessary for vaporization is defined in the following equation.

$$I_{min} = dL_v\sqrt{\frac{a}{t}} \qquad 3.3$$

Where d = density of the target; L_v = latent heat of vaporization of the target; and a = thermal conductivity [17].

A schematic representation of the events occurring during laser ablation is shown in Fig. 3.3. As can be seen, coupling of the optical energy of the laser into the solid sample results in ejection of atoms, ions, and particles. Laser-sample interaction and ablation mechanisms are not fully understood and many models have been proposed [18]

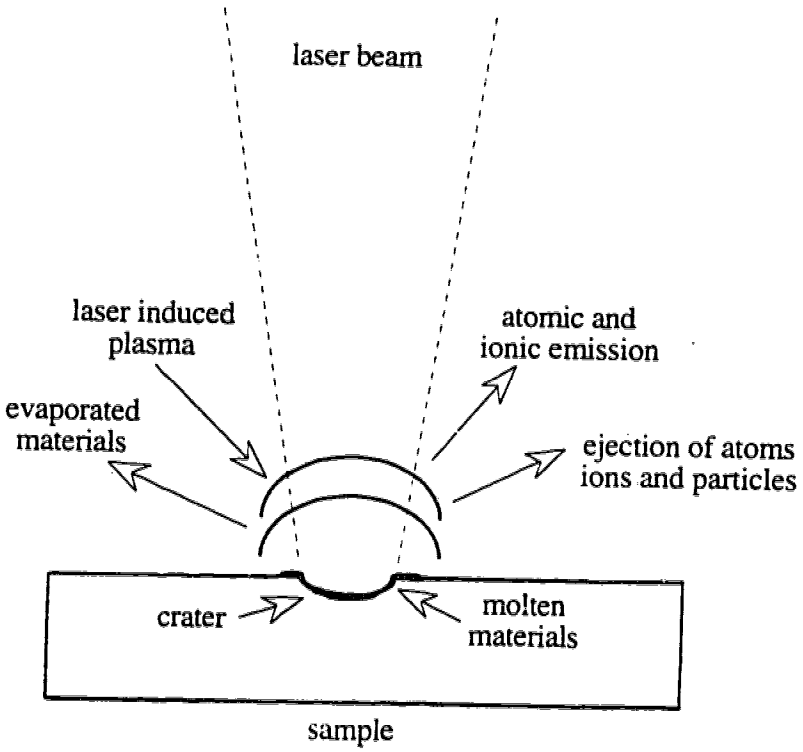

Fig. 3.3 Processes of laser ablation.

to explain this complex phenomena. However, two general mechanisms have been proposed by Ready [19] based on laser irradiance, pulse duration, and properties of the sample material such as latent heat of vaporization, heat conductivity, and reflectivity at the laser wavelength.

Vaporization of sample material is likely the dominant mechanism of sample removal when the laser irradiance is less than approximately 10^6 W/cm^2 and the pulse duration is on the order of μs. The sample is vaporized at the centre of the laser spot and the amount of material removed during the laser pulse is influenced by the thermal and optical properties of the sample. Absorption and reflection of the laser radiation determine the fraction of irradiance absorbed and the depth of optical absorption within the sample. The rapid expansion due to vaporization causes sample material to be ejected as a plume of vapor and liquid particles. In this operating mode, the quantity of mass removed is difficult to predict since the optical and thermal properties of the sample vary during the laser pulse. Preferential vaporization of volatile elements may occur since the interaction between the laser radiation and the sample is predominantly thermal. This results in an enrichment of volatile elements and a depletion of refractory elements in the ablated material as compared to the bulk sample [20-21].

Q-switched lasers are capable of high laser irradiance (beyond 10^9 W/cm^2) and have pulse durations on the order of ns. When subjected to these conditions, material is ejected from the sample via a mechanism other than thermal vaporization. Within a fraction of the laser pulse duration, the surface temperature is heated past its vaporization temperature and there is a rapid increase in pressure over the irradiated surface. The pressure, from the recoil of the vaporized material, can be as high as 10^6 atmospheres [22] and it is this pressure which prohibits the sample from further vaporizing until the underlying layers reach a critical temperature. At this critical point, an over-heated melt

is released explosively from the solid surface. This explosion produces shock waves which cause further fragmentation of the sample. Preferential vaporization should be negligible when considering the explosive interaction of a high powered Q-switched laser with a solid sample. This process can generate ejected material with the same chemical composition as found in the bulk sample. However, preferential vaporization may occur as a result of a plasma-material interaction since a short lived plasma is created at the sample surface. Plasma temperatures can be in excess of 10^4 K and have durations of μs. In general, matrix effects are minimized by using high power lasers.

Many different types of lasers, operating at a variety of wavelengths, have been used for laser ablation studies. Perhaps the most common laser used is the Nd-YAG laser, operating at its fundamental wavelength of 1064 nm. This has been the laser of choice because it is relatively inexpensive, easy to use, and provides high sensitivities in the sub-μg/g range for solid samples [23-24]. However, the wavelength of the laser can be important in affecting the laser-material interaction process. Mermet *et al.* [25] have demonstrated the large differences between UV and IR lasers for laser solid sampling. They quantified the ablated mass produced from lasers operating at 193, 308, 355, 532, and 1064 nm and found that the ablated mass was 20 times greater for a UV wavelength than for an IR wavelength. In the case of the UV laser, direct LA taking place in the first few ns is the major mechanism responsible for the removal of sample material. This is in contrast with an IR laser where plasma shielding of the laser radiation increases the temperature of the plasma, leading to increased selective removal of material by the plasma. Improved sampling efficiency, provided by UV lasers, results in increased sensitivity for LA-ICP-AES. This can be achieved using a frequency-tripled Nd-YAG laser or an eximer laser.

The generation of particles and the particle size distribution are important aspects of the laser ablation process. Thompson *et al.* [26] have investigated the particulate matter that was produced using a ruby laser with a maximum output energy of 1 J, with variable degrees of Q-switching. Particle sizes and morphology were determined by scanning electron microscopy by collecting the ablated material onto filter paper. For the ablation of metal surfaces, the ablated material consisted of spheres, ranging in size from 10 μm to less than 1 μm, and amorphous material. This type of particle size distribution was consistent across a wide range of metals with diverse physical characteristics. Samples investigated were aluminum, tin, steel, and tantalum. These metals showed consistent results despite changes in the Q-switching. The particles where virtually perfect spheres and the amorphous material had the appearance of condensate from the gaseous state. The spherical particles could be the result of condensation from the gas phase via a liquid to a solid phase, or could have simply cooled from a liquid melt. However, particles in this size range were not consistent with condensation from the gas phase [27]. Therefore, the bulk of the ablated material was represented by spherical particles which were merely melted and then removed explosively from the laser ablation crater. A significant amount of the ablated material was found in the form of welded groups of 10-20 spheres. It is unlikely that these large aggregates are transported more than a few cm through the connective tubing.

Particle entrainment and transport from the ablation chamber to the ICP torch is dependent on the particle size distribution of the ablated material [28]. For LA-ICP-AES, the overall efficiency can be defined as the fraction of ablated material that is atomized/ionized and excited in the ICP. This efficiency is determined by the particle size distribution and is the convolution of the particle size distribution in the primary source, the transfer function of the cell and connective tubing, and the response function of the ICP. In an ideal situation, the ablation cell and transfer tube should transport

particles over a broader size distribution than that produced by the ablation event. In other words, to attain maximum transport efficiency, the transfer function should be broader than the source distribution. The response function of the ICP falls off for particles larger than about 10 μm since large particles are incompletely vaporized in the ICP [29]. The exact nature of particle vaporization in an ICP is dependent on the physical properties of the particles and the temperature and residence time in the plasma. Therefore, the ablation cell and connective tubing need only transport particles up to some size limit which corresponds to the maximum size of particle vaporized and excited in the ICP.

Arrowsmith and Hughes [28] studied the entrainment and transport of ablated plumes for subsequent elemental analysis experimentally and by model calculations for Mo metal. They used a Q-switched Nd-YAG laser operating at its fundamental wavelength with a pulse duration of 8 ns and a maximum output energy of 180 mJ. Particle size distributions were determined by light scattering covering the size range 0.2-12 μm. The ablated material was transported to a particle counter under the same conditions as those used for elemental analysis. The particle size distribution measured at the end of the transfer tube by ablation of Mo metal is shown in Fig. 3.4. The distribution peaks at 0.2-0.3 μm, which is the lowest channel on the particle counter, and then declines quickly to 0.5 μm. It is possible that a large number of particles with a diameter less than 0.2 μm are generated. This was confirmed by collecting particles from the laser plume and sizing the deposited material by SEM. A large number of particles were observed with a diameter of less than 0.5 μm. A small number of particles were detected at 5-12 μm but these large particles accounted for approximately 50% of the ablated mass. The calculated transport efficiency for Mo particles at various flow rates and tube diameters is shown in Fig. 3.5. Small particles. with diameters less than 0.001 μm, were transported poorly through the connective tubing because of diffusion losses to the inside

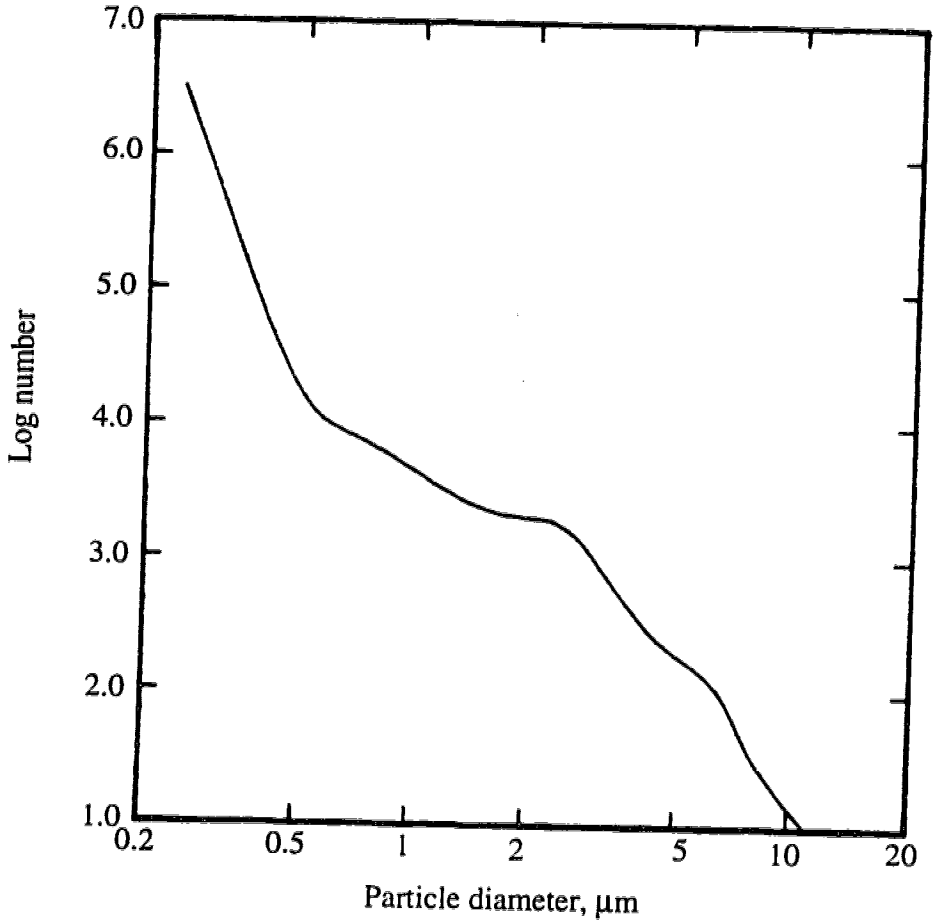

Fig. 3.4 Particle size distribution from the ablation of Mo metal. Ablated material was transported to the particle counter under the same conditions as transportation to the ICP torch [28].

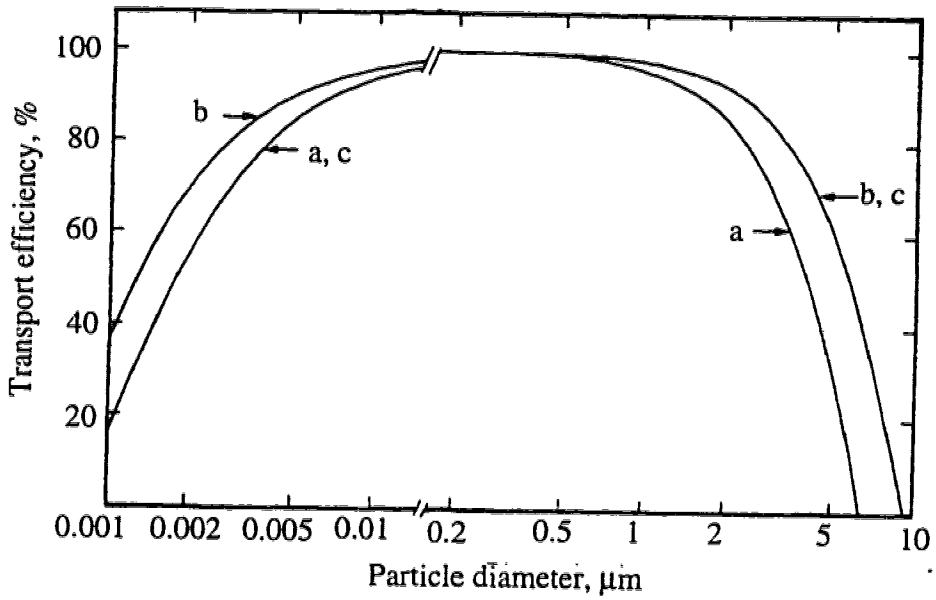

Fig. 3.5 Calculated transport efficiency for Mo particles for various flow rates, tube i.d.'s, and lengths (a, 1.5 l/min, 4.5 mm, 80 cm; b, 1.5 l/min, 4.5 mm, 40 cm; c, 1.5 l/min, 2.25 mm, 80 cm) [28].

of the tube walls. Large particles were not transported efficiently because of gravitational deposition. Gravitational deposition appeared to be the major loss mechanism since relatively large particles were formed during ablation or by coalescence within the transfer tube. Particles above 5 μm in the primary source were unlikely to be transported to the ICP.

Improvements in precision and increases in signal for LA-ICP-AES measurements have been observed when the transport tube length and diameter is reduced [30]. This is explained by a broadened tube transfer function giving greater overlap with the primary source particle distribution. If the transfer function completely overlaps the primary distribution, no further improvements in intensity and precision will be obtained. This makes a strong argument for the use of in situ LA-ICP-AES [31], a technique which eliminates the aerosol transport step associated with conventional LA sample introduction systems.

3.4 Introduction to time resolved measurements

Fig. 3.6 is a schematic representation showing how an analog signal from a PMT is amplified and digitized. The PMT generates a photocathodic current which is amplified by a current-to-voltage amplifier with appropriate bandwidth. The resulting signal is then digitized by an analog-to-digital converter (ADC). The ADC is typically located on a data acquisition board, located in a computer. This arrangement allows the digitized signal to be stored on the computer's hard drive and analyzed at the experimenters convenience. The digitization rate and bandwidth are separate entities of the measurement system and should not be confused with each other. For a dc amplifier, the bandwidth (Δf) is the range of frequencies which will be amplified up to the -3 dB point of the circuit. Simply stated, if the frequency components of the signal fall within

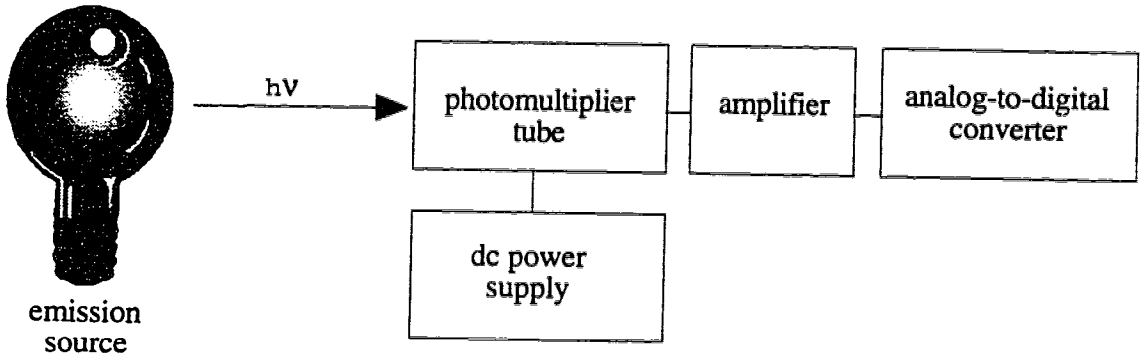

Fig. 3.6 Schematic representation of signal acquisition and digitization using a PMT as the detector.

the bandwidth of the amplifier, the signal will be amplified with minimal distortion. Therefore, to make accurate time resolved measurements of transient signals, a high bandwidth preamplifier is necessary. The amount of bandwidth required will be determined by the duration of the transient event. For example, narrow emission pulses will require more bandwidth than broad and slowly changing emission pulses. The ability of the amplifier to accurately respond to instantaneous signal changes is often measured in terms of the rise time (t_r). The rise time is the time required for the output of the amplifier to go from 10% to 90% of the applied change. The following equations show the relationship between the t_r, the RC time constant, and the bandwidth of a simple dc amplifier.

$$t_r \approx \frac{1}{3\Delta f} \qquad 3.4$$

$$RC = \frac{1}{2\pi\Delta f} \qquad 3.5$$

A very simple measurement circuit can be made with a series RC circuit where the output of the PMT is read across the capacitor. A variety of resistors and capacitors can be used to achieve the desired level of amplification, low pass filtering, and bandwidth.

Fig. 3.7 shows the amplifier frequency response as the rise time of a dc amplifier is changed from 0.01 - 10 ms. At -3 dB, the output voltage is equal to 0.707 of the input voltage ($dB = 20\log V_{out}/V_{in}$). Peak-shaped signals contain Fourier components from dc out to very high frequencies and, under ideal circumstances, the rise time should be chosen so that the bandwidth of the signal is within the bandwidth of the amplifier. In practice, peak-shaped signals may contain frequency components which lie outside the bandwidth of the amplifier. For example, the Fourier expansion of a square wave is a series that extends infinitely to the high harmonics, since an instantaneous transition from

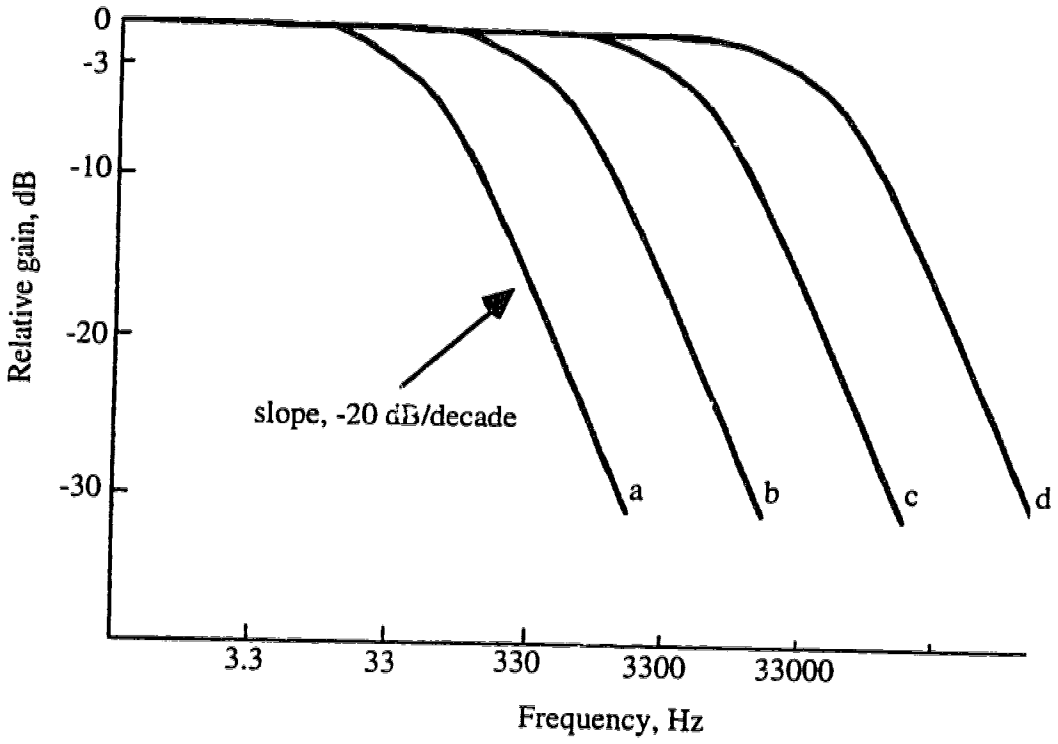

Fig. 3.7 Amplifier frequency response at various rise times (a, 10 ms; b, 1.0 ms; c, 0.1 ms; d, 0.01 ms).

one voltage level to another contains frequency components to infinity. Therefore, it is common practice to limit the bandwidth of the signal by placing a low-pass filter prior to the amplifier. This ensures that the signal bandwidth is within the amplifier bandwidth, however, the low pass filter may distort the signal to some degree.

The data acquisition rate (or digitization rate) of the ADC is another important parameter when measuring transient events. The quantitative basis for the data acquisition rate is provided by the Nyquist sampling theorem, which states that the acquisition rate must be twice the highest frequency component of the signal. If the sampling rate is too low, undersampled high frequencies will show up as spurious low frequencies. This error is known as aliasing. To avoid aliasing, the same low-pass filter, as described in the previous paragraph, can be used to limit the signal bandwidth and the data acquisition rate set to at least twice the filter bandpass. Fig. 3.7 shows that a rise time of 0.01 ms provides a large bandwidth of 33.3 kHz which can be used to acquire transient events containing high frequency components. To acquire data without aliasing, a data acquisition rate of at least 66.6 kHz would be required to take full advantage of the amplifier bandwidth with a t_r of 0.01 ms.

It is important to keep in mind that the output of a PMT, under low incident light levels, is composed of discrete current pulses. The number of these pulses is directly proportional to the number of photons incident on the photocathode. Therefore, photon counting [32-33] can be used to accurately quantify incident light levels. Photon counting represents the ultimate in terms of time resolved measurements with a PMT. Photoelectric current pulses are shown in Fig. 3.8 and have peak widths on the order of 5 ns. The application of photon counting in spectrophotometric measurements has been primarily limited to the area of Raman spectroscopy [34]. More recently [35], detection of individual photons has provided a way of monitoring individual chemical reactions in

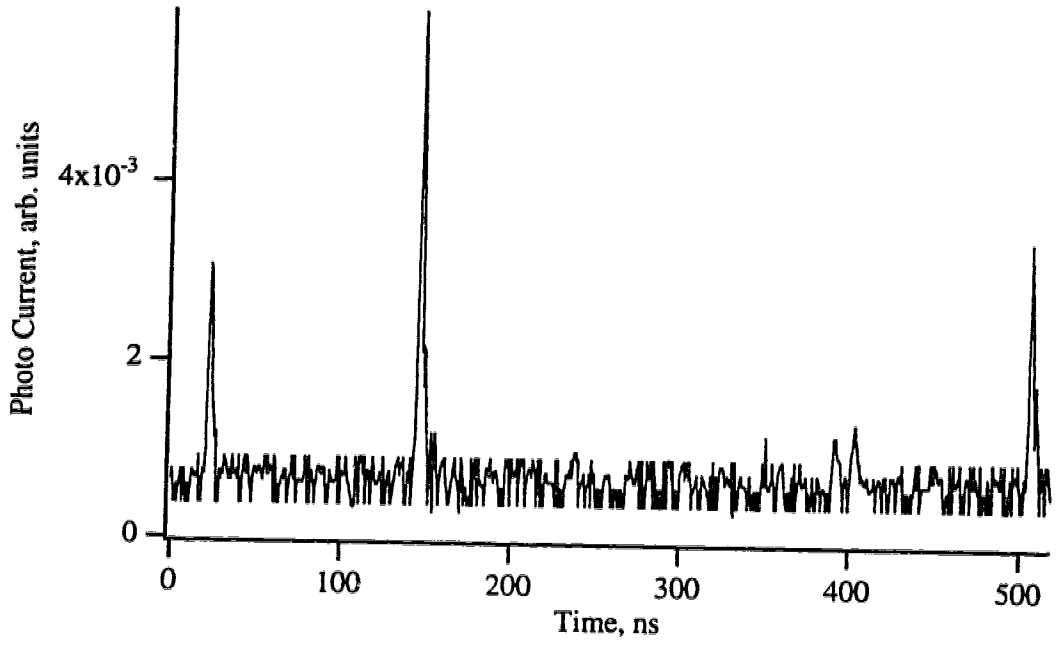

Fig. 3.8 Photoelectric current pulses observed from a PMT.

solution, since chemical reactions that form an excited state may relax to the ground state with photon emission. Time resolved measurements will provide analysts with a new way of observing emission events.

References

1. W. Jambers, L. De Bock and R. Van Grieken, *Analyst* **120**, 681 (1995).
2. M. V. Johnston and A. S. Wexler, *Anal. Chem.* **67**,721A (1995).
3. M. Grasserbauer, Mikrochim. Acta [Wien] **III**, 415 (1983).
4. J. W. Olesik and S. E. Hobbs, *Anal. Chem.* **66**, 3371 (1994).
5. M. Thompson, C. D. Flint, S. Chenery and K. Knight, *J. Anal. At. Spectrom.* **7**, 1099 (1992).
6. W. T. Chan and R. E. Russo, *Spectrochim. Acta* **46B**, 1471 (1991).
7. H. Kawaguchi, N. Fukasawa and A. Mizuike, *Spectrochim. Acta* **41B**, 1277 (1986).
8. T. Nomizu, S. Kaneco, T. Tanaka, D. Ito, H. Kawaguchi and B. Vallee, *Anal. Chem.* **66**, 3000 (1994).
9. S. Kaneco, T. Nomizu, T. Tanaka, N. Mizutani and H. Kawaguchi, *Analytical Sciences* **11**, 835 (1995).
10. M. Thompson, C. D. Flint and S. Chenery, *J. Anal. At. Spectrom.* **3**, 1133 (1988).
11. K. Knight, S. Chenery, S. W. Zochowski, M. Thompson and C. D. Flint, *J. Anal. At. Spectrom.* **11**, 53 (1996).
12. U. K. Bochert and W. Dannecker, *J. Aerosol Sci.* **20**(8), 1525 (1989).
13. J. A. C. Broekaert, B. Wopenka, H. Puxbaum, *Anal. Chem.* **54**, 2174 (1982).
14. R. Guevremont and K. N. De Silva, *Spectrochim. Acta* **47B**, 371 (1992).
15. *Environmental Particles, Vol. I and II, IUPAC Monography*, J, Buffle and H. P. van Leeuwen, Eds. (Chelsea, MI: Lewis Publishers, 1992).
16. X. R. Liu, The direct analysis of materials with inductively coupled plasma spectrometry. Thesis, University of Alberta (1994).
17. L. Moenke-Blankenburg, *Spectrochim. Acta Rev.* **15**, 1 (1993).
18. R. E. Russo, *Appl. Spectrosc.* **49**, 14A (1995).

19. J. F. Ready, *Effects of High-Power Laser Radiation*, Academic Press, New York (1971).

20. J. M. Baldwin, *Appl. Spectrosc.* **24**, 429 (1970).

21. W. T. Chan, X. L. Mao and R. E. Russo, *Appl. Spectrosc.* **46**, 1025 (1992).

22. T. J. Goldsack, K. D. Kilkenny, B. J. MacGowan, S. A. Veats, P. F. Cunningham, C. L. S. Lewis, M. H. Key, P. T. Rumsby and W. T. Toner, *Opt. Commun.* **42**, 55 (1982).

23. A. L. Gray, *Analyst* **110**, 551 (1985).

24. J. W. Arrowsmith, *Anal. Chem.* **59**, 1437 (1987).

25. C. Geertsen, A. Briand, F. Chartier, J. L. Lacour, P. Mauchien, S. Sjostrom and J. M. Mermet, *J. Anal. At. Spectom.* **9**, 17 (1994).

26. M. Thompson, S. Chenery and L. Brett, *J. Anal. At. Spectrom.* **5**, 49 (1990).

27. E. R. Buckle and K. J. A. Mawella, *J. Aerosol Sci.* **18**(2), 139 (1987).

28. P. Arrowsmith and K. Hughes, *Appl. Spectrosc.* **42**, 1231 (1988).

29. P. Proulx, J. Mostaghimi and M. I. Boulos, *Plasma Chem. Plasma Process.* **7**, 29 (1987).

30. T. Ishizuka and Y. Uwamino, *Spectrochim. Acta* **38B**, 519 (1983).

31. X. R. Liu and G. Horlick, *Spectrochim. Acta* **50B**, 537 (1994).

32. M. L. Franklin, G. Horlick and H. V. Malmstadt, *Anal. Chem.* **41**, 2 (1969).

33. H. V. Malmstadt, M. L. Franklin and G. Horlick, *Anal. Chem.* **44**, 63A (1972).

34. Spectrochemical Analysis (J. D. Ingle and S. R. Crouch), Prentice-Hall, Englewood Cliffs, New Jersey, 1988.

35. R. M. Wightman, M. M. Collinson and E. Ritchie, paper no. 182, presented at the 47th Pittsburgh Conference (Chicago, IL, March 1996).

Chapter 4

Time resolved particle analysis by LA-ICP-AES: lateral viewing

4.1 Purpose of this study

It is understood that the material produced from laser ablation of a solid surface is a cloud of particles in the micron to sub-micron size range. In a conventional analysis, the ablated plume is transported to the torch via connective tubing. This transportation process dilutes the ablated plume with the carrier gas and introduces individual particles to the ICP torch in a sequential manner. It has been proposed [1-2] that recording the emission signal from selected peaks and rejecting the background signal between the peaks would result in a superior measurement technique. Detection limits would be substantially reduced since the signal would be integrated for only the duration of the emission event. This chapter describes such a measurement technique which is based on high bandwidth amplification and fast analog-to-digital conversion rates.

A wealth of information is available from a single laser ablation event when the event is observed as the sequential emission of individual particles. This type of measurement not only provides lower detection limits, but the laser ablation event itself can be studied in greater detail. Particle counting and size distributions can be determined which give information regarding the system's transportation and vaporization efficiency. Insight can also be gained into factors like fractional ablation. Fractionation occurs when the elemental proportions in the ablated material are not representative of the bulk concentrations in the solid sample [3]. This can be a severe problem for quantitative analysis by LA-ICP-AES and a detailed multi-element determination on an

individual particle basis would provide insight into understanding this fractionation effect.

This chapter specifically deals with individual particle analysis where the particles are generated by the laser ablation of a solid surface. However, the concepts and measurement criteria presented here are not exclusively reserved for laser ablation. Particles can be introduced into an ICP in a variety of ways. For example, the nebulization of slurries or the introduction of atmospheric aerosols are also methods of particle analysis. The importance of slurry analysis and particle characterization has been highlighted in a recent review [4], relating to environmental analytical chemistry.

4.2 Instrumentation

A schematic diagram showing the setup of the LA-ICP-AES system is shown in Fig. 4.1. A Nd:YAG laser was used to ablate the surface of a solid sample, creating particles which were entrained by a flowing Ar stream. The Ar was the central flow channel of an ICP torch and carried the particles into the plasma. Elemental emission was imaged onto the entrance slit of a direct-reading polychromator where PMTs transduced the optical emission pulses to electrical current pulses. A current-to-voltage converter, with a t_r of 0.01 ms, amplified the signal and the signal was digitized by an ADC board inside a personal computer. The laser and ADC board were triggered simultaneously. Therefore, the ADC sampled the background signal for a short period of time (approximately 1 s) before particles entered the plasma. This time coincided with the particle transport time from the ablation chamber to the ICP torch. Connective tubing of 3/16" i.d. was used to transport the ablated material. For single channel time resolved measurements, a digitization rate of 18 μs/point (the ADC board maximum) was chosen and a total of one million points were digitized. This resulted in an acquisition time of 18

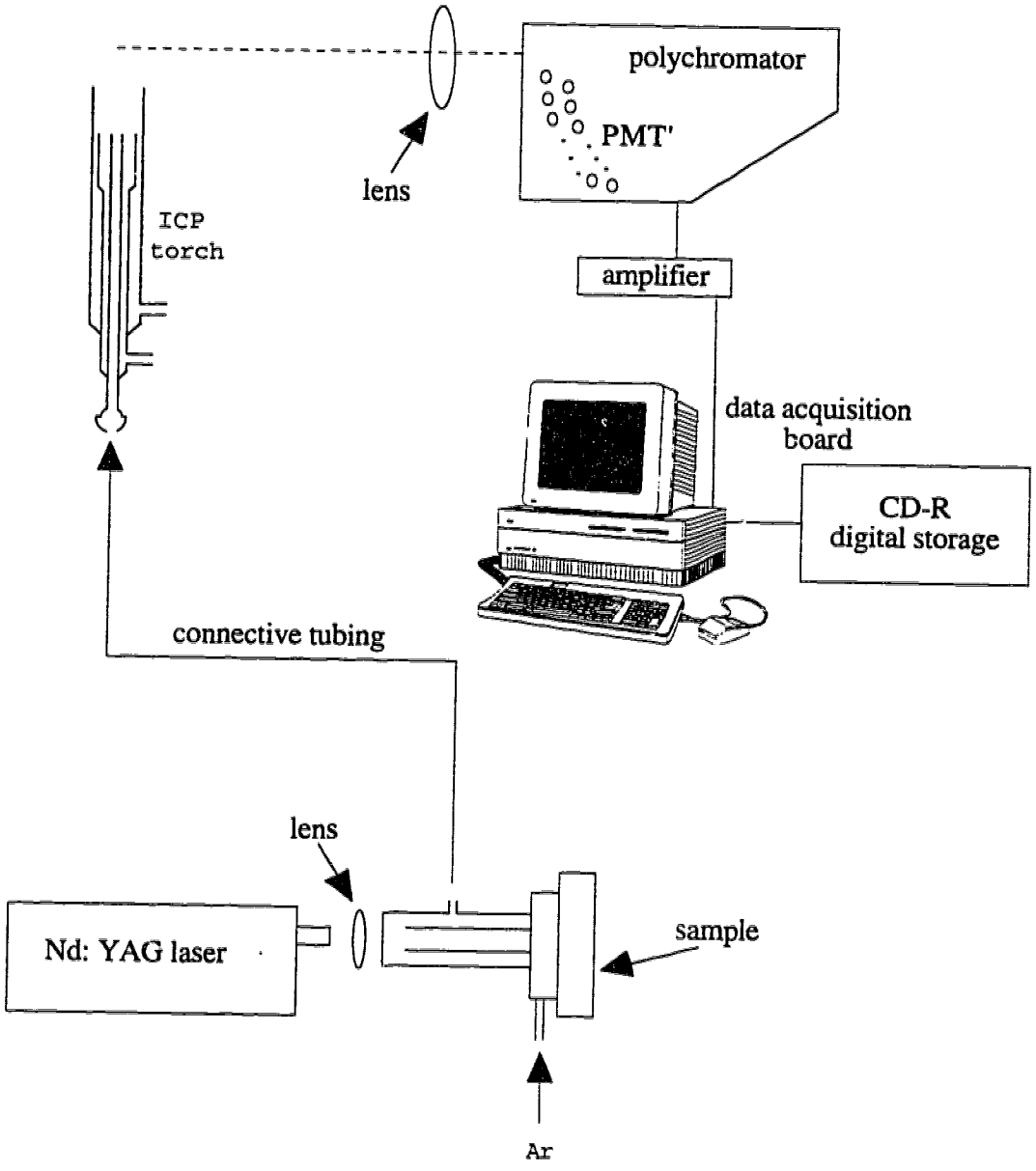

Fig. 4.1 Schematic representation of experimental setup.

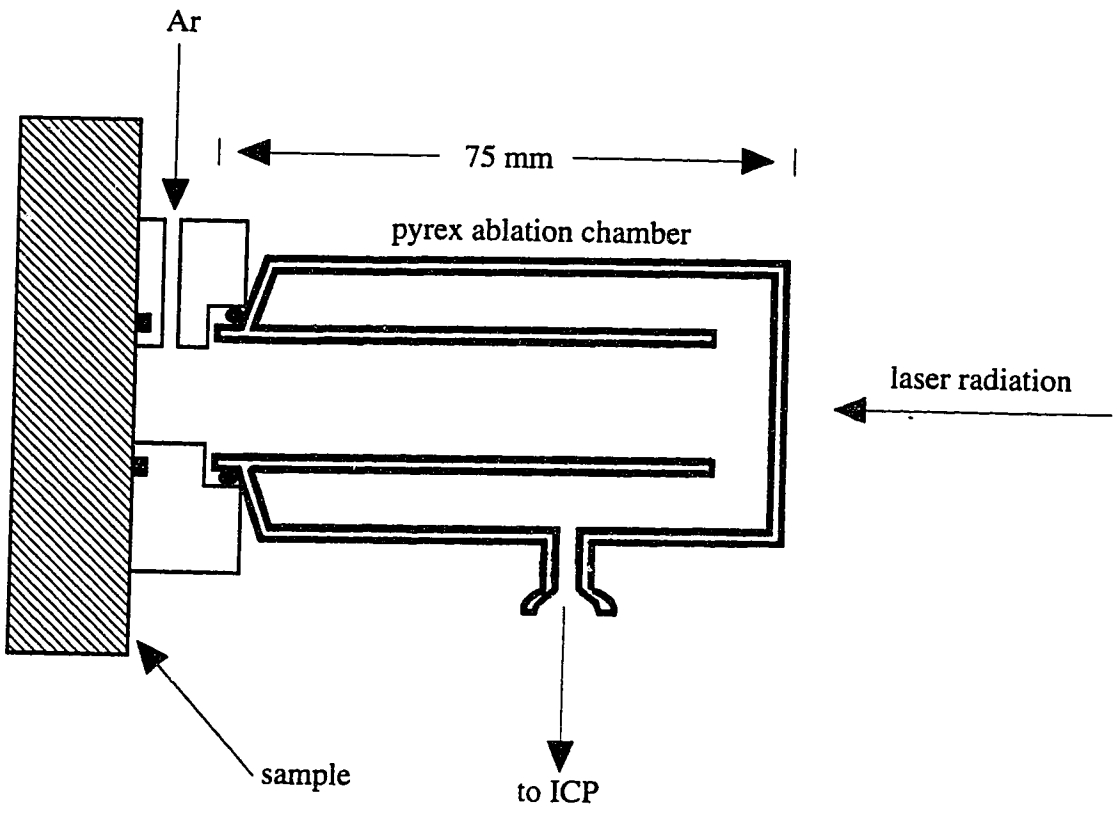

Fig. 4.2 Laser ablation chamber showing the directional flow of Ar.

s, enough time for the vast majority of ablated particles to be carried to the plasma. A single digitally stored emission profile required 9.8 MB of storage memory and a recordable CD device was used to archive these data files. The basic hardware components and experimental parameters are listed in Table 4.1.

A schematic diagram of the ablation chamber, which was also used in previous studies [5-6], is shown in Fig. 4.2. Laser radiation was focused with a 13.5 cm focal length lens and ablated the solid sample. Ejected particles had to traverse a double-pass ablation chamber before entering the connective tubing. The ablation chamber was designed in this way so that larger particles, which would be incompletely vaporized in the plasma, would be left behind in the chamber. Chamber dimensions and Ar flow rates were not manipulated to maximize the transport efficiency of the system.

4.3 Samples

The solid samples used in this study are listed in Table 4.2 along with the matrix they were found in and their respective concentrations.

4.4 Calibration

Any technique which introduces solid samples into an ICP has, by its very nature, unique and hard to overcome calibration problems. For example, to properly calibrate the emission intensity in LA-ICP-AES standards must be available which closely match the physical and chemical matrix of the sample. Since *a priori* knowledge of the sample matrix is often unknown, the analyst is left to make assumptions regarding the sample matrix, assumptions which can adversely affect the outcome of the analysis. In ideal circumstances, the matrix of the sample should match the matrix of the standards used for

Table 4.1 Hardware specifications and operating parameters for LA-ICP-AES: lateral viewing.

ICP	Plasma Therm ICP 5000
ICP operating conditions	Forward power 1.25 kW; reflected power <50 W; observation height 14 mm above load coil
Ar flow rates	Central 0.8 l/min; auxillary 1.0 l/min; plasma 16 l/min
Spectrometer	1.0 m, Pachen -Runge mount, 29 channel direct reader, 1200 groove/mm concave grating
Elements and wavelengths	Al I 237.357 nm, Fe II 259.940 nm, Cu I 324.754 nm, Cr II 205.559 nm, Zn I 213.856 nm
Amplifier	Keithley 427 current amplifier, 0.01 ms rise time
PMT voltage	-840 V
Data acquisition	Lab-LC board (National Instruments Corp., Austin, TX), 12-bit ADC, 18 μs/point used for time resolved acquisitions
System computer	Macintosh PowerPC Performa 5200CD, 24 MB RAM, 75 MHz clock speed
Software	System software 7.5.1, SpectroPlot [7]
Digital storage	Compact disc recordable system (CD-R), (JVC, Irvine, CA), model # BC-CR2000, 650 MB/CD
Digital oscilloscope	Hewlett Packard 54542A, 4 channel
Laser	Nd:YAG, 100 mJ per pulse, 1064 nm, 15 ns pulse laser width

Table 4.2 Samples used for LA-ICP-AES.

Matrix	Element	Sample no.	Respective concentration, % w/w
Aluminum	Cu	Alcoa SS-380-6	3.58
Steel	Fe, Cu, Zn	SRM 1261a	95.6, 0.042, 0.0001
Stainless steel	Cr, Cu	SRM 1171	17.4, 0.021
Brass	Cu	SRM C1106	59.08

calibration. This is in fact possible in many circumstances and has enabled LA-ICP-AES to become an accepted technique for many analyses. Internal standardization is often used where the emission from the most abundant element in the sample is ratioed against the emission from the analyte, correcting for instrumental drift. However, for individual particle analysis the problem of finding matrix-matched standards is much more difficult. In this case, not only does the chemical composition of the standard have to be known but the size of the particle must also be known. Standards which meet these criteria are simply unavailable and the analyst is forced to use alternative methods of signal calibration.

As described in the previous chapter, monodisperse droplet generators can be used to introduce particles of known size and composition into the ICP [8]. The droplet generator is made from a length of tubing with a piezoceramic-tube on the end. When a voltage pulse is applied to the transducer and solution flow rate through the tube is accurately controlled, droplets are produced with a very narrow size distribution. Since the composition of the solution introduced to the tubing is known, the droplets produced will contain a known amount of standard. The droplets are desolvated in a furnace before entering the ICP, producing a salt particle of known size and composition. Although this method has been used with some success to calibrate particle emission in the ICP, true matrix-matched standards are impossible to prepare since the particles produced from the generator result from the desolvation of aqueous solution. Particle emission from salt particles may be different than from metallic solids and this difference has yet to be studied. Also, the use of a monodisperse droplet generator adds another level of complexity to the measurement system. Simpler and more straight forward methods of signal calibration are desired.

Calibration of particle emission has been achieved by simply aspirating a solution of known concentration with a standard nebulizer [9-11]. Although this method does not consider the potential matrix problem of emission from salt particles versus the emission from solid metallic spheres, it has been used successfully. Thompson *et al.* [9] determined the empirical formula of an unknown mineral by LA-ICP-AES with solution calibration. Sensitivity ratios were calculated by conventional nebulization of aqueous solutions of known composition. This calibration was validated by laser microprobe analysis of mineral grains of known composition. Moenke-Blankenburg *et al.* [10] have also proposed a method of calibration based on solution nebulization. In their experimental setup, the Ar carrier gas was divided into two separate streams. One pathway led to the ablation chamber and the other pathway led to a standard nebulizer and spray chamber. Following the ablation and spray chamber, the two Ar streams were mixed in front of the ICP torch. During the calibration step the standard solutions were nebulized and passed directly from the spray chamber to the ICP. When the sample was introduced by laser ablation, a blank solution was nebulized at the same time. This ensured that the liquid or water introduction into the ICP was the same for both the calibration and sample introduction steps. Finally, Nore et al. [11] have developed a technique for monitoring air quality with regard to metallic aerosol concentrations by ICP-AES. They also have calibrated elemental emission intensities using solution nebulization. In this case, an ultrasonic nebulizer was used and Be, Co, Cd, and Pb were detected and calibrated in atmospheric aerosols.

Another technique which uses solution calibration of particle emission is slurry nebulization of particles with ICP-AES. Even though the discrete emission events are not resolved, slurry nebulization is a popular technique, specifically in the area of environmental analytical chemistry [4]. Babington-type nebulizers are often used to prevent plugging of the small diameter tubing found in concentric or cross-flow

nebulizers. Standardization of the slurry sample is simply achieved by nebulizing a solution with known elemental concentrations. Acquisition parameters are kept the same for both the standard and analyte introduction.

Pneumatic nebulization of standard solutions was the method chosen for emission calibration of the laser ablated plumes studied in this chapter. A Meinhard nebulizer and Scott type spray chamber simply replaced the ablation chamber as shown in Fig. 4.1. This method was chosen because of its inherent simplicity and a detailed description of the calibration procedure is given in the following section.

4.4.1 Calibration procedure

The purpose of the calibration procedure is to determine the mass of individual particles from their emission pulses. The mass of the elemental standard which reached the ICP can be calculated by measuring the solution uptake rate of the pneumatic nebulizer, knowing the solution concentration and duration of signal acquisition, and assuming a transport efficiency of 1%. This value can then be used to calibrate particle emission and an example of this calculation is provided in this section.

A multi-element solution was prepared which contained 5 μg/ml of Fe, Al, Cu, and Zn in 2% HNO_3. For emission calibration, this solution was aspirated into the ICP and the resulting signal was acquired with the same acquisition parameters as used for the determination of the ablated material i.e., single channel acquisition with the rise time on the amplifier set to 0.01 ms and a data acquisition rate of 18 μs/point. Again, a total of one million data points were collected and digitally stored. The elemental emission intensity was integrated over an 18 s period and the net signal was determined by subtracting a solution blank. The blank was acquired with the same gain and acquisition

parameters as the standard. To calibrate for individual particle emission the integrated peak area of the particle emission was determined, and by comparison to the integrated signal from solution nebulization, the mass of the detected particle was calculated. An example of this calculation is given below for the calibration of the particle emission of Fe in steel. The particle which was calibrated is shown in Fig. 4.3a and is the largest particle in the temporal profile, appearing at 4.9 s.

The integrated peak area for Fe emission was measured from point no. 271,149 - 271,173 (out of one million points) and had a value of 94.38. This value was corrected to 943.8 since the gain on the amplifier was an order of magnitude higher for the solution calibration procedure. The integrated signal for the solution nebulization of the Fe standard was 478,000 over 18 s. This was corrected to a value of 296,000 after subtraction of the solution blank. The solution flow rate to the nebulizer was measured to be 0.52 ml/min and the total mass of Fe standard reaching the nebulizer over an 18 s period was determined by the following calculation.

$$(5\ \mu g/ml)\ (0.52\ ml/min)\ (18/60) = 0.78\ \mu g \qquad 4.1$$

Assuming a transport efficiency of 1% between the nebulizer and the ICP, 7.8 ng of Fe reached the torch over an 18 s period. Since a value of 7.8 ng of Fe corresponds with a net emission intensity of 296,000, the mass of Fe observed in the particle emission can be calculated by comparison. This is shown below where M_p is equal to the mass of Fe in the selected particle.

$$M_p = (7.8\ ng)\ (943.8/296{,}000) \qquad 4.2$$
$$= 25\ pg$$

This calibration procedure is used to calculate detection limits and particle size distributions.

Validation of the calibration calculation is provided by calculating the size of particle which would result from a 25 pg mass of Fe. Since the transportation of a particle from the ablation chamber to the ICP is dependent on the particle size, the calculated particle size must fall within acceptable limits in order for the calibration to be valid. The density of Fe is 7.86 g/cm^3 and, therefore, the volume of Fe is 3.2 x 10^{-12} cm^3. Assuming a spherical particle, the radius is equal to 0.9 μm and, therefore, the diameter is 1.8 μm. As shown in Fig. 3.5, a particle size of 1.8 μm would be in the upper range of particle sizes which are transported to the ICP with high efficiency. Since the calibrated Fe particle was the largest in the temporal emission profile of Fig. 4.3a, the calibration of particle emission by solution nebulization appears to be reasonably valid. Although certain assumptions have been made, the calibrated emission peaks are at the very least reasonable and the conclusions drawn from this calibration are justified. For the calculations presented here, the particle is assumed to be 100% Fe since the original steel sample was 95.6% Fe.

If fully characterized particle standards become available in the future, the nebulization of a suspension of these particles would overcome many standardization problems. Calibration would be performed directly from the solid particle standard.

4.5 Time resolved analysis by LA-ICP-AES: fundamental properties

The temporal emission profile of an ablation event is quite different than signals generated by a conventional acquisition. This difference is clearly illustrated in this section. A comparison between a low-bandwidth LA-ICP-AES acquisition is made with

a high-bandwidth (temporally resolved) acquisition. Emission profiles of individual particles are presented and peak width comparisons are made. Frequency spectra from time resolved and conventional LA-ICP-AES are compared. A frequency spectrum from a solution nebulized sample is also presented to further highlight the unique signal properties of time resolved LA-ICP-AES.

4.5.1 Particle emission observed from one laser pulse

An Fe emission profile showing individual peaks from particle emission is presented in Fig. 4.3a, where each spike in the profile represents emission from one particle. This profile was generated by one laser ablation pulse of a steel sample. Particle emission is observed at approximately 1 s in the profile, which represents the time required for the ablated particles to be transported to the ICP. Of significant importance is the near zero background level on top of which particle emission is observed. This results in a high signal-to-noise ratio and is responsible for the very low detection limits achieved with individual particle analysis. Fig. 4.3a represents one million digitized data points and requires 9.8 MB of storage space. To gain an appreciation for the size and information contained in this data file, the analyst must take the time to expand selected portions to properly view the particle emission. Scale expansion of Fig. 4.3a is shown in Fig. 4.3b and Figs. 4.4a and b. Fig. 4.3b represents 87,365 digitized points and requires 867 KB of memory. The largest peak found in Fig. 4.3b is the second most intense peak observed in Fig. 4.3a. Further scale expansion is observed in Figs. 4.4a (15,456 points) and b (126 points). The largest peak shown in Fig. 4.4a is the single peak observed in Fig. 4.4b. The emission peak shown in Fig. 4.4b originates from the detection of one particle introduced into the ICP. The baseline peak width is approximately 0.5 ms and corresponds with the time it takes for the vapor from a particle to vertically traverse the

entrance slit of the polychromator. Peak widths for different sized particles will be discussed in the following paragraph.

Emission characteristics from 10 of the most intense peaks of Fig. 4.3a are tabulated on Table 4.3 and six of these peaks are shown in Fig. 4.5. The peak widths were measured at the baseline and an average value of 0.48 ± 0.05 ms was recorded. The velocity of a particle (or vapor originating from a particle) has been calculated to be 20 m/s [12] as it travels through the normal analytical zone of the ICP. Since the entrance slit on the polychromator used in this study was 2.0 cm high and the plasma was magnified 1:2 onto this slit, the time required for a particle to vertically pass the entrance slit was 0.5 ms. The results shown in Table 4.3 support this calculation. Other researchers have also determined peak widths from particle emission which were determined by the velocity of the particle as it passed through the plasma [13].

Emission characteristics of 10 of the weakest peaks of Fig. 4.3a are tabulated in Table 4.4 and selected peaks are shown in Fig. 4.6. In these examples, the emission intensities were low, showing peaks which were almost buried in the background noise. The peak widths were again measured at the baseline and a value of 0.37 ± 0.05 ms was calculated. This value is 0.11 ms less than the value reported when considering larger particles and can be explained by considering the sensitivity of the technique. As the particles and their associated emission peaks become smaller, the emission profile from an individual particle appears to drop down into the baseline. Therefore, it is reasonable to measure narrower peak widths for smaller particles as compared to larger particles. The ICP-AES system used for this analysis has a definite detection limit for particle analysis and when the emission peaks approach this detection limit, the peak widths will be reduced.

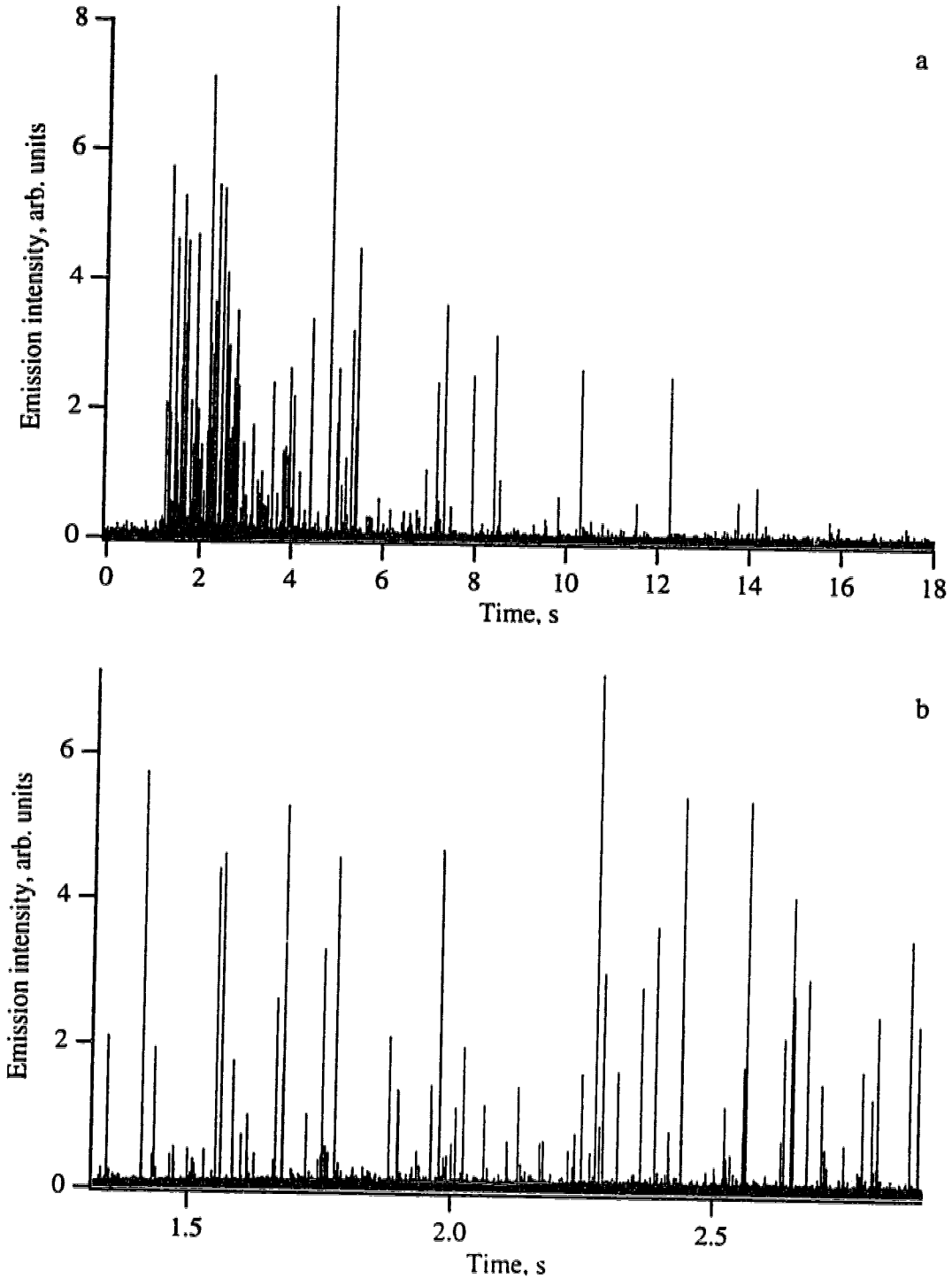

Fig. 4.3 The entire (a) and scale expanded (b) emission profiles of Fe from a steel sample, SRM 1261a.

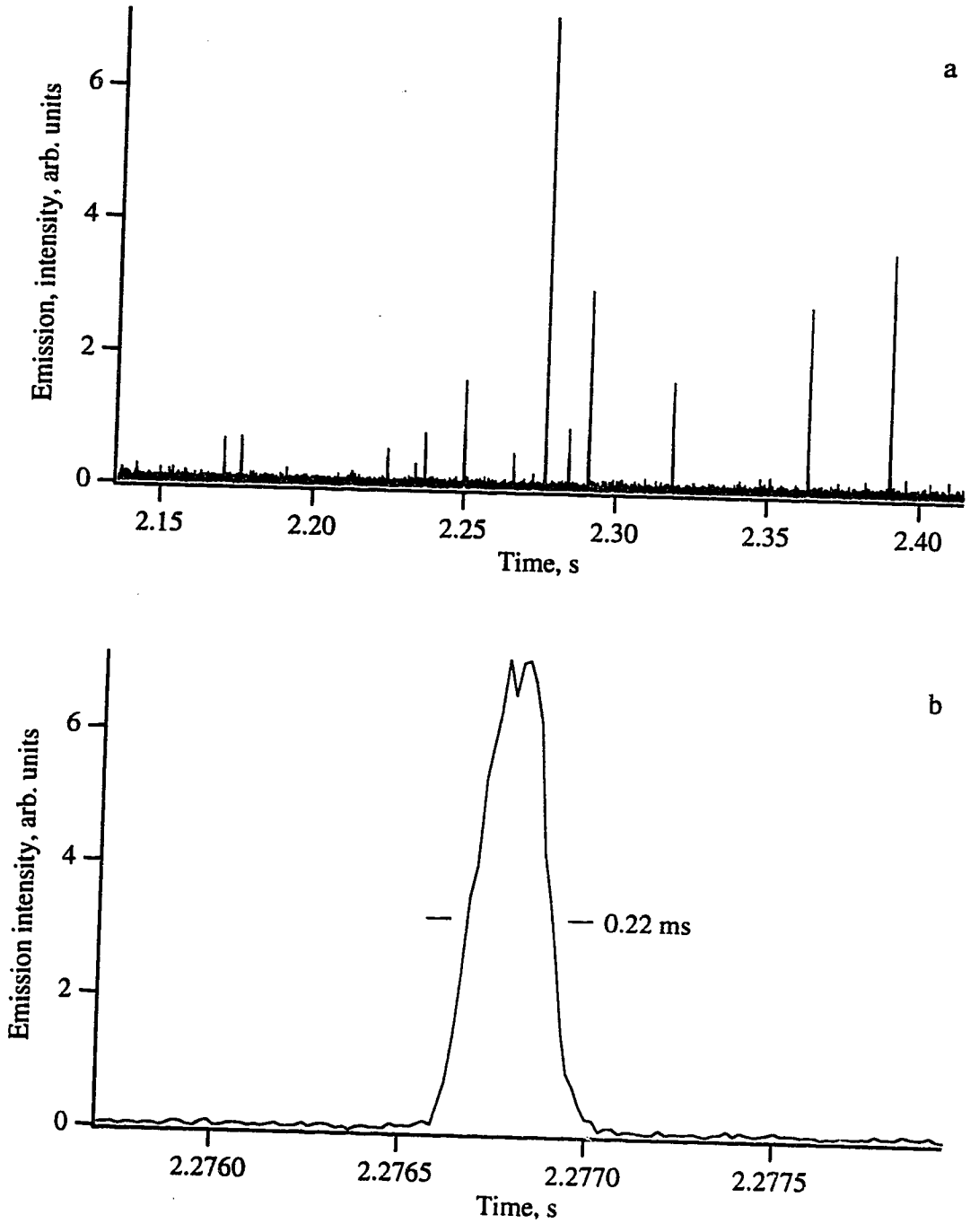

Fig. 4.4 Further scale expansion of the Fe emission profile found in Fig. 4.3.

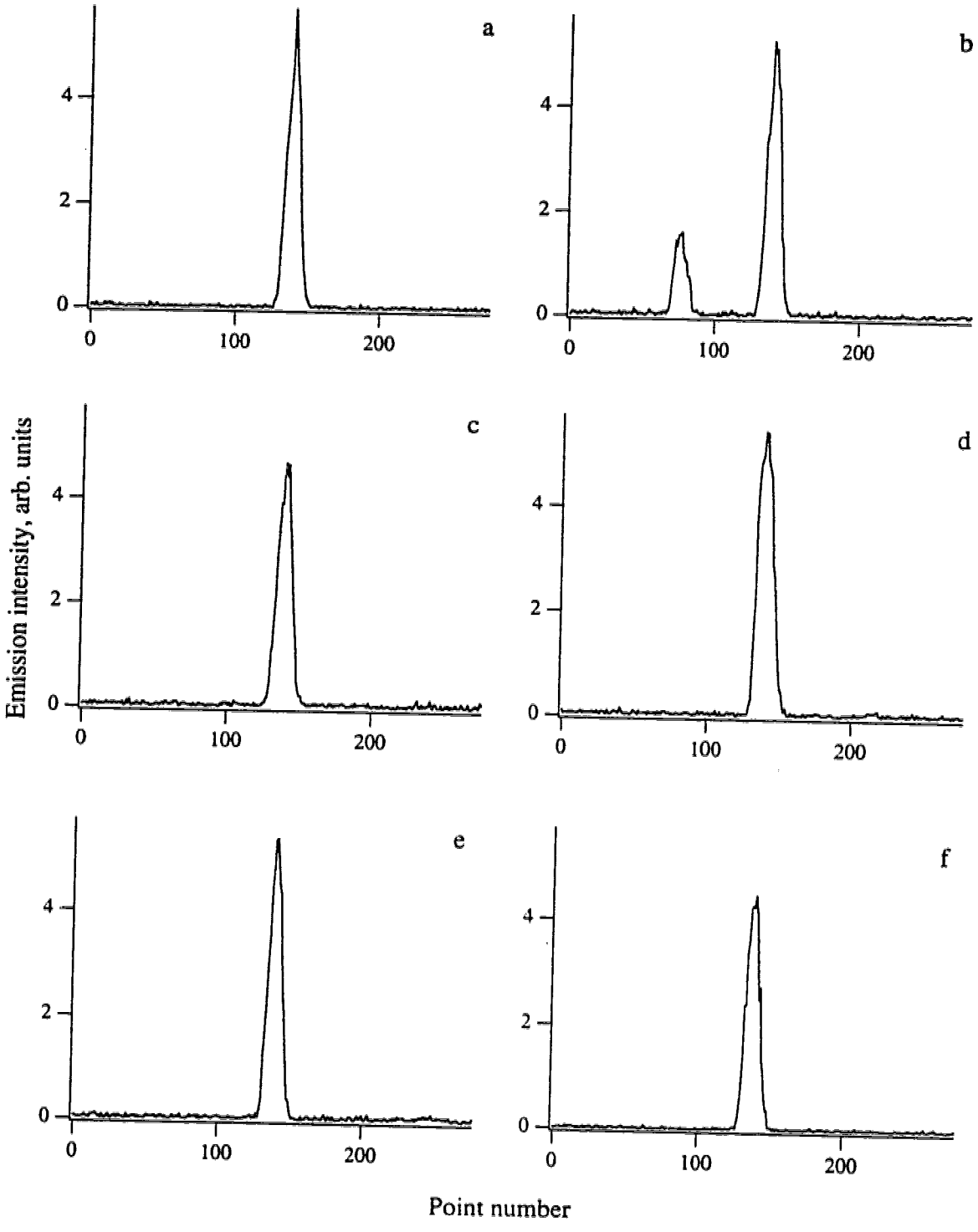

Fig. 4.5 Emission profiles of large particles found from Fig. 4.3a.

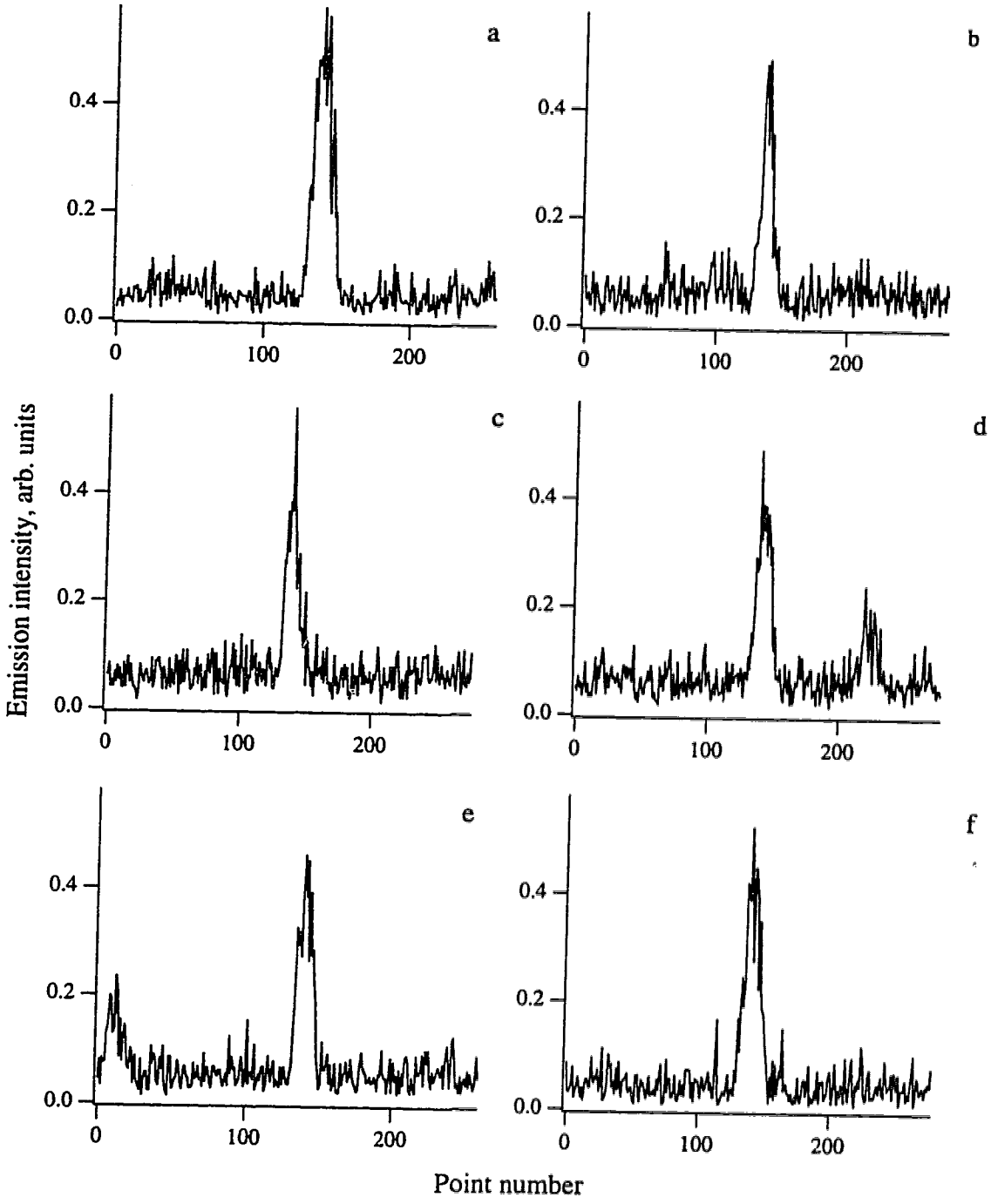

Fig. 4.6 Emission profiles of small particles from Fig. 4.3a.

Table 4.3 Emission characteristics of 10 of the most intense peaks of Fig. 4.3a.

	Time, s	Major peaks, peak height	Peak width, ms
a)	1.411578	5.742	0.486
b)	1.680948	5.286	0.450
c)	1.978236	4.700	0.522
d)	2.439612	5.459	0.468
e)	2.562804	5.403	0.414
f)	5.493906	4.482	0.414
g)	1.562688	4.348	0.486
h)	1.780506	4.580	0.504
i)	2.276766	7.139	0.486
j)	4.880898	8.203	0.594

Table 4.4 Emission characteristics of 10 low intensity peaks of Fig. 4.3a.

	Time, s	Minor peaks, peak height	Peak width, ms
a)	1.473282	0.579	0.468
b)	1.992762	0.493	0.324
c)	2.266344	0.559	0.360
d)	2.525256	0.491	0.360
e)	2.969514	0.461	0.342
f)	3.415068	0.522	0.432
g)	1.277694	0.273	0.396
h)	3.114018	0.342	0.360
i)	3.420126	0.437	0.360
j)	4.071132	0.452	0.324

Figs. 4.5 and 4.6 represent a total of 278 digitized points for each emission profile, resulting in a 5.0 ms window. The emission profiles for the particles represented in these figures are typical of all particle emission profiles as viewed laterally in the plasma. Similar emission profiles were observed whether the analyzed element represented a major or minor proportion in the original solid sample. As observed in Figs. 4.5 and 4.6, the emission profiles were symmetrical i.e., there were no leading or tailing edges to the emission from individual particles. This has two implications. Firstly, symmetrical peak shapes imply that the particle is completely vaporized as it enters the viewing zone of the polychromator. The centre of the observation zone was 14 mm above the load coil and it is reasonable to assume that the particles are completely vaporized as they enter this zone. Secondly, symmetrical peak shapes show that the instrument response function is adequate to respond quickly to the temporal emission events caused by particle introduction.

Emission profiles from Cu in brass and Al in a high alloy aluminum sample are shown in Fig. 4.7. These examples, including the previous figures showing the emission of Fe in a steel sample, illustrate individual particle emission from a variety of matrices where the emission profile is from the most abundant element in the solid matrix. Collectively, these emission profiles provide information on particle vaporization in the ICP. Incomplete particle vaporization can occur if the particle is too large and is not fully vaporized as it passes the observation region of the plasma. However, the double pass ablation chamber and the connective tubing eliminated large particles since they settled out due to gravity before reaching the torch. This is confirmed by viewing the large emission pulses of Figs. 4.3a and 4.7a and b. If large particles were not completely vaporized, then the largest emission pulses would all tend to plateau at a certain level. Since the intensity of emission pulses appear to be randomly distributed, it can be assumed that all particles are completely vaporized in the plasma. Complete particle

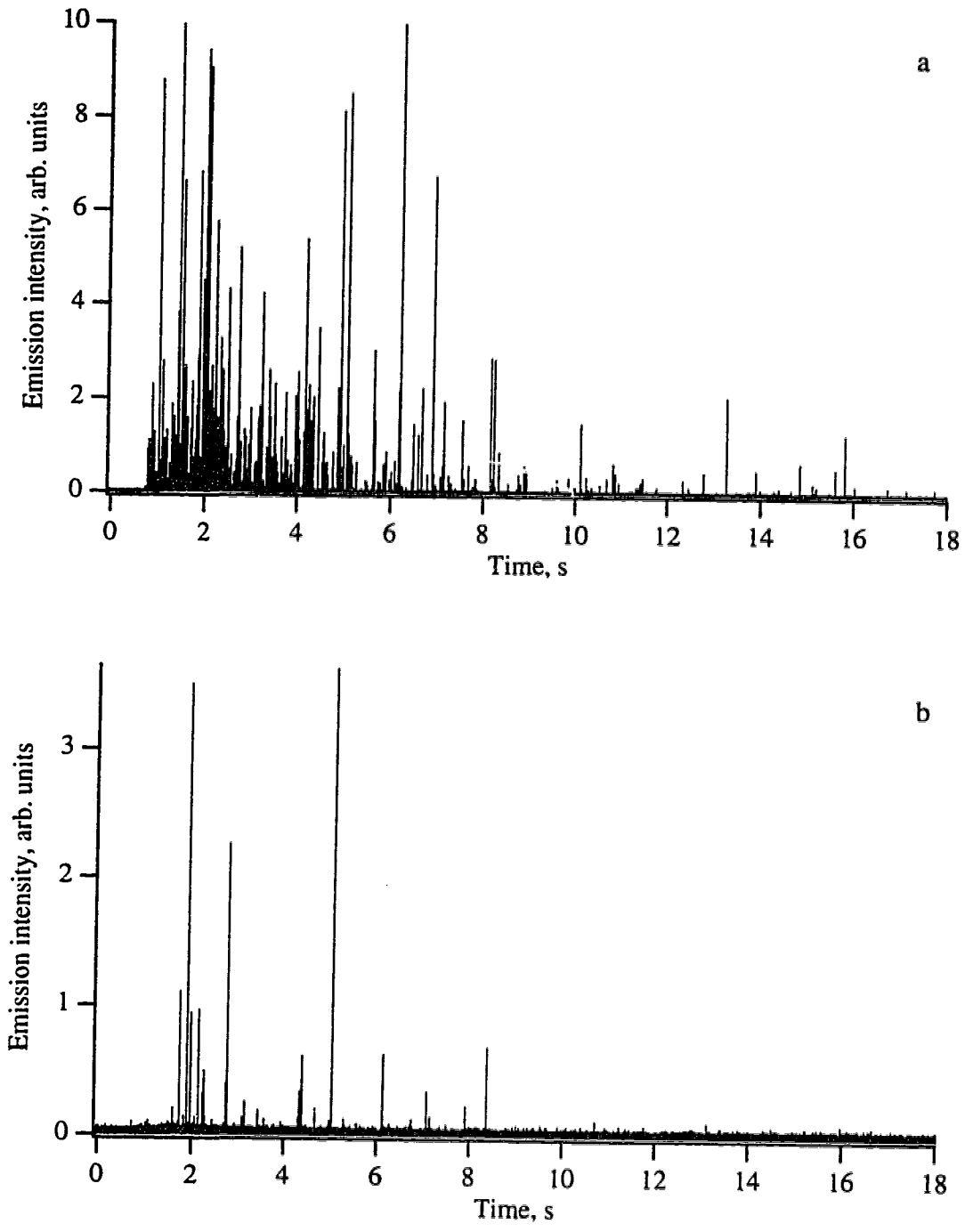

Fig. 4.7 Emission profiles of Cu in Brass, SRM C1106, (a) and Al in an Aluminum sample, Alcoa SS-380-6, (b).

vaporization is necessary for accurate quantitative analysis of both major and minor elements in individual particles.

Emission profiles of minor elements in a steel sample are shown in Fig. 4.8. Similar emission profiles were observed regardless of whether the element represented a major or minor constituent of the original sample. Pulse height and width distributions were not dependent upon elemental concentration of the solid sample. It is clearly illustrated that even minor elements can easily be detected. In this case, Zn and Cu had concentrations of 0.0001 and 0.042% w/w in the original steel sample. However, the elemental concentration of the particles is not necessarily the same concentration as that found in the original sample. Multi-element analysis of individual particles will be presented in section 4.11 and will show that elemental concentrations can vary dramatically on a particle to particle basis.

4.5.2 Comparison to a conventional laser ablation acquisition

A conventional laser ablation signal acquisition is defined as an acquisition which does not resolve individual particle emission. Since commercially available spectrometers come packaged with integrating detection electronics designed for solution nebulized samples, detection of laser ablated plumes has conventionally been done in an integrating manner. In other words, the detection electronics smear out the emission pulses from individual particles. For comparison purposes, a conventional acquisition was made of a single laser ablated plume to highlight the differences between time resolved and integrating detection.

Two Fe emission profiles are illustrated in Fig. 4.9 and they both originate from a single laser ablated plume of a steel sample. A conventional acquisition is shown in Fig.

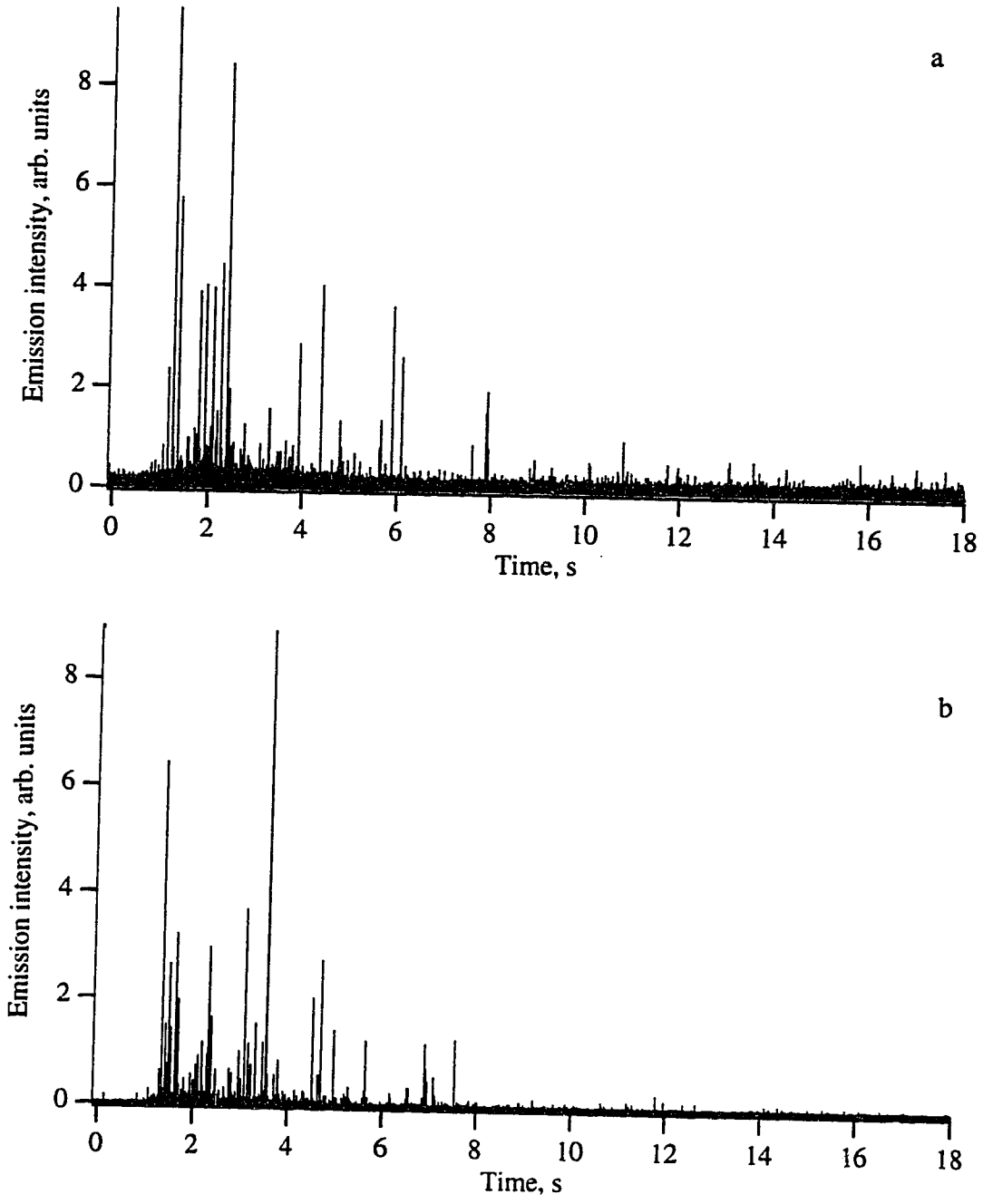

Fig. 4.8 Emission profile from Zn in steel, SRM 1261a, 0.0001%, (a) and Cu in steel, SRM 1261a, 0.042%, (b).

4.9a and represents 512 digitized points acquired at 100 ms/point with an amplifier rise time of 300 ms. This data file takes up 17 KB of digital memory, which is substantially different from the time resolved emission profile shown in Fig. 4.9b. The emission profile in Fig. 4.9b is the same profile as already seen in Fig. 4.3a. As already stated, the emission profile of Fig. 4.9b represents one million digitized points and takes up 9.8 MB of digital memory.

Many differences are observed in the emission profiles of Figs. 4.9a and b. First of all, a relatively smooth emission profile is observed for Fig. 4.9a. The long rise time of the current-to-voltage amplifier was responsible for smoothing out the emission pulses from individual particles. The emission profile was sitting on top of a relatively large background level and the average value of the background was measured to be 1.3 V between 17 and 18 s. The high background level was caused by a high gain setting on the current-to-voltage amplifier. For these examples, the gain for the conventional analysis was 100 times larger than the gain for the time resolved analysis. A small fluctuation in the background level is observed at approximately 0.5 s in the temporal emission profile. This fluctuation was caused by a laser induced pressure pulse. When the laser fired, a pressure wave propagated from the ablation chamber, through the connective tubing, and to the ICP. As the pressure wave entered the plasma, it altered the plasma conditions and a shift in the background level was observed. A similar effect has been observed for the steady state emission signal of Cu [14], where the pressure pulse reduced the Cu emission by approximately 50%. Emission of Fe begins approximately 1 s later in the conventional profile as compared to the time resolved profile. The long rise time of the amplifier was responsible for the delay in the observed emission. The Fe emission profile is not completely smooth; small and relatively wide spikes were observed. These spikes were a result of the random emission pulses from individual particles or groups of particles.

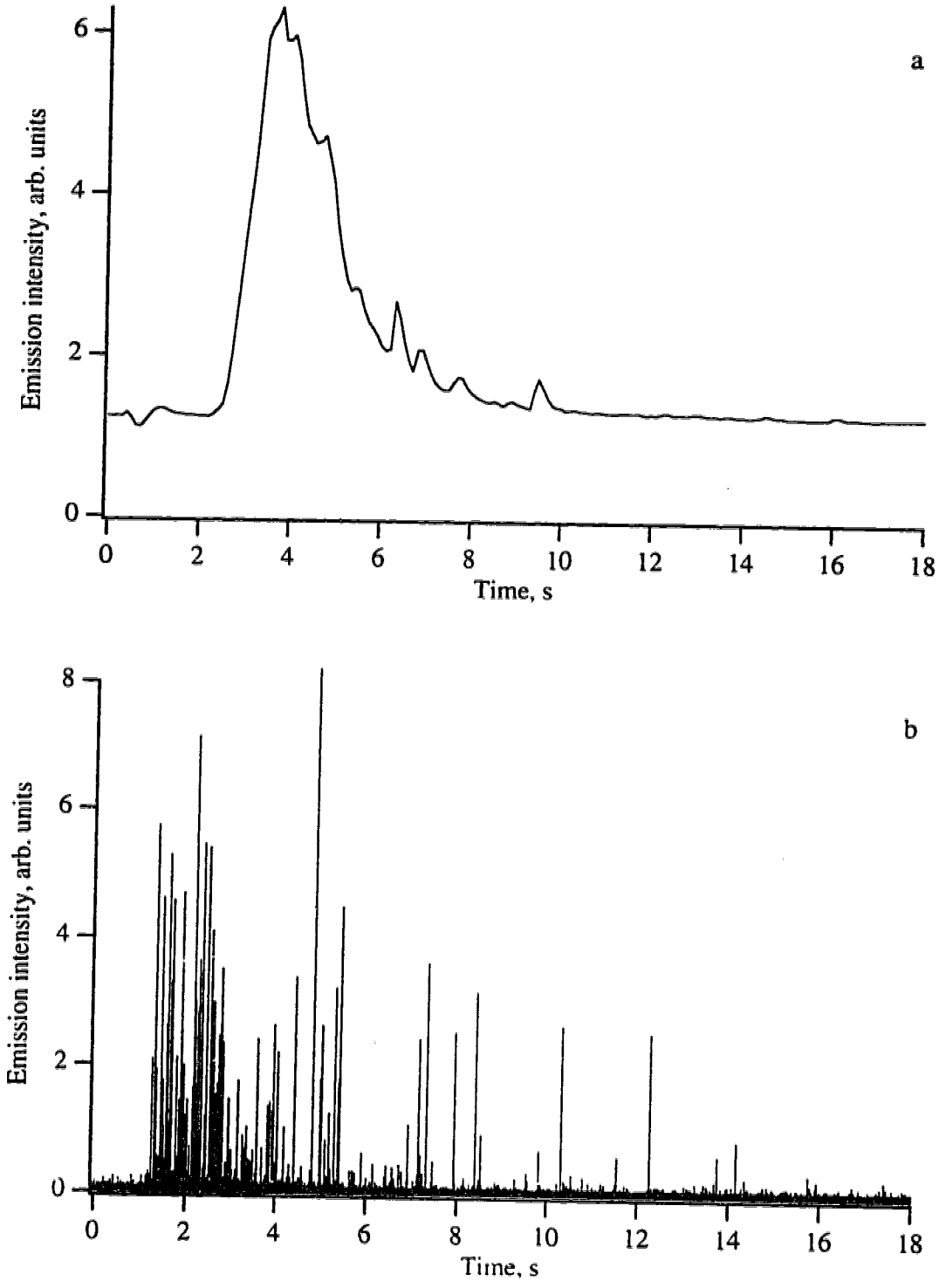

Fig. 4.9 Emission profile of Fe, SRM 1261a, from a conventional laser ablation acquisition (a) and from a time resolved acquisition (b).

To further illustrate the difference between conventional and time resolved analysis, a detection limit was calculated from the emission profile in Fig. 4.9a. The integrated Fe emission profile was calibrated against solution nebulized standards as discussed in section 4.4. The mass of Fe, responsible for the emission profile of Fig. 4.9a was calculated to be 2.9 ng and a detection limit (3σ) of 31 pg was determined. This value is approximately 1000 times larger than the detection limits calculated for individual particles of Fe, which will be illustrated in section 4.6. It is obvious that time resolved analysis of particle emission provided much higher sensitivities than those obtained by conventional analysis.

4.5.3 Comparison of frequency spectra: time resolved versus conventional analysis

It is important to consider the frequency composition of the signal when choosing parameters such as the acquisition bandwidth and the digital sampling rate. Low-pass digital filtering can also be used more effectively when the frequency composition of the signal is known. Low-pass digital filtering is used in section 4.6 to improve the sensitivity of time resolved analysis. Frequency spectra were calculated for time resolved LA-ICP-AES, conventional LA-ICP-AES, and high-bandwidth solution nebulization ICP-AES. These spectra show the frequency composition of the respective signals and further illustrate their fundamental characteristics. A comparison to the background frequency spectra was made in all cases.

The frequency spectrum of Fe emission from a single laser ablation plume is shown in Fig. 4.10a. This spectrum was generated by calculating the Fourier transform of the first 262,144 points of the Fe emission profile shown in Fig. 4.3a. The most significant frequency components of the signal extended from dc to beyond 4000 Hz. However, frequencies contained in the signal also extended beyond 5000 Hz and up to

the maximum frequency determined in the original spectrum (27,778 Hz). This is confirmed by comparison with the frequency spectrum of the blank in Fig. 4.10b. Beyond 5000 Hz the average intensity of the blank was lower than the average intensity of the sample, which indicated that signal information is contained in frequencies beyond 5000 Hz. These high frequency components of the signal provided subtle information regarding the peak shape. Therefore, to obtain the maximum amount of peak shape information, a digitization rate of 55.6 kHz was used. This digitization rate was the fastest rate which could be sustained on the ADC used in this study.

Since most of the signal information was contained at frequencies below 5000 Hz, low pass digital filtering can be used to smooth the emission profile, thereby reducing the noise and improving the signal to noise ratio. Digital filtering involved taking the Fourier transform of the signal to convert the information from the time to the frequency domain. The frequency domain signal was then multiplied by the desired frequency response of the filter. The inverse Fourier transform of the product then yielded the filtered signal in the time domain. The effects of low-pass digital filtering are illustrated in section 4.6 and show how it can be used to dramatically lower detection limits.

The frequency spectrum of a signal generated by conventional laser ablation is shown in Fig. 4.11a. This is a frequency spectrum of the emission profile shown in Fig. 4.9a. The majority of the signal information was found at very low frequencies, from 0 to 1 Hz in this case. When compared to Fig. 4.10a, it is obvious that the signal from a conventional laser ablation emission profile was fundamentally different than a time resolved emission profile. The low bandwidth electronics used in the conventional analysis removed much of the signal information contained in the emission profile.

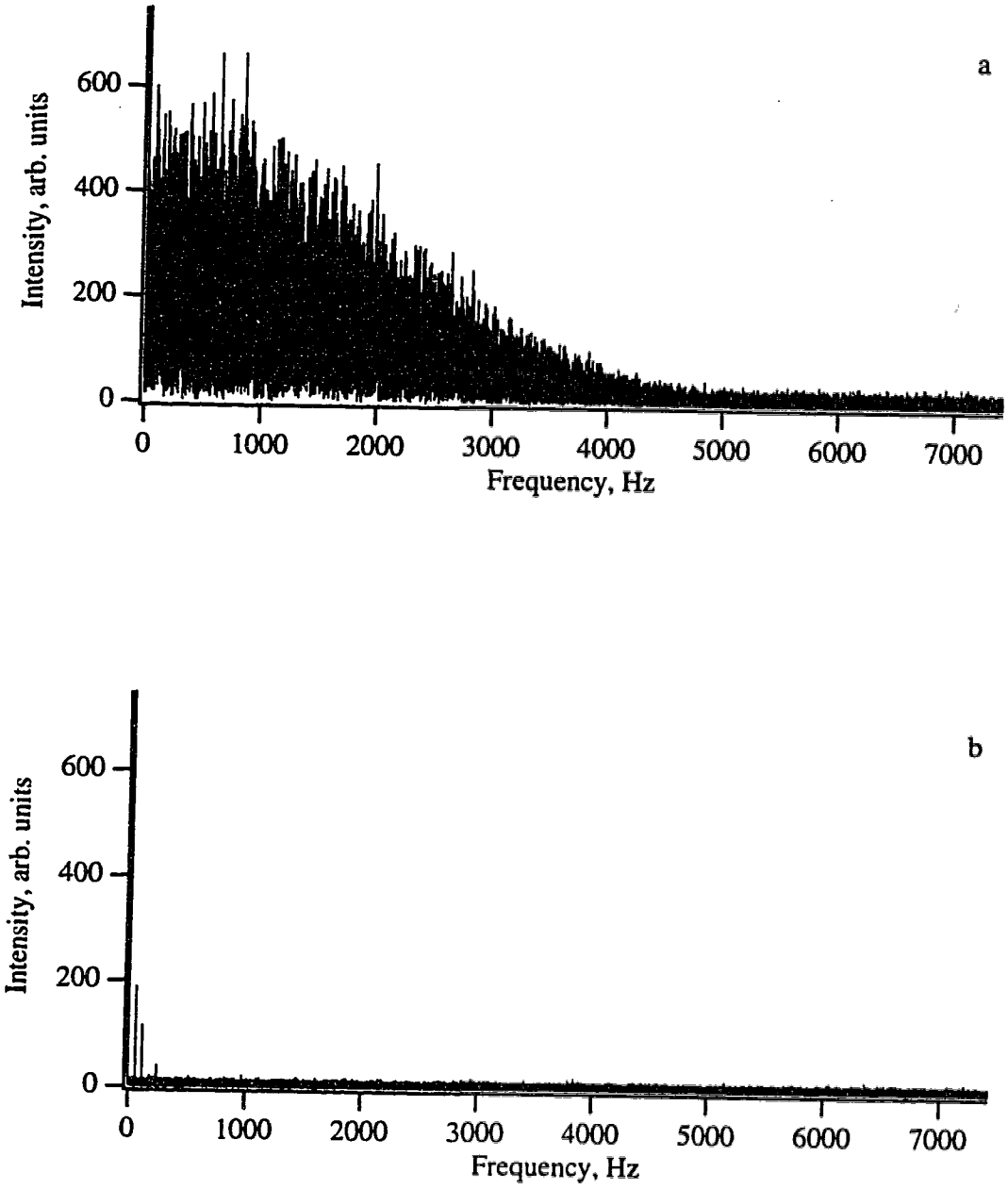

Fig. 4.10 Frequency spectra of the emission profile shown in Fig. 4.3a (a) and from a laser blank (b).

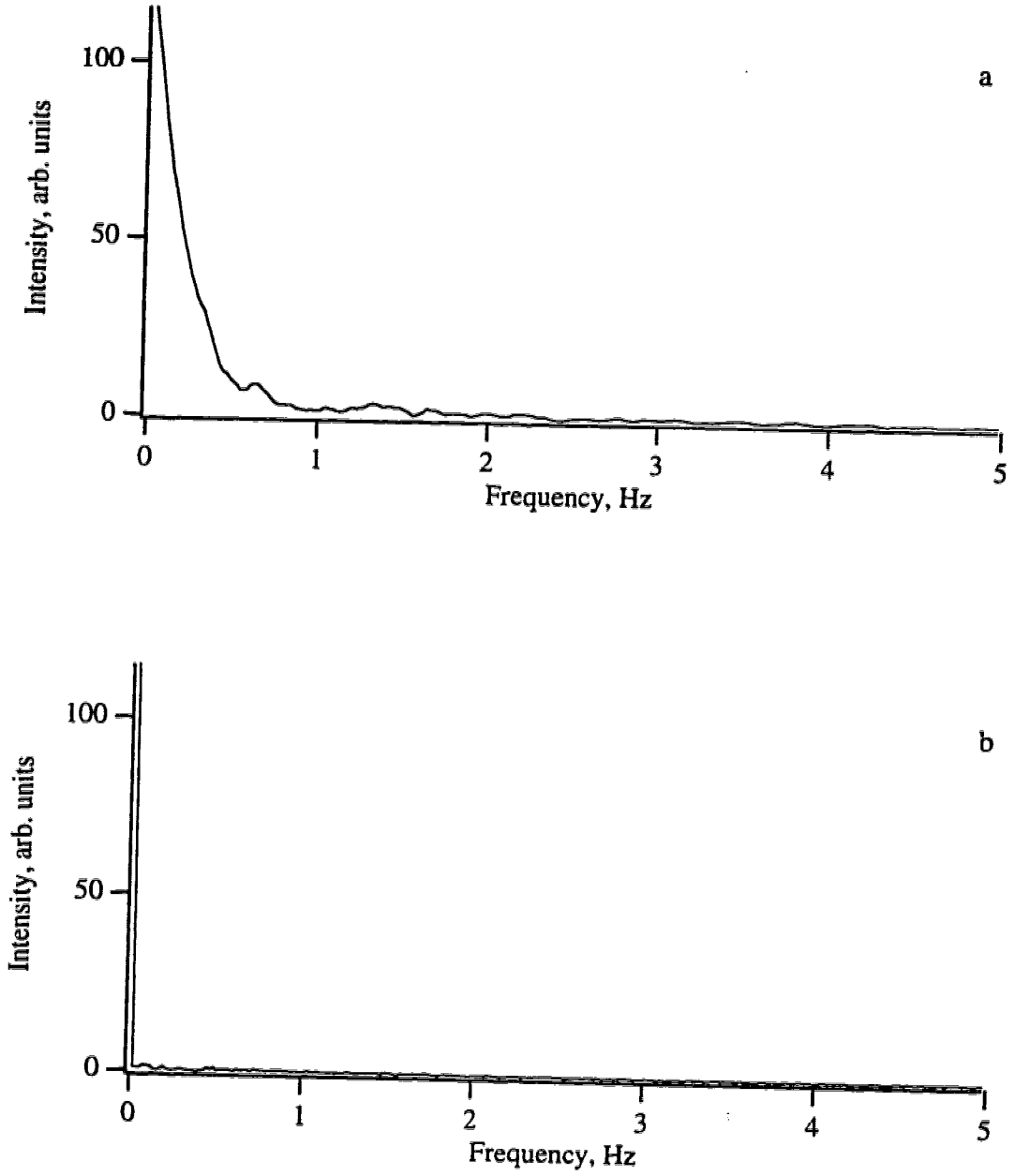

Fig. 4.11 Frequency spectra of the emission profile shown in Fig. 4.9a (a) and laser blank (b).

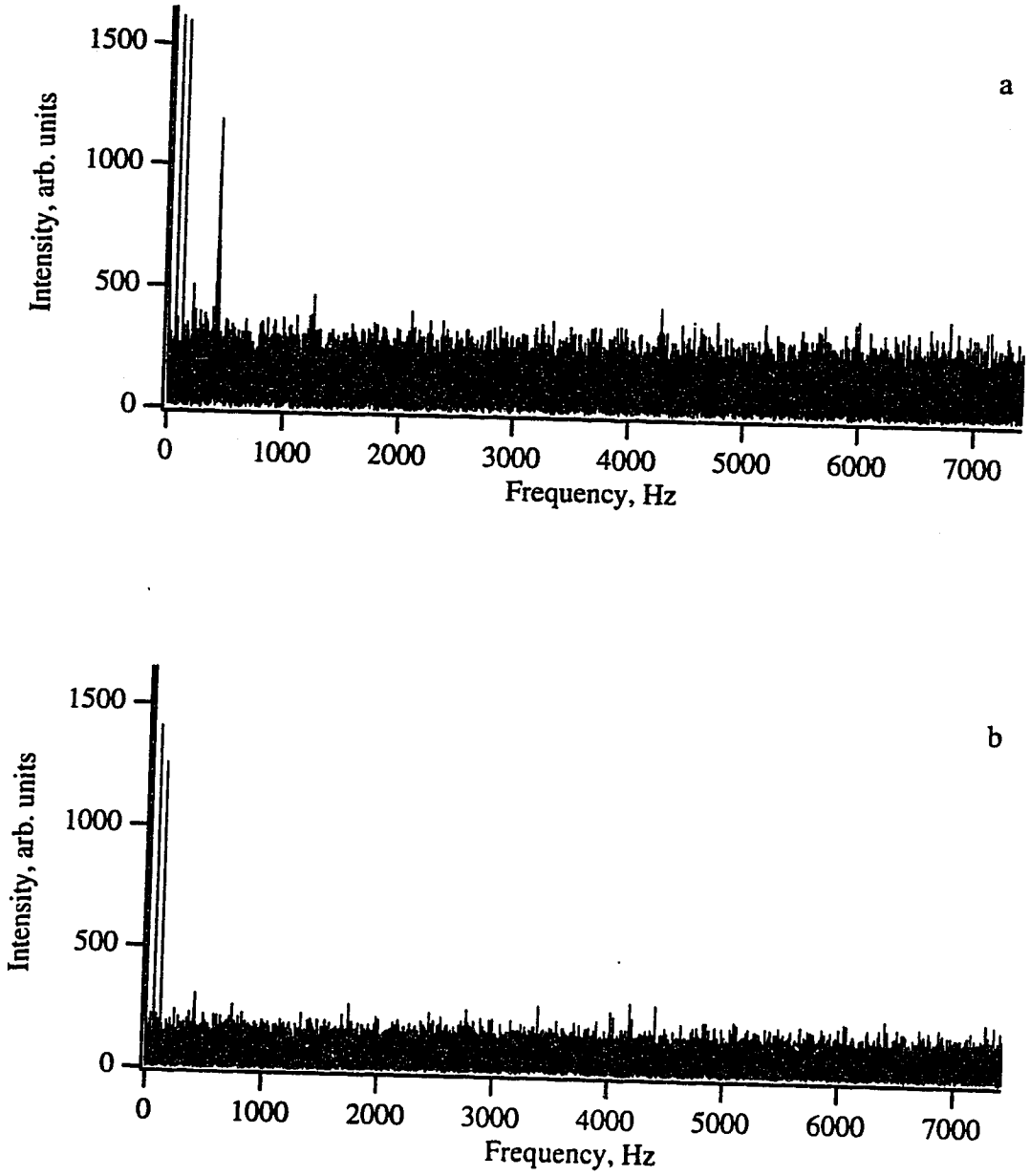

Fig. 4.12 Frequency spectra of emission from 5 μg/ml Fe solution (a) and solution blank (b).

To show how the signal from a solution nebulized sample was different than the signal from a laser ablated plume, the frequency spectra from a 5 μg/ml Fe solution and the solution blank are presented in Figs. 4.12a and b. Data were acquired with the same rise time and digitization rate as that used for the time resolved analysis of laser ablated plumes. Comparing Fig. 4.12a with 4.10a, it is obvious that the signal obtained from solution nebulization does not contain the same high frequency components as those seen in the time resolved laser ablation acquisition. The signal presented in Fig. 4.12a contains most of its information at 0 Hz, and this is why the conventional method of detecting a PMT signal is to measure its dc level. The spectra presented in Figs. 4.12a and b appear very similar, however, subtle differences do exist. The spectrum from the 5 μg/ml sample contained a higher dc level as well as a peak around 400 Hz. This peak is highlighted in Fig. 4.13 and resulted from the signal modulation as a result of plasma rotation [15]. Power line frequencies at 60 and 120 Hz are clearly seen in Fig. 4.13. These line frequencies were present, to varying extents, in all high bandwidth acquisitions.

4.6 Detection limit calculations

Elemental detection limits from individual particles were calculated to show the superiority of individual particle analysis compared with conventional acquisitions. Detection limits were lowered by averaging multiple peaks and further reduction in the detection limit was observed by digitally filtering the averaged peak profiles. Detection limits were calculated for Fe, Cu, and Zn in a steel sample and emission profiles from the individual particles, average of multiple particles, and digitally filtered average of multiple particles are shown in Figs. 4.14 to 4.16. Detection limits (3σ) were calculated based on the peak heights and the background noise was calculated by taking the standard deviation of 16 points from the baseline. These figures show the dramatic improvement

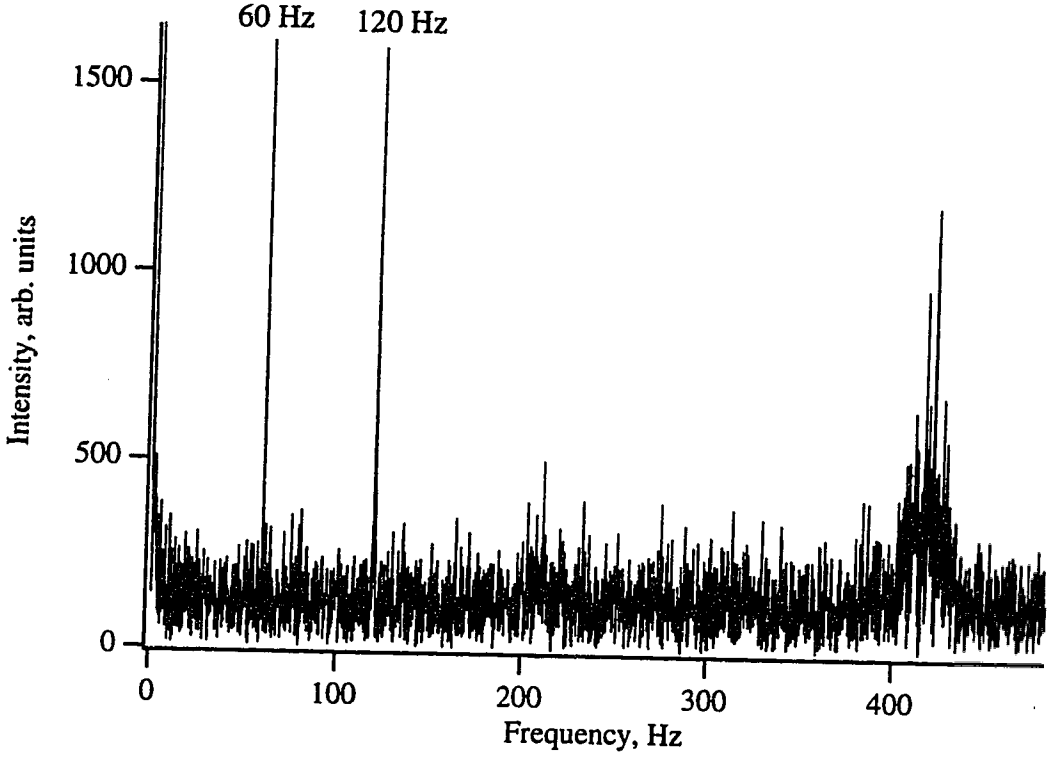

Fig. 4.13 Expanded portion of frequency spectrum shown in Fig. 4.12a.

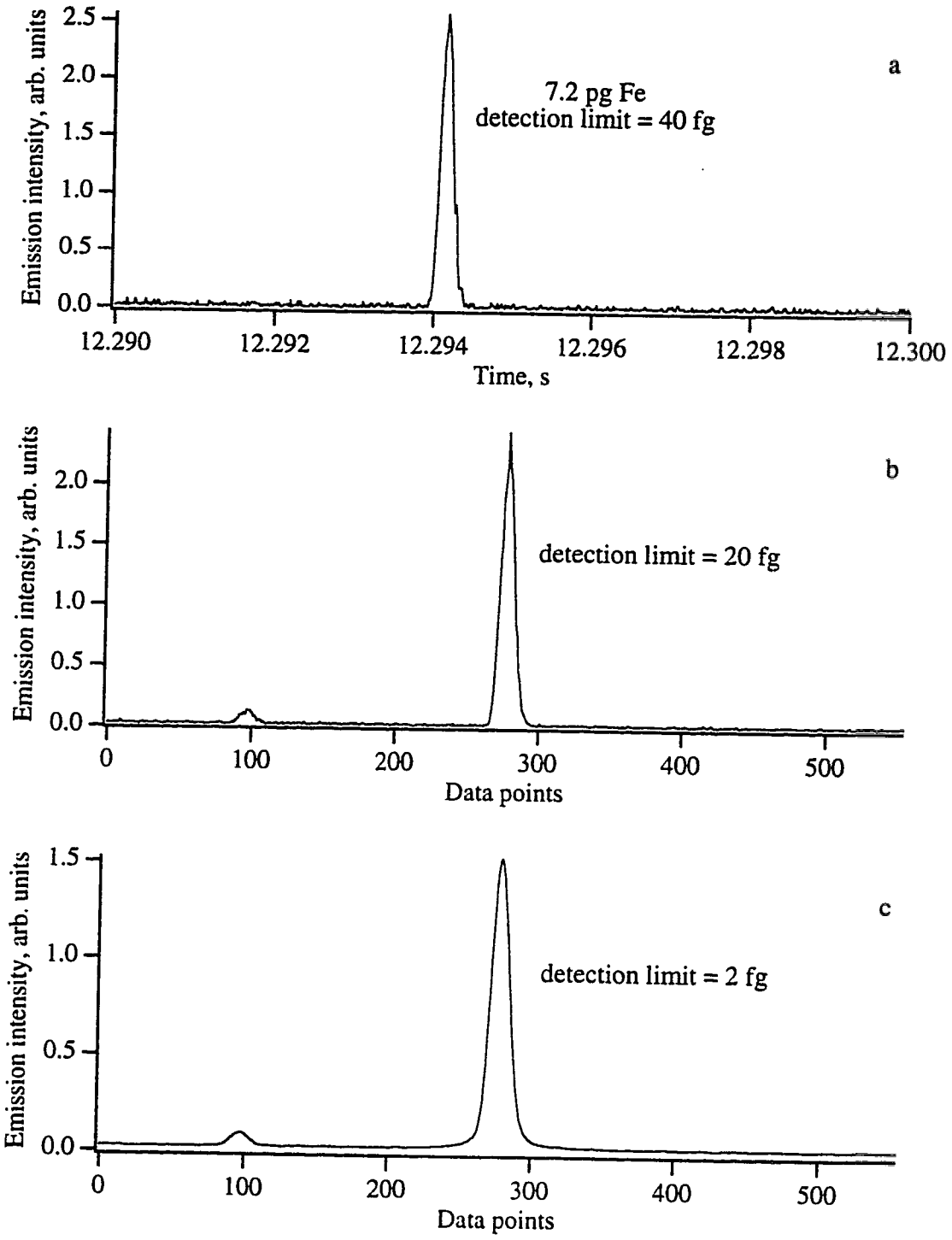

Fig. 4.14 Emission profiles of Fe in steel, SRM 1261a, single particle profile (a), average of 10 profiles (b), and digitally filtered average profile (c).

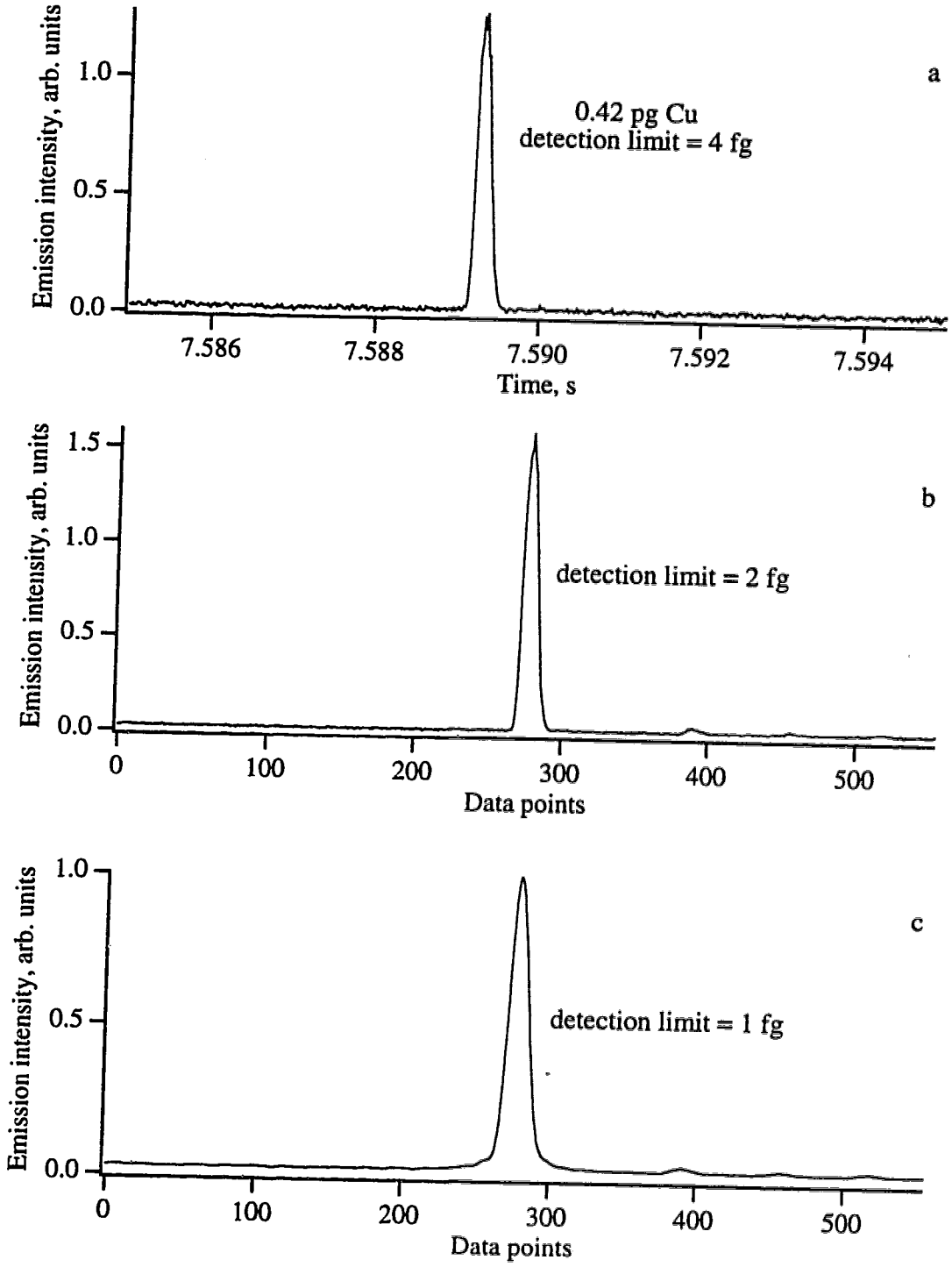

Fig. 4.15 Emission profiles of Cu in steel, SRM 1261a, single particle profile (a), average of 5 profiles (b), and digitally filtered average profile (c).

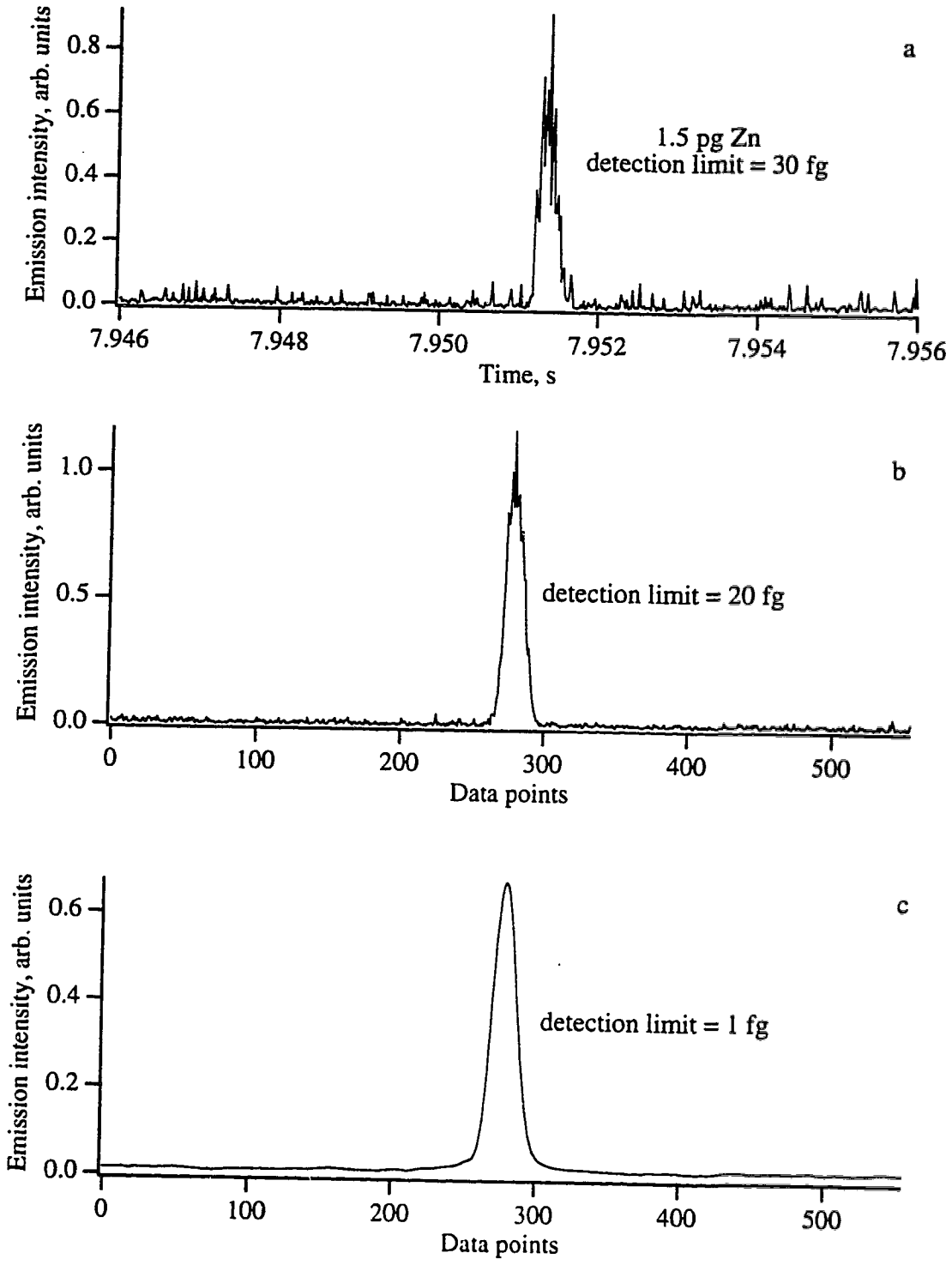

Fig. 4.16 Emission profiles of Zn in steel, SRM 1261a, single particle profile (a), average of 6 profiles (b), and digitally filtered average profile (c).

Table 4.5 Summary of detection limits obtained by different methods.

Element	Conc. in solid sample % w/w	Detection Limit			
		Single peak	Peak ave.	Filtered peak	Solution Introduction
Fe	95.6	40 fg	20 fg	2 fg	40 pg
Cu	0.042	4	2	1	20
Zn	0.0001	30	20	1	30

in the signal to noise ratio which is achieved by peak averaging and digital filtering. Results are summarized in Table 4.5 and the lowest detection limits obtained were 2, 0.6, and 0.8 fg for Fe, Cu, and Zn respectively. These detection limits are believed to be the lowest observed for ICP-AES. Previous work by Kawaguchi *et al.* [16] gave a detection limit of 3 fg of Zn in an individual particle by ICP-MS. By using multiple peak averaging and digital filtering, the results shown in Table 4.5 indicate that ICP-AES can achieve the same sensitivity as ICP-MS for single particle analysis.

A comparison between detection limits obtained by solution nebulization and individual particle analysis is also presented in Table 4.5. Detection limits from single particle analysis were approximately 1000 times lower than from those obtained from solution nebulization. When considering the digitally filtered profiles, detection limits were better than 10,000 times lower compared to solution nebulized samples. This comparison was made to re-emphasize the significant improvements in sensitivity which can be achieved by introducing analyte into the plasma as a single discrete particle.

Using conventional acquisition parameters, it was shown in section 4.5.2 that the detection limit for Fe from a single laser ablation plume was 31 pg. It is obvious that single particle analysis of the laser ablated plume produces a much lower detection limit. As shown in Table 4.5, the detection limit for Fe from a single particle was 40 fg, almost 1000 times lower than the detection limit obtained by considering the entire emission profile from a conventional analysis.

4.7 Cu emission from a steel sample

A detailed study was done of the emission profile of Cu (0.042% w/w) in a steel sample. This emission profile has already been shown in Fig. 4.8b. The mass of Cu

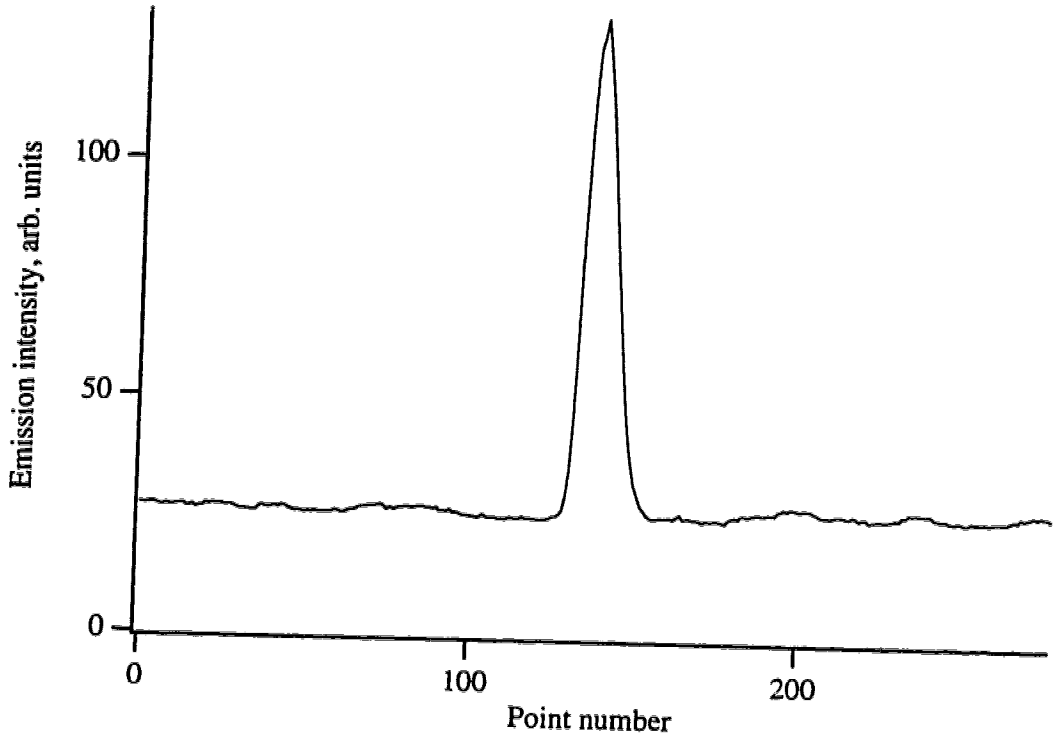

Fig. 4.17 Sum of 649 individual emission profiles of Cu in steel, SRM 1261a.

detected in this emission profile was calculated to be 160 pg by integrating the entire profile, correcting for the background emission, and calibrating it against a solution standard. To determine how much of this total mass could be accounted for by the observed particle emission, all detectable emission peaks were summed. In total, 649 peaks were summed and this summation is shown in Fig. 4.17. Calibration of this summed peak gave a mass of only 62 pg. There is, therefore, 93 pg of Cu which are unaccounted for by considering the observed particle emission. To help explain this discrepancy, the particle size at the detection limit of the measurement system is discussed below.

The detection limit for a single particle of Fe from a steel sample (95.6% Fe) has already been determined to be 40 fg. Determining a particle size based on this detection limit gave a particle size of 0.2 μm. By observing Fig. 3.5, it is obvious that a particle size of 0.2 μm can be transported with high efficiency to the plasma. Also, Fig. 3.4 indicated that laser ablation produces many particles in this size range. Therefore, the unaccounted mass of Cu from the emission profile of Fig. 4.8b can be explained by considering the detection limit of the measurement system. The detection of Cu is simply not sensitive enough to detect the majority of the particles reaching the torch. In this study, undetected particles simply add to the background noise of the emission profile. This will be shown in the following section.

4.8 Correlation of particle emission and baseline noise

The previous section suggested that particles which were too small to be detected would add to the baseline noise. Since the majority of particles were detected within the first 6 s of the emission profile, it is reasonable to assume that the background noise would be largest during this time frame. This is illustrated in Figs. 4.18-20 which show

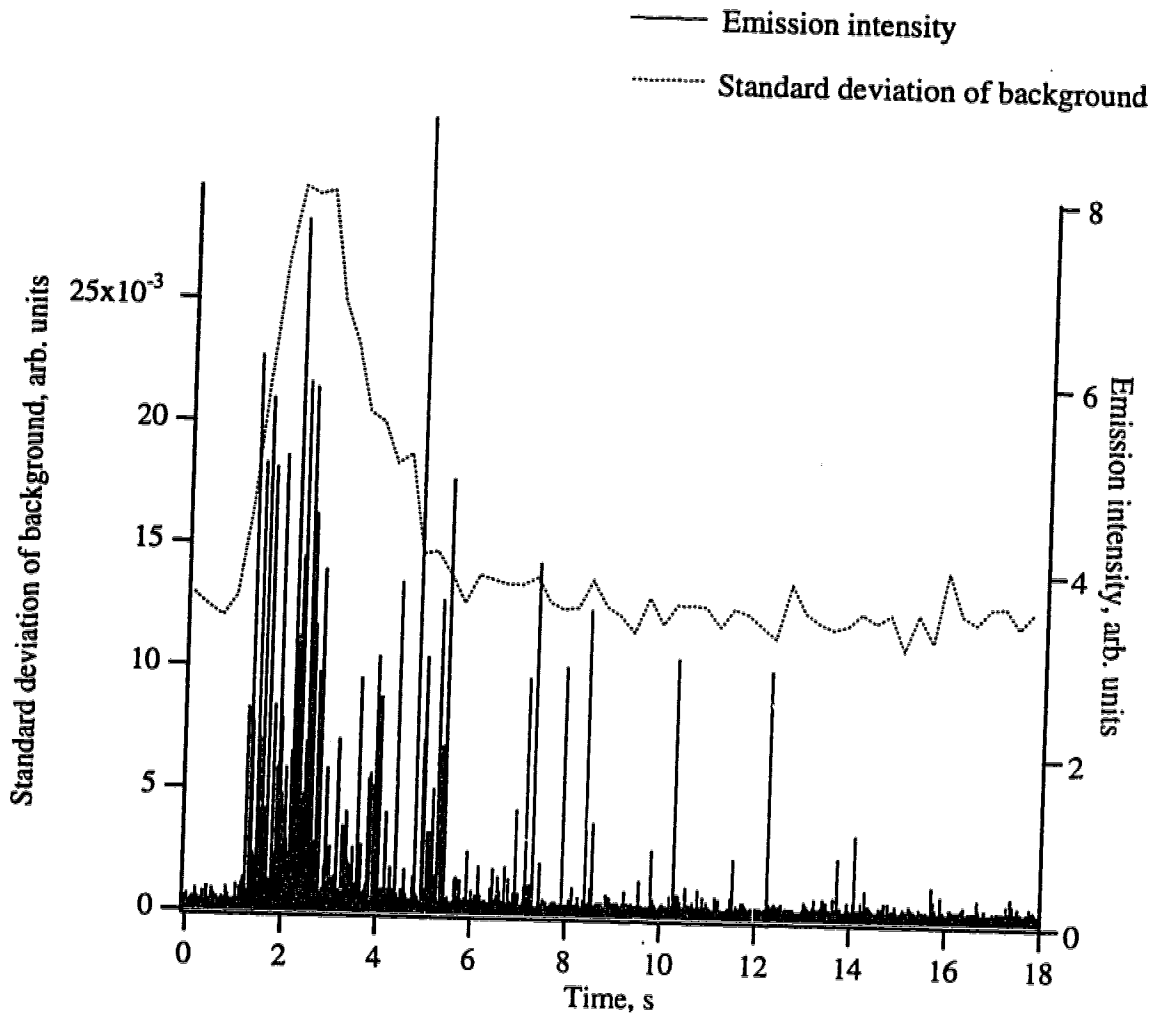

Fig. 4.18 Correlation of baseline noise with emission profile of Fe in steel, SRM 1261a.

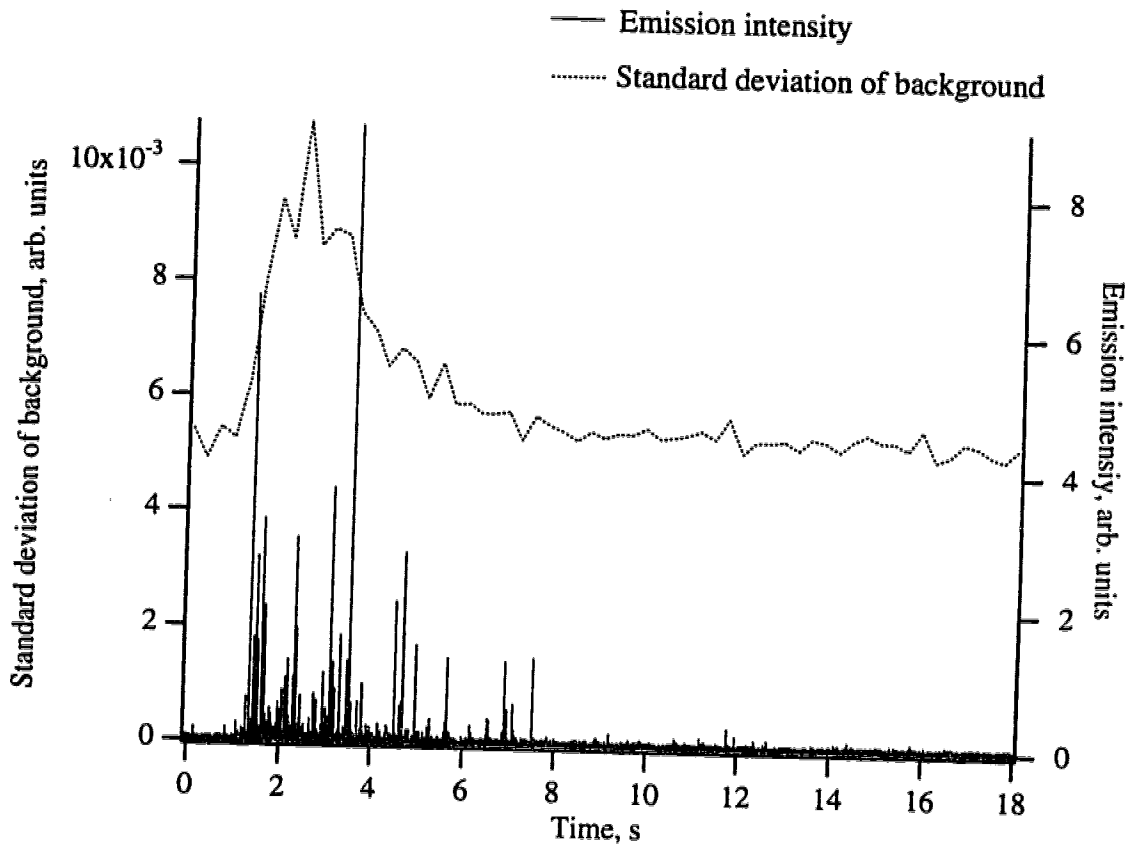

Fig. 4.19 Correlation of baseline noise with emission profile of Cu in steel, SRM 1261a.

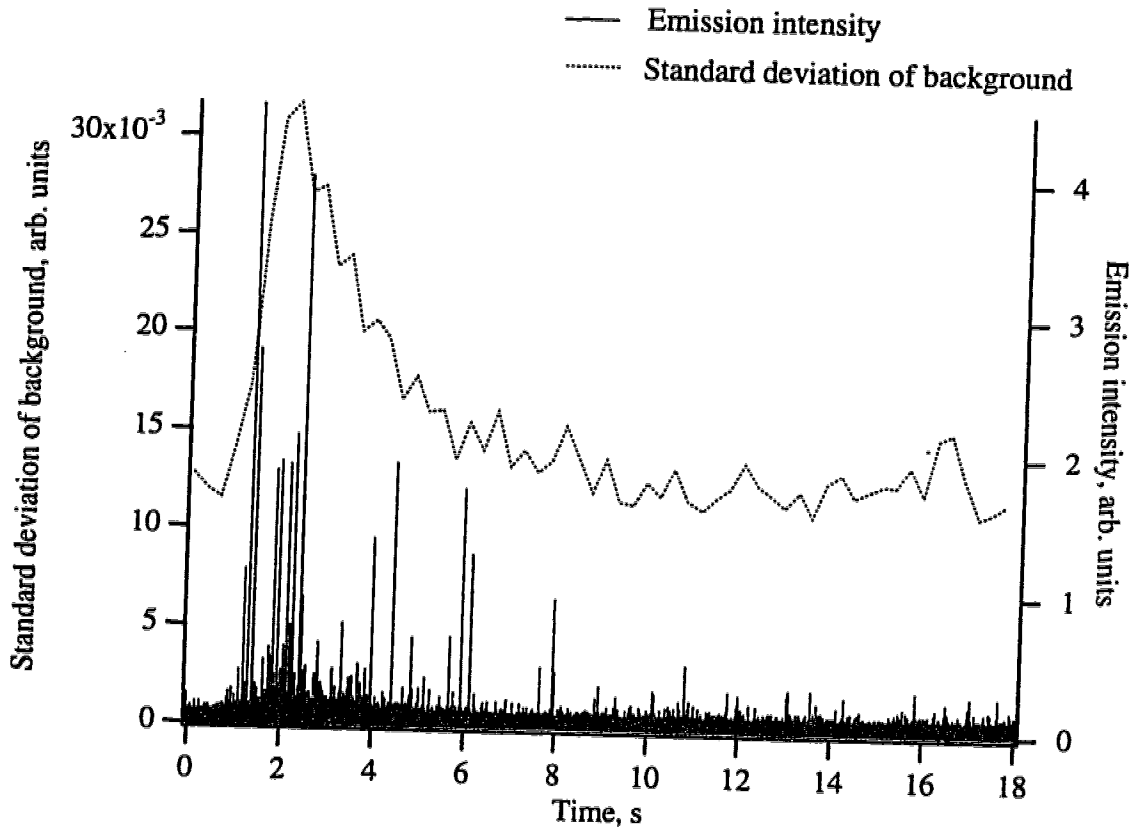

Fig. 4.20 Correlation of baseline noise with emission profile of Zn in steel, SRM 1261a.

how the baseline noise was correlated with the particle emission. A sharp increase in the baseline noise was observed when the frequency of particle emission was largest. The baseline noise was measured over 768 points (13.8 ms) as the standard deviation in the baseline.

The baseline noise profile affects which peaks should be averaged when multiple peaks are averaged to improve detection limits. Emission peaks should be chosen where the baseline noise is at a minimum so that the averaged profile has the highest signal-to-noise ratio. This, however, will exclude most of the peaks since the baseline noise is highest when the frequency of particle emission is greatest. For section 4.6, the averaged emission peaks came from regions which had the lowest background noise.

The baseline noise profile also has implications relating to the previous section which stated that there was a significant amount of analyte which was undetectable as particle emission. The particles are present but are simply too small to be detected and their emission adds to the baseline noise. This is confirmed by the noise profiles shown in Figs. 4.18-20.

4.9 Baseline shifts as a result of undetected particle emission

If enough undetected particles are present in the emission profile, it is reasonable to assume that the baseline would shift upwards during the time of maximum particle emission frequency. This is observed in Fig. 4.21 which shows unresolved particle emission from both a major and minor element in a sample matrix. An emission profile of Cu in a brass sample is shown in Fig. 4.21a and a profile of Cu in a steel sample is shown in Fig. 4.21b. Both of these profiles were collected from the first laser pulse on a fresh surface. The first few laser pulses on a fresh surface are known to ablate much

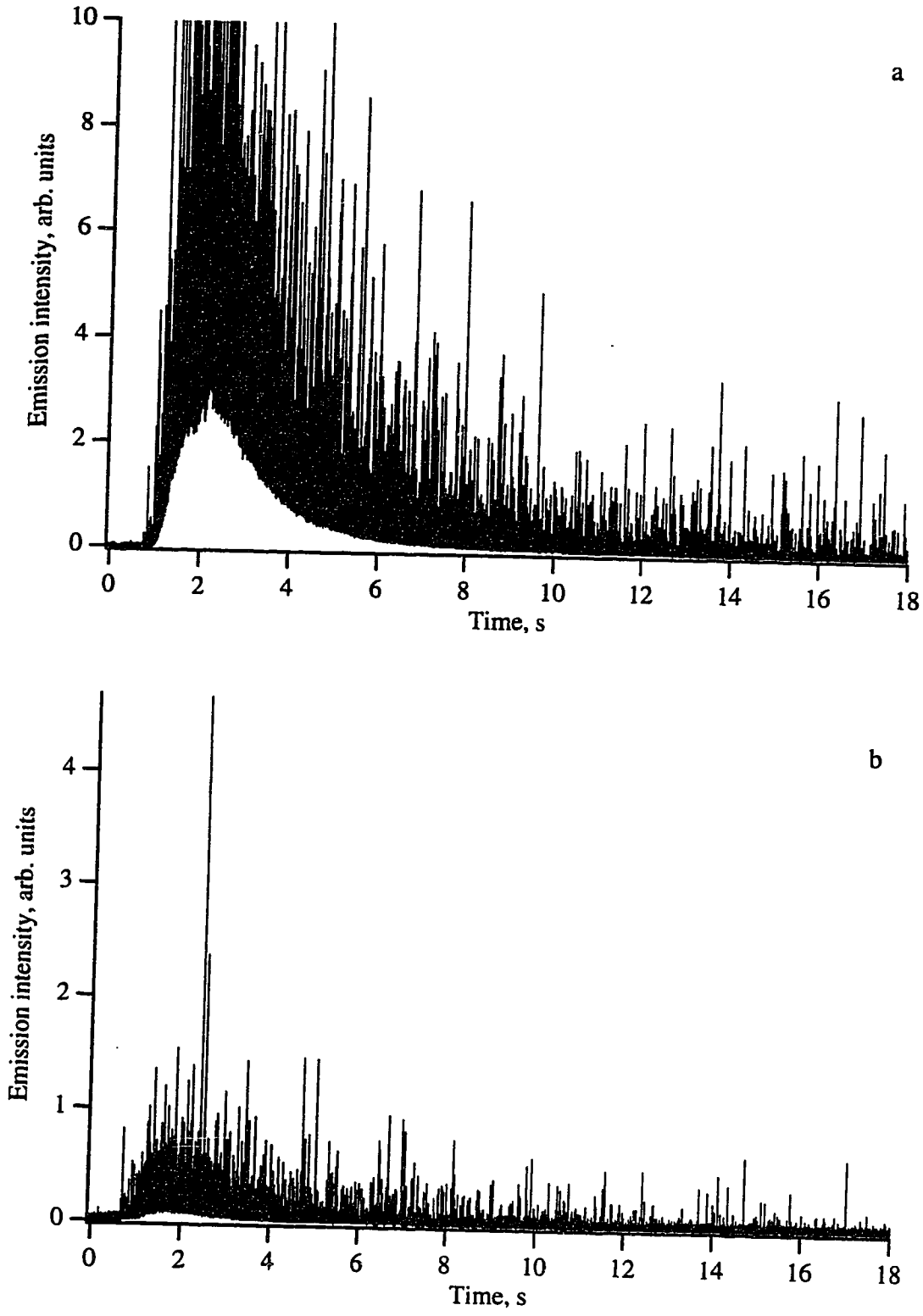

Fig. 4.21 Observation of baseline shifts due to an abundance of unresolved particles. Emission profile of Cu in brass, SRM C1106, (a) and Cu in aluminum, Alcoa SS-380-6, (b).

more material than later pulses and this was confirmed in this study. Emission from many small particles, which were too small to be independently resolved, caused the baseline to shift upwards. This effect was also observed for elements other than Cu. This was also observed for Fe in a steel sample, Zn in a brass sample, and Al in an aluminum sample.

Shifts in the baseline are undesirable for techniques such as particle counting and the determination of particle size distributions. Computer software routines can be used to automatically count all peaks above a user defined threshold level. However, baseline shifts would preclude the use of such techniques. It would also be difficult to calculate particle size distributions based on peak height determinations since corrections would have to be made for the shifting baseline. Particle size distributions are calculated in the next section from emission profiles which did not have shifting baseline levels.

4.10 Particle size distributions

Particle size distributions provide important information regarding the ablation event and subsequent transportation of the ablated particles to the ICP. Two particle size distributions are shown in Fig. 4.22. The original emission profiles for Figs. 4.22a and b have already been shown in Figs. 4.3a and 4.7a respectively. Fig. 4.22a was generated from an emission profile of Fe in steel and Fig. 4.22b was generated from the emission profile of Al in an aluminum sample. Particles were identified by using a software technique which found all peaks above a user-defined threshold level. The threshold level was chosen so that the software program would find the most emission peaks while discriminating against noise peaks. Particle sizes were determined by multiplying the peak heights by an appropriate conversion factor which had been determined based on solution calibration.

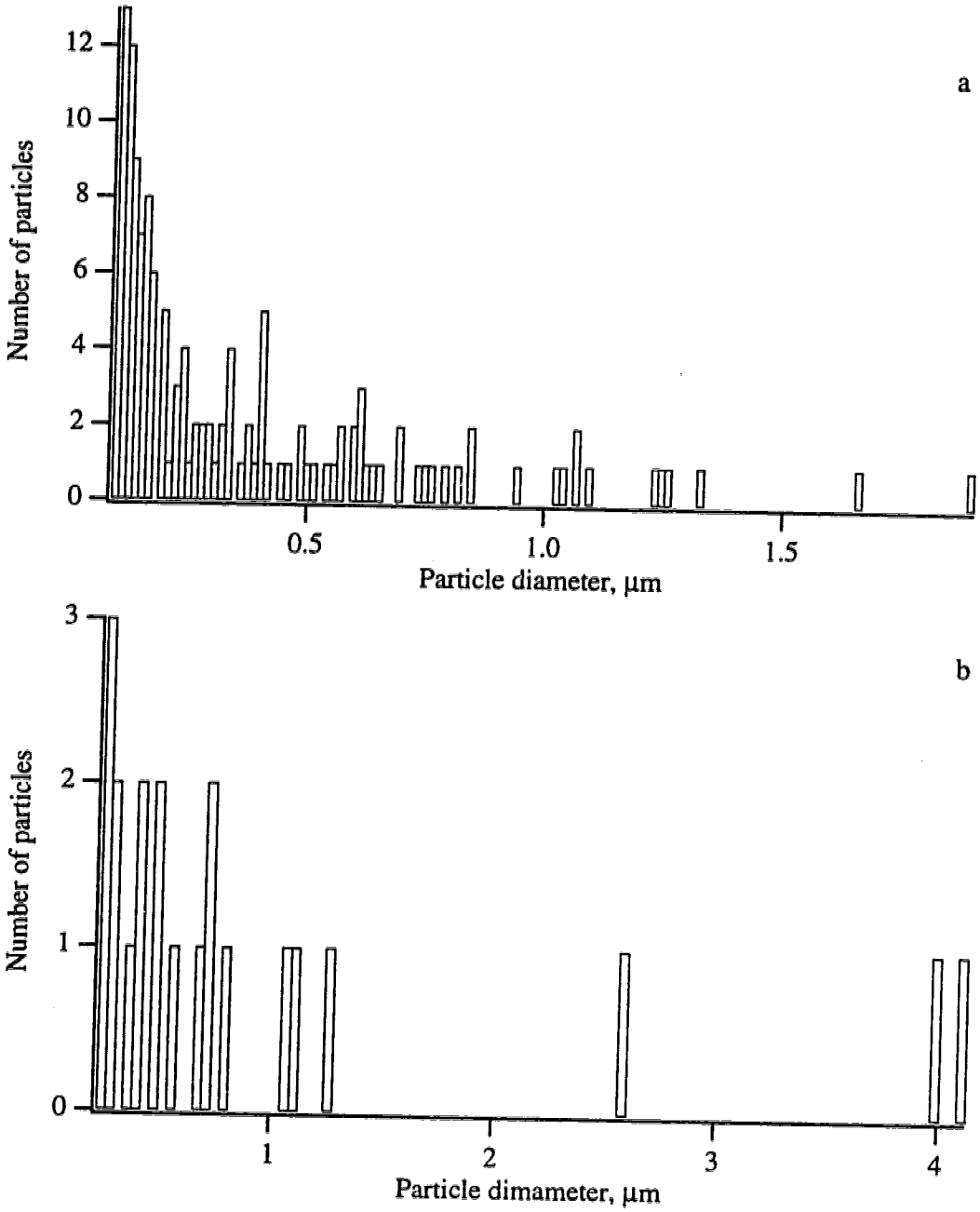

Fig. 4.22 Particle size distributions for Fe in steel, SRM 1261a, (a) and Al in aluminum, Alcoa SS-380-6 (b).

Comparing Fig. 4.22a to 4.22b, significant differences are observed. A total of 131 peaks were used to construct the distribution of the Fe particles, while only 21 particles were used for the Al distribution. This difference could be related to the differences in laser-material interaction between steel and aluminum. Simply stated, the laser ablation of the steel sample could result in more particles being produced when compared to the aluminum sample. However, no reports of this type of matrix effect have been recorded in the literature and this explanation seems doubtful.

Another way of explaining the difference in particle numbers is to consider the relative gain used to acquire each profile. The gain for the Fe acquisition was 10 times higher than the gain for the Al acquisition. This means that more particles will be detectable for the Fe distribution. The amplifier gains were chosen to maximize the intensity of the emission peaks while still keeping them in the range of the ADC. This implies that the particle sizes for the Al profile were larger than the particle sizes observed for the Fe emission profile, and this is confirmed by observing the particle size distributions shown in Fig. 4.22. Even if the particle size distribution between Fe and Al were identical in the ablation chamber, it is still reasonable to assume that larger Al particles will be transported to the ICP than Fe particles. This assumption is made by considering the density of Fe and Al. The density for Fe is 7.86 g/cm^3 while the density of Al is only 2.70 g/cm^3. This means that the transportation efficiency of large particles will be greater for Al than for Fe since fewer Al particles will settle out of the flowing Ar stream by gravitational deposition.

Consideration of particle size distributions is important when choosing ablation chambers, Ar flow rates, and dimensions of the connective tubing. The transportation efficiency profile, as shown in Fig. 3.5. will be shifted towards larger particles as the particles become less dense. This means that smaller diameter connective tubing, which

favors the transportation of larger particles, could be used when transporting particles with a lower density. Consideration of the particle's density and the particle size distribution at the ICP will result in more efficient transportation of the laser ablated plume.

4.11 Simultaneous multi-element determinations

The most significant aspect of multi-element analysis, as related to LA-ICP-AES, is its ability to determine whether the elemental concentrations within individual particles correspond to the elemental concentrations of the bulk sample. Insight into the enhanced emission of selected elements [17] is gained by an understanding of the elemental concentrations within individual particles. Justification of the relatively large particle sizes for minor elements found in a steel sample will also be presented. This section presents multi-element analysis, on an individual particle basis, for solid samples of steel and stainless steel.

4.11.1 Instrumentation

Multi-element emission spectra were collected on a 4 channel digital storage oscilloscope. The output of the PMTs were fed directly into the 1 MΩ input of the scope, bypassing the current-to-voltage amplifier used for single channel acquisitions. Emission profiles were multiplied by -1 so that they would be seen as having positive peaks. All channels of the scope were triggered simultaneously and the scope allowed for flexible triggering conditions. For example, in a multi-element analysis the scope could be set up to trigger off of the emission event of a specific element. In that way, difficult to observe scenarios could be captured.

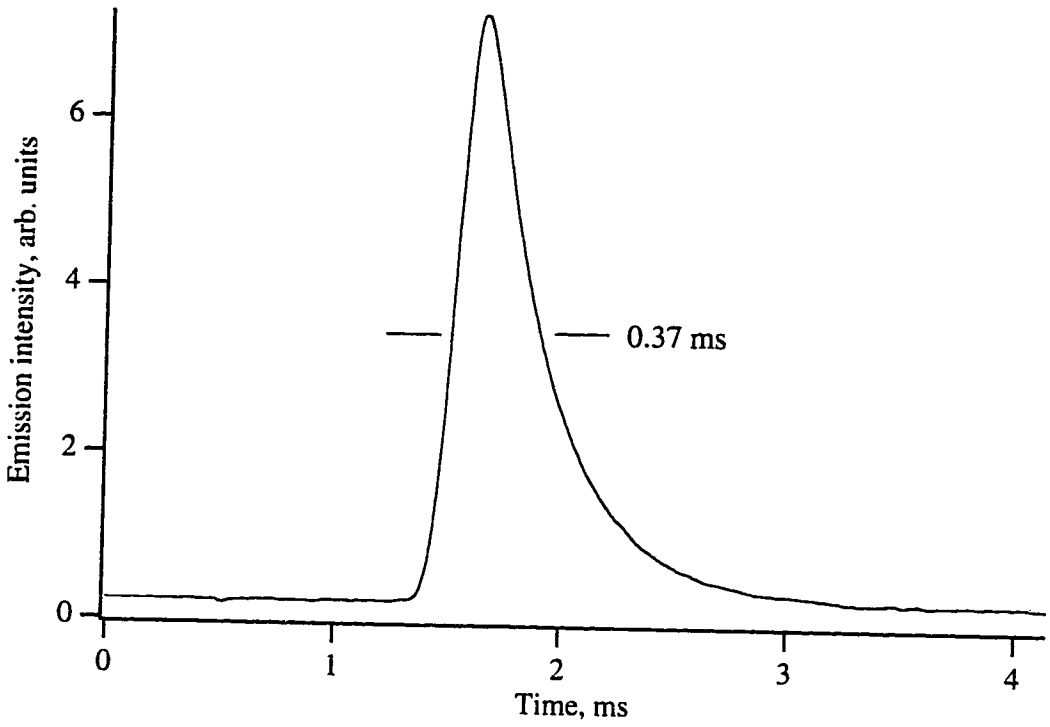

Fig. 4.23 Emission profile of a single Fe particle showing poor response of the digital oscilloscope with a 1 MΩ input.

An emission pulse from a single Fe particle was detected with the oscilloscope and is shown in Fig. 4.23. This emission profile reveals a lower acquisition bandwidth than the single channel acquisition provided by the current-to-voltage amplifier in combination with the data acquisition board. The peak shape has been altered by the acquisition electronics and is significantly wider than the previously shown peaks from particle emission. The FWHM is 0.15 ms longer than the profile shown in Fig. 4.4a and significant broadening of the peak is observed at the baseline. Because of these concerns, the 4-channel scope was only used to acquire simultaneous multi-channel profiles and was not used to access peak shape information.

4.11.2 Simultaneous multi-element emission profiles

As mentioned, multi-element acquisitions on a particle-to-particle basis determine whether the individual particles have the same elemental composition as the bulk sample. This information can give insight into enhanced emission effects of selected elements. In this section, simultaneous multi-element emission profiles are shown from two different samples.

A multi-element emission profile produced from the laser ablation of a stainless steel sample is presented in Fig. 4.24. This figure represents only a small portion of the original emission profile. The original profile consisted of 32,768 points (the scope maximum) digitized at a rate of 0.2 ms/point. This gave a total acquisition time of 6.6 s. For this profile the laser was fired at a continuous rate of 1 Hz, providing a steady stream of particles to the ICP. Simultaneous emission profiles from Cu, Cr, and Fe are presented in Fig. 4.24. These profiles clearly show particle-to-particle heterogeneity. For example, there is no associated Cr and Fe emission pulse which correlates with the Cu emission pulse at approximately 3.6 s. Also, there is no associated emission pulse for Cu which

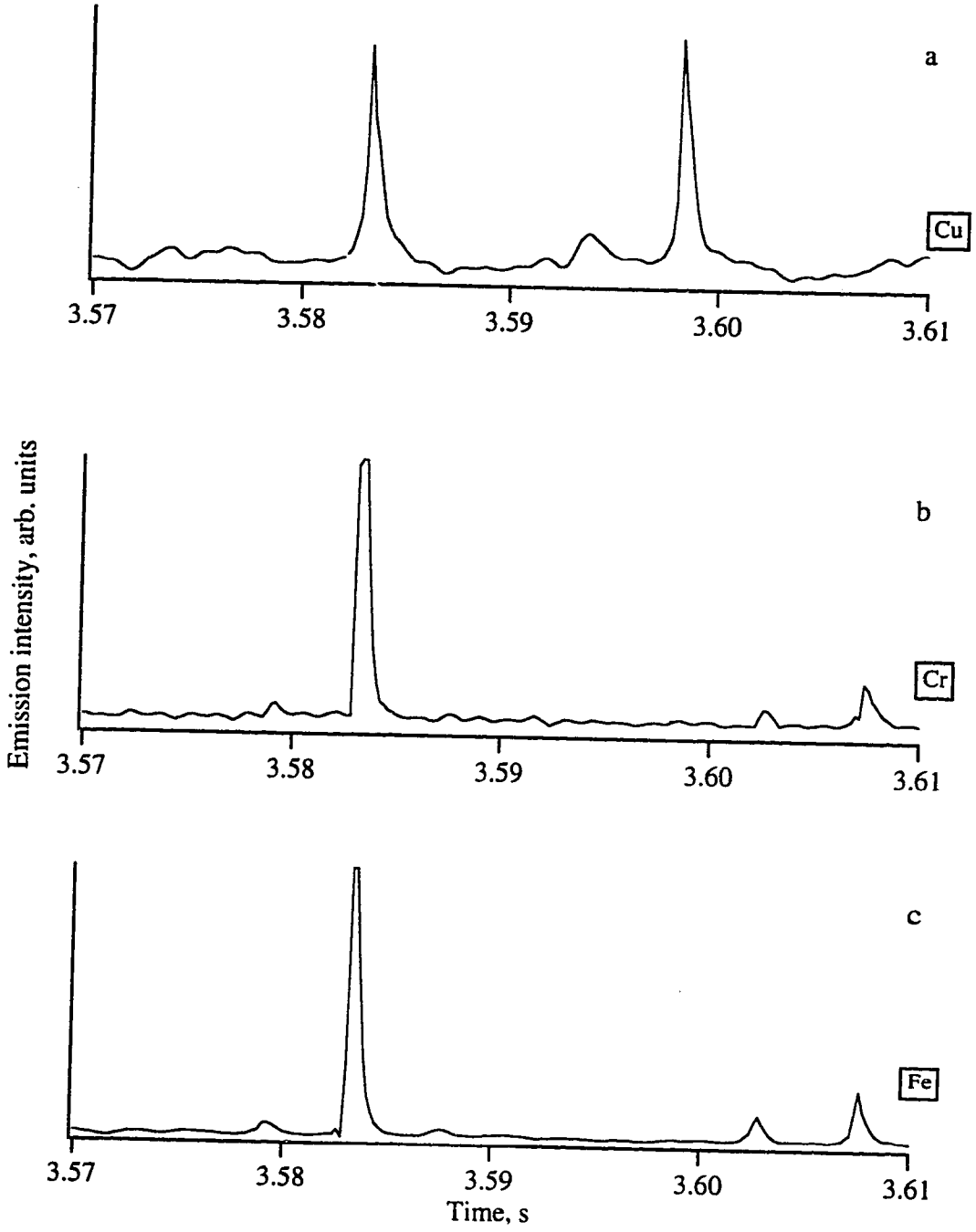

Fig. 4.24 Simultaneous multi-element emission profiles of Cu (a), Cr (b), and Fe (c) from stainless steel, SRM 1171.

correlates with the two emission peaks seen for Cr and Fe between 3.60 and 3.61 s. Thompson *et al.* [13] have demonstrated particle heterogeneity from a stainless steel sample over only a 3 ms time frame and with only 2 particles. The acquisition, only partially represented in Fig. 4.24, was over a much longer time frame and a correlation analysis was performed which quantified the degree of particle heterogeneity. This correlation analysis is presented next.

Cross correlation is a mathematical method which is used to determine the similarity between two sets of data. Given two sets of digitized values, represented by two arrays, the mathematical operation can be explained as follows. Assume array (a) is fixed in position and array (b) is moved from the left to the right across array (a) step by step. The sum of all products, corresponding to where array (a) and array (b) are overlapped, forms array (c). Array (c) contains 2n-1 points where n equals the number of points contained in array (a) and (b). The point in array (c) which corresponds with the maximum degree of overlap between array (a) and (b) is referred to as the $\tau = 0$ point. To make comparisons between successive correlations, arrays (a) and (b) must be normalized before performing the cross correlation. The arrays are normalized by subtracting the mean of the array and dividing by the standard deviation. For identical arrays which have been normalized, the $\tau = 0$ point in the correlation function is equal to the number of data points in the original arrays.

Cross correlations of the emission profiles in Fig. 4.24 are presented in Figs. 4.25-26. The entire correlation functions are shown in Fig. 4.25 for the correlation of emission profiles for Fe to Cr, Fe to Cu, and Cu to Cr. Fig. 4.26 is simply an expanded view of the data shown in Fig. 4.25. The values of $\tau = 0$ for the cross correlation of Fe to Cr, Fe to Cu, and Cu to Cr are 30,269, 8068, and 7726 respectively. This implies that Fe and Cr are almost perfectly correlated, being present together in nearly all the particles in the

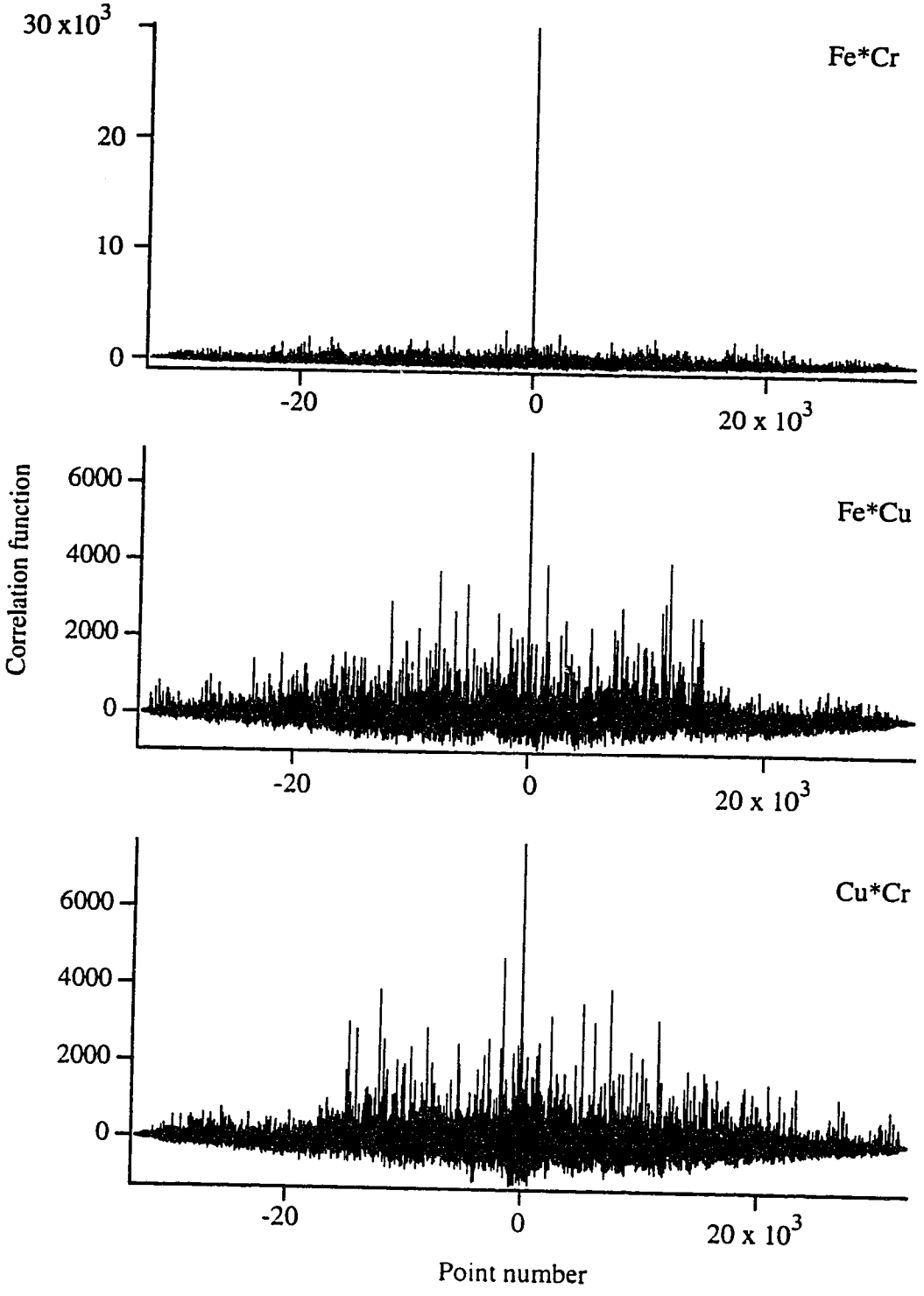

Fig. 4.25 Cross correlation functions from emission profiles of Fe, Cu, and Cr.

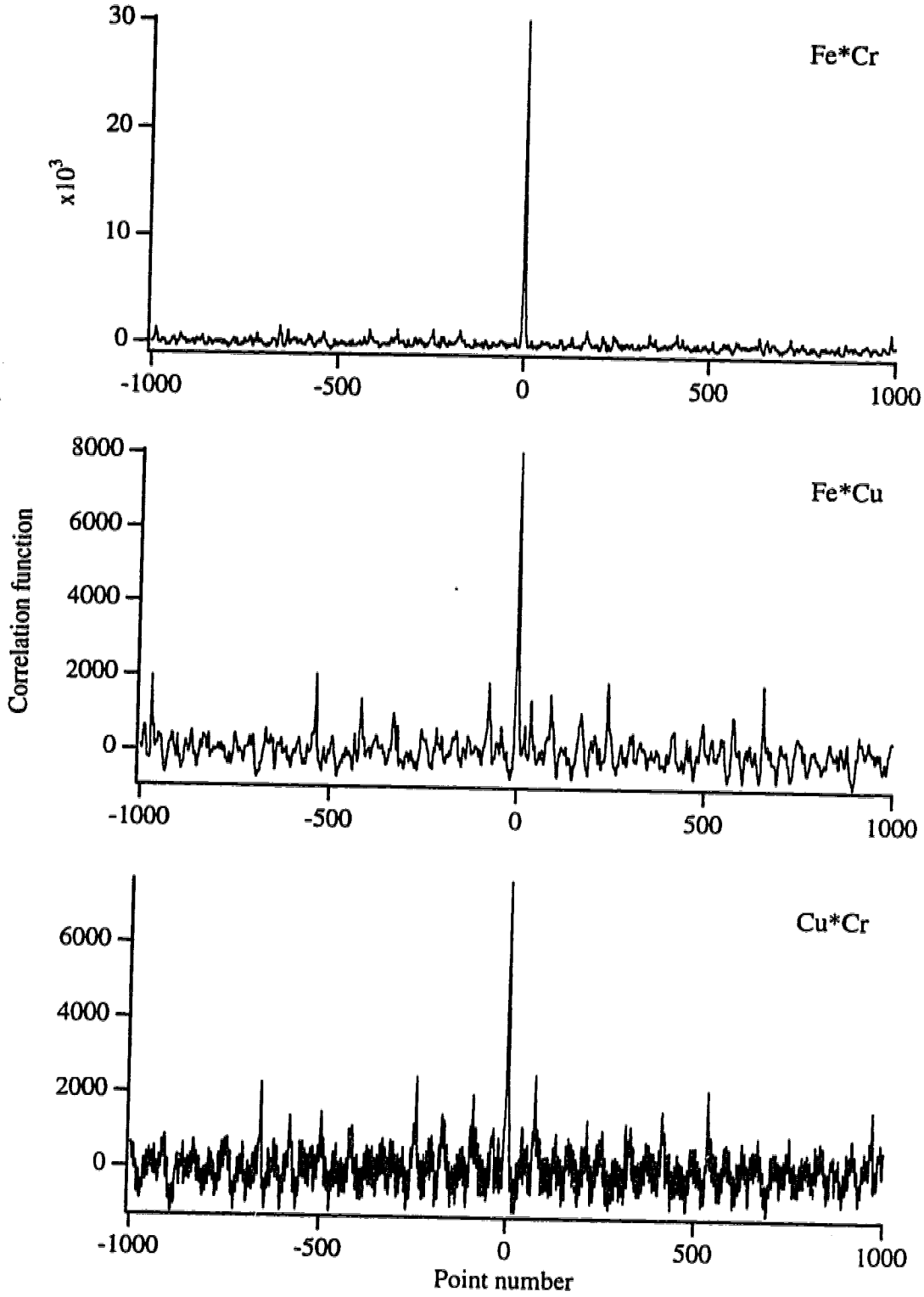

Fig. 4.26 Expanded view of the cross correlation functions shown in Fig. 4.25.

original emission profile. A perfect correlation would result in a $\tau = 0$ value of 32,768, which is the total number of data points in the emission profile. Very poor correlation exists for Fe to Cu and Cr to Cu, implying that Cu was present in particles independent of the presence of Fe and Cr. This has been explained by Thompson et al. [18] who stated that inclusions can be preferentially mobilized into the ablation melt at discrete times within the train of laser pulses. These inclusions contain crystal grains of elements. Therefore, the composition of the material ejected from the solid sample can vary with time and this has been confirmed by the correlation functions presented in this study. A more thorough multi-element investigation on a particle-to-particle basis would provide greater insight into the number of different particles present in the laser ablation plume and would give information regarding the metallurgy of the solid sample. Clearly, a more detailed study would be possible if a large number of elemental profiles could be determined simultaneously.

Simultaneous multi-element emission profiles were also collected from a steel sample and are shown in Figs. 4.27-28. This is the same steel sample which was used previously to determine detection limits for Fe, Cu, and Zn. The mass of Cu and Zn contained in an individual particle has been shown in Figs. 4.15a and 4.16a to be 0.42 and 1.5 pg respectively. However, the concentration of Cu and Zn in the steel sample was only 0.042 and 0.0001% respectively. Therefore, it is impossible for these particles to have the same elemental concentrations as found in the bulk sample since the particle sizes would then be ridiculously enormous. This apparent inconsistency is resolved by the multi-element emission profiles shown in Figs. 4.27-28, which show at least four different types of particles. A particle which contains only Fe and not Cu or Zn is shown at the 15 ms mark of Fig. 4.27a. Similarly, a particle which contains only Cu is shown at the 15 ms mark of Fig. 4.27b. A particle which contains all three elements is located at 15 ms in Fig. 4.28a and a particle which contains Cu and Zn but not Fe is located at 15

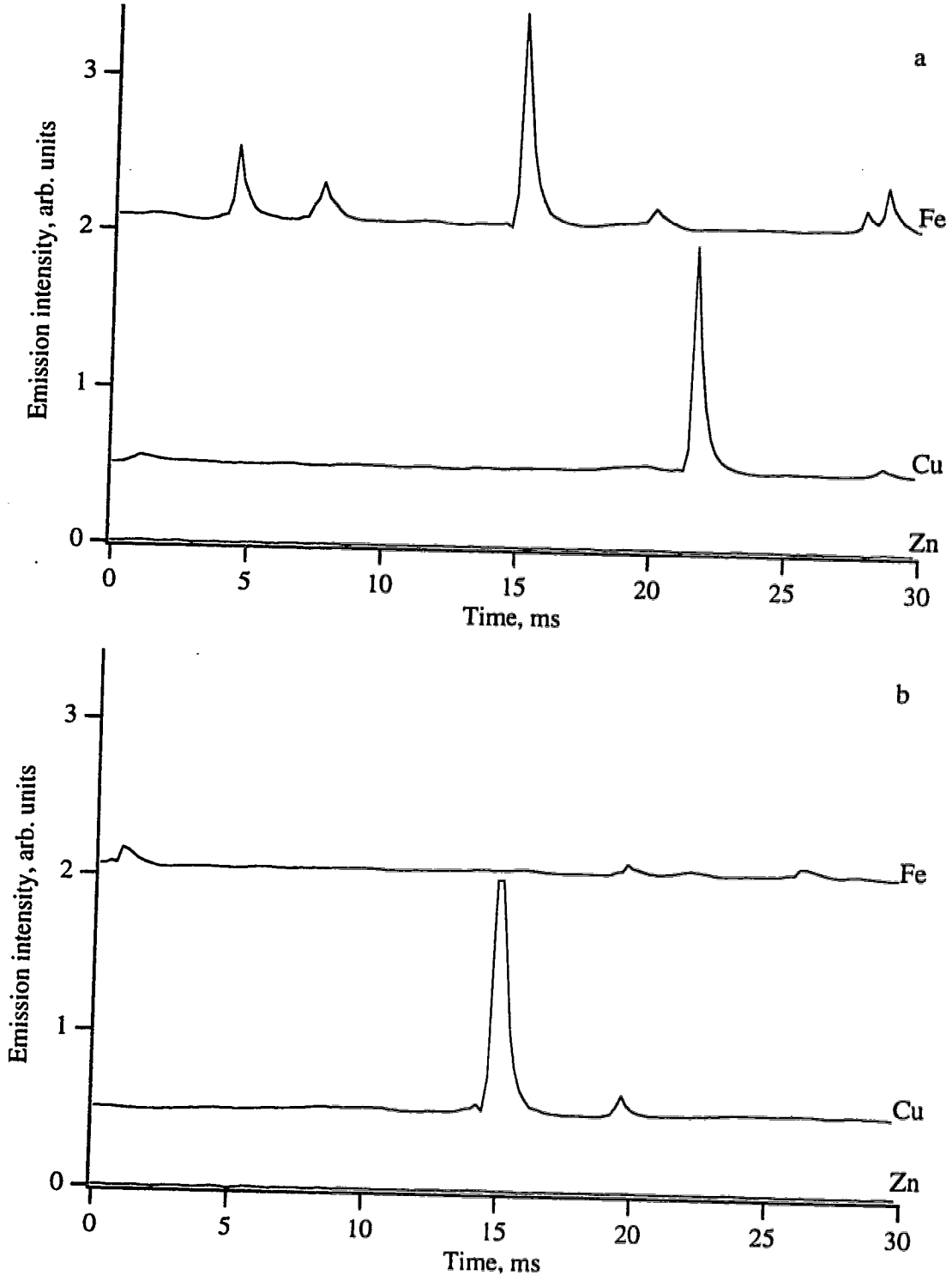

Fig. 4.27 Simultaneous multi-element emission profiles (a) and (b) of Fe, Cu, and Zn from steel, SRM 1261a.

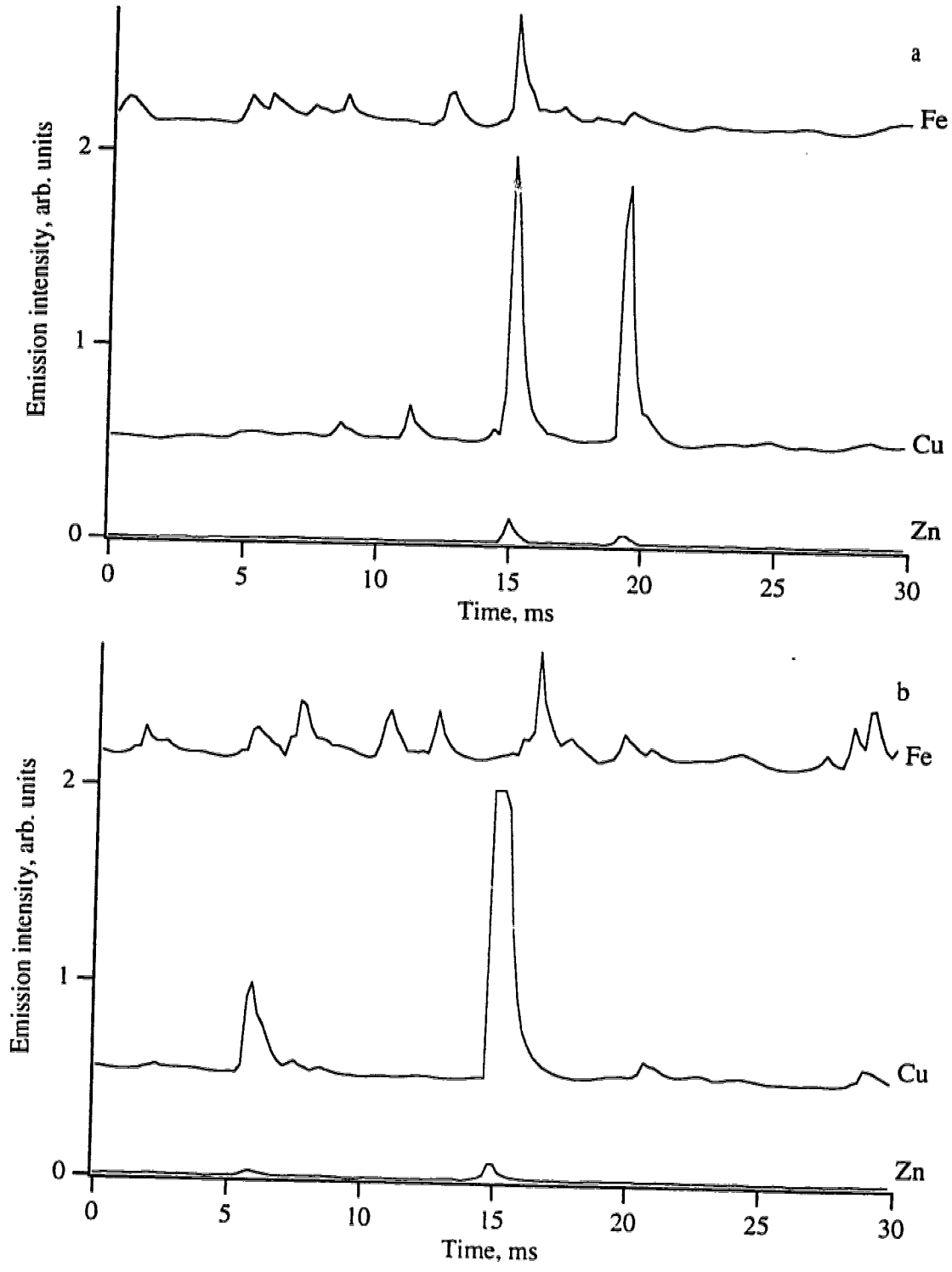

Fig. 4.28 Simultaneous multi-element emission profiles (a) and (b) of Fe, Cu, and Zn from steel, SRM 1261a.

ms in Fig. 4.28b. This shows very clearly that the elemental concentration of the individual particles does not match the concentration found in the sample. Therefore, the particle masses calculated and shown in Figs. 4.15a and 4.16a are justifiable.

4.12 Summary and future direction

Time resolved analysis of individual particles has been shown to greatly improve the mass detection limits for LA-ICP-AES. Multiple peak averaging and digital filtering were used to further improve the sensitivity of the analysis. Insight into the selective enhancement in emission intensities has been gained by constructing particle size distributions and by simultaneous multi-element analysis. Although not illustrated in this chapter, multi-element characterization of environmentally significant particles could be achieved with ICP-AES. This would provide a rapid and efficient means of identifying environmental particles and would be beneficial in their source appointment.

Individual particle analysis from a single laser ablation event has been achieved in a time resolved manner. The data files however are very large, approaching 10 MB for a single channel acquisition. A simultaneous multi-element characterization of a single laser ablation event could be achieved but the digital storage requirements for such an acquisition would be very large. However, recent advances in personal computers and digital storage may make such an acquisition possible on a routine basis. The development of recordable CDs has allowed the storage of up to 650 MB of data, providing mass storage and retrieval of digital data. In the near future, the development of DVD technology may allow up to several GB of digital data storage space. As personal computers become faster and faster, the manipulation of these large data files will become more common.

References

1. M. Thompson, C. Flint and S. Shenery, *J. Anal. At. Spectrom.* **3**, 1133 (1988).
2. M. Thompson, C. Flint, S. Chenery and K. Knight, *J. Anal. At. Spectrom.* **7**, 1099 (1992).
3. E. F. Cromwell and P. Arrowsmith, *Appl. Spectrosc.* **49**, 1652 (1995).
4. M. S. Cresser, J. Armstrong, J. M. Cook, J. R. Dean, R. Watkins and M. Cave, *J. Anal. At. Spectrom.* **10**, 9R (1995).
5. X. Feng and G. Horlick, *J. Anal. At. Spectrom.* **9**, 823 (1994).
6. X. R. Liu and G. Horlick, *Spectrochim. Acta* **50B**, 537 (1994).
7. G. B. King and G. Horlick, *Spectrochim. Acta* **47B**, E353 (1992).
8. J. W. Olesik and S. E. Hobbs, *Anal. Chem.* **66**, 3371 (1994).
9. M. Thompson and M. Hale in: *Prospecting in Areas of Glaciated Terrain*, Institute of Metallurgy Special Publication, London, 225, 1984.
10. L. Moenke-Blankenburg, *Spectrochim. Acta* **15B**, 1 (1993).
11. D. Nore, A. M. Gomes, J. Bacri and J. Cabe, *Spectrochim. Acta* **48B**, 1411 (1993).
12. F. Qin, Pulsed signal fluctuations in ICP-AES. Thesis, University of Alberta (1992).
13. M. Thompson, C. D. Flint, S. Chenery and K Knight, *J. Anal. At. Spectrom.* **7**, 1099 (1992).
14. W. T. Chan and R. E. Russo, *Spectrochim. Acta* **46B**, 1471 (1991).
15. R. M. Belchamber and G. Horlick, *Spectrochim. Acta* **37B**, 17 (1982).
16. S. Kaneco, T. Nomizu, T. Tanaka, N. Mizutani and H. Kawaguchi, *Analytical Sciences* **11**, 835 (1995).
17. E. F. Cromwell and P. Arrowsmith, *Appl. Spectrosc.* **49**, 1652 (1995).
18. M. J. Thompson, S. Chenery and L. Brett, *J. Anal. At. Spectrom.* **5**, 49 (1990).

Chapter 5

Preliminary investigation of axially viewed emission profiles from individual particles

5.1 Introduction

A recent trend in ICP-AES has been to turn the ICP torch on its side and view the emission from an axial perspective. There are presently seven instrument manufacturers who have developed ICP emission spectrometers based on axial viewing of the plasma [1]. In keeping with the trend of axial viewing, this chapter will present time resolved emission profiles from individual particles as viewed axially in the plasma.

The previous chapter described lateral viewing of particle emission and it was shown that the emission profiles did not vary from element to element. There was also no difference in emission profiles for ion emission compared to atom emission and the duration of the emission profile was simply related to the transit time of the vapor plume. Axial viewing of emission from individual particles may provide different information since the emission is observed for a longer time. Axial viewing of analyte emission can begin in the zone located within the ICP load coil and can extend well into the recombination zone of the plasma. As a consequence of this long observation time, it can be assumed that axially viewed emission profiles from individual particles will provide information concerning a particle's vaporization, atomization, ionization, and emission characteristics. Axial viewing of the plasma could also lead to lower detection limits for particle analysis and detection of a broader particle size distribution.

It is also anticipated that the temporal emission profile from individual particles will clarify the spatial characteristics of analyte emission. Vertical emission profiles of analyte elements in the axial channel of the ICP have been constructed when introducing the analyte by solution nebulization [2-7]. These results have lead to a greater fundamental understanding of the ICP and have allowed analysts to optimize experimental conditions used for routine analysis. Introduction of the analyte into the ICP by solution nebulization results in a range of particle sizes, based on the size distribution of droplets exiting the spray chamber. Since particles of different sizes will have different spatial emission characteristics, the emission profiles generated from solution nebulized samples may not accurately reflect plasma conditions when acquired in a time-integrated manner. This chapter presents the axial emission profiles from individual particles in a time resolved manner.

5.2 Axial viewing of ICP emission

Axial viewing of the emission from the ICP requires simple mechanical changes to conventional lateral viewing and a schematic representation of an axially viewed plasma is presented in Fig. 5.1. The torch is positioned horizontally and the central axis of the plasma is optically aligned with the entrance slit of the spectrometer. An air cutoff stream is positioned past the tip of the plasma to protect the optics from thermal damage and to remove cooler absorbing atoms from the tail plume of the plasma. A circular aperture is placed in front of the entrance slit to remove unwanted background emission. Although axial viewing of the ICP was first studied in 1976 [8], it took almost twenty years for this feature to become commercially available. Axial viewing of the plasma has not been studied as thoroughly as lateral viewing, but it has been the subject of several reports [9-11].

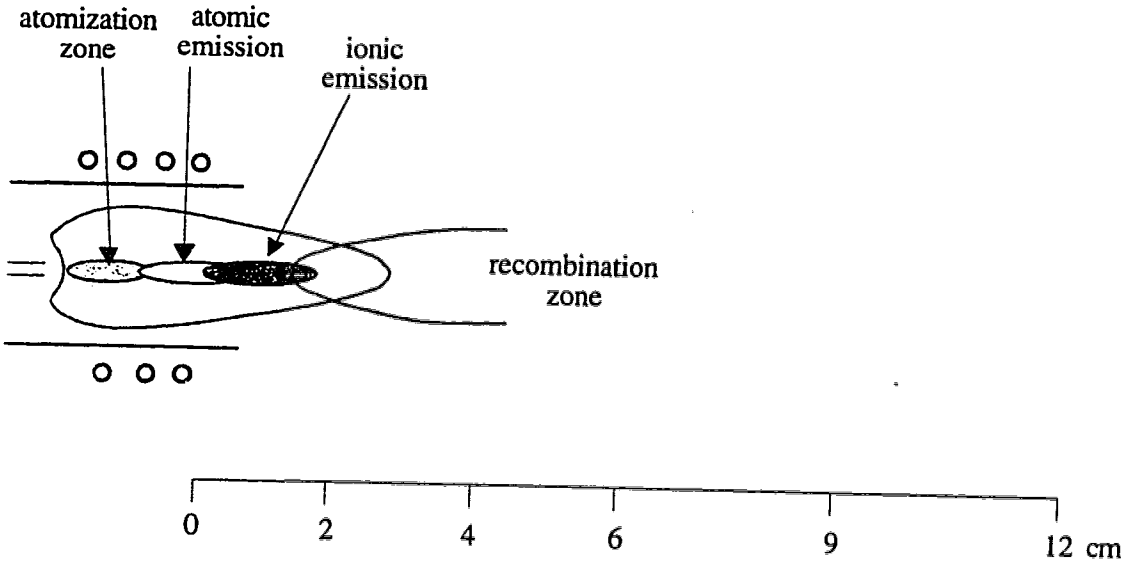

Length of the plasma as determined by the position of the air cutoff stream.

Fig. 5.1 Schematic of axially oriented ICP.

There are a number of advantages to viewing the ICP axially as opposed to laterally. The vertical extent of the plasma which is observed for axial viewing is determined primarily by the depth of field of the optical system and the position of the air cutoff stream. This is unlike lateral viewing, where the observed height of the plasma is determined by the spectrometer slit height. Therefore, the use of axial viewing is aimed at improving the efficiency of the observation of the central channel of the ICP. Since analyte emission is observed over a larger spatial region, lower detection limits are achieved. Detection limits have been lowered by 2 to 10 times for axial viewing of plasma emission. Compromised conditions are required for the lateral acquisition of simultaneous multielement determinations of 'hard' and 'soft' emission lines. This occurs since the 'soft' emission lines are most intense low in the plasma while the 'hard' lines are most intense higher in the plasma. However, since the spatial region observed by axial viewing is larger than for lateral viewing, simultaneous emission from 'hard' and 'soft' lines is possible without using compromised conditions. The linear dynamic range observed for axial viewing is comparable to what is achieved for lateral viewing. The linear range is shifted towards lower values since the sensitivity of axial viewing is improved.

The greatest limitation of axial viewing is the decrease in the robustness of the ICP system. One of the greatest advantages of ICP-AES is its relative freedom from matrix effects. However, since the zone located within the ICP load coil is observed during axial viewing, matrix effects occurring in this zone are observed. Optimization of plasma power and carrier gas flow are required to minimize these effects. Further studies are necessary to determine optimal operating conditions to remove these unwanted matrix effects.

5.3 Time resolved emission from individual particles in an axially viewed helium microwave induced plasma

A commercially available particle analyzer system has recently been developed which was based on an axially viewed helium microwave induced plasma (MIP) [12-14]. Time resolved emission from individual particles was observed on four channels simultaneously. Therefore, this instrument was capable of obtaining information on the elemental composition, size, and number of specific particles in a collected sample. This instrument was targeted for use in the semiconductor industry for aerosol monitoring. Careful quality control of clean room environments is important since stray particles can negatively impact yields in semiconductor manufacturing. Other suggested areas of application were in the quality control of powdered materials such as ceramics, pigments, catalysts, and metals.

In a typical aerosol analysis, particles were collected on a nuclepore filter paper of 0.4 μm pore diameter. The filter was placed in a helium atmosphere and the particles were introduced to the MIP by aspiration with a flow of helium gas. Since impurity gases other than helium were excluded from the plasma, stable operation of the MIP was maintained. Fibre optics transmitted the emission pulses to four separately tunable spectrometers based on PMT detection. The peaks of these emission pulses were captured with a data converter which had a temporal resolution of 130 μs. Therefore, the time and voltage associated with each emission pulse was recorded on four channels and was stored for subsequent analysis. Colloid materials from solution samples could be analyzed in a similar manner after the particles were removed by filtration.

The He-MIP was used as a plasma emission source since it can efficiently excite emission from elements such as the halogens. However, examples of halogen analysis of

individual particles were not reported for the particle analyzer system. Compared with the ICP, the MIP is less robust. It suffers from matrix effects since the plasma gas temperatures and operating powers are insufficient to completely vaporize large or refractory samples. Since the ICP is better characterized and more analysts are familiar with its operation, the use of an ICP as an emission source for individual particle analysis seems logical. This chapter presents a preliminary investigation of time resolved particle analysis from an axially viewed ICP.

5.4 Instrumentation

Temporal emission profiles originating from laser ablated plumes were collected as described in Chapter 4. The only difference was that a scanning monochromator was used to observe the emission pulses from an axially oriented ICP. The scanning monochromator allowed for greater flexibility compared to the direct reader used in Chapter 4. For example, atom and ion lines from the same element could be monitored. The experimental parameters and components are listed in Table 5.1 and the samples used in this study are listed in Table 5.2. Unless otherwise stated, the equipment used for the acquisition of axial emission was the same as the equipment described in Chapter 4. A digitization rate of 18 μs/point with a t_r of 0.01 ms produced resolved emission profiles originating from individual particles.

Table 5.1 Hardware specifications and operating parameters for axially viewed emission profiles from individual particles.

ICP	Plasma Therm ICP 2500
ICP operating conditions	Forward power 1.25 kW; reflected power <25 W;
Optics	4 in focal length imaging lens; plasma imaged 1:1 at a position 14 mm beyond the load coil
Ar flow rates	Central 0.8 l/min; auxiliary 1.0 l/min; plasma 14 l/min
Spectrometer	Heath 0.35 m Model EU-700
Slit width	40 μm
Circular aperture	4 mm, unless otherwise stated
Elements and wavelengths	Ca II 393.367 nm, Mg I 279.553 nm, Mg II 279.553 nm, Cu I 324.754 nm, Cu II 224.700 nm, Fe I 373.487 nm, Co I 345.351 nm, Cd I 228.802 nm, Cd II 226.502 nm.
PMT voltage	-600 V

Table 5.2 Samples used for axially viewed ICP-AES investigation.

Matrix	Element	Sample	Respective concentration, % w/w
Aluminum	Cu	Alcoa SS-380-6	3.58
Steel	Fe, Cu, Mg Ca	SRM 1261a	95.6, 0.042, 0.00018, 0.000028
Brass	Cu	SRM C1106	59.08
Mossy Cd	Cd	Matheson Coleman & Bell	99.9
Co metal	Co	Fisher Scientific Co.	99.4

5.5 Axially viewed emission profiles from individual particles

5.5.1 Preliminary optimization

The only experimental parameters which were varied during this study were the plasma length and the diameter of the circular aperture in front of the entrance slit. The length of the plasma was determined by the position of the air cutoff stream. See Fig. 5.1. The plasma length was measured from the top of the load coil and was varied between 2 and 12 cm. At 2 cm, the air cutoff stream was located directly inside the luminous portion of the plasma and interfered significantly with the emission profiles from individual particles. The circular aperture removed unwanted background emission from the plasma and was varied between 1 and 5 mm. The effect of various aperture diameters and plasma lengths was initially studied for solution nebulized samples to gain a better understanding of the axially viewed ICP. These results are shown in Fig. 5.2 and will be compared with the results of particle emission profiles in section 5.5.4.

The emission intensity of a solution nebulized copper sample and the signal-to-background noise ratio for the same sample at various aperture diameters and plasma lengths is shown in Fig. 5.2. The emission signal was acquired under the same bandwidth parameters as used for particle analysis and was integrated for 1 s. The background noise represents the standard deviation of the 1 s acquisition when aspirating the solution blank. The emission signal increased as the aperture diameter increased for all plasma lengths investigated. It is interesting to note that the emission intensity increased between plasma lengths of 4 to 6 cm. When the plasma is viewed laterally, the vertically viewed portion of the plasma normally extends from about 10 to 20 mm above the load coil. It is obvious from Fig. 5.2a that emission occurred well beyond this range. For axial viewing of solution nebulized samples, there appears to be no benefit of

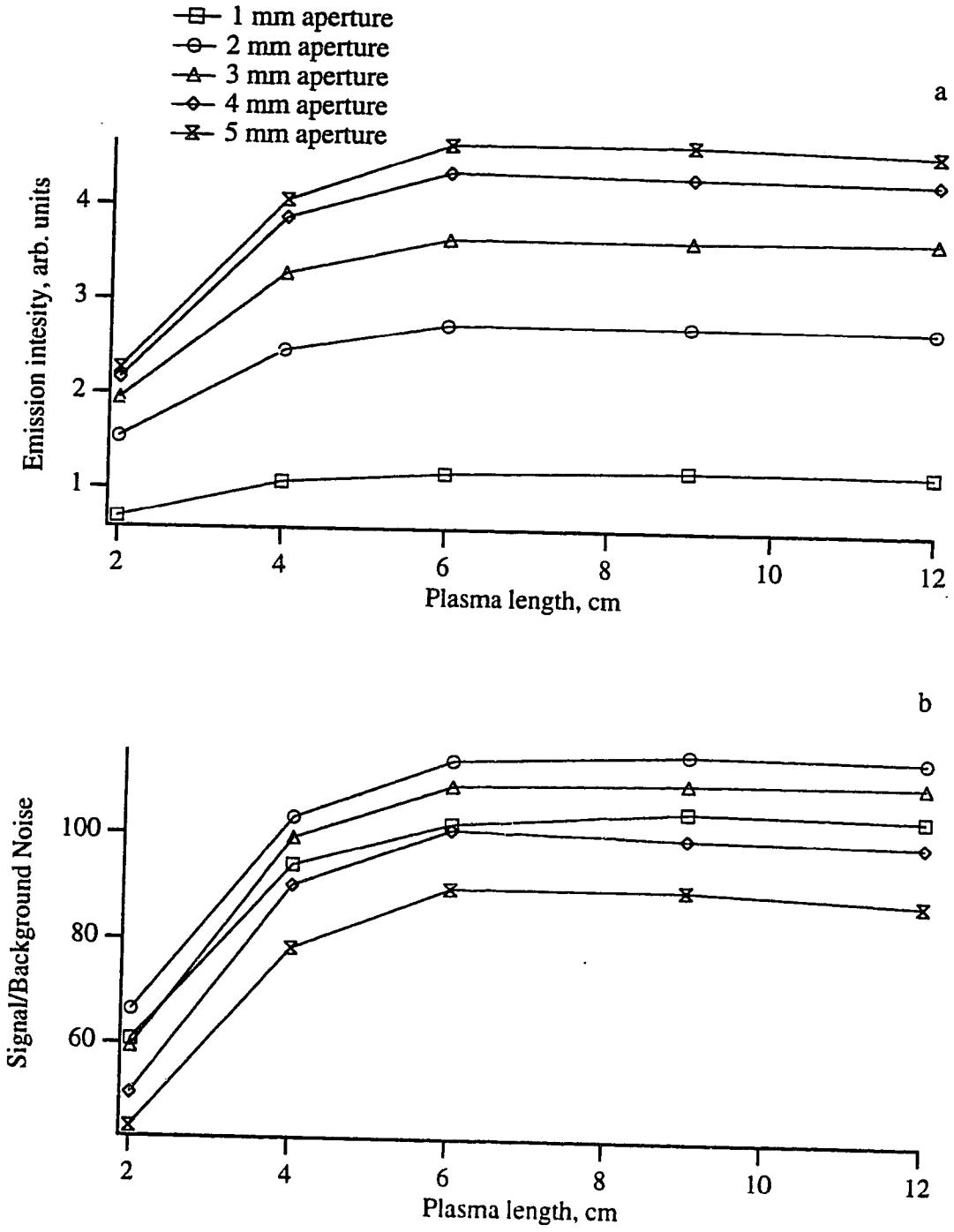

Fig. 5.2 Solution nebulization of 5 µg/ml Cu. Emission intensity as a function of plasma length (a) and signal-to-background noise as a function of plasma length (b) at various aperture diameters. Cu I 324.754 nm.

allowing the plasma to extend beyond 6 cm. The ability of the circular aperture to remove unwanted background emission is observed in Fig. 5.2b. A 2 mm aperture gave the highest signal-to-background noise ratio. Increasing the aperture beyond 2 mm for solution nebulized samples resulted in a poorer acquisition in terms of the signal-to-background noise ratio.

Particle emission profiles were acquired for Cu by the laser ablation of a brass sample and baseline peak widths at various plasma lengths and apertures are shown in Fig. 5.3. At all plasma lengths, the baseline width of the emission profile from individual particles was independent of aperture diameter. This implies a high degree of directional stability for the vapor plume from individual particles as they moved through the plasma. As long as the vapor plume from an individual particle stayed aligned with the central optical axis of the torch and spectrometer, emission from the vapor plume was observed. If the vapor plumes diffused away from the central optical axis, their peak widths would increase with increasing aperture diameters. Emission from vapor plumes of individual particles was observed well into the recombination zone of the plasma since baseline peak widths increased for plasma lengths up to 12 cm. This contrasted with data shown in Fig. 5.2a where the emission intensity from solution based samples increased only up to a plasma length of 6 cm. This difference could arise from the difference in particle sizes produced from solution nebulized samples versus laser ablation. If we assume a mean droplet diameter of 10 μm entering the ICP with an analyte concentration of 5 μg/ml, then the mass of the desolvated salt particle will be on the order of 1 to 2 fg. The trajectory of this small particle could move it off the central optical axis sooner than the relatively large particles produced from laser ablation.

For the rest of this study, an aperture diameter of 4 mm was used. Although a smaller diameter could have been chosen, an aperture of 4 mm was selected to ensure that

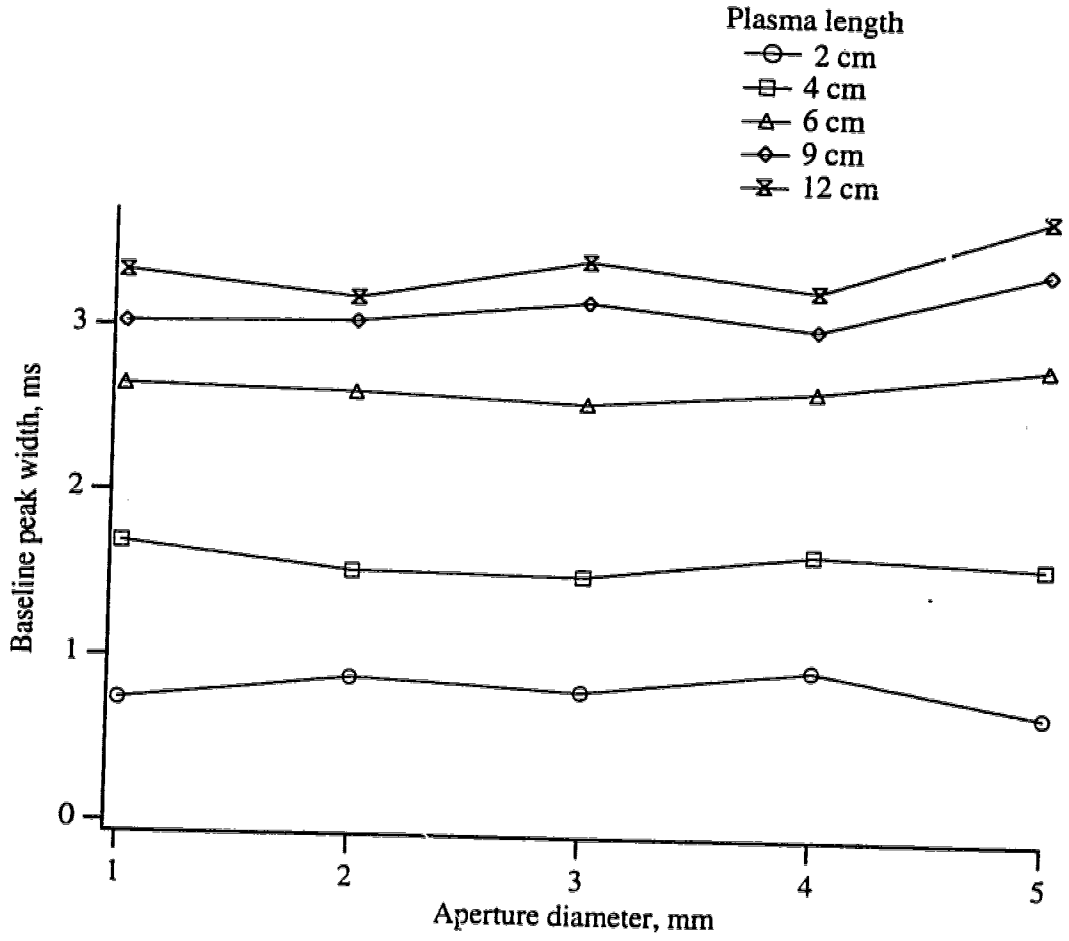

Fig. 5.3 Baseline peak width as a function of aperture diameter at various plasma lengths. Particle emission monitored from Cu I 324.754 nm.

the majority of emission pulses were observed by the spectrometer. The detection limits which were calculated from emission profiles would have been reduced had a smaller diameter been chosen.

5.5.2 Entire emission profiles from one laser ablation pulse

Entire emission profiles from one laser ablation event are presented in Figs. 5.4 and 5.5. The emission from Fe in a steel sample is shown in Fig. 5.4a and the emission from Mg in the same steel sample is shown in Fig. 5.4b. These emission profiles look similar to the profiles observed with lateral viewing of the plasma as shown in Chapter 4. The shift in the background shown for Fe emission in Fig. 5.4a was also observed when the plasma was viewed laterally. This effect was always more pronounced for the initial few laser ablation shots on the solid sample. Individual particles were vaporized in the high temperature plasma and the emission pulses from the vapor plumes of individual particles were observed as spikes in the temporal profiles. An obvious shift in the baseline is observed for the Fe emission from a steel sample in Fig. 5.4a. As discussed in Chapter 4, this shift in the baseline was the result of emission from the vapor plume of many small particles. The emission profile from a minor elemental constituent in the steel sample is shown in Fig. 5.4b. The concentration of Mg in the steel sample is only 0.00018% but emission pulses are easily seen in the high bandwidth acquisition.

A 9 s emission profile from a powdered sample of Co is shown in Fig. 5.5. When the time scale was expanded, individual emission peaks were temporally resolved. A light covering of Co powder was applied to adhesive tape and the tape was placed in the laser ablation chamber. The Co powder was mobilized into the Ar stream when the laser fired and particles of Co were transported to the ICP. Particles can be individually detected regardless of the source of the particles. High bandwith detection of individual

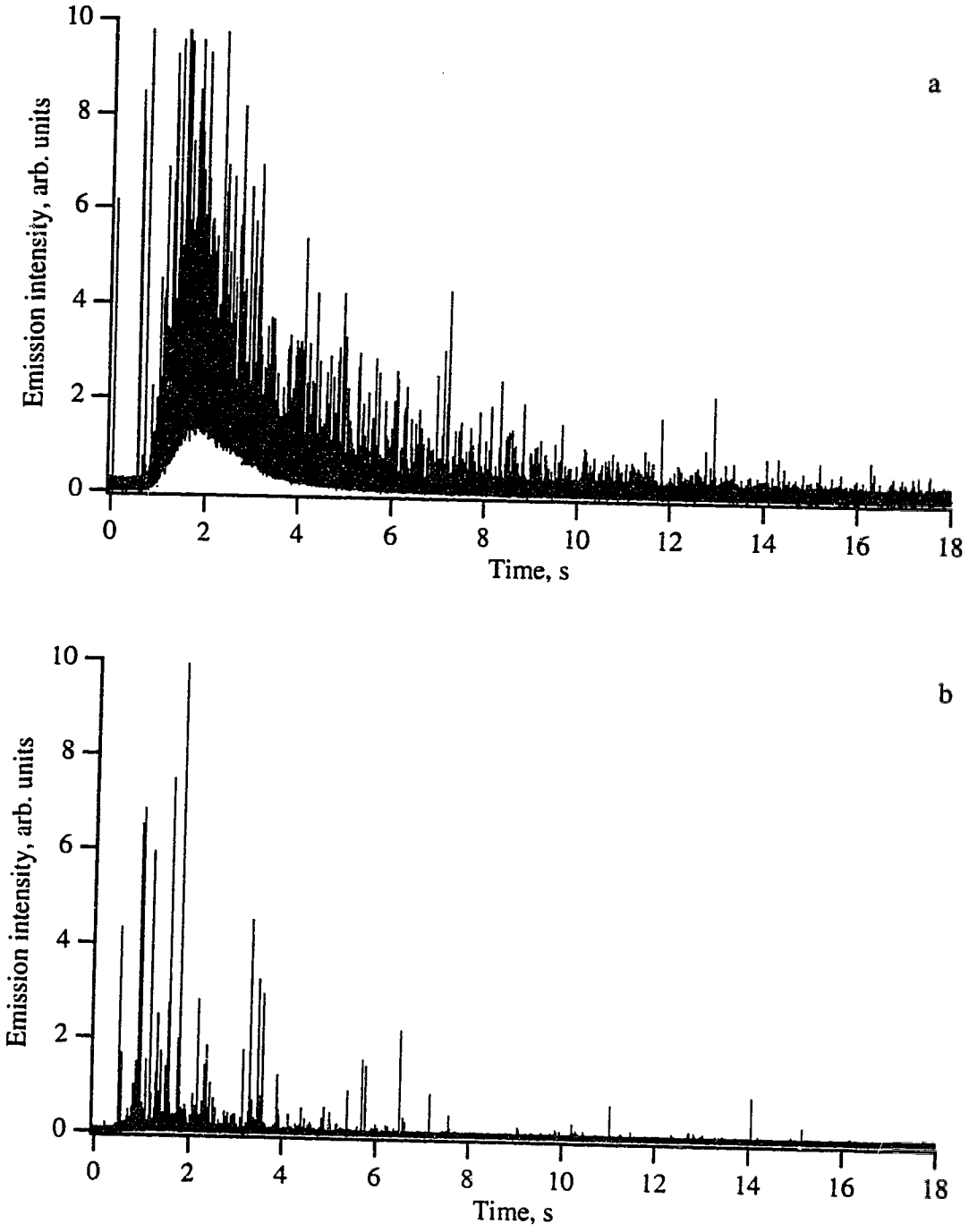

Fig. 5.4 Emission profiles of Fe in steel, SRM 1261a, Fe I 373.487 nm (a) and Mg in steel, SRM 1261a, Mg II 279.553 nm (b).

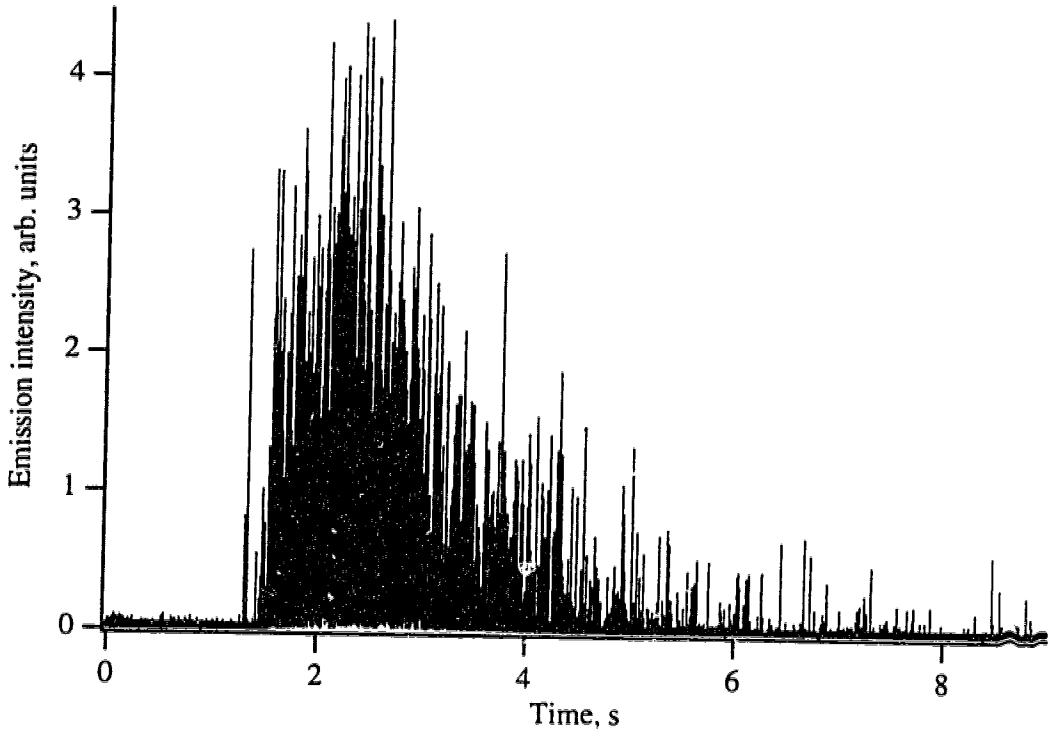

Fig. 5.5 Emission profile of Co, Co powder Fisher Scientific Co., Co I 345.351 nm.

particles can therefore be applied to powder and slurry analysis and is not restricted to laser ablation. Emission from the vapor plumes of individual particles of Co are shown in the following section.

5.5.3 Examples of emission profiles from vapor plumes of individual particles

Profiles of emission plumes from individual particles are shown in Figs. 5.6 to 5.12 and all these profiles were collected with a plasma length of 12 cm. The elemental mass responsible for these profiles is indicated on the figures. Mass calibration was accomplished by solution nebulization as discussed in Chapter 4. In order to make visual comparisons between different emission profiles, the emission intensity was normalized so that all the profiles showed the same peak height.

The atomic and ionic emission profiles of Cu in different matrices are shown in Figs. 5.6 and 5.7. Emission of Cu in steel is shown in Fig. 5.6 and emission of Cu in aluminum is shown in Fig. 5.7. Regardless of the sample matrix, the atomic Cu profile slowly returns to the baseline after the main emission peak. This will be referred to as the secondary emission profile. Atom and ion emission profiles are shown in Figs. 5.8 and 5.9 for Mg and Cd respectively. The atomic emission from these elements did not show a secondary emission profile. Secondary emission is clearly observed in Figs. 5.10a and b for Fe and Co. For Co, the secondary peak was very intense, surpassing the intensity of the primary emission peak. The secondary emission observed for these examples was not a result of the overlap of emission profiles from separate particles since all the peaks in the entire profile showed this effect. Emission profiles shown in Fig. 5.11 illustrate this secondary effect for multiple emission peaks of Co.

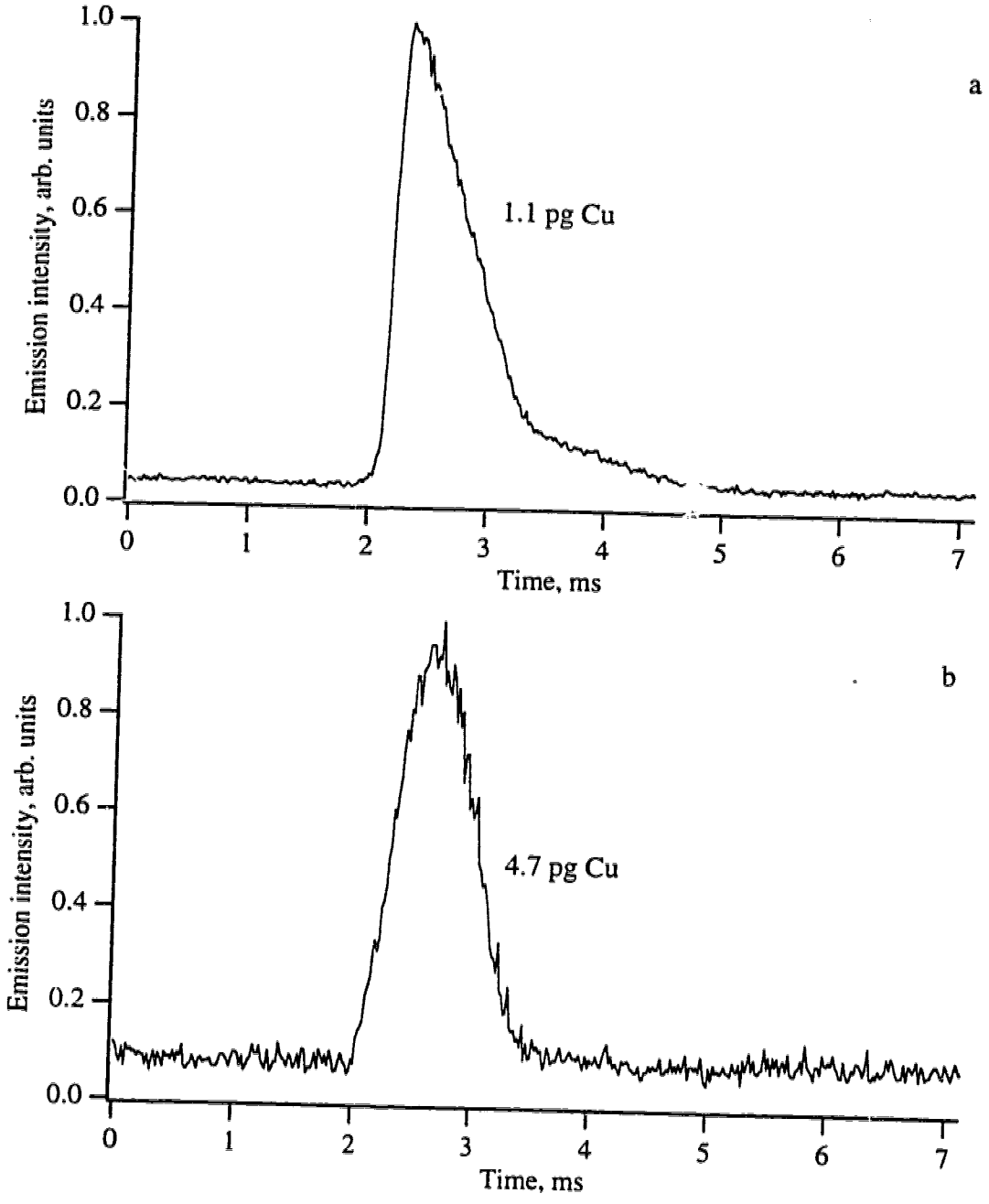

Fig. 5.6 Individual particle emission profiles of Cu in steel, SRM 1261a, Cu I 324.754 nm (a) and Cu II 224.700 nm (b).

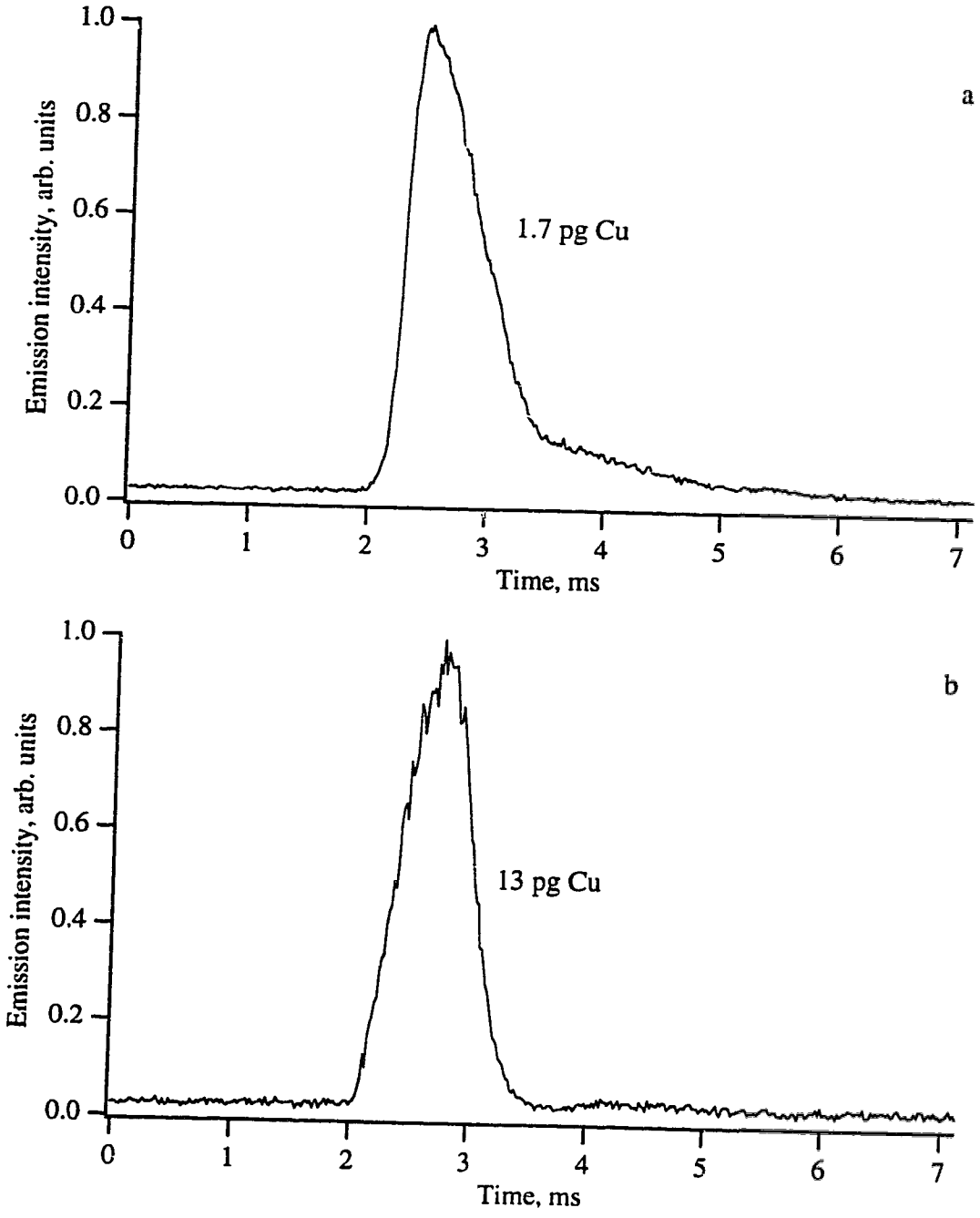

Fig. 5.7 Individual particle emission profiles of Cu in Aluminum, SS-380-6, Cu I 324.754 nm (a) and Cu II 224.700 nm (b).

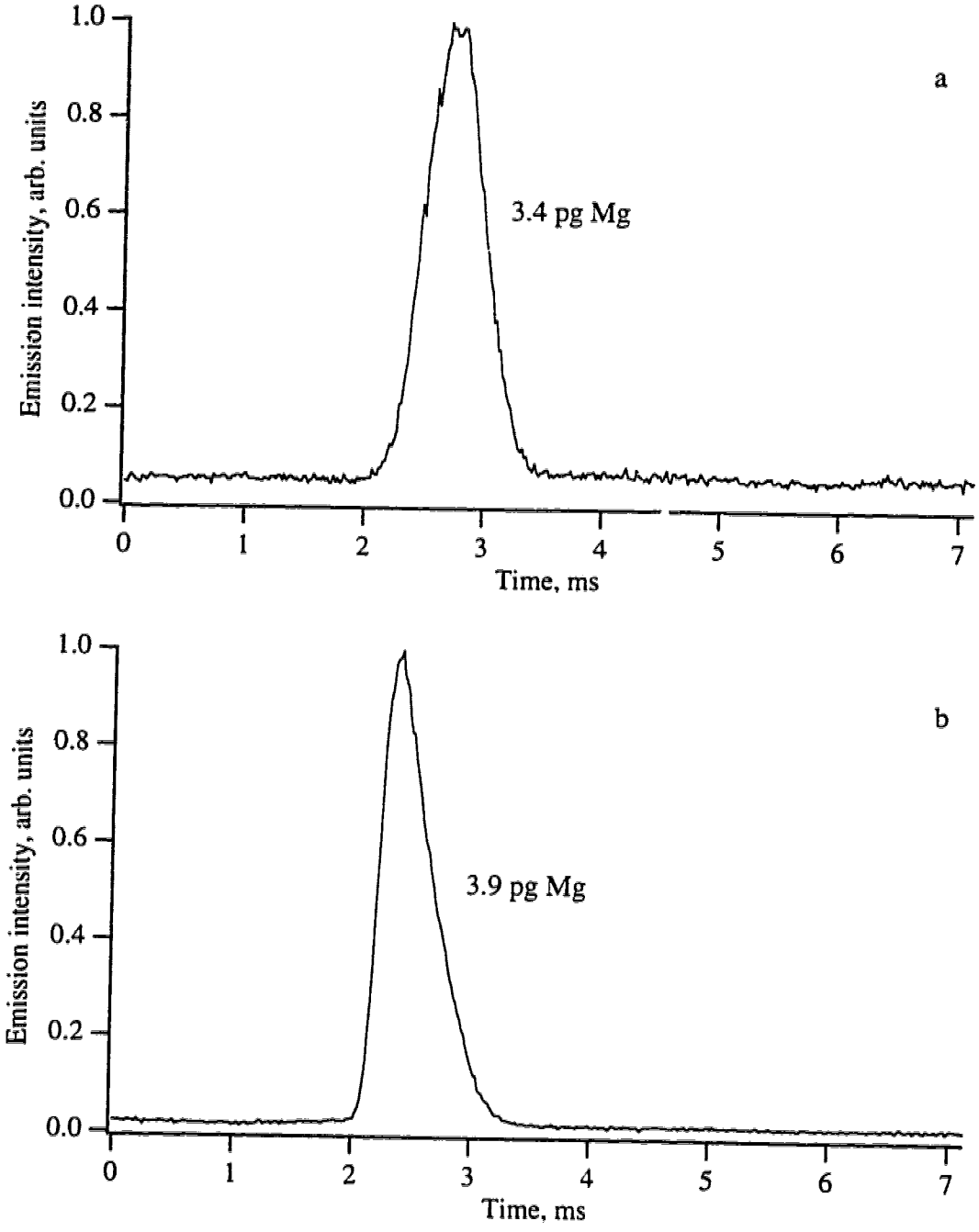

Fig. 5.8 Individual particle emission profiles of Mg in steel, SRM 1261a, Mg I 285.213 nm (a) and Mg II 279.553 nm (b).

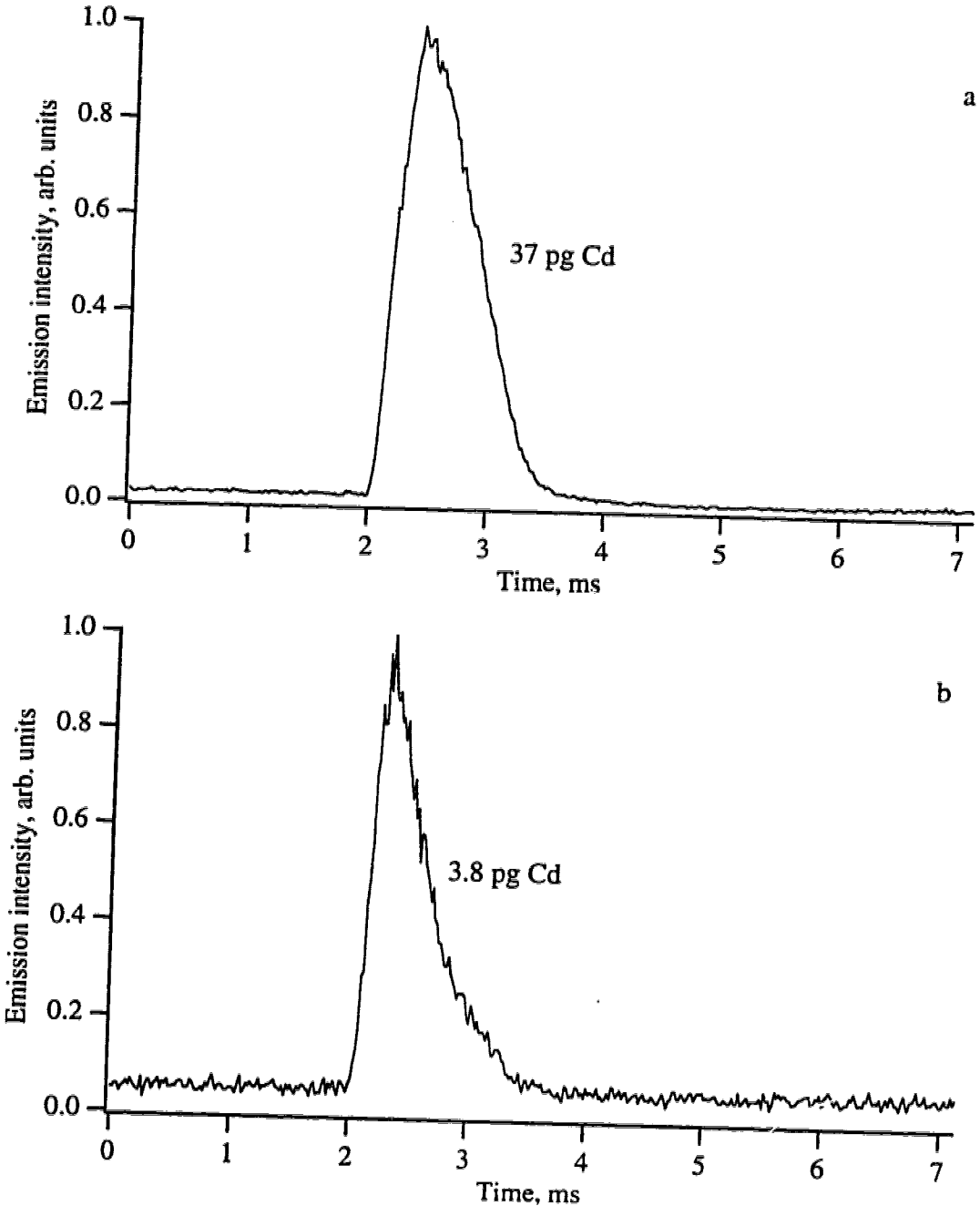

Fig. 5.9 Individual particle emission profiles of Cd, Mossy Cadmium Matheson Coleman and Bell, Cd I 228.802 nm (a) and Cd II 226.502 nm (b).

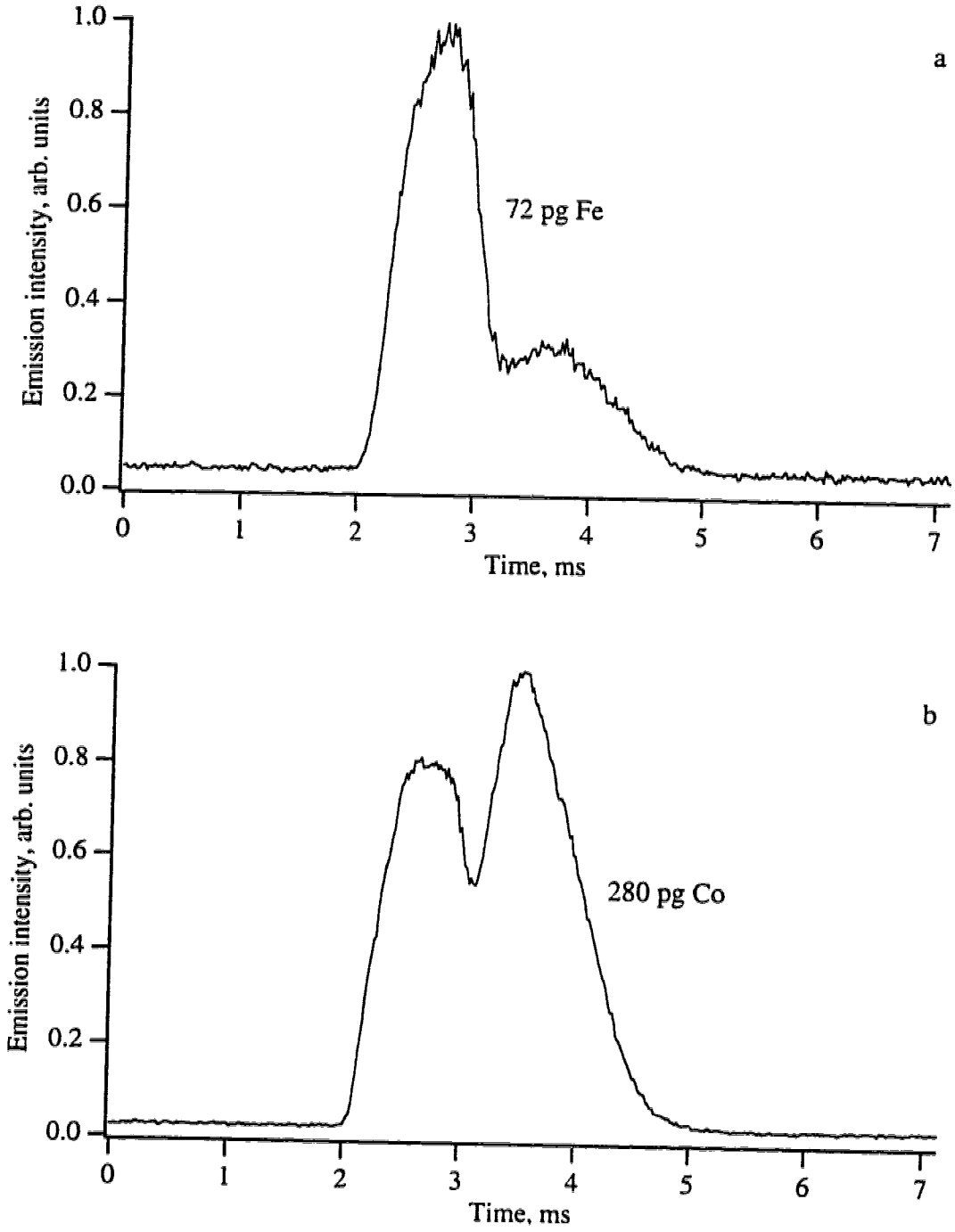

Fig. 5.10 Individual emission profiles of Fe in steel, SRM 1261a, Fe I 373.487 nm (a) and Co, Co powder Fisher Scientific Co., Co I 345.351 nm (b).

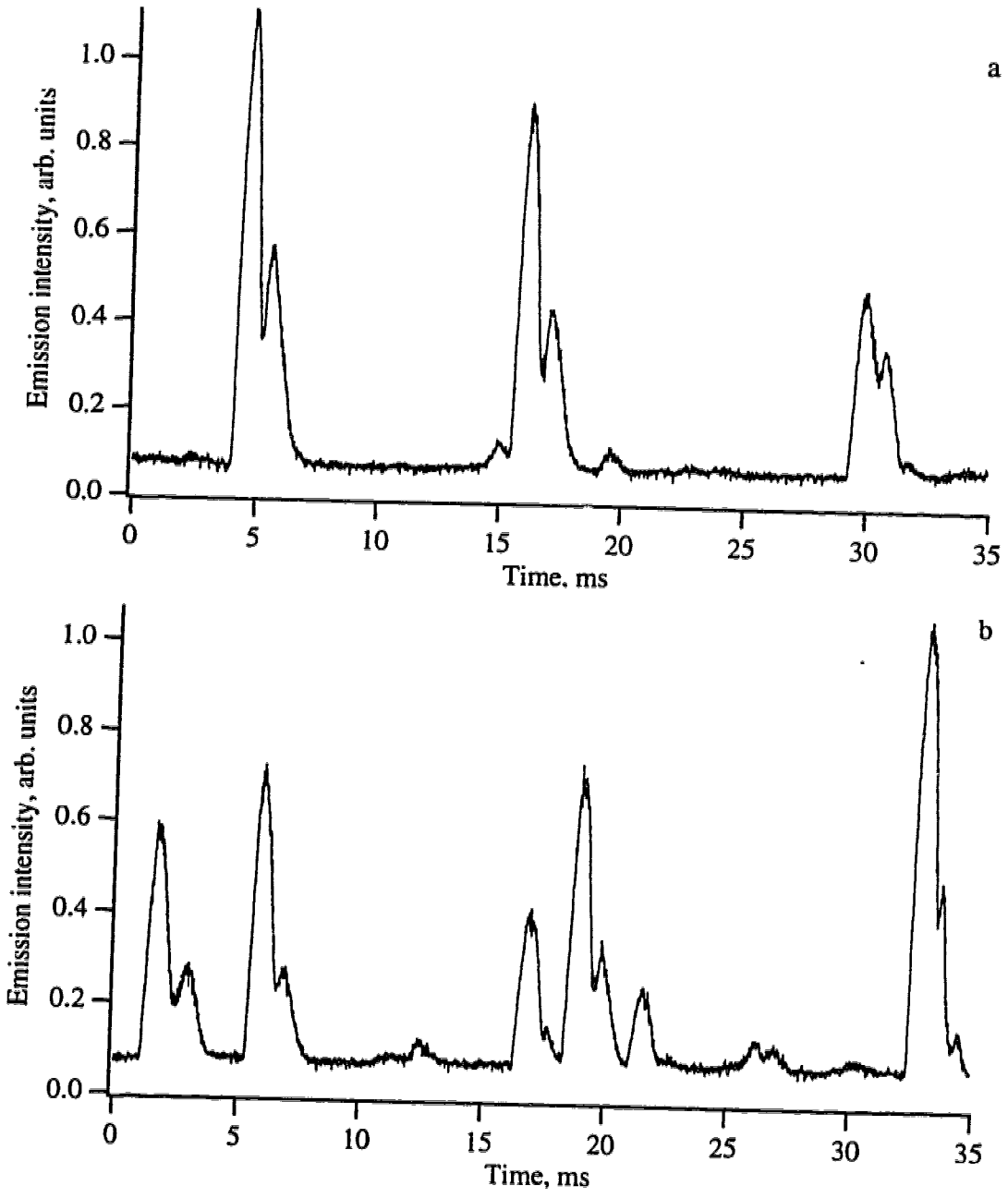

Fig. 5.11 Emission profiles of Co, Co powder Fisher Scientific Co., Co I 345.351 nm. Profiles (a) and (b) both show secondary emission effect.

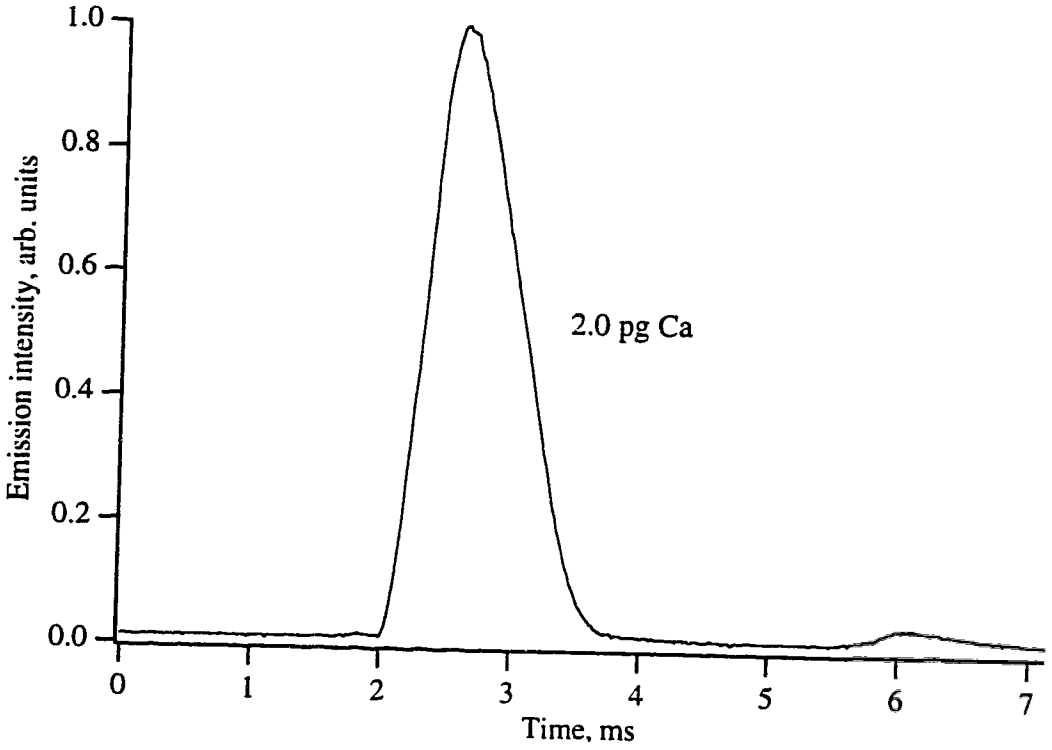

Fig. 5.12 Individual particle emission profile of Ca in steel, SRM 1261a, Ca II 393.367 nm.

A detection limit of 6 fg was calculated from the emission profile of Cu in Fig. 5.6a. This is only marginally higher than 4 fg which was the detection limit calculated for Cu in steel when viewed laterally in the plasma, as shown in the previous chapter. It was initially assumed that axial viewing of particle emission would provide lower detection limits than lateral viewing. Greater sensitivities for axial viewing were not observed in this study and can be attributed to several factors. First of all, different spectrometers were used for lateral and axial viewing. The spectrometer used for lateral viewing has a 1.0 m focal length compared with 0.3 m for the spectrometer used for axial viewing. This difference in focal length resulted in an increased background noise for axial viewing and resulted in higher calculated detection limits. Also the PMT voltage was not the same for both measurement systems. For lateral viewing the PMT voltage was -840 V and for axial viewing the voltage was -600 V. This difference could account for the similar sensitivities observed for lateral viewing and axial viewing. Particle size distributions for axial viewing were not calculated but would be similar to those observed for lateral viewing since similar sensitivities were observed in both cases.

Vertically resolved emission profiles have been observed for Fe [4] and Co [7] in a conventional laterally viewed plasma. The Fe emission profile showed a secondary emission peak similar to that observed in Fig. 5.10a. However, the Co emission profile did not show this feature. These profiles were acquired with solution nebulized samples and not from individual particles viewed axially in the plasma. Therefore, the emission profiles acquired in these previous studies came from many desolvated small particles of different sizes. Since the particles were of varying sizes, the vertical emission profiles may not have been as well resolved as the profiles presented in this study. For the case of Co, it is possible that the previous study did not look far enough into the recombination zone of the plasma to observe the secondary emission effect.

As noted on Fig. 5.10b, the mass of Co was calibrated to be 280 pg. This is very large in comparison with other observed masses and can be explained in two ways. First of all, Co was introduced to the plasma by ablating a small powdered sample of Co. Since the particles were not solely produced by laser ablation, it is possible that larger particles present in the original powdered sample could have been detected. The solution calibration procedure could also be in error. Recall from Fig. 5.2a that the emission intensity for a solution nebulized Cu sample did not increase when the plasma length was increased from 6 to 12 cm. The secondary emission effect observed for laser ablated particles of Cu, Fe, and Co may not be observed for solution nebulized samples of these elements. Therefore, the calibrated masses for atomic Cu, Fe, and Co are likely in error and are larger than they should be.

A Ca emission profile from an individual particle is shown in Fig. 5.12. This profile illustrates the very high emission intensity of the Ca II 393.367 nm line. A high signal-to-background noise ratio is observed for only 2.0 pg of Ca. This high sensitivity will be further illustrated in section 5.5.5 where detection limits for Ca will be presented. The Ca originated from a low alloy steel sample which contained only 0.000028% Ca. The next section highlights the differences between lateral versus axial viewing of the plasma for individual particle detection.

5.5.4 Emission peak widths from individual particles

When particle emission profiles were viewed laterally in the plasma, there was no discernible difference between ion and atom peak widths. All peak widths were determined by the transit time of the vapor plume through the observation region of the plasma and were on the order of 0.5 ms. It was assumed that peak widths determined

from an axially viewed plasma would vary depending on whether the emission line was from an atom or ion line. A detailed investigation of peak widths from a selected number of ion and atom lines is presented in this section.

Tabulated baseline peak measurements are presented in Tables 5.3 and 5.4 for atom and ion emission lines respectively. Reported peak widths were the mean value of, at most, ten peaks. The emission peaks which were selected were approximately the same intensity since peak widths were somewhat dependent upon emission intensity. However, since the particle sizes were not identical, peak widths varied marginally from particle to particle. This is reflected in the relatively large standard deviation reported for each measurement.

When the plasma length was limited to 2 cm, the emission profiles from individual vapor plumes were dramatically effected. This is shown in Fig. 5.13 where the emission profile was abruptly terminated after slowly rising to a maximum value. This occurred since the air cutoff stream sliced into the luminous zone of the plasma, abruptly terminating analyte emission. When comparing the peak widths for Mg and Cu, the peak widths from atomic emission were slightly larger that for ionic emission for a plasma length of 2 cm. This is a reasonable expectation since atomic emission occurred before ionic emission for an individual particle as it entered the plasma. This is also shown in Fig. 5.1 where the relative positions of atomic and ionic emission are presented. The velocity of vapor from 0 to 20 mm above the load coil was approximately 20 m/s [15] and it should be possible to determine the relative spatial position of atomic and ionic emission based on the vapor velocity and the peak width. However, the large uncertainty associated with the peak width measurements prohibit an accurate calculation. This problem would be avoided if atom and ion emission was recorded simultaneously.

Table 5.3 Baseline peak widths of atomic emission profiles

	Baseline peak width, ms				
Plasma length	Mg I	Cu I	Fe I	Co I	Cd I
2 cm	0.89±0.12	0.80±0.06	0.67±0.10	0.64±0.07	0.87±0.12
4 cm	1.27±0.12	1.59±0.25	1.37±0.19	1.45±0.27	1.61±0.19
6 cm	1.34±0.14	2.44±0.27	2.40±0.30	2.34±0.21	1.75±0.14
9 cm	1.23±0.09	2.84±0.41	2.79±0.30	2.89±0.42	1.78±0.17
12 cm	1.22±0.07	3.02±0.26	3.01±0.31	3.00±0.40	1.85±0.28

Table 5.4 Baseline peak widths of ionic emission profiles.

	Baseline peak width, ms			
Plasma length	Ca II	Mg II	Cu II	Cd II
2 cm	0.85±0.08	0.87±0.16	0.79±0.13	0.77±0.11
4 cm	1.80±0.14	1.42±0.18	1.37±0.21	1.41±0.09
6 cm	1.89±0.30	1.41±0.13	1.35±0.07	1.44±0.10
9 cm	1.99±0.26	1.39±0.16	1.37±0.12	1.48±0.16
12 cm	1.96±0.11	1.34±0.10	1.33±0.09	1.39±0.04

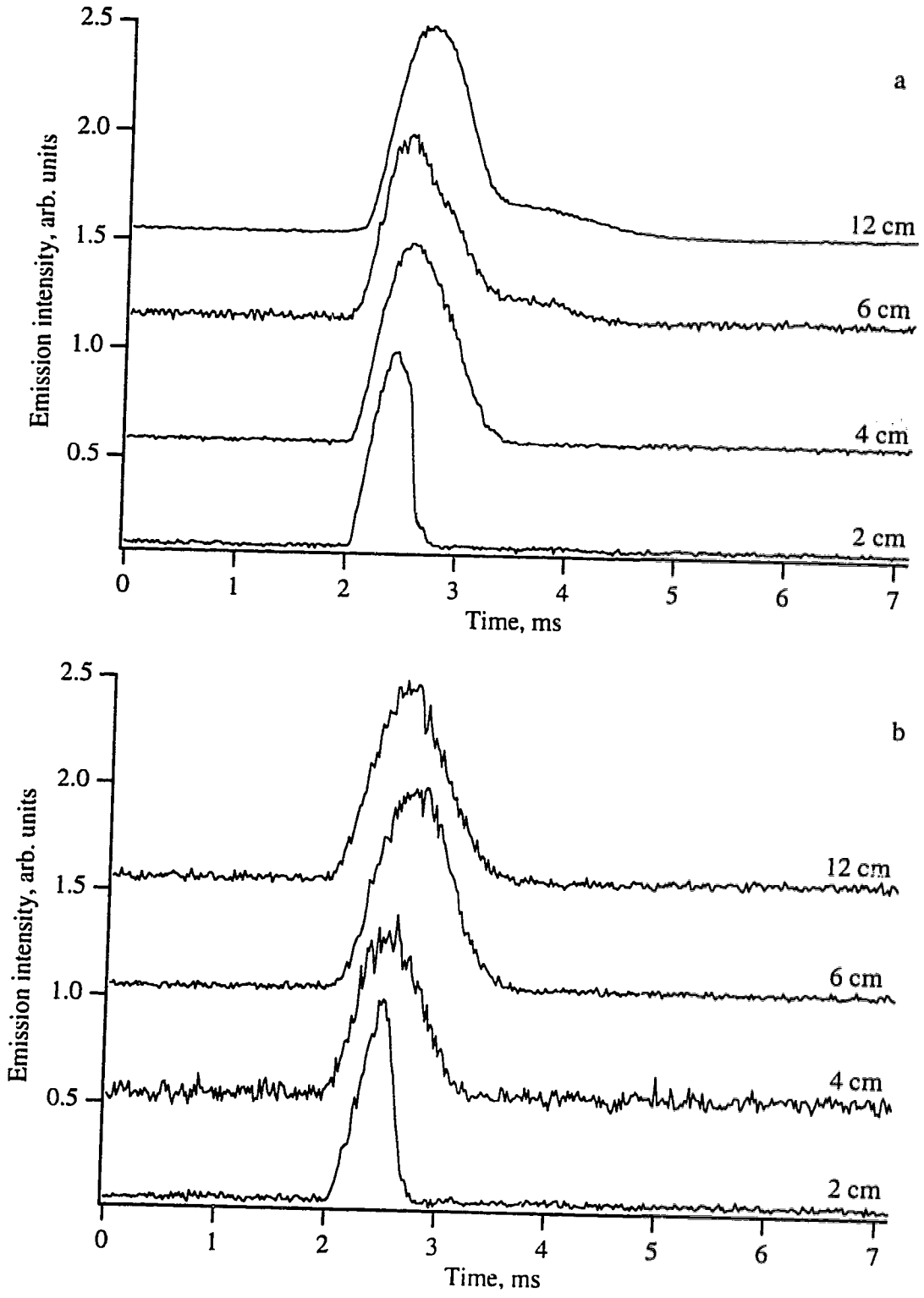

Fig. 5.13 Emission profiles of Cu in brass, SRM C1106, for various plasma lengths. Atom profiles Cu I 324.754 nm (a) and ion profiles Cu II 224.700 nm (b).

The tabulated data from Tables 5.3 and 5.4 are plotted in Figs. 5.14 and 5.15. The interpretation of the baseline measurements for the ion lines, as illustrated in Fig. 5.14, is straightforward. For the ion lines, the peak widths increased as the plasma length increased between 2 and 4 cm. This resulted from the air cutoff stream interfering with analyte emission at the 2 cm position. As the plasma length increased from 4 to 12 cm, no further increase in emission peak width was observed. Spatial emission studies have shown that the position of ionic emission is relatively consistent between elements and is maximized between 15 to 20 mm above the load coil, depending on operating conditions [2]. This is confirmed by the data presented in Fig. 5.14 where all the peak widths, except Ca, were closely grouped together. The peak widths calculated for Ca were significantly larger than the peak widths of the other ionic emission lines. This is understandable when considering that the Ca II 393.367 nm emission line was significantly more intense than the other ionic emission lines studied. It has already been shown in Tables 4.3. and 4.4 that the peak width can vary more that 1 ms when comparing an intense emission profile to a weak profile. Therefore, it is reasonable to assume that the intense emission line of Ca would yield peak widths which were larger than the widths calculated from the other elements.

Peak widths calculated for atom lines are shown in Fig. 5.15. The peak widths for Cu, Fe, and Co increased for plasma lengths from 2 to 12 cm. Peak widths for Mg and Cd, however, followed a similar behavior as those calculated from the ion lines i.e., they were relatively consistent between plasma lengths of 4 to 12 cm. The increasing peak width for atomic Cu emission at increasing plasma lengths is illustrated in Fig. 5.13a. For comparative purposes the emission peak widths for ionic Cu is shown in Fig. 5.13b. A secondary emission profile is observed in Fig. 5.13a for the Cu atom emission when the plasma length was 6 and 12 cm. As previously noted, this secondary emission profile occurred after the initial atomic emission and is responsible for the large peak widths

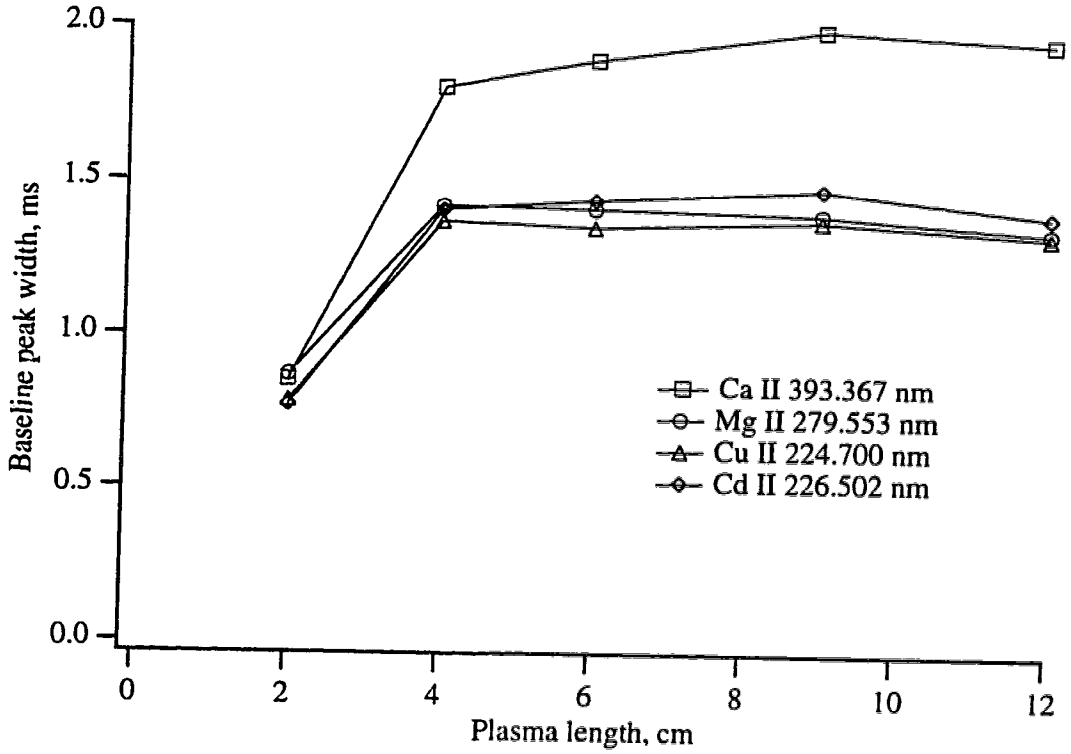

Fig. 5.14 Baseline peak widths of particle emission profiles as a function of plasma length. Ion lines.

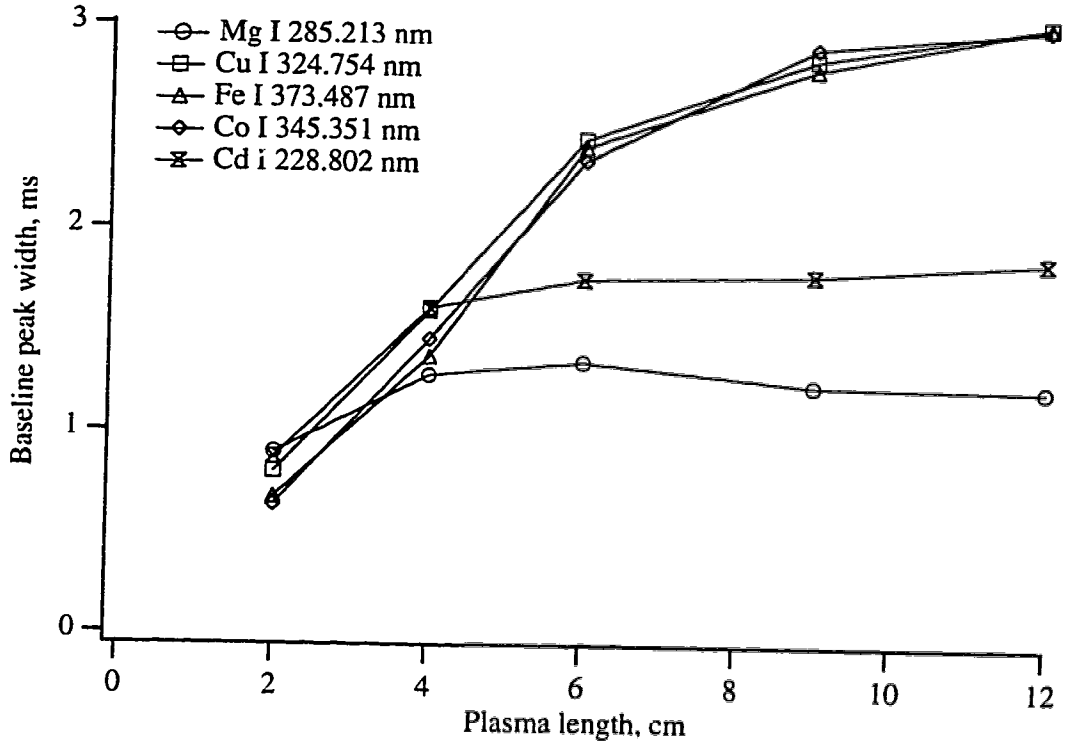

Fig. 5.15 Baseline peak widths of particle emission profiles as a function of plasma length. Atom lines.

which were calculated. There is obviously a different mechanism involved in producing this secondary emission profile and this mechanism will be discussed in the following paragraph.

The proposed mechanism which is responsible for the secondary emission profile observed for Cu, Fe, and Co involves ion-electron recombination. This secondary emission profile was observed in the outer portions of the ICP tail where the electron and gas temperatures were cooler than near the load coil. Ion-electron recombination rates are significantly increased in a cooler plasma where the relative velocities of the ions and electrons are reduced. Analyte ions combine with free plasma electrons and the electrons move downward through the high-lying neutral electronic energy levels until a large energy gap is reached. At this point, the excited atomic species will relax to the ground state by either a radiative or non-radiative process. The high temperature and pressure found in the ICP resulted in a high collisional frequency for species in the plasma. Any ion-electron recombination which occurred in the ICP produced an excited state atomic species which was quickly collisionally deactivated without the emission of radiation [16]. Therefore, ion-electron recombination was responsible for producing ground state atomic species in the outer portions of the ICP tail. A thermal mechanism for atomic emission is likely responsible for the subsequent emission of these ground state atoms.

This secondary emission effect was not observed for Mg and Cd. Ion-electron recombination is known to occur for these elements since recombination lasers based on stimulated emission from Mg and Cd atomic lines have been observed [17]. Therefore, we can assume that ion-electron recombination occurred for these elements in the recombination zone of the ICP. The absence of emission from the atoms produced for Mg and Cd by recombination is explained by considering the upper electronic energy levels responsible for emission. These levels are 3.82, 4.02, 4.18, 4.34, and 5.41 eV for

Cu, Co, Fe, Mg, and Cd respectively. The upper electronic levels for Mg and Cd were higher than the other transitions studied and this explains the lack of a secondary emission feature for these elements. Although Mg and Cd atoms are produced, there is insufficient thermal energy in the tail portion of the ICP to excite atomic emission.

Referring back to Tables 5.3 and 5.4, the peak width for Mg ions was greater than Mg atoms and, conversely, the peak width for Cd atoms was greater than Cd ions. This is explained by the relative ionization potential of Mg compared with Cd. The ionization potential for Mg is 7.646 eV and the ionization potential for Cd is 8.993 eV. Calculations showed that 98% of Mg and 85% of Cd was present as ions in the ICP [18]. Therefore, it is reasonable to assume that the ratio of ion-to-atom peak widths would be larger for Mg than for Cd. These ratios could be followed to optimize experimental conditions for axially viewed particle emission in the ICP.

5.5.5 Detection limits for Ca emission

Detection limits for Ca emission were calculated from the emission profiles shown in Figs. 5.16a to c. Detection limits were determined in an attempt to show the lowest detection limits ever reported for ICP-AES. For the acquisition, the gain on the amplifier was 1000 times higher than the gain used to record the emission profile shown in Fig. 5.12. This was done to avoid a quantizing noise limited background. The vast majority of emission pulses saturated the amplifier and exceeded the range of the ADC. By carefully searching the temporal profile of the laser ablation event, 10 peaks were found which were within the range of the ADC. One of these peaks is shown in Fig. 5.16a and represented only 24 fg of Ca. The average of all 10 of the peaks is shown in Fig. 5.16b. To further reduce the background noise, the averaged profile was digitally low pass filtered. This filtered profile is shown in Fig. 5.16c and a detection limit of 0.01

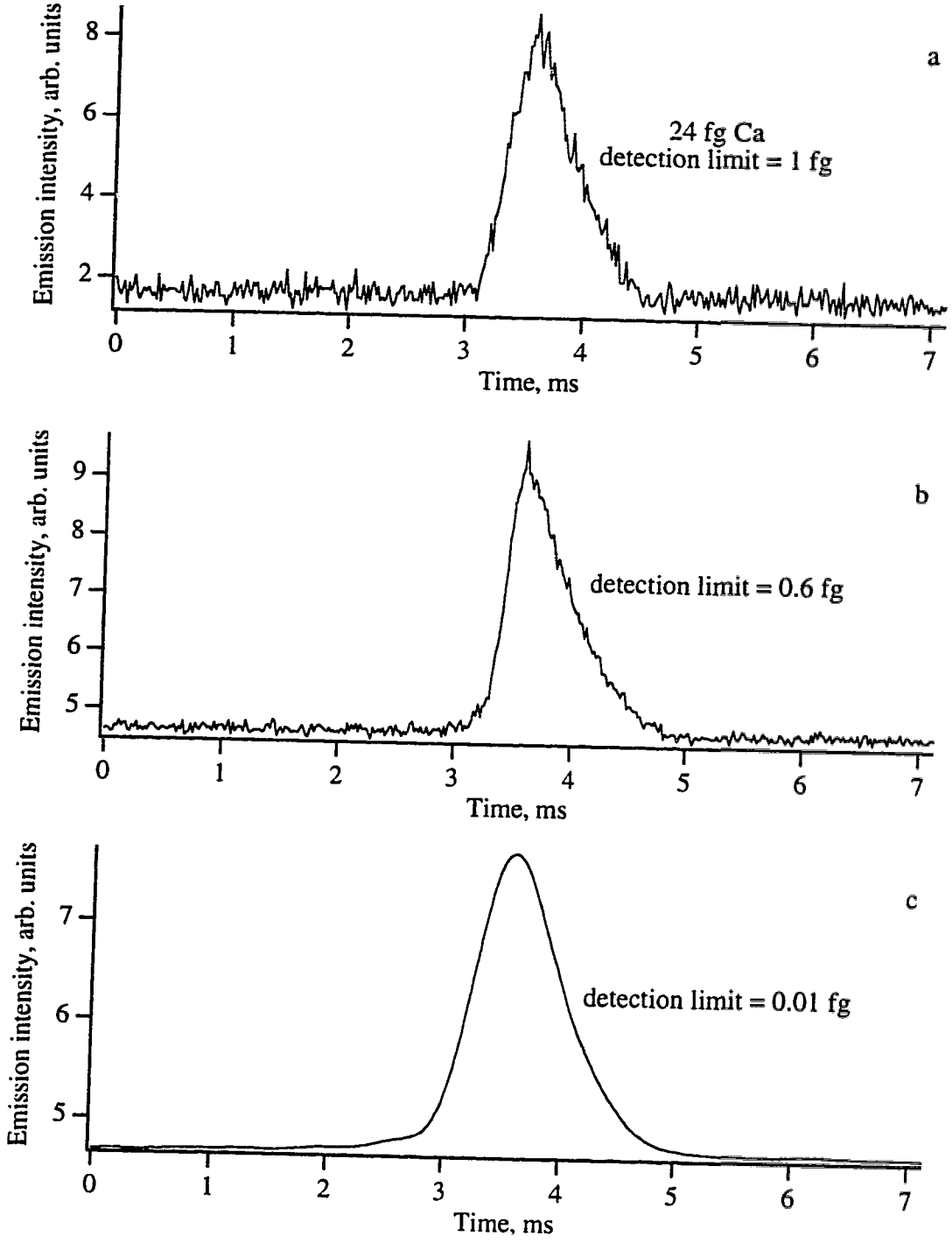

Fig. 5.16 Emission profiles of Ca in steel, SRM 1261a (0.000028%), single particle profile (a), average of 10 profiles (b), digitally filtered average profile (c).

fg (i.e., 10 ag) was calculated. It is obvious that time resolved particle analysis by ICP-AES can be used to determine minor elemental components within individual particles.

5.6 Conclusion

Emission from the vapor plume of individual particles was observed as the vapor moved down the central optical axis of an axially viewed ICP. For emission lines from low energy atomic transitions, a secondary emission profile was observed which was attributed to ion-electron recombination with subsequent thermal excitation. If the velocity of the vapor plume in the recombination zone were accurately known, accurate spatial emission profiles could be determined from the introduction of individual particles. Based on the results from the current investigation, axial viewing of the plasma did not provide an advantage compared to lateral viewing. This investigation was preliminary and further work is necessary to explore characteristics of axially viewed emission from particle introduction.

References

1. J. M. Mermet and E. Poussel, *Appl. Spectrosc.* **49**, 12A (1995).
2. M. W. Blades and G. Horlick, *Spectrochim. Acta* **36B**, 861 (1981).
3. B. L. Caughlin and M. W. Blades, *Spectrochim. Acta* **39B**, 1583 (1984).
4. H. Kawaguchi, T. Ito and A. Mizuike, *Spectrochim. Acta* **36B**, 615 (1981).
5. R. S. Houk and J. A. Olivares, *Spectrochim. Acta* **39B**, 575 (1984).
6. R. S. Houk, J. K. Schoer and J. S. Crain, *Spectrochim. Acta* **42B**, 841 (1987).
7. T. E. Edmonds and G. Horlick, *Appl. Spectrosc.* **31**, 536 (1977).
8. M. H. Abdalla, R. Diemiaszonek, J. Jarosz, J. M. Mermet, J. Robin and C. Trassy, *Anal. Chim. Acta* **84**, 271 (1976).
9. D. R. Demers, *Appl. Spectrosc.* **33**, 584 (1979).
10. L. M. Faires, T. M. Bieniewski, C. T. Apel and T. M. Niemczyk, *Appl. Spectrosc.* **39**, 5 (1985).
11. J. C. Ivaldi and J. F. Tyson, *Spectrochim. Acta* **50B**, 1207 (1995).
12. E. E. S. Frame, Y. Takamatsu and T. Suzuki, *Spectroscopy* **11**, 17 (1996).
13. H. Takahara, M. Iwasaki and Y. Tanibata, *Yokogawa Technical Report* no. 17, 51 (1993).
14. H. Takahara, M. Iwasaki and Y. Tanibata, *IEEE Trans. Instrum. Meas.* **44**, 819 (1995).
15. F. Qin, Pulsed signal fluctuations in ICP-AES. Thesis, University of Alberta (1992).
16. Y. Shao, A spectral study of excitation processes in a glow discharge. Thesis, University of Alberta (1995).
17. W. T. Silvast, L. H. Szeto and O. R. Wood, *Appl. Phys. Lett.* **36**, 615 (1980).
18. R. S. Houk, *Anal. Chem.* **58**, 97A (1986).

Chapter 6

Summary and future directions

Two plasma emission techniques have been studied in this thesis. A high powered HCD with a unique sample introduction interface was designed, constructed, and evaluated. Time resolved measurements showing detection of individual particles with ICP-AES were also performed.

6.1 Continuous sample introduction to a HCD

A sample introduction interface and high powered HCD was designed which accommodated solution, solid, and gaseous samples. The emphasis was placed on continuous solution sample introduction into an operating discharge. Stable discharge operation was maintained by removing the bulk of the solvent with a heated desolvation chamber and water cooled condenser. Sensitive detection of aqueous samples was achieved and sub ng/ml detection limits were observed for selected elements. For dilute solutions, memory effects were minimal and a quantitative response was observed for Li.

In comparison to the ICP, the HCD which was developed cannot be considered a robust plasma source. Discharge stability was difficult to maintain when aspirating solutions which had a dissolved analyte concentration above 50 μg/ml. The Mg II/Mg I line intensity ratio also reflected the lack of discharge robustness since the ratio was maximized at 0.4. For an optimized ICP, this ratio is around 10 and a value below 4 corresponds to a high sensitivity towards matrix effects [1]. It is difficult for a 125 W HCD to compare favorably with a 1500 W ICP for the continuous introduction and analysis of solution based samples.

Improvements in discharge stability and sensitivity towards analyte detection can be realized if a greater proportion of the solvent is removed. Limited discharge power is available and power is required to desolvate aerosol droplets, dissociate solvent molecules, and excite the solvent fragments. Less power is then available to vaporize, atomize, and excite the analyte species. Commercially available membrane desolvators have been used to reduce solvent loading of the ICP [2] and could be used in conjunction with the HCD for the same purpose.

The high powered HCD could be effectively used as an emission detector for gas chromatographic (GC) effluents since the solvent is efficiently removed from the analyte in the chromatographic separation. Since the HCD operates at relatively low powers and consumes modest amounts of plasma gas, it could be economically used as a GC detector. Continued research is required before the HCD is used as a general emission source for the routine analysis of solution, solid, and gaseous samples.

6.2 Time resolved detection of individual particles by ICP-AES

Entire emission profiles of a single laser ablation event were detected in a time resolved manner by ICP-AES. These large profiles showed emission profiles from the vapor plumes of individual particles. Mass detection limits were improved by observing the emission from the vapor plume of a single particle as compared with integrating the entire emission profile of the laser ablation event. High sensitivities were observed for time resolved measurements and detection limits for Fe, Cu, Zn, and Ca were 2 fg, 1 fg, 1 fg, and 10 ag respectively. Single particle analysis allowed the calculation of particle size distributions and these distributions provided insight into particle transport efficiencies. Simultaneous multi-element determinations on individual particles were performed and

showed that elemental concentrations, on a particle to particle basis, did not reflect the bulk concentrations in the solid sample. Multi-element determinations can also be used to distinguish between different types of particles in a complex mixture.

Comparisons between lateral and axial viewing of the plasma were made for the detection of individual particles. Emission peak widths of ion and atom lines were larger for axial viewing than for lateral viewing of the plasma. Laterally viewed emission plumes from single particles had peak widths which were determined by the transit time of the vapor plume through the observation zone of the spectrometer. Elements with atomic emission lines of low excitation energies showed a secondary emission profile due to ion-electron recombination.

The detection and characterization of individual particles by ICP-AES is not restricted to LA. Time resolved measurements can also be made for slurry analysis and for the direct introduction of powders into the ICP. Therefore, single particle analysis could be used to characterize environmental particles, paints, oils, or dust samples. As the speed of computers increase and the storage of large digital files becomes more practical, individual particle analysis will become more common.

Axial viewing of particle emission provides a method of observing the spatial behavior of analyte emission. In the past, spatial profiles have been recorded from solution nebulized samples. However, solution nebulization introduces particles with a range of sizes into the plasma. This has the effect of distorting subtle emission features of the spatial profile. Accurate spatial profiles can be recorded by observing the emission profiles originating from single particles. The simultaneous observation of an ion and atom line of the same element would provide a better understanding of particle vaporization, ionization, and excitation in the plasma.

It has been speculated that atomic mass spectrometry may one day replace emission spectrometry for routine elemental analysis. However, it is difficult to imagine a mass spectrometry technique which is simultaneous and as sensitive as the high bandwidth ICP-AES measurements which were presented. In reply to a recent review of atomic mass spectrometry [3], atomic spectroscopists can still do it with light.

References

1. J. M. Mermet, *Anal. Chim. Acta* **250**, 85 (1991).

2. R. I. Botto and J. J. Zhu, *J. Anal. At. Spectrom.* **9**, 905 (1994).

3. M. W. Blades, *Appl. Spectrosc.* **48**, 12A (1994).

Appendix

Experimental attempts at ES nebulization

The experimental configurations used to introduce solution samples into an operating GDD are shown in Fig. A.1. Voltage biasing to the ES tip, front plate, and sampling plate are given in Fig. 2.13. A sample flow rate of 10 μL/min through the ES tip was used. A counter-current flow of Ar was used as a curtain gas to exclude uncharged solvent droplets from entering the interface. It was anticipated that positively charged analyte ions would become desolvated through the process of ES ionization, accelerated into the plasma, and detected by their characteristic emission wavelengths.

A simple experimental configuration is shown in Fig. A.1a. The ES interface was bolted onto the outside of a GDD and the GDD employed a pin-shaped cathode. It was anticipated that positively charged analyte ions would enter the negative glow region of the discharge and be attracted to the cathode. Excitation process in the glow discharge, as outlined in Table 1.1, could then produce excited state ions and atoms. Unfortunately, analyte emission was not observed. A more elaborate interface is shown in Fig. A.1b and a detailed cross-sectional drawing of the HCD is shown in Fig. 2.1. The glass tube provided the interface from atmospheric pressure to the low pressure in the HCD. This interface was described in detail in chapter two and was used successfully to introduced solution nebulized samples into the HCD via a Meinhard nebulizer, spray chamber, desolvation chamber, and condenser. It was thought that this interface could also be used for solution sample introduction via ES nebulization. Again, analyte emission was not observed.

Failure to observe analyte emission could be the result of plasma potentials associated with the discharge. Charge separation in the discharge causes the majority of the applied voltage to be dropped over the cathode dark space. This places an effective anode in close proximity to the cathode and could shield the cathode from positive ions. Positive ions introduced by ES nebulization could be repelled by this effective anode instead of attracted to the cathode. A more detailed study is required to determine the potential usefulness of ES nebulization into a GDD.

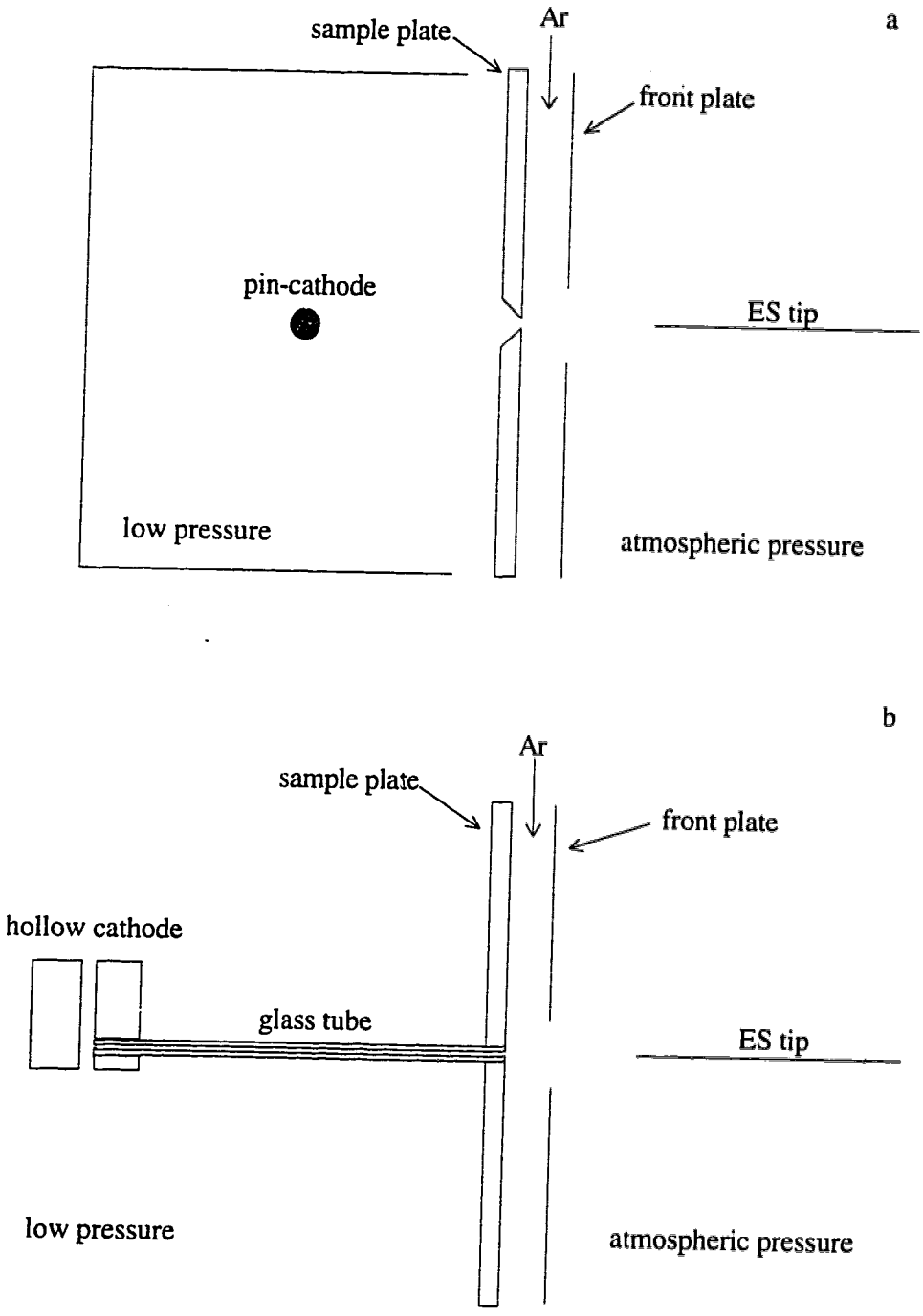

Fig. A.1 Experimental attempts at ES nebulization into a GDD with a pin-cathode (a) and a hollow cathode (b).